



UNIVERSITAT<sup>DE</sup>  
BARCELONA

## Resistive Switching in Nano-Optoelectronic Devices: Towards an Optical Memristor

Juan Luis Friero Castro



Aquesta tesi doctoral està subjecta a la llicència **Reconeixement 4.0. Espanya de Creative Commons.**

Esta tesis doctoral está sujeta a la licencia **Reconocimiento 4.0. España de Creative Commons.**

This doctoral thesis is licensed under the **Creative Commons Attribution 4.0. Spain License.**

Doctoral Thesis

Resistive Switching in  
Nano-Optoelectronic Devices:  
Towards an Optical  
Memristor

Juan Luis Frieiro Castro



UNIVERSITAT<sub>DE</sub>  
BARCELONA



# Resistive Switching in Nano- Optoelectronic Devices: Towards an Optical Memristor

Memoria presentada para optar al grado de doctor  
por la

Universidad de Barcelona

Programa de doctorado en Nanociencias



Autor: Juan Luis Frieiro Castro

Directores:



Dr. Sergi Hernández Márquez Prof. Blas Garrido Fernández



y tutor: Prof. Blas Garrido Fernández

Departamento de Ingeniería Electrónica y Biomédica

Facultad de Física



UNIVERSITAT DE  
BARCELONA



A mi familia

M<sup>a</sup> Isabel y Juanjo

Maria

Bea

FUNDAMENTALES



# Abstract

---

Resistive switching devices have been a topic of great interest since 2008 when theory and physical devices were correlated, as they could lead the next generation of memories and processors. These devices present a behavior that allows them to modify their electrical resistance between two or more states and retain them without the need for external energy. In comparison with market-dominant flash or DRAM memory technologies, information storage is changed from charge accumulation to resistance state.

The possibility of having at least two resistance states (high resistance identified as 0 and low resistance as 1) makes them a promising candidate for digital memories, with the additional advantages of faster switching speeds, lower dimensions for single devices and lower power consumption, when compared to current memories. These point towards resistive switching devices replacing flash memories and being integrated into RAM in the future.

Since their first physical realization, great advances have been made in terms of modelling, materials, device structure, and integration and scaling into arrays and chips. In addition, the properties of resistive switching devices have opened the door for other applications beyond pure memory and the conventional von Neumann architecture. These include *computing in memory*, as well as *brain inspired* and *neuromorphic* computation, where the analog (more than two states) capabilities of resistive switching devices are more recently gaining attention.

Within the context of resistive switching research, this Doctoral Thesis proposes one new field that can benefit in the future by the inclusion of such devices: Optoelectronics. The combination of electronic and photonic devices aims to profit from both and diminish their disadvantages. Devices that can emit, detect, transmit and control light are now included in various applications.

The main objective of this Doctoral Thesis is thus the development of a new concept of devices, which we have called *optical memristors*. When this research began, just a few works were available in the literature, being the presented approach of high novelty. In essence, two types of devices have been attempted and realized: memristors with

## Abstract

electroluminescence or electrical response on light exposure. Notwithstanding, both had a particular requirement: transparent materials were necessary for light to be transmitted through the electrodes to the active layers of the devices.

The first approach to light emitting memristors presented explores the possibilities of light emitting devices based on rare earth ions. These elements are commonly employed in displays for the fabrication of phosphorus layers that are excited by a blue emitting device. When properly used as dopants, these elements are optically active and can be electrically excited within a matrix of different material. Thus, the emission of such devices based on Al/Tb/Al/SiO<sub>2</sub> layers is studied. A change of emission is identified with resistive switching capabilities of these devices, though a low number of cycles is possible.

A second approach starts from an already transparent conductive oxide (TCO) that has shown resistive switching properties in the literature: ZnO. This material presents advantages when compared to the most employed TCO, ITO, because of its non-toxicity and abundance. In addition, it can be doped with rare earth ions that are optically active. In the same way as the previous approach, resistive switching of these devices is possible, but the inclusion of rare earth ions quenches their emission.

Finally, a different strategy allows for the objective results to be achieved. Silicon oxide is employed as an already reported material with resistive switching properties, where Si nanocrystals (NCs) are embedded as luminescent centers. Their combination results optimal for the target application, yielding durable devices with differentiated emissions dependent on the resistance state and that avoid its overwriting when read.

Furthermore, the range of optical properties, that become available to these devices through the presence of Si NCs, is extended to that of electrical response on light exposure. The devices become optically-readable taking profit of the photovoltaic effect of their tandem solar cell structure, distinguishing high and low current extractions dependent on the resistance state.

Last, the effect of resistive switching and the presence of conductive filaments in these solar cells is explored, achieving increased efficiencies when compared to pristine devices.

## List of Acronyms

<b>ALD</b>	Atomic Layer Deposition
<b>AMOLED</b>	Active-Matrix Organic Light-Emitting Diode
<b>BCC</b>	Body Centered Cubic
<b>CC</b>	Current Compliance
<b>CCD</b>	Charge-Coupled Device
<b>CF</b>	Conductive Filament
<b>CIGS</b>	Copper Indium Gallium Selenide
<b>CL</b>	Cathodoluminescence
<b>CMOS</b>	Complementary Metal-Oxide-Semiconductor
<b>CTZS</b>	Copper Zinc Tin Sulfide
<b>EBE</b>	Electron-Beam Evaporation
<b>ECM</b>	Electrochemical Metallization
<b>EDX</b>	Energy-Dispersive X-ray spectroscopy
<b>EL</b>	Electroluminescence
<b>EQE</b>	External Quantum Efficiency
<b>FinFET</b>	Fin-shaped Field Effect Transistor
<b>FN</b>	Fowler-Nordheim
<b>HRS</b>	High Resistance State
<b>ITO</b>	Indium Tin Oxide
<b>IRDS</b>	International Roadmap for Devices and Systems
<b>ITRS</b>	International Technology Roadmap for Semiconductors
<b>IQE</b>	Internal Quantum Efficiency
<b>LCD</b>	Liquid Crystal Display
<b>LED</b>	Light-Emitting Diode
<b>LRS</b>	Low Resistance State
<b>MIM</b>	Metal-Insulator-Metal
<b>MOS</b>	Metal-Oxide-Semiconductor

## List of Acronyms

<b>MOSFET</b>	Metal-Oxide-Semiconductor Field-Effect Transistor
<b>ML</b>	Multilayer
<b>NIR</b>	Near-Infrared
<b>NREL</b>	National Renewable Energy Laboratory
<b>PCM</b>	Phase Change Memory
<b>PECVD</b>	Plasma-Enhanced Chemical-Vapor Deposition
<b>PF</b>	Poole-Frenkel
<b>PL</b>	Photoluminescence
<b>PMT</b>	Photomultiplier Tube
<b>QD</b>	Quantum Dots
<b>QLED</b>	Quantum Dot Light-Emitting Diode
<b>RAM</b>	Random-Access Memory
<b>RE</b>	Rare Earth
<b>ReRAM</b>	Resistive Random-Access Memory
<b>RGB</b>	Red-Green-Blue
<b>RS</b>	Resistive Switching
<b>SCLC</b>	Space-Charge-Limited Conduction
<b>Si NCs</b>	Silicon Nanocrystals
<b>SMU</b>	Source-Measurement Unit
<b>SQ</b>	Shockley-Queisser
<b>SRO</b>	Silicon-Rich Oxide
<b>SRON</b>	Silicon-Rich Oxynitride
<b>TAT</b>	Trap-Assisted Tunneling
<b>TCO</b>	Transparent Conductive Oxide
<b>TEM</b>	Transmission Electron Microscopy
<b>UV</b>	Ultraviolet
<b>VCM</b>	Valence Change Memory
<b>XRD</b>	X-ray Diffraction
<b>XPS</b>	X-ray Photoelectron Spectroscopy
<b>μLED</b>	Micro Light-Emitting Diode

# Acknowledgments

---

Nadie hace una tesis doctoral solo. Creo que todo el que entra a un programa de doctorado es consciente de que sin la multitud de personas que rodean al doctorante, este sería un trabajo imposible de hacer. Hablo no solo profesionalmente, sino también desde el aspecto más personal del día a día.

En primer lugar, me gustaría agradecer la oportunidad que me dieron Dr. Sergi Hernández y Dr. Blas Garrido de hacer un doctorado. Desde esa primera reunión para decidir un TFM allá por 2017, me sentí parte del *GOP*, y ellos mismos mostraron interés en que siguiera después con mi carrera científica en el doctorado. Ellos me han dado todas las herramientas a lo largo de los primeros años para llegar al punto de trabajo autónomo que se consigue con la experiencia.

En cuanto a la financiación, me gustaría remarcar la oportunidad de elaborar múltiples informes para el *Ministerio de Educación, Cultura y Deporte*, el *Ministerio de Ciencia, Innovación y Universidades* y el *Ministerio de Universidades* (espero no haberme dejado ninguno) sobre el desarrollo de mi tesis en el marco de una beca FPU 2016, la cual empecé a disfrutar en 2018. Así mismo, me gustaría remarcar la posibilidad de trabajar en el proyecto nacional *METALONIC*. Este me ayudó a entender como es el trabajo científico antes de continuar con el proyecto nacional *PRITES* y el europeo *DROP-IT*, menciones especiales al ser parte de mi trabajo en los últimos dos años aunque no formen parte de los resultados aquí presentados.

Quiero dedicar también un gran “thank you” a nuestros colaboradores externos e internacionales durante estos años, por sus conocimientos, presentaciones, discusiones, muestras, medidas y otras aportaciones. Entre ellos, me gustaría señalar especialmente al Dr. Jordi Ibáñez del Institut de Ciències de la Terra Jaume Almera, a Dr. Xavier Portier y Dr. Christophe Labbe, junto con el Dr. Clement Guillaume de CIMAP (Caen), y a Dra. Margit Zacharias y Dr. Sebastian Gutsch, junto con Deniz Yazicioğlu del IMTEK (Freiburg); por la oportunidad de trabajar juntos en dispositivos emisores de luz basados en ZnO y tierras raras, y su conocimiento en la fabricación de nanocristales de Si para desarrollar *memristores ópticos*, objetivo final de este trabajo.

## Acknowledgments

Volviendo a Barcelona, me llevo de estos años una gran lista de amigos que he podido conocer en cinco años. Empezando por mis otros directores de tesis, los post-docs que tanto me han ayudado y sin los cuales no estaría escribiendo nada similar a lo que hay aquí: Dr. Oriol Blázquez, Dr. Julià López-Vidrier y Dr. Giovanni Vescio. Sinceramente, muchas gracias por vuestra ayuda en los laboratorios y en esas conversaciones amenas y personales tan necesarias, he aprendido mucho de vosotros. También agradezco al resto de gente del Despatx Patera (¿a quién sino a nosotros se le ocurre hacer un logo de un despacho?): Dr. Javier Blanco Portals, Dr. Lluís López-Conesa, Dra. Gemma Martí, Dr. Pau Torruella, Adrià Huguet, Daniel del Pozo, Sergio González, Joshua Diago y otros que hayan pasado por aquí estos años, sois únicos. Entre todos me gustaría señalar a Catalina Coll, a la que siento no haber escuchado en julio de 2017, pero que tanto me ha ayudado con clases, gestiones y en lo personal.

Agradezco a la gente del departamento de ingeniería electrónica y biomédica que me hayan acogido como lo han hecho: Dr. Manel López, Dra. Raquel Pruna, Dr. Daniel Navarro-Urrios, Dr. Albert Cirera, Dr. Paolo Pelegrino, Dra. Sonia Estradé, Dra. Francesca Peiró, Dr. Albert Romano, Roser Marzo, Martín Morales Antonio Cruz, Andrés Romero, Sergio Rodríguez, y el jefe Dr. Albert Cornet.

Y por último y por ello más importante, tengo que dar las gracias a mis familias. Mi familia de amigos de vuelta en Galicia: Iñaki, Maiky, Gonzalo, Rafa, Rodri, Taju, Diana, y Uxía; y los nuevos en Sabadell: Ally, Lidia y Manu. A Charo y Pepín por hacerme parte de su familia. A Inma y Óscar por tratarme como a un hijo más. A Martín y Miguel, mis pies en la tierra. A todos mis tíos, primos por su apoyo constante. A mis abuelos Toña, Leo, Juan y Luis por enseñarme quién soy. A mi hermana María, un símbolo de esfuerzo a quién me quiero parecer. A mis padres Isa y Juanjo, el apoyo y la confianza inagotables, que siempre están y tienen las palabras necesarias. Y a Bea, mi inspiración, mi fuerza, mi orientación, todo.

Gracias.

# Table of Contents

---

Abstract .....	I
List of Acronyms .....	III
Acknowledgments .....	V
Table of Contents .....	VII
1.    Introduction .....	1
1.1. From electronics to optoelectronics .....	1
1.2. Memristors.....	3
1.3. Light emitting devices .....	5
1.4. Objectives.....	6
1.5. Outline of the Thesis .....	7
2.    Background and State of the Art .....	11
2.1. Materials for optoelectronics .....	11
2.1.1. Indium Tin Oxide (ITO).....	11
2.1.2. Zinc oxide (ZnO) .....	11
2.1.3. Silicon (Si) .....	14
2.1.4. Silicon dioxide (SiO <sub>2</sub> ).....	16
2.1.5. Silicon nanocrystals (Si NCs).....	17
2.2. Light emitting devices .....	21
2.2.1. Excitation .....	22
2.2.2. Semiconductor LEDs and exciton recombination.....	24
2.2.3. Rare Earth electronic transitions .....	25
2.3. Photovoltaic devices.....	27
2.4. Resistive switching devices for optoelectronics.....	32
3.    Materials and Methods.....	45
3.1. Employed materials.....	45
3.2. Fabrication techniques .....	47
3.2.1. Electron beam evaporation (EBE) .....	47
3.2.2. Radiofrequency magnetron sputtering.....	49

## Table of Contents

3.2.3. Plasma-enhanced chemical-vapor deposition (PECVD)	50
3.2.4. Atomic layer deposition (ALD)	51
3.3. Characterization techniques	53
3.3.1. Optical characterization	53
3.3.2. Electrical and electro-optical characterization	57
4. Electroluminescence of Rare Earth containing devices	69
4.1. Rare earth-doped ZnO	69
4.1.1. The effect of high temperature annealing	70
4.1.2. Devices for RGB electroluminescence	86
4.2. Electroluminescence from multilayered Al/Tb/Al/SiO <sub>2</sub>	100
4.2.1. Effect of Tb-doping on resistive switching	113
4.2.2. Replacement of Tb with Eu for red emission	115
5. Resistive switching of ZnO	117
5.1. Resistive switching properties of ITO/ZnO/ <i>p</i> -Si	117
5.1.1. Effect of terbium doping	127
5.2. Electroforming under incident light	130
6. Combined properties in Si NC-containing devices	141
6.1. Si NCs embedded in SiO <sub>2</sub> by electron beam evaporation	142
6.2. Resistance state read through light emission	154
6.3. Resistance state read through light absorption	170
6.4. Photovoltaic improvement with electroforming	179
7. Summary and Conclusions	193
7.1. Rare earth-doped electroluminescence	193
7.2. Resistive switching of ZnO	194
7.3. Resistive switching of Si NCs in SiO <sub>2</sub>	195
7.4. Future prospects	196
8. Resumo en Galego	197
9. Scientific and Academic Contributions	201
9.1. List of publications	201
9.2. Paper contribution statement	202
9.3. Participation in conferences	203

9.4. Participation in scientific projects.....	206
9.5. Teaching.....	207
9.6. Supervision of students .....	208



# Introduction

---

## 1.1. From electronics to optoelectronics

In the second half of the 20<sup>th</sup> century, great advances achieved in the research of electronic materials and devices yielded results in the form of full operational machines: microcontrollers. Among the many breakthroughs, the most important ones are attributed to the invention of bipolar and metal-oxide-semiconductor field-effect-transistors (MOSFET), of integrated circuits and microprocessors, posing the basis of nowadays' micro and nanoelectronics. Further technological developments have allowed for a continuously-growing computational power with the MOSFET as a basis, increasing in each generation of microprocessors the density of these devices. In 1975, G. Moore corrected his prediction from 1965 of the number of transistors in a chip doubling every year to every two years, as it can be corroborated in Figure 1.1.<sup>[1]</sup> This is known as Moore's law, and up to now it has been proven right, utilizing the concept of nodes referencing the gate length of transistors as designation of the technology advancements (up to the 22-nm node).<sup>[2,3]</sup> The evolution in the form of nodes has continued since 2010, but other devices such as fin-shaped FETs (FinFETs) and novel materials are now employed, and the original meaning of "technology node" has been lost to only reference advances in the fabrication process. As of 2021, the 5-nm node is already in production, and the 3- and 2-nm nodes have been announced for 2023 and 2024, respectively. Nevertheless, a constant fear to the end of this law threatens the electronics industry, due to the limitation in reducing the size of transistors, thus requiring of advances in lithography processes almost impossible to achieve, as well as an increase in the power consumption of fabricated chips.

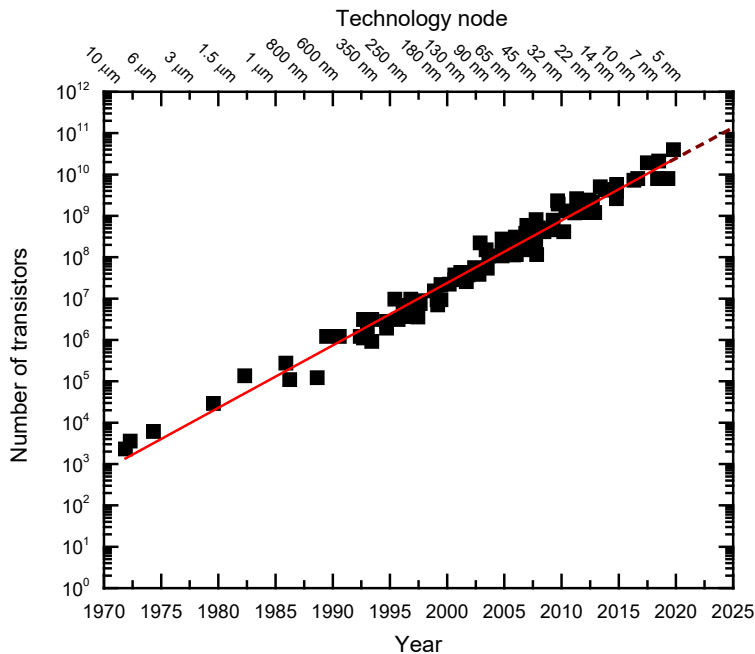


**Figure 1.1.** Number of transistors per microprocessor, per year. Red line serves as guide to the eye, following Moore’s law. Data from reference [1].

Thus, the electronics industry has been researching not only on shrinking the size of devices, but also on other approaches that could empower electronic devices. Alternative materials or faster devices will be the future of the industry, as stated by the “Beyond CMOS” approach supported by the International Roadmap for Devices and Systems (IRDS), formerly known as the International Technology Roadmap for Semiconductors (ITRS).<sup>[4]</sup>

In this context, the field of photonics is gaining a lot of attention. During the last decades, this research carried out on light collection and transmission has been applied to electronics, creating the field of optoelectronics. Optoelectronics uses light-emitting, detecting and controlling devices to take advantage of the possibility of transmitting information faster and with lower losses using photons instead of electrons. In addition, light can be used for processing and sensing in devices that mix optical and electrical signals.

So far, the field of electronics has evolved hand in hand with research in silicon. Though some of its electronic properties, i.e. mobility and noise currents, are slightly inferior to other semiconductors such as germanium, indium arsenide, gallium nitride or gallium arsenide, it being the second most abundant material in the Earth’s crust, easy to extract and process into a high purity, gives it the edge over others.

Nevertheless, there is still a challenge remaining to be solved by the research community. The fact is that, as good as Si can be in electronics, it also exhibits limited performance for light emission. This is due to the fact that its indirect band gap highly reduces the probability of band-to-band transitions or makes them very inefficient.

Both the requirements of higher computing power and efficient chips, and the barrier of Si to its use in photonics have become the main challenge to be tackled by the field of optoelectronics.

## 1.2. Memristors

The main challenge in the electronics industry today is derived from the von Neumann bottleneck: The design of computers nowadays limits their processing capabilities by the data transfer between the processors and the memories, which renders the CPU idle while processed data is transferred to the memory and while new data and algorithms are recovered. In this sense, memristors offer different solutions. These devices are based on different physical processes that either create or destroy conductive filaments in a dielectric layer, thus changing its resistance.

Memristors can be used mainly as memories, with the added benefit of their low size and heat dissipation, which will allow for their integration directly on the processing chips. Compared to hard drive disks and flash memories, they are faster in performance, cheaper to produce and allow for a higher density of information storage. In addition, when compared to random-access memories (RAMs), memristors present the advantage of being non-volatile. All these properties resulted in a fast research race since they were first fabricated in 2008,<sup>[5]</sup> with many companies advancing resistive random-access memory (ReRAM) but never being fully commercially available. They are not yet the memory of choice for most computing applications due to several challenges derived from the interconnection of various memristors, such as sneak currents and the associated resistance of the wiring.<sup>[6]</sup>

Given their outstanding properties, memristors may very well become the next generation of computing devices. It has been highly reported the capability of memristors to mimic neurons synaptic behavior, in the sense that they can vary their conductance incrementally with applied voltage pulses and the timing between

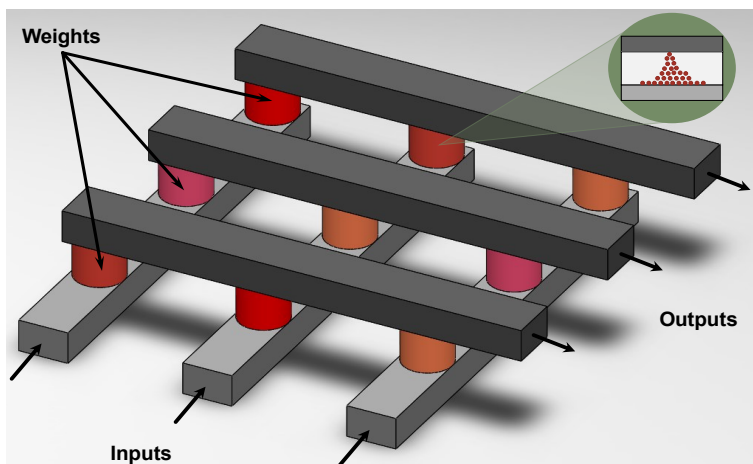


**Figure 1.2.** Crossbar array system of memristors. Inputs and outputs are selected through the different lines. Weights controlled by the conductance of each device store the instructions to be executed. Furthermore, if their conductance is dependent of a train of pulses they receive, they behave like a human brain neuron.

them.<sup>[7-9]</sup> If a set of conductance values of an array of memristors is thought to represent an algorithm to be executed, a signal would be transmitted from neuron point to neuron point simply by multiplying it by the weight of the synapsis (given by the conductance). This means that an array of memristors as shown in Figure 1.2 combines the memory for the algorithms and the processing ability, consequently avoiding the von Neumann bottleneck. Another advantage of this system is the possibility of using analog signals without the need for convertors into digital.<sup>[6,10,11]</sup>

To further exploit the possibilities offered by memristors, in this Doctoral Thesis it is introduced the concept of *optical memristor*. This encompasses the capabilities of a purely electrical memristor with those of optoelectronic devices. The basic operation of a memristor is done through electrical signals, large for write operations and small for read. Specifically, optical memristors that emit light or absorb it depending on their resistance state have been researched, facilitating the conversion of the read operation. These works may be the inspiration for a new generation of optoelectronic devices that can act memories and processors modulated by light signals.

### 1.3. Light emitting devices

Humans have always been dependent on light sources, for protection and for developing their activities during nighttime. Light sources developed with technology, starting from combustion of wood, candles and oils to modern electrical sources. Within this, different sources have appeared, such as the original incandescent light bulb, fluorescent tubes, or tungsten halogen among others. Nowadays, these technologies are less employed as light emitting diodes (LEDs) have quickly developed in the second half of the 20<sup>th</sup> century and beginning of the 21<sup>st</sup>, and especially since the invention of the blue LED.<sup>[12]</sup>

These light sources present themselves as more efficient when compared to others and offer the possibility of tuning their spectrum of emission. The possibility of making LED systems at a very low scale has allowed their use not only as illumination sources but also as a part of displays and light sources in optoelectronics systems. Within these fields and even while being in the market, LEDs and other light emitting devices based on the electroluminescence phenomenon are still highly researched for improvements at the material level, in the search of not only more efficient but also green materials (materials that are abundant, easy to process, non-toxic and with long expected lives).

Furthermore, in combination with light detectors, light emitting devices have created the field of optoelectronics. Their role is key as they transform electrical and optical signals from one to the other, enabling complex processing using electrical circuits in the former and faster transfer with reduced losses and cross-talking in the latter.<sup>[13]</sup>

Apart from memristors, light-emitting devices fabricated with green materials easy to process are also presented in this Doctoral Thesis. Many of the elements or fabrications processes of light emitting devices employed nowadays are moderate or highly toxic for humans and other life forms. In this list we can find liquid-crystal displays (LCD), LEDs and organic LEDs (OLEDs) or quantum dots (QD).<sup>[14,15]</sup> For this reason the use of zinc oxide doped with rare earth ions has been proposed, the first being safe for humans even after ingestion (it is used in sunscreens and as food additives).<sup>[16]</sup> In contrast, rare earth ions employed correspond to the family of non-radioactive lanthanides, considered to have a low toxicity compared to other elements. For this reason, they are only used as a dopant in very small quantities.<sup>[17]</sup>

## 1.4. Objectives

As previously introduced, the electronics industry is constantly researching ways to increase computing power and reduce energy consumption. Some of these lines of research have pointed towards light as a solution since it travels faster than electrical signals and with lower losses. As well, other approaches to solve both problems include new devices with different functionalities. In this sense, memristors have made a name for themselves as key devices that can perform both processing and memory operations reliably and with low power consumption. In accordance with these two lines, one objective of the present Doctoral Thesis is the study of green materials for both light emitting and/or resistive switching devices; that is, mainly employing abundant materials like  $\text{SiO}_2$  or  $\text{ZnO}$  that are easy to process and non-toxic, together with small amounts of others. In addition, the combination of both device capabilities, namely resistive switching and light emission and absorption, has been explored, achieving a novel concept of devices in *optical memristors*. For resistive switching, extensive literature on materials and device structures has been explored, to form a clear picture of the requirements for this property to emerge. In terms of light emission and aiming at the combination with resistive switching, a doping strategy with optically active materials is proposed.

All these devices will satisfy the added requirement of being compatible with the basis of nowadays' electronics industry, complementary metal-oxide-semiconductor (CMOS) fabrication techniques. This means that all aspects from fabrication processes to device structure and materials have been selected to fit the requirements from industry. A device that combines a resistive switching memory with the possibility of being read either electrically or optically, could pave the way for a new genre of optoelectronic devices.

After identifying the main goal of this Doctoral Thesis, this could be divided into less ambitious objectives. Each objective will be devoted to a different device structure or functionality, starting from basic properties such as resistive switching or light emission studied individually, and ending with the combination of them. Hence, these different steps can be listed as follows:

- Investigate and optimize the electrical and optical properties of  $\text{ZnO}$  as a metal oxide semiconductor deposited by sputtering for

doping with rare earths emitting in the visible, and by ALD to be used as top transparent contacts.

- Design and develop single RGB light emitting devices based on ZnO and compatible with Si technologies, as well as combining them onto a white light emitting device
- Explore the fabrication of RGB light emitting devices doping with the same rare earth elements in SiO<sub>2</sub>.
- Study and optimize ZnO as transparent active layers for high performance resistive switching devices and monitor the effect of incident light on their operation.
- Optimize the fabrication conditions of Si NCs superlattices to achieve resistive switching and improve their optoelectronic properties, to develop light emitting and absorbing optical memristors.

## 1.5. Outline of the Thesis

In the present Doctoral Thesis, different devices corresponding to the fields of electronics and optoelectronics have been fabricated, characterized and modelled. *Chapter 2: Theoretical background* includes a summary of the history and working principle of the three main devices of interest in this work, that is, light emitting, photovoltaic and resistive switching devices. In *Chapter 3: Materials and methods*, an in-depth description of the materials, fabrication and characterization techniques is given, which lays the ground for the following three chapters compounding the results of the different works carried out. *Chapter 4: Electroluminescence of Rare Earth containing devices*, *Chapter 5: Resistive switching of ZnO*, and *Chapter 6: Combined properties in Si NCs-containing devices* present the results corresponding to the performed research, focused in three different types of devices: light emitting devices based on rare earth ions as their luminescent center, resistive switching devices made of zinc oxide (ZnO) on Si substrates, and resistive switching devices including silicon nanocrystals (Si NCs) that interact with light, respectively. Last, *Chapter 7: Conclusions and future prospects*, includes the final remarks and conclusions reached during this Doctoral Thesis, as well as a brief description of other work carried out in parallel regarding the fabrication of other devices.

## **References**

- [1] “42 Years of Microprocessor Trend Data | Karl Rupp,” can be found under <https://www.karlrupp.net/2018/02/42-years-of-microprocessor-trend-data/>.
- [2] G. E. Moore, *Electronics (Basel)* **38**, 114, 1965.
- [3] G. E. Moore, *IEEE Solid-State Circuits Society Newsletter* **11**, 36, 2006.
- [4] “IEEE International Roadmap for Devices and Systems - IEEE IRDS™,” can be found under <https://irds.ieee.org/>.
- [5] D. B. Strukov, G. S. Snider, D. R. Stewart, R. S. Williams, *Nature* **453**, 80, 2008.
- [6] M. A. Zidan, J. P. Strachan, W. D. Lu, *Nature Electronics* **1**, 22, 2018.
- [7] S. Slesazeck, T. Mikolajick, *Nanotechnology* **30**, 352003, 2019.
- [8] M. Pedro, J. Martin-Martinez, M. B. Gonzalez, R. Rodriguez, F. Campabadal, M. Nafria, X. Aymerich, *Microelectronic Engineering* **178**, 89, 2017.
- [9] S. Poblador, M. B. Gonzalez, F. Campabadal, *Microelectronic Engineering* **187–188**, 148, 2018.
- [10] D. Ielmini, H.-S. P. Wong, *Nature Electronics* **1**, 333, 2018.
- [11] D. Ielmini, *Microelectronic Engineering* **190**, 44, 2018.
- [12] J. F. Waymouth, in *Handbook of Advanced Lighting Technology*, Springer International Publishing, Cham, pp. 3–40, 2017.
- [13] J. Piprek, *Semiconductor Optoelectronic Devices*, Elsevier, 2003.
- [14] S. R. Lim, J. M. Schoenung, *Journal of Hazardous Materials* **177**, 251, 2010.
- [15] S. R. Lim, D. Kang, O. A. Ogunseitan, J. M. Schoenung, *Environmental Science and Technology* **45**, 320, 2011.
- [16] Ü. Özgür, Y. I. Alivov, C. Liu, A. Teke, M. A. Reshchikov, S. Doğan, V. Avrutin, S. J. Cho, H. Morko, *Journal of Applied Physics* **98**, 1, 2005.

- [17] J.-C. G. Bünzli, I. McGill, in *Ullmann's Encyclopedia of Industrial Chemistry*, Wiley-VCH Verlag GmbH & Co. KGaA, Weinheim, Germany, pp. 1–53, 2018.



# Background and State of the Art

---

## 2.1. Materials for optoelectronics

In the following, the different materials employed for the development of different optoelectronic devices throughout this Doctoral Thesis are described. The importance of each material in the electronic and optoelectronic fields is remarked, as well as the parameters that should be considered in their fabrication process to reach the desired properties.

### 2.1.1. Indium Tin Oxide (ITO)

Commonly known as ITO, this material has been the reference for TCO materials in both LEDs and solar cell structures for the last decades. It is a semiconductor with a wide bandgap, larger than 3.5 eV, which exhibits a very high optical transparency in the visible range of the electromagnetic spectrum, and a high conductivity due to the carriers donated to the conduction band by Sn.<sup>[1]</sup> Its composition may be varied depending on the desired properties, but it comprises a high amount of In<sub>2</sub>O<sub>3</sub> (~90 % ) in a body centered cubic (BCC) crystal structure in which tin (Sn) is introduced as a substitutional element to indium, thus distorting the BCC structure. Initially, In<sub>2</sub>O<sub>3</sub> boosts a very high transparency but at the expense of dielectric behavior in transport. However, the introduction of Sn increases the number of free carriers and thus the overall conductivity of the films while worsening transparency. Therefore, a compromise between the optical and electrical properties must be achieved by introducing the proper amount of Sn.

### 2.1.2. Zinc oxide (ZnO)

Zinc oxide is an outstanding material that has been studied for a very long time, mainly due to it having applications in a large variety of fields such as medicine, food industry, fabrication of sunscreens, paints

and coatings and many others. This is thanks to the wide range of interesting properties it exhibits, together with its large abundance, non-toxicity and ease in fabrication and manipulation.

Regarding electronics and photonics, ZnO is a semiconductor with a direct wide bandgap of 3.3 eV, slightly lower than ITO. Its crystalline structure presents two variants: hexagonal wurtzite, the most stable and thus the most common one, and cubic zincblende, which mainly appears when employing a cubic-structure substrate. In both cases, zinc and oxygen atoms are tetragonal centers, meaning that they are in the center of a tetragon surrounded by four complementary atoms.<sup>[2]</sup>

Most fabrication methods give as a result an intrinsically *n*-type doped ZnO, due to the appearance of defects in its structure, mainly attributed to zinc interstitials ( $\text{Zn}_i^{2-}$ ) and oxygen vacancies ( $\text{V}_o^{2+}$ ). This fact results in carrier concentrations around  $10^{16} \text{ cm}^{-3}$  and electron mobilities of  $300 \text{ cm}^2 \text{ V}^{-1} \text{ s}^{-1}$ . This material also exhibits a high transparency in the visible and NIR of  $\sim 85\%$ , making it a good candidate for a new generation of TCOs that can substitute ITO with its inconvenient use of In, toxicity and scarcity.<sup>[3]</sup> Its conductivity can be further increased via Al-doping, at the expense of optical transparency.<sup>[4]</sup>

The main interest around ZnO focuses on its use as a LED material, where it could serve as a substitutional material to the renown GaN. Both materials have a very similar direct bandgap (3.4 eV in the case of GaN), same hexagonal wurtzite crystalline structure and similar lattice parameters ( $a = 3.25 \text{ \AA}$ ,  $c = 5.20 \text{ \AA}$  for ZnO and  $a = 3.19 \text{ \AA}$ ,  $c = 5.19 \text{ \AA}$  for GaN).<sup>[2,5]</sup> The main difference between both materials comes in the form of the exciton binding energy, which is much larger in the case of ZnO (60 meV versus 25 meV in GaN), which leads to a high exciton stability even at room temperature (thermal energy of  $\sim 26 \text{ meV}$ ). However, there is a reason for which ZnO has been left behind in this application. As previously explained, a *p-n* junction is required in LED systems in order to have electron-hole recombination and spontaneous emission of photons; in the case of ZnO, which is intrinsically *n*-type, the *p*-type counterpart remains very difficult to obtain.<sup>[6]</sup>

Just like in the case of ZnO, GaN intrinsic defects provide a *n*-type doping to the material. However, studies over the years have yielded good *p*-type GaN films. Doping approaches for *n*-type GaN were relatively early achieved during the 1960s, mainly through the

introduction of Si as substitute to Ga. It was with the development of the blue LED in the late 1980s (Noble Prize in 2014) that research started yielding novel GaN  $p$ -type doping methods which included the use of Zn and Mg, as well as the production of high quality doped InGaN and AlGaIn, necessary for the fabrication of heterojunctions and quantum wells.<sup>[7]</sup>

With respect to ZnO, studies suggest that substituting Zn with group-III elements or O with group-VII elements provides donors and thus an  $n$ -type doping.<sup>[2]</sup> Indeed, Al, Ga and In doping has already been proved by different research groups.<sup>[8–10]</sup> As well, the introduction of acceptors to ZnO has been reported to be possible with group-I or group-V elements, partially replacing Zn or O, respectively.<sup>[11]</sup> Instead, the main issue concerning  $p$ -type doping is the compensation of intrinsic defects and low solubility. Doping with group-I elements introduces additional problems such as elements occupying interstitial sites rather than substitutional ones, which increases the lattice strain. Similar problems can arise with group-V elements, except for N. The latter is indeed the most promising candidate, although doping is still complicated due to the low reactivity of a nitrogen source during the deposition process of ZnO and its low solubility.<sup>[12]</sup>

To avoid the requirement of a  $p$ - $n$  junction, doping with optically active centers is also possible in ZnO, e.g., the inclusion of either nanostructures of different elements or rare earth ions, as it will be introduced in *Section 2.2.3. Rare Earth electronic transitions*. In addition to the fabrication of LEDs, ZnO is also listed as a promising material for solar cells and general-purpose light detectors, as its bandgap would allow the efficient absorption of UV and blue light, with the same requirement as LEDs, containing a  $p$ - $n$  junction.

Among other oxides explored, ZnO has also demonstrated resistive switching properties.<sup>[13]</sup> This material, as well as most oxides, presents a valence change mechanism for switching, where oxygen ions (and thus oxygen vacancies) diffuse through the layer due to the applied external electric field towards one of the electrodes. These ions are accumulated at the interface, leaving behind a network of vacancies that form metallic conductive filaments, connecting the electrodes. The intrinsically defective nature of ZnO, with naturally present zinc interstitial and oxygen vacancy defects, eases the formation of these filaments, thus making it a great candidate for resistive switching devices. Together with its wide range of properties (piezoelectricity, bio, chemical and gas sensing, waveguiding, photodetection, photovoltaic

material, TCO or UV-light emission) ZnO emerges as a great candidate aiming towards a new generation of multifunctional devices with RS as their key property in the future of memory and computing devices.

### 2.1.3. Silicon (Si)

Over decades of intense research in microelectronics one element has raised to be the standard for any electronic device, chip or circuit: silicon. Its very high abundance in the Earth's crust (only second to oxygen) makes it a cheap element, added to an easy refinement and purification process. Silicon wafers, obtained via the Czochralski method for growth of single crystal semiconductors and posterior cut and polish, are nowadays the base platform for fabrication of all electronic systems.

Silicon is a group-IV element; thus, it has 4 electrons available to form covalent bonds: two in the 3s and two in the 3p orbitals. Indeed, in a pure silicon crystal each atom is covalently bond to another four atoms in a tetrahedral configuration. Regarding its electronic properties, silicon is a semiconductor with an energy band gap of 1.12 eV. This bandgap is indirect, meaning that electron transitions between the conduction and valence bands requires the interaction with phonons, thus reducing the probability of occurrence. This has been the bottleneck for the inclusion of photonics into the silicon electronics platforms already developed.

Nevertheless, doping via ion implantation with group-III (mainly B, but also Al and Ga) and group-V elements (mainly P, but also As and Sb) substitutional elements easily allows for the addition of donor and acceptor levels within the bandgap, respectively resulting in *n*-type and *p*-type doping of Si. All these characteristics added to its high electron and hole mobility (1400 and 450 cm<sup>2</sup> V<sup>-1</sup> s<sup>-1</sup>, respectively), have made Si the prevalent element for the electronics industry.

In terms of devices, a *p-n* junction of differently-doped Si sets the basis of a diode, a basic circuit element built around the creation of an electron and hole depletion region at the interface between both doping sides. This can be compensated under forward polarization, but not under reverse, as it can be seen in Figure 2.1, creating conducting and non-conducting states.

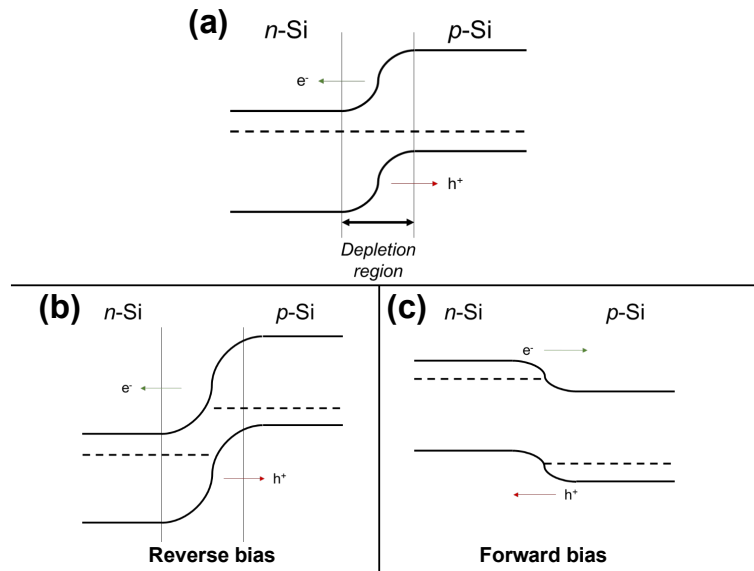


**Figure 2.1.** Energy band diagrams for a  $p$ - $n$  junction. **(a)** Under no bias, a depletion region is created at the interface. **(b)** Under reverse bias, the size of the depletion region is increased. **(c)** Under forward bias, depletion region is decreased until it disappears, when conduction is facilitated.

Moreover, the creation of a MOSFET opened the way for the digital era we are living in. As it is shown in Figure 2.2, this device is based on the fabrication of a  $n$ - $p$ - $n$  horizontal structure in silicon, controlled by three terminals: source, gate and drain. A depletion region is created at the  $p$  zone. Via application of an external electric field at the metal-oxide system on top of the  $p$  region (gate voltage), a channel of carriers can be created and tuned in order to connect source and drain (both on top of  $n$  regions). Furthermore, the application of a bias between these two terminals allows for conduction of carriers. The advancement of electronic circuits continued with the development of the CMOS technology, which involves the fabrication of  $p$  and  $n$  transistors in parallel with shared contacts.

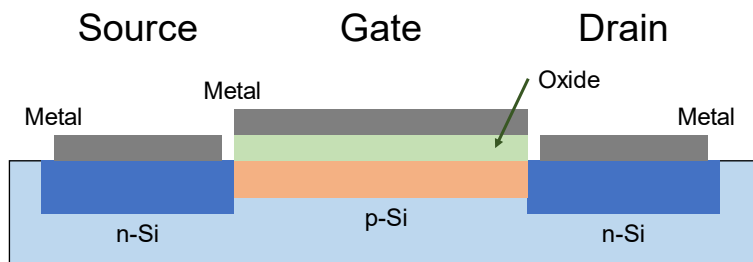


**Figure 2.2.** Sketch of a MOSFET transistor, including the three contacts (source, gate and drain) and the different layers employed.

While the first transistors had a size, given by the length of the channel, of 10–20  $\mu\text{m}$ , technological advances rapidly allowed the formulation of Moore's law (Gordon Moore, co-founder of Intel; 1965)<sup>[14,15]</sup> – the number of transistors per chip will double every two years – a consequence of the fast downscaling of the MOSFET and other improvements. This prediction has been somewhat maintained over the decades with the creation of nodes, technological points where fabrication of transistors evolves. The node of 45 nm marks the beginning of the use of *high-k* materials like  $\text{HfO}_2$  as dielectrics and TiN instead of poly-Si as the gate contact, and at the 22-nm node devices change from MOSFETs to FinFETs. As of 2021, we are employing 7-nm node transistors, and production is moving towards 5 nm, although larger sizes are still used by some manufacturers. For the moment, the trend is expected to be followed, and reach the 3-nm node by 2023. But predictions of Moore's law are believed to stop being fulfilled as we reach limitations in the lithography processes required for the fabrication of these transistors, as well as the increase in power consumption of chips. For the latter reason, memristors are of high research interest as possible substitutes of transistors due to their lower power consumption. Still to this day, these electronic devices and many others are fabricated on Si substrates and with Si layers, making this element the basis of electronics.

### 2.1.4. Silicon dioxide ( $\text{SiO}_2$ )

Parallel to the development of Si as the reference semiconductor in electronics, other materials were as well highly researched in the search of better semiconductors, conductors and dielectric materials in terms of their electric properties as well as fabrication advantages. Within the latter group,  $\text{SiO}_2$  stood out in the beginning due to its easy integration with the Si lattice and controlled fabrication processes. As technology advanced,  $\text{SiO}_2$  was replaced in its role by poly-Si and high-k dielectrics, as fabrication and integration became easier and dielectric properties of these materials surpassed those of  $\text{SiO}_2$ .

The use of  $\text{SiO}_2$  has been reduced over time, being now employed in large electronic devices (technology node over 45 nm) as well as in advanced fabrication processes of micro and nano devices, acting as a dielectric and diffusion barrier that enables precision fabrication and doping of different parts of electronic nanodevices. The process requires the growth of  $\text{SiO}_2$  over the whole surface of the wafer to then be

patterned to open windows where the following fabrication step is required. The removal of SiO<sub>2</sub> is done via etching of unprotected zones of the SiO<sub>2</sub>, leaving part of the substrate underneath visible. In these zones, processes like deposition of metal contacts or doping by ion implantation is precisely performed before removing the excess of SiO<sub>2</sub> and materials deposited over it. Several repetitions of these steps are required for the fabrication of the nanodevices employed nowadays.

### 2.1.5. Silicon nanocrystals (Si NCs)

While the great electrical properties of Si have allowed for a fast development of the electronics industry, its optical properties have posed a drawback to its widespread use in photonics. This is due to its indirect band gap and to the photon emission being in the NIR spectral range, missing the visible part of the spectrum and the third window of telecommunications used since the 1990s in optical fibers ( $\lambda \approx 1550$  nm); as well as the previous ones employed (first window,  $\lambda \approx 850$  nm; second window  $\lambda \approx 1310$  nm). To address this problem, the research community has looked for other semiconductors like, for instance, other group-IV elements or group III-V combinations. A second approach that has yielded good results is the study of properties of nanostructured materials, including Si.

Apart from resulting in good conduction properties, the band gap energy of Si being  $E_g = 1.12$  eV makes it a great candidate for photonics, since it allows the transmission of lower energy light (such as that employed for the third window of photonics) in combination with a SiO<sub>2</sub> cladding. However, this band gap is not direct but rather indirect; implying that the band-to-band transition in Si not only requires of photon but also lattice-phonon interaction, largely reducing the probability of radiative recombination to take place. To solve this drawback, it was discovered that nanostructuring Si modifies the behavior of electrons and holes by taking advantage of the quantum confinement effect.

The first works that hinted towards the usefulness of nanostructured Si were reported in 1988 by Furukawa and Miyasato.<sup>[16]</sup> Visible light emission from Si was presented at room temperature for the first time.<sup>[17]</sup> The particularity of their work descended from their fabrication method, hydrogen plasma sputtering, which produced Si crystallites of sizes between 2 and 5 nm. They also analyzed the band gap of these structures via optical absorption, which resulted in values

corresponding to the visible range, and whose energy increased as the size of the crystal was reduced. All this was explained in the frame of the quantum confinement effect. In addition, it was Canham who first reported the photoluminescence spectra of nanostructured Si.<sup>[18]</sup> In this case, a porous Si matrix was chemically produced. A variation of the pores size determined the size of Si wires that formed the matrix and, in turn, their emission. The photoluminescence spectra exhibited a peak-like emission that could be tuned between  $\sim 790$  and  $\sim 970$  nm with the crystallite size. Again, this work was described following quantum confinement. This two works set the basis for the following decades of nanostructured Si research, exploiting the quantum confinement effect as an ideal model, and introducing Si in the photonics industry.

When a material is confined in size to the nanoscale, its properties change and can no longer be described via classical models: quantum behavior dominates. If bulk Si is thought of as a perfect crystal, meaning that there are no crystallographic defects and a periodic symmetry is maintained in all directions, the potential of any particle associated to it can be described by a periodic function. In the reciprocal space (mathematical description of the real lattice space), this wavefunction is called a *Bloch function*:

$$\Psi(\vec{r}) = e^{i\vec{k}\cdot\vec{r}}u(\vec{r}), \quad (2.1)$$

where  $u(\vec{r})$  is a function with the period of the lattice, and  $\vec{k}$  is the wavevector. This wavevector describes in the reciprocal space the propagation of the particle, together with the function  $u(\vec{r})$ .

Indeed, there are combinations of  $\vec{k}_1$  and  $\vec{k}_2$  that may result in the same wave function  $\Psi(\vec{r})$ . When this happens, these wavevectors are called *equivalent* and are separated by a reciprocal lattice vector. Here lies the importance of the first Brillouin zone, a mathematical description of the primitive cell of a lattice in the reciprocal space. It is formed by a restricted set of  $\vec{k}$  for each cell that are non-equivalent. Any other  $\vec{k}$  is equivalent to one in the first Brillouin zone. If the values of  $\vec{k}$  are restricted to those in the first Brillouin zone, then all Bloch functions have a unique  $\vec{k}$ , and thus can be described without redundancy. Within the first Brillouin zone, there are also some high-symmetry points that are dependent on the primitive cell.

The allowed energy states ( $E_n$ ) of these particles can be calculated through the Schrödinger equation:

$$H(\vec{r})\Psi(\vec{r}) = \left[ \frac{|\vec{p}|^2}{2m} + W(\vec{r}) \right] \Psi(\vec{r}) = E_n \Psi(\vec{r}), \quad (2.2)$$

where  $|\vec{p}|^2/2m$  and  $W(\vec{r})$  represent the kinetic and potential energies of the particle, respectively. For the case of a bulk semiconductor, the solutions are thus dependent, for each state  $n$ , on the wavevector  $\vec{k}$  as follows:

$$E(\vec{k}) = \frac{\hbar^2}{2m^*} (k_x^2 + k_y^2 + k_z^2), \quad (2.3)$$

where  $\hbar$  is the reduced Planck's constant and  $m^*$  is the effective mass of the particles. These solutions can be plotted in what is called a band diagram, with energy as a function of the wavevector. The wavevector is varied between the high symmetry points of the first Brillouin zone, in a path that completely describes all possibilities. Figure 2.3 presents the band diagram for bulk Si, where lower bands represent the allowed energies of holes and are called the valence band, whereas higher bands represent those of electrons and are called the conduction band. The space between them is the band gap, where no energy states are allowed.

It can be identified that for the case of Si, the change of an electron in energy between the conduction band minimum and the valence band maximum (by interaction with a photon with energy equal to or greater than the band gap) requires a change in the wavevector (indirect transition). This is produced by an interaction with the lattice via phonon particles creation or annihilation, which has a very low probability, thus rendering the whole transition improbable.

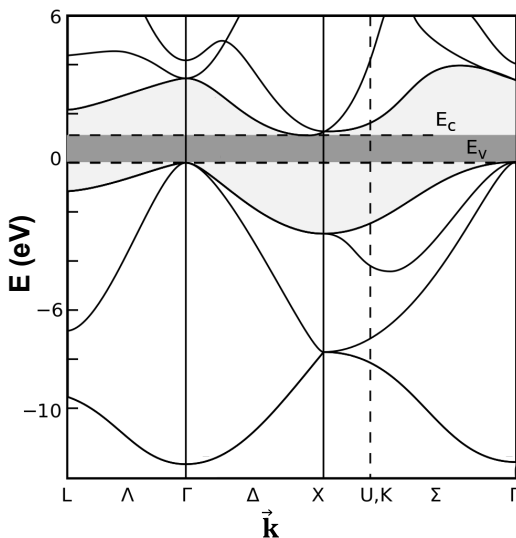


**Figure 2.3.** Diagram of the electronic band structure of bulk Si. Shaded region marks the band gap, where no states are allowed.

This behavior of particles within the infinite lattice is modified when one or more of the dimensions is reduced to the lattice parameter (from 10 to 100 times its value). For this case, boundary conditions must be considered, where the potential of the lattice becomes zero. To simplify things let us consider the case of only one restricted dimension:  $x$  (quantum well). The allowed energy states of a particle inside this structure are discretized, to maintain the continuity of both the wavefunction and its derivative at the boundaries:

$$E_n(\vec{k}) = \frac{\hbar^2}{2m^*} \left( \frac{n^2\pi^2}{t^2} + k_y^2 + k_z^2 \right), \quad (2.4)$$

where  $t$  is the thickness of the restricted dimension. As a direct consequence, not only the energy levels are discretized but also shifted, as they vary inversely with  $t^2$ . The energy of the valence band is decreased ( $\Delta E_{conf,h}$ ) and the conduction band increased ( $\Delta E_{conf,e}$ ), resulting in an overall increase of the band gap of the structure respect to the infinite case:

$$E_{g,QW} = E_{g,bulk} + \Delta E_{conf,e} + \Delta E_{conf,h} \quad (2.5)$$

Finally, in the case of Si NCs, all dimensions are constricted. The previous observation can be used when all three dimensions are reduced. Nevertheless, different groups have observed that a simpler relation can describe the variation of the band gap with the diameter of the NCs ( $d$ ) from their experimental results:

$$E_{g,NCs} = E_{g,bulk} + \frac{A}{d^N}, \quad (2.6)$$

where  $A$  is a fitting coefficient and  $N$  is the power index. This index is dependent on the interface of the NCs with the surrounding matrix, as it is never a perfect infinite potential barrier, in which case this value should be 2.

Indeed, the first important result of nanostructuring Si for photonics is the possibility of tuning the bandgap to a desired value by controlling the size of the NCs and the surrounding matrix. The other result is related to the indirect nature of the band gap of Si. When being nanostructured, the requirement of phonon interaction for electronic transitions is not lost. However, the reduced dimensions also have the effect of increasing the exciton binding energy, that is, the energy associated to the quasi-particle formed by an electron in the conduction band and its respective hole in the valence band. Its value is of  $\sim 15$  meV for bulk Si, and  $>100$  meV for Si NCs. The larger confinement in space causes the wavefunction of the particles to also spread over the

wavevector spectrum. In small NCs, the wavefunctions of electrons in the conduction band and holes in the valence band overlap at some values of  $\vec{k}$ , resulting in an increase in the probability of radiative exciton recombination (*quasi-direct* transition), up to 5 orders of magnitude when compared to bulk Si radiative quantum efficiency of  $\sim 10^{-6}$ .<sup>[19]</sup>

Within the range of applications of Si NCs in photonics, we can distinguish their use as light emitters and as absorbers in photovoltaic devices. In the former, studies are basically addressing the low efficiency of emission of Si NCs-containing devices. Different matrices such as  $\text{Si}_3\text{N}_4$ , SiC or  $\text{SiO}_2$  have been employed, and the mechanisms of charge transport and excitation have been widely discussed to improve the performance of the devices.<sup>[20–22]</sup> In contrast, in the latter application, one must note the importance that Si already had in photovoltaics before Si NCs. The tunable band gap of Si NCs with their size makes it a great candidate for the fabrication of multi-band gap solar cells and in particular, *all-Si tandem solar cells*, where a Si NC-containing layer (higher  $E_g$ ) is placed on top of a bulk Si cell (lower  $E_g$ ), which allows for selective and more efficient photon absorption along the solar cell stack.

## 2.2. Light emitting devices

Light emitting devices convert electrical power directly into light, being since the 1980s a process much more efficient than the incandescence or fluorescence of other well-known light sources (electrical into thermal and then into optical). These devices employ the physical phenomenon known as electroluminescence (EL), a result of the combination of the words *electro* (from electrical power) and *luminescence*. Since it was first observed from a SiC crystal in 1907,<sup>[23]</sup> electroluminescence has largely evolved and with it, the development of semiconductor materials, together with light emitting devices from the 1960s onwards.<sup>[24–26]</sup> Nowadays, we are surrounded by light emitting devices, in applications spanning from power indicators in the form of monochromatic lights to full displays of various sizes and degrees of miniaturization (that is, with different density of devices). In addition, a wide range of materials are employed for light emission such as semiconductors of group II-VI or III-V compounds, organic semiconductors, quantum dots, optically-active dopants like rare-earth ions, etc.

Most of the devices aimed towards light emission employ a basic diode structure consisting of a  $p$ - $n$  junction of semiconductors (as seen in *Section 2.1.3. Silicon*), being thus called light emitting diodes. Other approaches employ dopants or other luminescent centers mainly in a metal-oxide-semiconductor (MOS) structure, with these active centers embedded in the oxide material. In a standard LED configuration, the injection of electrons from the  $n$ -type material and holes from the  $p$ -type, promote the localization of these charges in the space charge region, leading to an increase in the radiative recombination rate of electron-hole pairs.

In some other cases, a transfer process of the energy of excitation to the luminescent centers is required. The radiative process of de-excitation can occur via inter-band transitions, intra-band transitions or localized states of impurities. In the case of semiconductors, this corresponds to the radiative recombination process of the electrons in the bottom of the conduction band with holes in the top of the valence band that can proceed via direct band to band recombination (free carriers) or via an impurity or trapped exciton. The resulting emission has the energy of the band gap minus the impurity or exciton energy if it were the case. Other optically-active centers will show emission because of the electronic transitions within the allowed energy states of an element. In this case, the excited electrons lose energy when relaxing their energy state in the form of the emission of photons, with their energy being equal to that of the transition.

In the following, the mechanisms of excitation of valence band-bound electrons in light emitting devices will be reviewed. In addition, the electron-hole pair recombination as well as the transitions of rare earth ions, both being the light emission mechanisms employed in this Doctoral Thesis, will also be covered.

### 2.2.1. Excitation

We can distinguish four main mechanisms of excitation in light emitting devices, as presented in Figure 2.4:

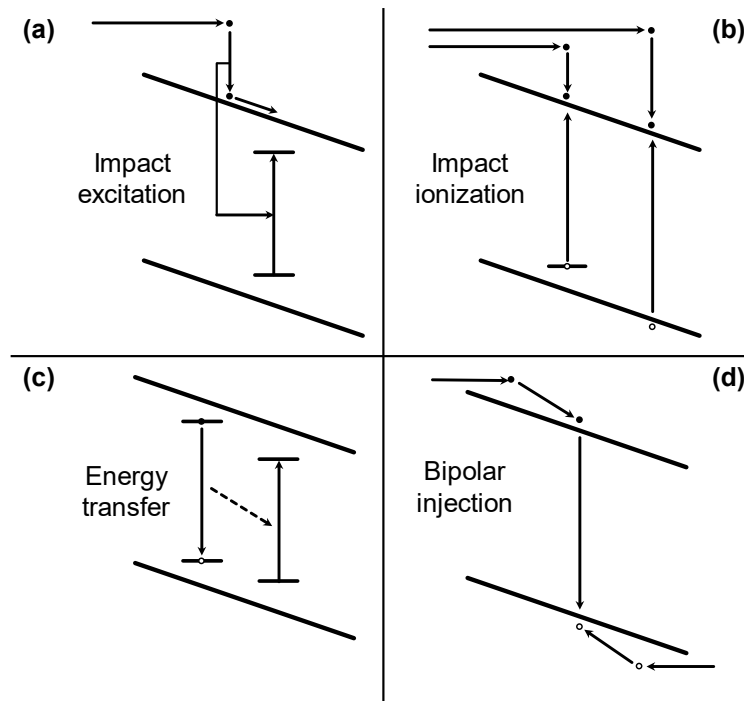


**Figure 2.4.** Main mechanisms for electroluminescence excitation: (a) impact excitation of accelerated electrons with impurities, (b) impact ionization of electrons with a semiconductor producing electron-hole pairs, (c) energy transfer between two radiative centers, and (d) bipolar injection of electrons and holes that recombine.

- **Impact excitation:** Electrons that are accelerated into the device (or the emitting layer) through the conduction band impact with impurities or dopants in an inelastic collision. These gain energy and are excited to a high energy state, which is relaxed after some time resulting in the emission of extra energy as a photon. It is the main mechanism in the excitation of rare earth (RE) ions and other impurities and it is used to understand and model light emitting devices with RE ions and Si NCs presented in this Doctoral Thesis.
- **Impact ionization:** Similar to impact excitation, an electron accelerated into an emitting layer may transfer energy via a collision directly to other electrons, freeing them and leaving behind ionized states.
- **Energy transfer:** The energy accumulated in a system can also be useful to excite luminescent centers by transferring it, as a consequence of their proximity to excited particles. This mechanism explains the occurrence of light emission from Eu/Tb co-doped ZnO being mainly related to Eu transitions, as ZnO, defects and Tb energies are partially transferred to Eu atoms.

- Electron-hole bipolar injection: Last and the main excitation mechanism in many LEDs, if an electron and a hole are simultaneously injected into a device from each electrode, they will be able recombine once they meet within the space charge region. This can be achieved with a proper device structure that allows injection of one carrier type while blocking the other carrier type, or by using alternating current.

### 2.2.2. Semiconductor LEDs and exciton recombination

In the case of electron-hole pairs created by bipolar injection in semiconductor LEDs formed by a  $p$ - $n$  junction, these electrons and holes tend to recombine to minimize the system energy. In particular, electrons are circulating through the conduction band and holes through the valence band. Once they meet in the space charge region (or intrinsic layer, quantum well, quantum dot, etc.), they recombine liberating an energy equal to that of the difference between the electron and the hole. Thus, through a careful selection of materials the energy of emission can be tuned. With this in mind, LEDs have been developed to emit from the ultraviolet part of the spectrum ( $\sim 200$  nm) to the infrared ( $\sim 2500$  nm).<sup>[27–30]</sup>

The band gap of a semiconductor is usually populated by additional states created by defects or impurities. In addition, thermal energy, either from the ambient or added to the material through non-radiative processes of de-excitation of carriers, local deviations in composition or structural defects, slightly modify the bands of the semiconductor. Thus, the color of emission of an LED is never formed by a single energy, but rather by a distribution centered around a main (most probable) energy. For visible light (400–700 nm) this distribution is sufficiently narrow for the human eye to perceive it as a single color. As well, brightness of this emission is controllable by the current circulating through the device, that is, the number of carriers available for radiative recombination.

The future for LEDs is bright. The conversion efficiency, especially that of blue emitting LEDs, compared to other technologies and the control of their properties have made semiconductor LEDs the most employed light sources nowadays, not only for displays with a precise control of the color of each pixel, but also for illumination substituting

low-efficiency sources previously employed (e.g., light bulbs). In the field of illumination, GaN-based blue emitting LEDs have enabled the fabrication of white emitting devices, either by a combination of red, green and blue LEDs or by using a blue LED and a white phosphor. When thinking about displays, LEDs rival with organic LEDs (OLEDs) and liquid-crystal displays (LCD). While OLEDs offer higher response times and purer blacks, LCD panels using LED for backlight and phosphors for light emission are still cheaper. Other technologies such as active-matrix OLED (AMOLED) or quantum dot LED (QLED) are entering the market, while microLEDs ( $\mu$ LEDs) of inorganic materials continue to be research for their potential to overcome the main disadvantage of OLEDs, their degradation.

### 2.2.3. Rare Earth electronic transitions

A different strategy employed for making light emitting devices to that of enhancing band-to-band recombination-related emission is based on the doping with optically-active centers. In this context, RE elements have demonstrated over decades outstanding optical and EL properties.<sup>[31]</sup> Among all these, it is especially notable the stable and narrow emission they exhibit, the different RE species covering a wide range of the electromagnetic spectrum, in some cases spanning from the near-infrared (NIR) to ultraviolet (UV).<sup>[32]</sup> Their hosting material specially affects the scattering of their emission, larger for polycrystalline and amorphous materials and weaker for crystalline matrices. RE elements are employed in the industry for the fabrication of LEDs as part of phosphorescent stacks that produce white light when optically excited. Additionally, the suitability of different host matrices,<sup>[31,33,34]</sup> including ZnO,<sup>[35–38]</sup> for containing optically-active RE dopants, has been extensively proved in the past, aiming at profiting from their emission after electrical excitation.

Rare Earth elements, also called lanthanides, present luminescence due to the electronic transitions within the inner 4f shell of these elements. This results in the emission of photons with a well-defined energy dependent on particular transitions. Nevertheless, the symmetry of RE elements inside the host is fundamental for these radiative transitions to be allowed, requiring a +3-valence state to become optically active. The ions are arranged to the loss of the two 6s-subshell electrons and one from the 4f subshell (which is already partially filled in its neutral state). Once this is achieved and they are

excited, radiative relaxation of these ions will take place mainly through two electronic transitions: one independent of the matrix result of intra-4f transitions protected by electrons in the larger radial-size  $5s^2$  and  $5p^6$  subshells; and another dependent of the matrix due to  $5d$ -to- $4f$  transitions, being  $5d$  the most external subshell after the loss of electrons in  $6s$ .<sup>[39–41]</sup> Emitted photons from these de-excitation processes result in intense narrow peaks distributed along the electromagnetic spectrum, making them great candidates for a new generation of light sources.

Working towards an end goal of a white light emitting device based on rare earths, a combination of red, green and blue emitting elements could be integrated into an RGB array of devices, enabling also the tunability of the final white emission. In this visible range of emissions, we can find three elements presenting the desired emissions: europium (Eu), terbium (Tb) and cerium (Ce). As previously detailed,  $5d$ -to- $4f$  and intra- $4f$  electronic transitions that take place in these elements when optically active in a trivalent state are represented in Figure 2.5.<sup>[35,42,43]</sup> The probabilities of each transition occurring are different and include a range of discrete emissions, meaning that not a single wavelength is

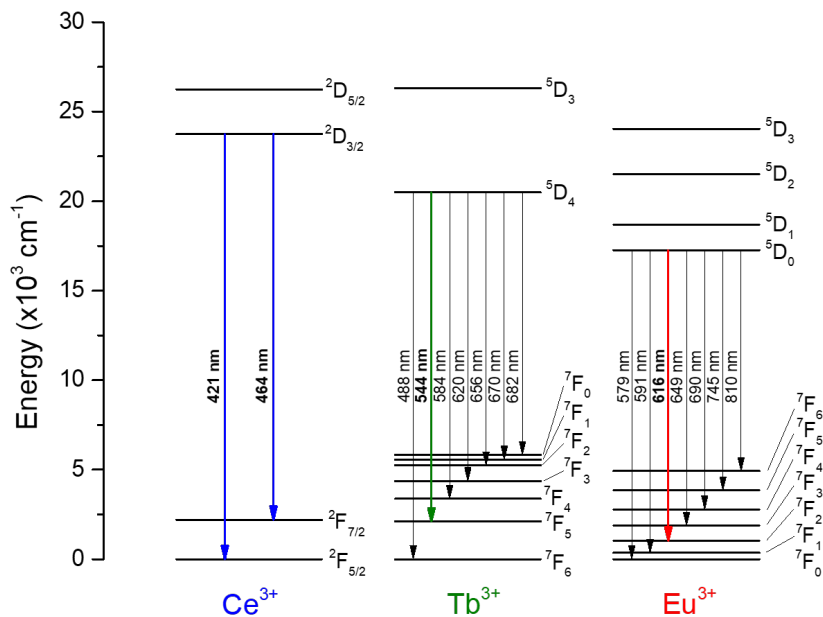


**Figure 2.5.**  $5d$ -to- $4f$  electronic transitions in the rare earth ions considered for this work ( $\text{Ce}^{3+}$ ,  $\text{Tb}^{3+}$  and  $\text{Eu}^{3+}$ ) and the wavelength corresponding to the resulting photons. The main transitions with higher probability of occurring have been highlighted in the schematics in blue, green and red, respectively for  $\text{Ce}^{3+}$ ,  $\text{Tb}^{3+}$  and  $\text{Eu}^{3+}$ .

emitted from each ion but rather a combination of them. Nevertheless, some transitions being more probable determine the resulting color we perceive. Following Figure 2.5 for the case of the three RE elements selected above: Ce has a blue emission (464 nm),<sup>[44]</sup> Tb yields green emission (544 nm)<sup>[45]</sup> and Eu a red one (616 nm).<sup>[46]</sup>

Due to the precise conditions required for the optical activation of RE ions, the doping,<sup>[36]</sup> fabrication process<sup>[47]</sup> or hosting material<sup>[37,48–50]</sup> become critical factors (among others) to obtain reliable devices that take profit of the luminescent properties these elements exhibit. Their use nowadays comprises different phosphors that transform blue light illumination into other colors. In this Doctoral Thesis it is proposed their direct electrical excitation via impact excitation, and to a lesser extent energy transfer, to achieve their emission.

## 2.3. Photovoltaic devices

The high increase in human population during the last decades has led to an even higher increase in energy demand. To supply all this energy, the main source employed up to now has been the burning of fossil fuels (oil, gas, coal). These resources are well known to be harmful for the planet Earth as the main source of greenhouse gas emissions. But a second problem that is only in the recent years gaining attention is their limited availability. In this context, new sources of energy need to take the lead in energy generation and substitute the old ones, overcoming the two exposed problems (avoiding the emission of harmful subproducts, and using natural renewable sources).<sup>[51]</sup>

The Sun is one of these highly researched sources. The amount of energy reaching the Earth that could be used by humans is estimated to be between  $3.9 \times 10^6$  and  $5.5 \times 10^6$  EJ per year, whereas the total energy produced was  $\sim 617$  EJ in 2019.<sup>[52,53]</sup> Indeed, the energy corresponding to the solar radiation reaching the upper part of the atmosphere is roughly 9000 times the amount of globally-consumed energy by the humankind (roughly 2000 times larger if taking into account only solar radiation reaching the sea level).<sup>[54]</sup> It becomes obvious that exploiting solar energy is key, as it could be the only source required by humankind to sustain its current way of life. This requires of both absorption and conversion of the solar energy into other types such as thermal, chemical or electrical. This latter energy form, one of the most employed, is simply achievable by photovoltaic devices.

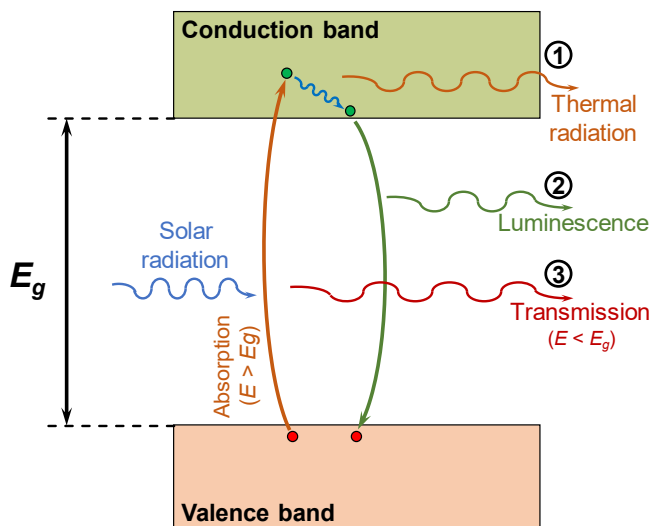


**Figure 2.6.** Absorption process of solar radiation in a solar cell semiconductor and associated losses: (1) thermal radiation to the lattice, (2) luminescence from recombination of electron-hole pairs, and (3) transmission of radiation with energy below the band gap.

Via semiconductor materials, a photovoltaic device takes profit of the energy of the incident photons to excite an electron from the valence band and promote it towards the conduction band, leaving a hole at the former. The presence of an internal electric field in the device achieved via a  $p$ - $n$  junction (as explained in *Section 2.1.3. Silicon*), separates the electron-hole pair before it is recombined, extracting each “particle” through opposite contacts of the device to the external circuit, where their energy will be used.

While the process is apparently simple (see Figure 2.6), many losses may lead to a low conversion efficiency. To start, the semiconductor band gap limits the minimum energy of the photons that are absorbed, the material being transparent to those photons with lower energy than the band gap (marked as 3 in Figure 2.6). Shockley and Queisser used this as an approximation to derive the theoretical efficiency limit of a single-junction cell as a function of the band gap, commonly known as the Shockley-Queisser (SQ) limit.<sup>[55]</sup> While the first calculation gave a maximum efficiency of 30% for the energy band gap of Si at 1.1 eV, it was later reviewed to be 33.7% at 1.34 eV.<sup>[56]</sup> This limit is mainly due to losses in non-radiative transitions in the form of thermal energy, released by electrons that are excited with energies higher than the band gap of the material when relaxing to the bottom of the conduction band (marked as 1 in Figure 2.6). In addition, radiative recombination of electron-hole pairs that result in luminescence (marked as 2 in Figure

2.6) also reduces the efficiency of photovoltaic devices. New approaches resulted from photovoltaics research have been able to raise the limit to 68.7% for infinite multi-junction solar cells, when different band gap materials are stacked together to efficiently absorb distinct parts of the solar spectrum.<sup>[57]</sup>

As a consequence of the determination of the SQ limit, the *First Generation Photovoltaics* started its development. Devices researched in this generation employed crystalline Si, as this element is the semiconductor that most closely resembled the theoretically required band gap, 1.12 eV. After the revision of the limit, the considered semiconductor became GaAs, with a band gap of 1.44 eV, leading to optimum photovoltaic performance with a single semiconductor.

The problem that resulted from the first generation was the requirement of thick layers (in the range from tenths to hundreds of  $\mu\text{m}$ ). The *Second Generation Photovoltaics* directly tackled this problem by researching new materials with higher absorption coefficients, allowing for nm-thick layers. Materials that stand out in this generation are CdTe, CIGS (CuInGaSe) and amorphous Si.<sup>[58,59]</sup> The drawback of these materials was their fabrication requirements of high vacuum and high annealing temperatures, reducing the benefit of low material costs. In addition, the lower thickness required by this layer allowed the fabrication of flexible devices, highly versatile for many applications.<sup>[60,61]</sup>

The most efficient list of materials would come with the *Third Generation Photovoltaics*, which included the concept of multi-junction combinations of materials as well as other aspects from nanotechnologies research. It was first proposed by M. Green,<sup>[62]</sup> and it employs materials with different band gaps to absorb different parts of the light spectrum, giving rise to the so-called tandem cells. Some materials commonly employed are group III-V semiconductors like InGaP, InGaAs, AlAs, AlN, etc. In this generation, there are also included other emerging technologies that are quickly rising in efficiency in the last years, including CZTS (CuZnSnS)-based, organic, perovskite-based and quantum materials.

The National Renewable Energy Laboratory (NREL) in the US maintains and publishes a database of demonstrated lab solar cell efficiencies since 1976.<sup>[63]</sup> Figure 2.8 displays the latest data as of the time writing of this Doctoral Thesis. It should be highlighted as of 2022, the maximum efficiencies of single-junction cells for Si and GaAs at

## Background and State of the Art

27.6% and 30.8%, respectively and using concentrators; thin film technologies at 23.4%; multi-junction or tandem cells at 47.1%; and emerging technologies including perovskite and perovskite/Si cells at 25.7% and 29.8%, respectively, quickly improving considering that they only appear in the data since 2013 and 2017, respectively.

In this Doctoral Thesis, the concept of an *all-Si tandem* solar cell is employed in combination with resistive switching for analyzing the electrical state of these devices (as will be explained in the following section) and for improving the carrier extraction efficiency when used as a photovoltaic device. This all-Si tandem cell consists of multilayers of Si nanocrystals embedded in SiO<sub>2</sub> for improved absorption of high energy photons and a Si substrate for the low energy photons absorption, as presented in Figure 2.7.

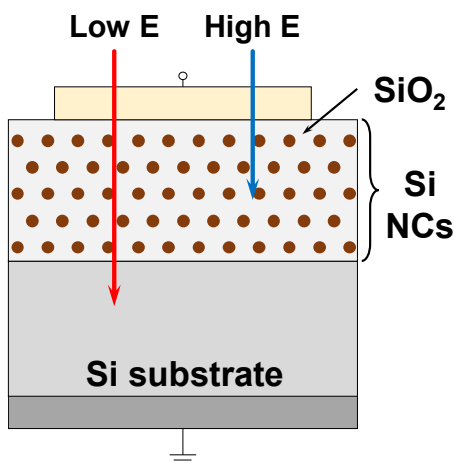


**Figure 2.7.** Schematic of an all-Si tandem solar cell with Si nanocrystals and crystalline Si for absorbing different parts of the spectrum more efficiently.



## 2.4. Resistive switching devices for optoelectronics

Resistive switching (RS) is a property shown by materials that are able to change their electrical resistance between different stable states in a reversible manner. The fact that this change can be performed cyclically has attracted the attention of the electronics community, as the different resistance levels could be used to represent logic states in different digital applications.

First mentions of this effect date back to the 1960's,<sup>[64-67]</sup> when several groups reported evidence of hysteresis in  $I(V)$  measurements with different materials sandwiched in a metal-insulator-metal (MIM) structure. It was in 1971 when all these works were given a theoretical background, as Leon Chua pointed out that a fourth passive basic circuit element should exist along with the *resistor*, the *inductor* and the *capacitor* (see Figure 2.9).<sup>[68]</sup> This element was mathematically described, modelled, and given the name of *memristor*, a contraction of *memory* and *resistor*. Both electrical and theoretical observations would be correlated in 2008, when Strukov *et al.*<sup>[69]</sup> explained how memristance took place at the nanoscale under electrical stress applied to different materials and particularly in  $TiO_2$ .

The concept of memristor, and thus memristance, implies that the change in the resistance produced in the material is progressive with the charge flow. While this could be useful, research has focused in employing mainly two states that changed abruptly to represent 0 or 1 in a new kind of memories known as resistive random-access memory

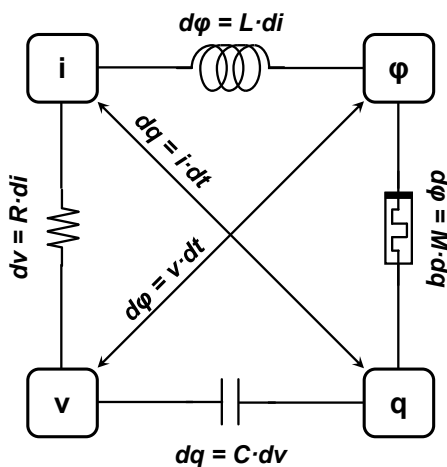


**Figure 2.9.** Deduction of the existence of the memristor by Leon Chua.<sup>[68]</sup> In clockwise direction, starting at the top, are represented the inductor, the memristor, the capacitor and the resistor; with their respective mathematical relations.

(ReRAM, sometimes RRAM) devices. These states are called low and high resistance states (LRS and HRS, respectively). While new device structures have been also explored, the basic MIM structure is maintained to this day.

In terms of device operation, RS devices can be unipolar or bipolar, depending on the requirement or not of a polarity change to modify the state of the device. Voltage applied in the form of  $I(V)$  curves or pulses can be employed to electrically stress the device and switch its state. Figure 2.10 represents both operation modes, along with the curve of a pristine device that is first submitted to a change, the LRS and HRS, the reset (LRS to HRS) and set (HRS to LRS) processes, and a current compliance value ( $I_{cc}$ ) to avoid irreversible damage to the device in the set process. It must be noted that whereas bipolar operation requires of set and reset occurring at different polarizations, unipolar only needs an applied voltage independent of the polarity, thus being plot within the same quadrants (1 or 3) of its graph.

From the physical point of view, devices that undergo resistive switching suffer modifications to their structure at the nanoscale. There are different mechanisms that could originate these modifications, and over the years more of them have appeared.<sup>[70–74]</sup> Table 2.I summarizes all of these. It should be noted that three of them, namely the phase change memory (PCM), valence change memory (VCM) and electrochemical metallization (ECM) stand out over the others as the most reported ones.

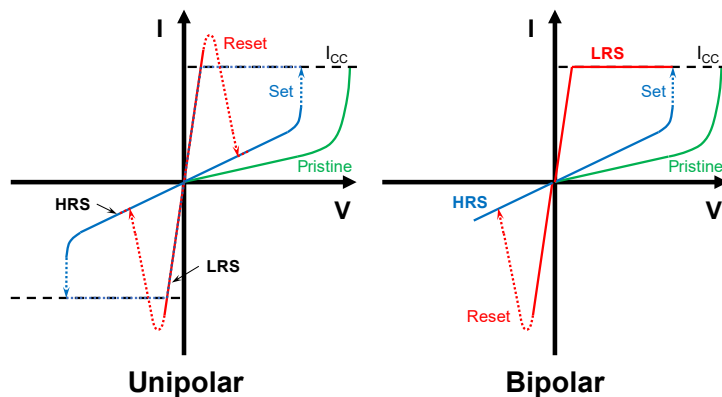


**Figure 2.10.** Unipolar and bipolar resistive switching operations. Unipolar devices can use both polarities to perform a reset or set operation, while bipolar devices have one single established polarity for each process. Virgin curves represent a device that is submitted to a change of resistance state for the first time.

**Table 2.I.** Resistive switching mechanisms, highlighting those most reported, their operation and the significance of redox-related chemical effects.

Resistive switching mechanisms	Ferromagnetic tunneling	Bipolar	Redox-related	
	Magnetoresistive Memory effect			
	Phase Change Memory (PCM) Effect			
	Thermochemical Memory Effect			
	Valence Change Memory (VCM) Effect			
	Electrochemical Metallization (ECM) Effect			Unipolar
	Electrostatic/Electronic Effects			
	Molecular Switching Effects			
	Nanomechanical Memory Effect			

As a quick overview, PCM effect is based in the heating of the insulating material with current until a change of phase is produced, the different phases presenting different electrical resistances. In the case of the ECM effect, a diffusion of metal ions from one of the electrodes toward the insulator results in a filament that connects with the other electrode, and which can be broken by heating the filament with high intensity currents. In the frame of this Doctoral Thesis, however, RS devices presented will focus on the VCM effect.

In VCM, the insulator material sandwiched between metals is usually a metal oxide (sometimes a nitride or an oxynitride). The process is represented in three stages in Figure 2.11. The first process of *electroforming* highly stresses the dielectric in a pristine state to the point of breaking the material and liberating  $O^{2-}$  ions, which then move with the applied external electric field and are accumulated at the interface with one of the metal contacts. The movement of this network of  $O^{2-}$  ions leaves behind conductive filaments (CFs) of nanosized dimensions made of O vacancies ( $V_{O^{2+}}$ ), which connect both electrodes through low resistance paths. This change is usually limited by setting a maximum allowed current to avoid irreversible damage (current compliance –CC–). The device lies now in the LRS. VCM is a bipolar-like RS mechanism, and as such, reversing the polarity allows for the reset process to take place. The accumulated  $O^{2-}$  ions move away from the electrode and occupy the generated vacancies in the CFs, re-oxidating them until the connections are broken. The device is now in the HRS. Since not all the  $O^{2-}$  ions reach a vacancy, the system does not recover the original pristine state. The set process is forced in the same polarity and in the same way as electroforming; nevertheless, since part

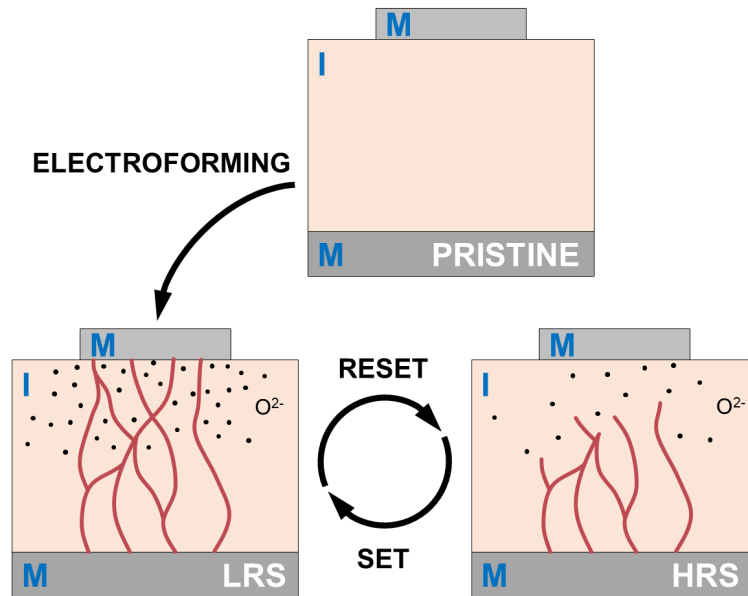


**Figure 2.11.** Schematic representation of the VCM effect in a MIM device, with a metal oxide as insulating layer. The insulator is originally in the pristine state. Via an external electric field, the electroforming process is promoted, a network of oxygen ions is liberated from the insulator and CFs are generated, thus achieving the LRS. Under a different electric field polarity, the CFs can be oxidized in the reset process, physically disconnecting the electrodes and reaching the HRS. Similar to electroforming, the set process reconnects the CFs to restore the LRS.

of the CFs are still maintained, the required electrical stress (applied external voltage) is reduced. The device can now be switched at will between LRS and HRS via set and reset operations.

The possibility of a unique CF being formed and being responsible for the change in conductivity cannot be discarded. Works that have shown *in situ* formation of CFs employ altered devices (normally reduced in one dimension) and thus their observations cannot be extrapolated to 3D devices, where the density of defects in the insulator (probable starting point for the CF formation) is much higher.<sup>[75,76]</sup> In any case, estimations of the sizes of the filaments can be done knowing the current density in the pristine and LRS states. It has been shown that CFs have sizes in the range of tenths of nanometers<sup>[13,77]</sup> and thus, that around 20 of them could be necessary to change the state of a large  $460 \times 460 \mu\text{m}^2$  device.<sup>[78]</sup> In addition, it has been found in the frame of this Doctoral Thesis for devices used in photovoltaics after electroforming processes limited at different CC, that the open circuit voltage ( $V_{oc}$ ) stayed almost constant while the short-circuit current

( $I_{sc}$ ) increased with the application of higher CC values. This can only be explained by the formation of new filaments connected in parallel, and not as one only filament increasing its size.<sup>[79]</sup>

Research in the field of resistive switching has evolved in the recent years. Pure digital memory applications of RS are closer to being integrated into final products, while others like brain-inspired or neuromorphic computing are promising for the future.<sup>[80]</sup> For the former, LRS and HRS can be used to store 1 or 0, respectively, in arrays of devices located at cross points of access wordlines and read bitlines. Full arrays using different RS mechanisms have already been shown and it is now a matter of time that they start replacing conventional Flash and DRAM memories.<sup>[81–86]</sup>

Beyond pure memory applications there can be identified two main applications of RS. First, computing in memory aims to combine memory and logic operations, classically separated in the von Neumann architecture, thus reducing the data transfer between units. Some logic processes could be implemented in memory arrays via small number of transistors, which would be easily connected to resistive switching devices as no additional elements would be required.

Secondly, and as previously mentioned, memristors are also being considered as the appropriate devices for neuromorphic computing. In this sense, the advantages of these systems will come from the combination of memory and computing in single devices (reducing the need for data transfer), the increase in information density due to the analog switching employed in these devices, and the addition of time-dependent information to that given by the resistance. It has been extensively shown that resistive switching devices can operate between more than two states and even gradually increase (potentiation) or decrease (depletion) their resistance. In addition, short-term and long-term plasticity (that is, retention of a state) of devices have been shown to appear with pulses of different frequency.<sup>[87,88]</sup> This means that the function of a human brain neuron could be replicated by a RS device operated under extremely precise conditions. Works with single devices have been already published,<sup>[87,89]</sup> but connections between many of these devices are not yet a reality. Only simulations of what could be possible have been reported.

In addition to studying the RS properties of different materials and devices, in this Doctoral Thesis it has been researched a new kind of devices which can be called *optical memristors*. In these devices, the RS

effect is combined with those previously described in this section (light emitting and photovoltaic devices). This requires transparent conductive oxide (TCO)-based electrodes as top contacts, which allow light to either enter or exit the devices while they are being operated. In the future, devices that can be electrically as well as optically written and read will be integrated into the field of optoelectronics, the combination of both electrical and optical signals being adequate to increase the range of applications to the photonics domain.

### **References**

- [1] B. G. Lewis, D. C. Paine, *MRS Bulletin* **25**, 22, 2000.
- [2] Ü. Özgür, Y. I. Alivov, C. Liu, A. Teke, M. A. Reshchikov, S. Doğan, V. Avrutin, S. J. Cho, H. Morko, *Journal of Applied Physics* **98**, 1, 2005.
- [3] E. M. Bomhard, *Environmental Toxicology and Pharmacology* **45**, 282, 2016.
- [4] P. Nunes, E. Fortunato, P. Tonello, F. Braz Fernandes, P. Vilarinho, R. Martins, *Vacuum* **64**, 281, 2002.
- [5] J. Zhang -, Y. Guo, Y. Wang, C. Li, al -, N. Alfaraj, J.-W. Min, C. Hong Kang, *Journal of Physics: Condensed Matter* **14**, R967, 2002.
- [6] F. Rahman, *Optical Engineering* **58**, 1, 2019.
- [7] S. Nakamura, M. Senoh, N. Iwasa, S. I. Nagahama, *Applied Physics Letters* **67**, 1868, 1998.
- [8] J. G. Lu, Z. Z. Ye, Y. J. Zeng, L. P. Zhu, L. Wang, J. Yuan, B. H. Zhao, Q. L. Liang, *Journal of Applied Physics* **100**, 073714, 2006.
- [9] H. Gómez, M. de la, *Materials Science and Engineering: B* **134**, 20, 2006.
- [10] A. J. Leenheer, J. D. Perkins, M. F. A. M. van Hest, J. J. Berry, R. P. O'Hayre, D. S. Ginley, *Physical Review B - Condensed Matter and Materials Physics* **77**, 115215, 2008.
- [11] C. H. Park, S. B. Zhang, S. H. Wei, *Physical Review B* **66**, 073202, 2002.

## Background and State of the Art

- [12] J. C. Fan, K. M. Sreekanth, Z. Xie, S. L. Chang, K. V. Rao, *Progress in Materials Science* **58**, 874, 2013.
- [13] F. M. Simanjuntak, D. Panda, K. H. Wei, T. Y. Tseng, *Nanoscale Research Letters* *2016 11:1* **11**, 1, 2016.
- [14] G. E. Moore, *Electronics (Basel)* **38**, 114, 1965.
- [15] G. E. Moore, *Neurologia (Barcelona, Spain)* **3**, 181, 1975.
- [16] S. Furukawa, T. Miyasato, *Physical Review B* **38**, 5726, 1988.
- [17] S. Furukawa, T. Miyasato, *Superlattices and Microstructures* **5**, 317, 1989.
- [18] L. T. Canham, *Applied Physics Letters* **57**, 1046, 1998.
- [19] D. Hiller, *Nanotechnology and Photovoltaic Devices: Light Energy Harvesting with Group IV Nanostructures* 99, 2015.
- [20] A. Zelenina, A. Sarikov, S. Gutsch, N. Zakharov, P. Werner, A. Reichert, C. Weiss, M. Zacharias, *Journal of Applied Physics* **117**, 175303, 2015.
- [21] D. Song, E. C. Cho, G. Conibeer, C. Flynn, Y. Huang, M. A. Green, *Solar Energy Materials and Solar Cells* **92**, 474, 2008.
- [22] J. López-Vidrier, S. Hernández, D. Hiller, S. Gutsch, L. López-Conesa, S. Estradé, F. Peiró, M. Zacharias, B. Garrido, *Journal of Applied Physics* **116**, 133505, 2014.
- [23] H. J. Round, *Electrical World* **49**, 309, 1907.
- [24] J. R. Biard, G. E. Pittman, *Semiconductor Radiant Diode*, 3293513, 1966.
- [25] J. R. Biard, E. L. Bonin, W. N. Carr, G. E. Pittman, in *1962 International Electron Devices Meeting*, IRE, pp. 96–96, 1962.
- [26] N. Holonyak, S. F. Bevacqua, *Applied Physics Letters* **1**, 82, 2004.
- [27] Y. Taniyasu, M. Kasu, T. Makimoto, *Nature* *2006 441:7091* **441**, 325, 2006.
- [28] H. Morkoç, S. Strite, G. B. Gao, M. E. Lin, B. Sverdlov, M. Burns, *Journal of Applied Physics* **76**, 1363, 1998.
- [29] K. Streubel, N. Linder, R. Wirth, A. Jaeger, *IEEE Journal on Selected Topics in Quantum Electronics* **8**, 321, 2002.

- [30] S. Nakamura, T. Mukai, M. Senoh, *Applied Physics Letters* **64**, 1687, 1998.
- [31] A. Kenyon, *Progress in Quantum Electronics* **26**, 225, 2002.
- [32] L. U. Khan, Z. U. Khan, in *Handbook of Materials Characterization*, Springer International Publishing, Cham, pp. 345–404, 2018.
- [33] N. V. Gaponenko, O. V. Sergeev, V. E. Borisenko, J. C. Pivin, P. Skeldon, G. E. Thompson, B. Hamilton, J. Misiewicz, L. Bryja, R. Kudrawiec, A. P. Stupak, E. A. Stepanova, *Materials Science and Engineering: B* **81**, 191, 2001.
- [34] J. Heikenfeld, M. Garter, D. S. Lee, R. Birkhahn, A. J. Steckl, *Applied Physics Letters* **75**, 1189, 1999.
- [35] Q. Luo, L. S. Wang, H. Z. Guo, K. Q. Lin, Y. Chen, G. H. Yue, D. L. Peng, *Applied Physics A: Materials Science and Processing* **108**, 239, 2012.
- [36] V. Anand, A. Sakthivelu, K. D. A. Kumar, S. Valanarasu, V. Ganesh, M. Shkir, A. Kathalingam, S. AlFaify, *Superlattices and Microstructures* **123**, 311, 2018.
- [37] S. Komuro, T. Katsumata, T. Morikawa, X. Zhao, H. Isshiki, Y. Aoyagi, *Applied Physics Letters* **76**, 3935, 2000.
- [38] M. Llusçà, J. López-Vidrier, A. Antony, S. Hernández, B. Garrido, J. Bertomeu, *Thin Solid Films* **562**, 456, 2014.
- [39] R. Röder, S. Geburt, M. Zapf, D. Franke, M. Lorke, T. Frauenheim, A. L. da Rosa, C. Ronning, *Physica Status Solidi (B) Basic Research* **256**, 1, 2019.
- [40] M. Ishii, S. Komuro, T. Morikawa, Y. Aoyagi, *Journal of Applied Physics* **89**, 3679, 2001.
- [41] J. Li, O. H. Y. Zalloum, T. Roschuk, C. L. Heng, J. Wojcik, P. Mascher, *Advances in Optical Technologies* **2008**, 2008, DOI 10.1155/2008/295601.
- [42] D. Umamaheswari, B. C. Jamalaiah, T. Sasikala, T. Chengaiah, I. G. Kim, L. Rama Moorthy, *Journal of Luminescence* **132**, 1166, 2012.

- [43] I. T. Sorokina, in *Solid-State Mid-Infrared Laser Sources*, Springer Berlin Heidelberg, Berlin, Heidelberg, pp. 262–358, 2003.
- [44] J. Li, O. H. Y. Zalloum, T. Roschuk, C. L. Heng, J. Wojcik, P. Mascher, *Advances in Optical Technologies* 2008, DOI 10.1155/2008/295601.
- [45] H. Jeong, S. Y. Seo, J. H. Shin, *Applied Physics Letters* **88**, 161910, 2006.
- [46] S. Boninelli, G. Bellocchi, G. Franzò, M. Miritello, F. Iacona, *Journal of Applied Physics* **113**, 143503, 2013.
- [47] D. J. Jovanović, Ž. Antić, R. M. Krsmanović, M. Mitrić, V. Crossed D Signorcrossed D Signević, B. Bártová, M. D. Dramićanin, *Opt Mater (Amst)* **35**, 1797, 2013.
- [48] A. Polman, *Journal of Applied Physics* **82**, 1, 1997.
- [49] K. Takahai, A. Taguchi, Y. Horikoshi, J. Nakata, *Journal of Applied Physics* **76**, 4332, 1994.
- [50] G. M. Ford, B. W. Wessels, *MRS Proceedings* **422**, 345, 1996.
- [51] J. Valenta, S. Mirabella, *Nanotechnology and Photovoltaic Devices*, Jenny Stanford Publishing, 2015.
- [52] H.-H. Rogner, in *World Energy Assessment: Energy and the Challenge of Sustainability*, New York, 2000.
- [53] IEA, “Key World Energy Statistics 2021,” can be found under <https://www.iea.org/reports/key-world-energy-statistics-2021>, 2021.
- [54] M. J. Ahmad, G. N. Tiwari, *International Journal of Energy Research* **35**, 271, 2011.
- [55] W. Shockley, H. J. Queisser, *Journal of Applied Physics* **32**, 510, 2004.
- [56] S. Rühle, *Solar Energy* **130**, 139, 2016.
- [57] A. de Vos, H. Pauwels, *Applied physics 1981 25:2* **25**, 119, 1981.
- [58] S. Niki, M. Contreras, I. Repins, M. Powalla, K. Kushiya, S. Ishizuka, K. Matsubara, *Progress in Photovoltaics: Research and Applications* **18**, 453, 2010.

- [59] T. Söderström, F. J. Haug, V. Terrazzoni-Daudrix, C. Ballif, *Journal of Applied Physics* **103**, 114509, 2008.
- [60] F. Kessler, D. Rudmann, *Solar Energy* **77**, 685, 2004.
- [61] J. Ramanujam, D. M. Bishop, T. K. Todorov, O. Gunawan, J. Rath, R. Nekovei, E. Artegiani, A. Romeo, *Progress in Materials Science* **110**, 100619, 2020.
- [62] M. A. Green, *Physica E: Low-dimensional Systems and Nanostructures* **14**, 65, 2002.
- [63] “Best Research-Cell Efficiency Chart | Photovoltaic Research | NREL,” can be found under <https://www.nrel.gov/pv/cell-efficiency.html>.
- [64] T. W. Hickmott, *Journal of Applied Physics* **33**, 2669, 2004.
- [65] S. Pakswar, K. Pratinidhi, *Journal of Applied Physics* **34**, 711, 2004.
- [66] J. F. Gibbons, W. E. Beadle, *Solid-State Electronics* **7**, 785, 1964.
- [67] T. Mukerjee, J. Allan, *Journal of Applied Physics* **35**, 2270, 2004.
- [68] L. Chua, *IEEE Transactions on Circuit Theory* **18**, 507, 1971.
- [69] D. B. Strukov, G. S. Snider, D. R. Stewart, R. S. Williams, *Nature* **453**, 80, 2008.
- [70] R. Waser, R. Dittmann, C. Staikov, K. Szot, *Advanced Materials* **21**, 2632, 2009.
- [71] I. Valov, *ChemElectroChem* **1**, 26, 2014.
- [72] I. Valov, R. Waser, J. R. Jameson, M. N. Kozicki, *Nanotechnology* **22**, 289502, 2011.
- [73] D. Ielmini, *Semiconductor Science and Technology* **31**, 1, 2016.
- [74] S. Aldana, P. García-Fernández, R. Romero-Zalaz, M. B. González, F. Jiménez-Molinos, F. Gómez-Campos, F. Campabadal, J. B. Roldán, *Journal of Physics D: Applied Physics* **53**, 225106, 2020.
- [75] M. S. Munde, A. Mehonic, W. H. Ng, M. Buckwell, L. Montesi, M. Bosman, A. L. Shluger, A. J. Kenyon, *Scientific Reports* **2017 7:1** **7**, 1, 2017.

- [76] S. Dueñas, H. Castán, H. García, O. G. Ossorio, L. A. Domínguez, H. Seemen, A. Tamm, K. Kukli, J. Aarik, *Journal of Electronic Materials* **2018 47:9 47**, 4938, 2018.
- [77] M. Lanza, G. Bersuker, M. Porti, E. Miranda, M. Nafría, X. Aymerich, *Applied Physics Letters* **101**, 193502, 2012.
- [78] J. López-Vidrier, Y. Berencén, S. Hernández, O. Blázquez, S. Gutsch, J. Laube, D. Hiller, P. Löper, M. Schnabel, S. Janz, M. Zacharias, B. Garrido, *Journal of Applied Physics* **114**, 163701, 2013.
- [79] J. L. Frieiro, J. López-Vidrier, O. Blázquez, J. Ibáñez, D. Yazıcıoğlu, S. Gutsch, M. Zacharias, B. Garrido, S. Hernández, *Solar Energy Materials and Solar Cells* **230**, 111252, 2021.
- [80] S. Slesazeck, T. Mikolajick, *Nanotechnology* **30**, 352003, 2019.
- [81] S. Pi, C. Li, H. Jiang, W. Xia, H. Xin, J. J. Yang, Q. Xia, *Nature Nanotechnology* **2018 14:1 14**, 35, 2018.
- [82] N. D. Rizzo, D. Houssameddine, J. Janesky, R. Whig, F. B. Mancoff, M. L. Schneider, M. Deherrera, J. J. Sun, K. Nagel, S. Deshpande, H. J. Chia, S. M. Alam, T. Andre, S. Aggarwal, J. M. Slaughter, *IEEE Transactions on Magnetics* **49**, 4441, 2013.
- [83] F. Arnaud, P. Zuliani, J. P. Reynard, A. Gandolfo, F. Disegni, P. Mattavelli, E. Gomiero, G. Samanni, C. Jahan, R. Berthelon, O. Weber, E. Richard, V. Barral, A. Villaret, S. Kohler, J. C. Grenier, R. Ranica, C. Gallon, A. Souhaite, D. Ristoiu, L. Favennec, V. Caubet, S. Delmedico, N. Cherault, R. Beneyton, S. Chouteau, P. O. Sassoulas, A. Vernhet, Y. le Friec, F. Domengie, L. Scotti, D. Pacelli, J. L. Ogier, F. Boucard, S. Lagrasta, D. Benoit, L. Clement, P. Boivin, P. Ferreira, R. Annunziata, P. Cappelletti, *Technical Digest - International Electron Devices Meeting, IEDM 2018-Decem*, 18.4.1, 2019.
- [84] T. Kim, H. Choi, M. Kim, J. Yi, D. Kim, S. Cho, H. Lee, C. Hwang, E. R. Hwang, J. Song, S. Chae, Y. Chun, J. K. Kim, *Technical Digest - International Electron Devices Meeting, IEDM 2018-Decem*, 37.1.1, 2019.
- [85] Y. Choi, I. Song, M. H. Park, H. Chung, S. Chang, B. Cho, J. Kim, Y. Oh, D. Kwon, J. Sunwoo, J. Shin, Y. Rho, C. Lee, M. G. Kang, J. Lee, Y. Kwon, S. Kim, J. Kim, Y. J. Lee, Q. Wang, S. Cha, S. Ahn, H. Horii, J. Lee, K. Kim, H. Joo, K. Lee, Y. T. Lee, J. Yoo, G.

## 2.4. Resistive switching devices for optoelectronics

Jeong, *Digest of Technical Papers - IEEE International Solid-State Circuits Conference* **55**, 46, 2012.

- [86] C. C. Chou, Z. J. Lin, P. L. Tseng, C. F. Li, C. Y. Chang, W. C. Chen, Y. der Chih, T. Y. J. Chang, *Digest of Technical Papers - IEEE International Solid-State Circuits Conference* **61**, 478, 2018.
- [87] S. H. Jo, T. Chang, I. Ebong, B. B. Bhadviya, P. Mazumder, W. Lu, *Nano Letters* **10**, 1297, 2010.
- [88] J. del Valle, J. G. Ramírez, M. J. Rozenberg, I. K. Schuller, *Journal of Applied Physics* **124**, 2018, DOI 10.1063/1.5047800.
- [89] D. Ielmini, *Microelectronic Engineering* **190**, 44, 2018.



# Materials and Methods

---

Along the work carried out during this Doctoral Thesis, many have been the materials deposited and characterized. Due to the range of applications that have been previously introduced for these materials in the field of Optoelectronics, their fabrication and characterization becomes an essential step to fully understand the properties shown in the final device structures. In this section, the most characteristic and relevant materials are introduced, along with the deposition techniques that have allowed obtaining the desired composition and/or structure.

## 3.1. Employed materials

For each material employed in this Doctoral Thesis, it is hereby included their main application within the frame of this work. The first two materials correspond to TCOs, as well as introducing ZnO as an active matrix and active layer material. Afterwards, Si and Si-related materials are introduced.

In the Chapters dedicated to the results, two ITO films will be employed as TCO for the top contact in two sets of devices: a rare earth-doped SiAlO LED (*Paper III*) and an all-transparent resistive switching device (*Paper IV*). Each film has been fabricated using a different method: whereas the LED was totally developed in the clean room of the Faculty of Physics of the UB, employing the electron beam evaporation (EBE) system available, the top contact in resistive switching device was deposited via electron beam evaporation and patterned via lithography at the *Institut de Microelectrònica de Barcelona - Centro Nacional de Microelectrónica (IMB-CNM)*.

In the context of this Doctoral Thesis, ZnO has been employed as TCO for top transparent contacts in devices such as LEDs or light-assisted resistive switching devices. As well, it is the host matrix for rare earth species that are optically active. Last, it is also the active material in resistive switching devices. Depending on the application, a different deposition method has been employed. When used as a TCO, atomic layer deposition (ALD) was preferable due to the high crystal quality that can be achieved resulting in a high optical transparency and good conductivity. In other uses, radiofrequency magnetron

## Materials and Methods

sputtering proved to be convenient for both rare-earth doping during the deposition process and as a way to produce intrinsically defective ZnO ready for RS applications. These two properties will be tested for the fabrication of a light emitting device with RS characteristics.

Along the work presented in this Doctoral Thesis, devices have been fabricated employing Si as an active layer or with current Si as the substrate. The reason under these fabrication conditions is the demonstration that all these devices are compatible with Si technology. Indeed, the resistive switching memories, light emitters and detectors hereby presented could easily be implemented on Si to ease the fabrication process and the advancement of electronic circuits by the integration of optical elements.

Whilst SiO<sub>2</sub> is no longer part of the final devices in nanoelectronics after being substituted by *high-k* dielectrics (HfO<sub>2</sub>, ZrO<sub>2</sub>, etc.), other research areas still use it for its combination of electrical and optical properties. Along the different works presented in this Doctoral Thesis, SiO<sub>2</sub> has served different purposes: as a protection layer against diffusion of atoms (*Paper III*); as a critical layer in the fabrication and operation of devices containing Si nanocrystals (*Papers VI–IX*), as will be further explained in its dedicated chapter; and, as previously described, as part of the fabrication processes of devices requiring high precision (*Papers IV, V*).

Within the frame of this Doctoral Thesis, both applications of Si NCs (as either light emitter or light absorber) have been considered together with the resistive switching of Si NCs-containing devices. In all cases, a SiO<sub>2</sub> matrix was employed as surrounding environment for the NCs, mainly fabricated via plasma-enhanced chemical-vapor deposition and using the superlattice approach. A first work demonstrates that Si NCs fabrication following the same approach is also possible using electron beam evaporation as the deposition technique (*Paper VI*). The other three works explore the concept of an *optical memristor*, a resistive switching device that interacts with light during operation. Both the electroluminescence and light absorption properties from Si NCs are exploited to read the state of the devices during electrical operation (*Papers VII and VIII*, respectively). The last work focuses on improving the efficiency of a Si-Si NCs-based tandem solar cell by introducing nanostructural modifications via resistive switching (*Paper IX*).

## 3.2. Fabrication techniques

In this section, the principal techniques used for the fabrication of devices employed in this Doctoral Thesis are described. For each process, the operation procedure is summarized and the key parameters that allow the control of the deposition process. In addition, the specific equipment as well as the works where each was employed are remarked.

### 3.2.1. Electron beam evaporation (EBE)

Electron-beam evaporation is a physical deposition process based on the generation of an intense beam of electrons from a filament, which is used to heat a target material until evaporation (the schematics of the EBE process is depicted in Figure 3.1). A high electric field is externally applied in order to accelerate electrons and extract them from the filament, creating the beam which is then directed by means of electromagnets inside the chamber to a target material contained inside a pocket (with a dedicated liner) and located at the bottom of the chamber. The electrons impact on the surface of the target and transfer their energy to the material, thus producing heat. Depending on the target material, either a sublimation or a melting plus evaporation processes can take place. After this, the released material travels to the substrate, located facing downwards at the top of the chamber, where its deposition occurs. The process needs a high vacuum of at least  $5 \times 10^{-4}$  mbar to increase the mean free path of both the electron beam and the evaporated material, avoiding unnecessary collisions with particles that could result in an inefficient and contaminated deposition.

There are many parameters to be controlled and altered during EBE deposition. Regarding the electron beam, the acceleration voltage, the intensity of the beam and the area in which it strikes the target material largely affect the evaporation rate. On the other end of the process, homogeneity of the deposited film is achieved by rotating the deposition substrate. Material growth is also affected by substrate temperature, which can be tuned with a lamp situated behind the substrate holder. The composition of the deposited films can be slightly altered by introducing a weak gas line (e.g., O<sub>2</sub>, N<sub>2</sub> or Ar). Last, the thickness of the resulting film is controlled via a quartz sensor located at the same distance from the target as the substrate, although slightly inclined (an additional correction for this angle is employed).

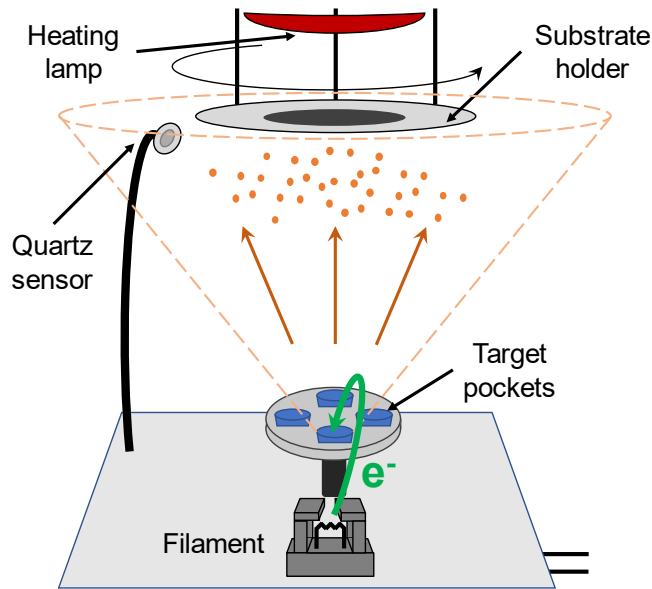


**Figure 3.1.** Sketch of the electron beam evaporation (EBE) system employed in this work. The beam is accelerated to be extracted from the filament and bent via magnetic fields to reach the target, from which material is evaporated and later deposited on the substrate at the top.

The equipment employed is available in the clean room of the Faculty of Physics of the University of Barcelona. This system comprises a PFEIFFER VACUUM Classic 500 chamber with a Ferrotec GENIUS electron beam controller and a Ferrotec CARRERA high-voltage power supply.

Within the results presented in this Thesis, the EBE system has been employed in various works. For the samples where ZnO is the active material in resistive switching (*Papers IV and V*), this technique was employed for both the bottom Al electrode and the top ITO contacts (patterned via photolithography). In samples of Si NCs MLs fabricated for resistive switching combined with optical properties (*Papers VII–IX*) and the samples of ZnO doped with rare earth ions for luminescence (*Paper II*), the bottom contact was made of Al deposited via EBE. Si NCs have also been deposited entirely via EBE following the same multilayer approach employed in other works with PECVD (*Paper VI*). An entire device structure in the form of ITO/15×(Al/Tb/Al/SiO<sub>2</sub>)/Si/Al was grown via EBE for green electroluminescent devices (*Paper III*). Last, although not included as part of the work in this Thesis, ITO NWs have been grown to study the effect of growth rate, time, temperature and substrate on their structure and properties as biosensors (see the list of papers in the CV section of the Doctoral Thesis).

### 3.2.2. Radiofrequency magnetron sputtering

The other physical deposition technique employed in this Thesis for the fabrication of devices is radiofrequency magnetron sputtering (Figure 3.2). In this process, a target of the material to be deposited and a substrate are placed one in front of the other inside a vacuum chamber. The term *sputter* refers to how the target material is removed to be deposited on the substrate. An inert gas, typically argon, is introduced in the chamber and, by means of an electric field, a plasma of this gas is created. The electric field accelerates the plasma towards the target material. Because the energy of the gas ions is higher than the binding energy of the atoms or molecules of the target, these bonds are broken, and the material is ejected and travels in all directions, being deposited on the surface of the substrate and on the chamber walls. The usage of an inert gas avoids interaction of the gas and the material once released from the target.

In order to maintain the gas available for the formation of plasma, a magnetic field is created inside the chamber that confines the electrons close to the target. In addition, if the target material is a dielectric, charge may be accumulated during the process. By means of an alternating electric field this charge is freed, the most typical frequency being 13.56 MHz, hence the radiofrequency term.

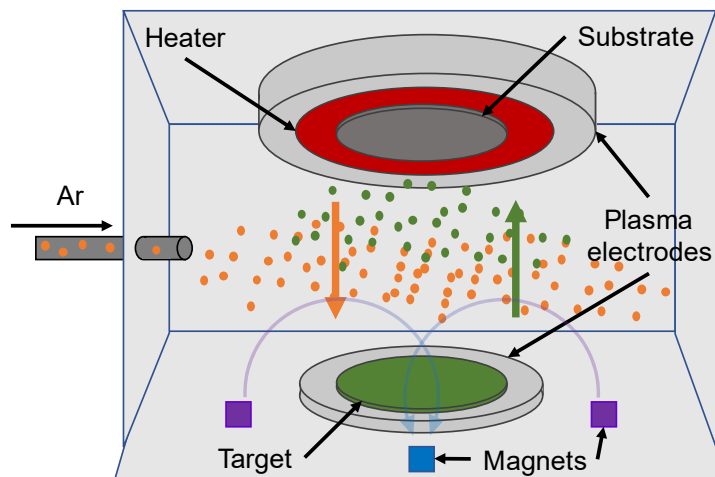


**Figure 3.2.** Sketch of a radiofrequency magnetron sputtering system. Argon gas is ionized and directed towards the target material, which is ejected and deposited on the substrate at the top. Magnets at the bottom maintain the electrons to recover the Ar gas and continue the process.

## Materials and Methods

The parameters that allow a high control of the deposition are the power of the electric source, the amount of Ar inside the chamber, the magnetic field strength, the substrate temperature and the vacuum pressure.

The equipment used in this Thesis is a “Meca 2000” system available at the *Center of Research on Ion Materials and Photonics* (CIMAP, University of Caen, France). Radiofrequency magnetron sputtering has been employed in this Doctoral Thesis for the deposition of ZnO with two purposes: as an active material in resistive switching devices and doped with rare earth ions as part of LED devices. For the latter, rare-earth oxide pellets were placed on top of the ZnO target before sputtering, thus allowing for a co-deposition of the ZnO matrix and the rare earth ions.

### 3.2.3. Plasma-enhanced chemical-vapor deposition (PECVD)

In contrast to the previous methods, plasma-enhanced chemical-vapor deposition (PECVD) is a chemical deposition technique. Its working principle is depicted in Figure 3.3. A mixture of gases is introduced into the chamber, where high vacuum has previously been achieved. Through electrical discharges produced by two electrodes, a plasma of these gases is produced, and they are dissociated. The resulting ions are then directed through the electrical discharge towards the substrate, located at one of the electrodes, where thin film deposition is desired, producing an ion bombardment of the substrate that removes contamination and increases material density. Upon contact with the substrate, these ions react with each other at a lower temperature than the normally required one due to their physical state (plasma of dissociated molecules). After their reaction, the resulting product is deposited onto the substrate.

Control of the substrate temperature, the amount of gas allowed to enter the chamber, and the electrical discharge are crucial for the deposition of high-quality thin films. Regarding this last parameter, the electrical discharge that produces the plasma is achieved via either radio frequency alternating current or direct current.

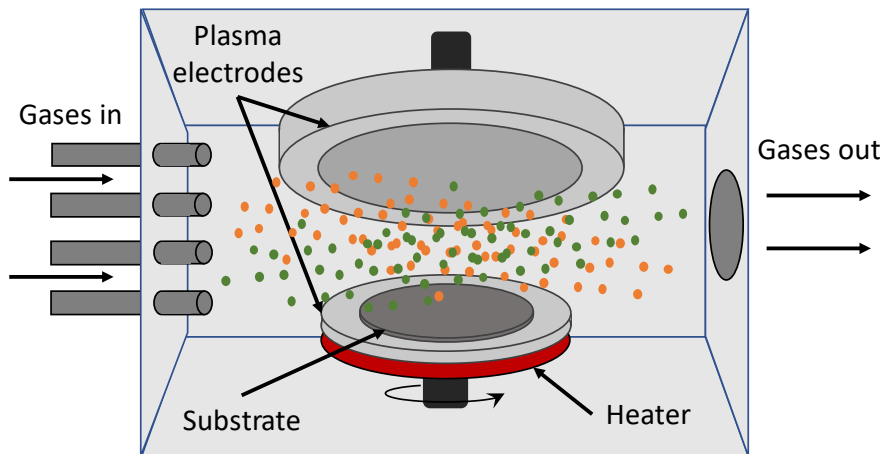


**Figure 3.3.** Sketch of the plasma-enhanced chemical-vapor deposition (PECVD) system employed in this work. The gases introduced into the chamber are ionized and dissociated through an electrical discharge, allowing their reaction and deposition onto the substrate.

The equipment used in this Doctoral Thesis is an Oxford Instruments “Plasmalab 100” system with a 13.56 MHz-driven parallel plate reactor; available at the *Institut für Mikrosystemtechnik* (IMTEK, Albert-Ludwigs Universität, Freiburg, Germany).

In the framework of this Thesis, PECVD has been employed for the fabrication of Si NCs in multilayer structures (*Papers VII–IX*). These structures are formed by alternating layers of silicon-rich oxynitride (SRON) and  $\text{SiO}_2$  with thicknesses of 4.5 nm and 1 nm, respectively. Via an annealing treatment at 1150 °C for 1 h under  $\text{N}_2$  atmosphere, the precipitation and crystallization of the Si excess within the SRON layers is promoted, forming the Si NCs. In addition, samples fabricated for resistive switching of Si NCs also include the deposition of a 2-nm  $\text{Si}_3\text{N}_4$  sublayer between the substrate and the multilayers in order to improve the injection of electrons in inversion conditions due to its positively fixed charges, consequence of its defective nature.

### 3.2.4. Atomic layer deposition (ALD)

The last deposition technique employed is also considered part of the chemical-vapor deposition methods, with the difference that the precursors are never at the same time inside the vacuum chamber. As the name clearly states, ALD is based on the deposition of atomic-thick layers of a material, one by one.

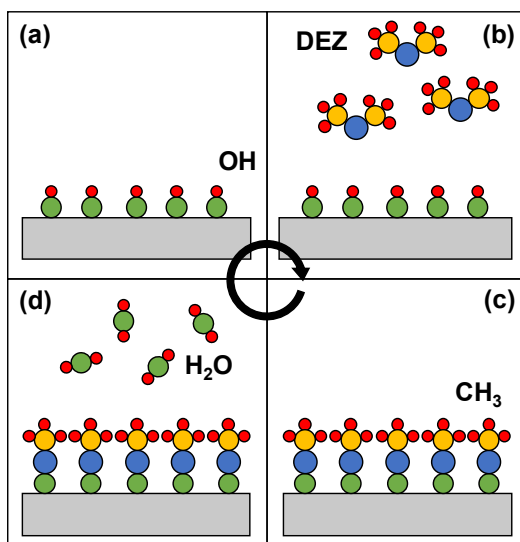


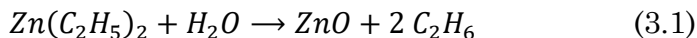
**Figure 3.4.** The four steps in the cycle of deposition of ZnO via ALD. **(a)** The chamber is purged of remaining water (and  $C_2H_6$ ) and the surface is left functionalized with OH groups. **(b)** DEZ enters the chamber and reacts with the OH. **(c)** Chamber is purged of residual DEZ and  $C_2H_6$ , and deposition surface is  $CH_3$  terminated. **(d)** Water enters and reacts.

The material growth is done by alternatively exposing a substrate to different precursors, usually two. These precursors are adhered to absorption sites on the surface of deposition until all are occupied, thus limiting the reaction to the surface so that only a layer is deposited at the time. Each precursor is purged from the chamber after the reaction, before the next one enters. As it might be expected, this method allows a high control of the final deposition thickness by varying the number of cycles performed. In addition, the fact that the deposition is controlled down to each layer results in very high-quality films, with low density of defects.

In this Doctoral Thesis, ALD has been employed for the deposition of ZnO as a high quality transparent conductive oxide.<sup>[1]</sup> This has been employed in devices as a top contact, as its combined high conductivity and transparency allow the electro-optical characterization of devices in a vertical configuration. In particular, ZnO top contacts are used in two main works: light emitting devices with rare earth-doped ZnO as the active material (*Papers I, II*), and light interaction of Si NCs-based resistive switching devices (*Papers VII–IX*). In both cases, the contacts were fabricated at the *Institut für Mikrosystemtechnik* (IMTEK, Albert-Ludwigs Universität, Freiburg, Germany), using a commercial “OpAL” Oxford Instruments system. For the growth of ZnO, the precursors

### 3.3. Characterization techniques

employed are diethylzinc [DEZ,  $\text{Zn}(\text{C}_2\text{H}_5)_2$ ] and water, following Figure 3.4 and the reaction:



The thickness of the contacts was 100 nm, and the devices were kept at 200 °C during deposition, which was previously found to be an optimal temperature. The contacts were patterned via conventional lithography, to a 500- $\mu\text{m}$  diameter circular shape.

## 3.3. Characterization techniques

Throughout the work carried out in this Doctoral Thesis, different techniques of characterization of materials and devices have been employed. What follows is a description of these techniques, the information they allow to be obtained, the control parameters and in which works they have been used.

### 3.3.1. Optical characterization

The interaction of matter with electromagnetic radiation is strongly dependent on the wavelength and polarization state of the incident light and the properties of the material, such as its atomic structure. Thus, by analyzing this interaction, different material properties can be studied. Among them and of high relevance are atomic energy levels, energy bands and the band gap energy of semiconductors and other optoelectronic materials.

As represented in Figure 3.5, light impinging in a material can undergo three major processes: transmission, reflection, and absorption. Whereas transmission alone is very important for applications of some materials, the analysis of their absorption spectrum is one of the ways to find some of the above commented material properties.

The absorption of light modifies the material to an excited state from which a relaxation takes place. This results in the release of acquired energy via thermalization of the lattice or emission of photons. This latter emission process is called photoluminescence, and its analysis yields information about the electronic transitions (band gap, inter-band or intra-band) occurring during relaxation.

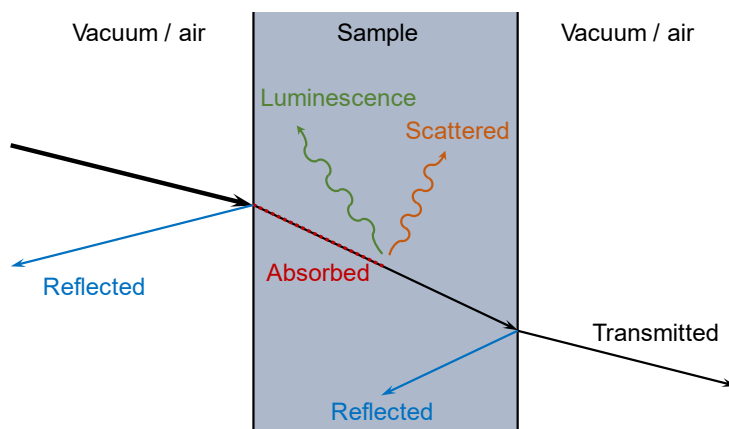


**Figure 3.5.** Main interaction processes of incident light with a material, including transmission, reflection, scattering, absorption and emission.

Last, a second order process can also take place: scattering. In this case light interacts with phonons and plasmons in the material and is dispersed. If no energy is lost, elastic or Rayleigh scattering occurs, while in the opposite case it is called inelastic or Raman scattering. The origin of inelastic scattering lies in the interaction of light with the vibrations of the lattice, highly related to the crystalline state of the material under study.

In the present Doctoral Thesis, PL has been mainly used. This technique is non-destructive, useful and fast for the characterization of semiconductor band gaps and rare earth electronic transitions. While absorption can give similar information, sample preparation requires of transparent substrates and isolation of the target material for a correct characterization. Last, Raman scattering informs on the crystalline structure of materials and the stress it is under (tensile or compressive, if any); this characterization being limited to the surface with a penetration depth dependent on the wavelength employed. These two latter techniques are thus a great complement, sometimes necessary, to the accessibility of PL measurements.

### 3.3.1.1. Photoluminescence (PL)

As previously introduced, PL describes a process of emission of photons by a material when relaxing from an excited state, reached by the absorption of incident light (presented in Figure 3.6). Indeed, other luminescent process are possible, depending on the excitation mechanism. Thermoluminescence (excitation with thermal energy),

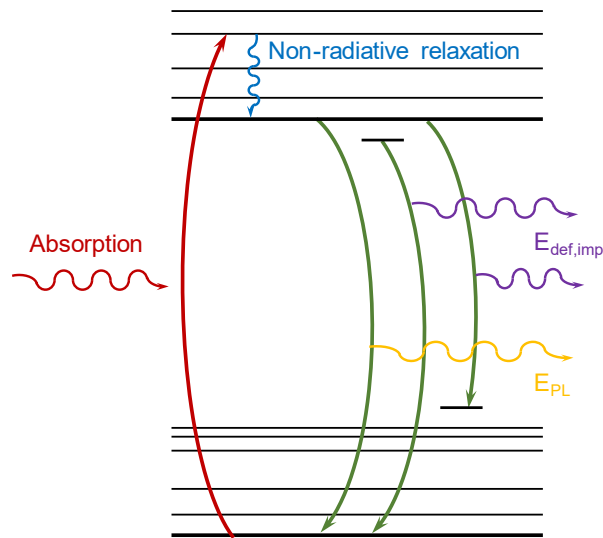


**Figure 3.6.** Representation of an energy band diagram with absorption and photoluminescence processes. Photoluminescence emission can have two origins: either from material electronic transitions (represented in yellow) or from interaction of the material with defects and/or impurities it may contain (represented in purple).

electroluminescence (electron injection) or cathodoluminescence (cathodic rays) are also highly employed for the study of semiconductors and semiconductor devices in the frame of optoelectronics.

In the process of absorption, electrons acquire energy and reach an excited state within their allowed energies. For this process to occur, the incoming energy needs to be large enough to overcome any forbidden states, such as the band gap. The excited electrons remain bound to the created hole, if they are not set free, in what is known as a bound exciton (an electron-hole pair). The electron and the hole then relax towards a state of minimum energy via non-radiative processes, that is, thermalizing their surroundings to afterwards recombine. In this recombination process the electron drops to a lower energy state occupying the site of the hole and emitting the excess energy in the form of a photon. The energy of these photons (or its corresponding wavelength) will be determined by the transition of the electron, which can be of band-to-band origin, such as the band gap in semiconductors between the conduction band and the valence band; or intra-band origin due to the presence of additional states in the band gap created by the presence of defects or impurities in the semiconductor lattice; or of inter-band origin like the radiative electronic transitions that take place in some trivalent rare-earth ions, as previously detailed.

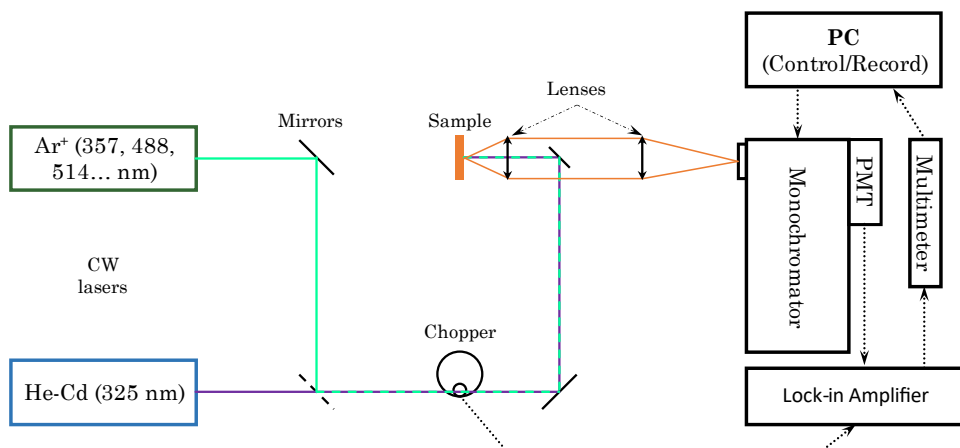


**Figure 3.7.** Scheme of the PL setup available at the UB. The use of mirrors and a backscattering configuration for sample excitation and signal acquisition greatly reduces the space required.

The intensity of emission yields a qualitative measurement of the number of active luminescent centers, but this measurement additionally depends on the energy of the excitation source and the presence of defects and impurities.<sup>[2]</sup>

In the frame of this Doctoral Thesis, the experimental PL setup employed is depicted in Figure 3.7. This system has the possibility of using one of two different continuous-wave lasers by changing the position of a mirror, depending on the excitation wavelength necessary: Ar<sup>+</sup> (488 nm, 514 nm or others) or He-Cd (325 nm). A mechanical chopper breaks the beam to an 11 Hz frequency, allowing it to be distinguished by the lock-in amplifier from other background light reaching the monochromator. The excitation of the samples is done with a mirror and two lenses in a backscattering configuration, which reduces the space required for the setup, and focuses the emission at the entrance of the monochromator. A computer controls the monochromator movement while recording the voltage signal given by the multimeter, equivalent to the emission intensity for each wavelength.

Most experimental setups for PL spectroscopy use wavelength to refer to the photons collected, as it is easier for the user to identify what is being measured in terms of position in the electromagnetic spectrum. However, the discussion and modelling of PL emission should always be done in terms of the photon energy, magnitude that contains the physical significance. The direct conversion from wavelength to energy (and vice versa) is:

$$E = \frac{hc}{q\lambda} \Rightarrow E [eV] \approx \frac{1239.5[eV \cdot nm]}{\lambda[nm]}, \quad (3.2)$$

where  $h$  is Planck's constant,  $c$  is the speed of light in vacuum,  $q$  is the elementary charge and  $\lambda$  the wavelength of the photons (in nm).

However, when performing this operation, it should also be considered that the intensity measured must also be transformed, since the interval of change in each magnitude differs because of their inverse relation. As a consequence, the interval in wavelength,  $d\lambda$ , is not of equal to that corresponding to the energy spectrum,  $dE$ . The additional transformation required is (from conservation of energy):

$$\begin{aligned} dI(\lambda) d\lambda &= -dI(E) dE \\ \Downarrow \\ dI(\lambda) &= -dI(E) \frac{dE}{d\lambda} = -dI(E) \frac{d}{d\lambda} \left( \frac{hc}{q\lambda} \right) = dI(E) \frac{1239.5 [eV \cdot nm]}{\lambda^2 [nm^2]}, \quad (3.3) \end{aligned}$$

where the minus sign represents the opposite trend exhibited by energy with respect to wavelength.

### 3.3.2. Electrical and electro-optical characterization

#### 3.3.2.1. Electrical measurements

The electrical characterization carried out in this work has mainly been done in the form of current-voltage [ $I(V)$ ] measurements in a two-probe vertical configuration, where the bottom contact was grounded and common for many devices and the top contact selected them individually. In these measurements, the applied external voltage is always forced through the top contact and thus the circulating current across the device is measured. Parameters such as the voltage step, hold time, step time, current compliance, and start and end voltages are individually set for each measurement.

Other electrical measurements that have been performed include constant applied current or voltage [ $V(t)$  or  $I(t)$ , respectively], pulsed applied voltage, conductivity measurements for material characterization and  $I(V)$  curves at different temperatures.

The equipment employed for these measurements is a *Cascade Microtech Summit 11000* probe station coupled to an *Agilent B1500A* semiconductor device analyzer. The probe station is closed, creating a

## Materials and Methods

Faraday cage that insulates the devices from external electromagnetic noise. The chuck of the station is a 6" metallic platen that serves as back contact while holding the samples in place with vacuum and heating them if required. The system has four contact probes with a 10- $\mu\text{m}$  diameter gold tip, and they are directly connected to the source-measurement units (SMUs) of the analyzer. A *Seiwa Optical 888L* microscope allows the visualization of the top contact and the probes, especially useful for contacting. Last, the SMUs are interchangeable components of the analyzer that are able to apply either current or voltage while simultaneously measuring the other. From the different existing types of SMUs, the system employed has available two for high power, one for medium power, one for high resolution and one for pulsed measurements.

### 3.3.2.1.1. Charge transport in dielectrics

The study of devices presented in this Doctoral Thesis, which employ metal oxides as their active layers, requires a throughout study of how they conduct carriers. Indeed, metal oxides are semiconductors that can be either intrinsic or doped (or defective), meaning that they will behave closer to a dielectric or a metal, respectively. Their charge transport mechanisms largely affect their properties under study, such as light emission through excitation, light absorption through carrier diffusion and extraction before recombination, and resistive switching through the ease of material breakdown and  $\text{O}^{2-}$  diffusion.

The study of charge transport allows device fabrication to engineer the active materials to highly control their electrical properties. These properties are influenced by material parameters such as carrier density, mobility, layer thickness and temperature. In addition, device structure and applied external voltage also alter the conduction of materials. This can be easily visualized in Figure 3.8 using a metal-oxide-semiconductor (MOS) structure as an example, the same one employed in devices that will be presented in the following three chapters of results. In flat band conditions, an external applied voltage counters the internal potential that is created by the system in equilibrium, a result of the difference in Fermi energies between the metal and the semiconductor [Figure 3.8(a)]. When a negative voltage is applied to the metal contact [Figure 3.8(b)], the majority carriers in the  $p$ -type semiconductor (holes) are attracted to the interface with the oxide and trapped there while part of the electrons cross over from the electrode towards the semiconductor. This is known as the

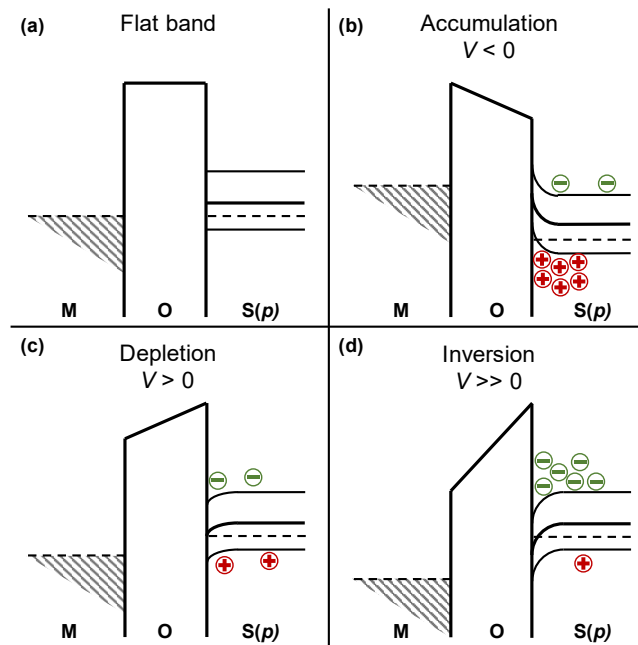


**Figure 3.8.** Energy band diagram of an ideal MOS structure with a  $p$ -type semiconductor in **(a)** flat band, **(b)** accumulation, **(c)** depletion and **(d)** inversion conditions.

accumulation regime. If a positive bias is applied [Figure 3.8(c)], the majority carriers are depleted (depletion regime) from the interface with the oxide and an ionized negative charge appears at the interface. Further increasing this biasing takes the system to inversion conditions [Figure 3.8(d)], where minority carriers are highly concentrated at the interface with the oxide and are able to cross the oxide barrier in a significant number, being thus the conduction of the system supported by minority carriers.<sup>[3]</sup>

In this structure, the conduction of carriers through the dielectric is possible despite its low conductivity because of its low thickness, causing large applied external electric fields with low voltages required. As well, increased temperature due to device operation and ambient conditions can also aid in the circulation of carriers. The analysis of the conduction mechanisms is typically performed in the accumulation regime, where the potential drop occurs in the dielectric (in depletion and inversion, part of the voltage drop takes place in the semiconductor and it would have to be considered). Since different mechanisms can occur simultaneously, knowing how to distinguish them is helpful for the optimization of the device performance. Conduction in these structures is divided into two types: electrode-limited and bulk-limited

mechanisms. A close inspection and analysis of current dependence on applied voltage, from the electrical characterization performed on a particular device, will shed light to the dominant charge transport mechanism at different each voltage range.<sup>[3–6]</sup>

▪ Electrode-limited mechanisms

These mechanisms are dependent on the electrode-dielectric interface, which controls the injection of carriers. Both the potential barrier height and the effective carrier mobility in the dielectric contribute to how carriers move through the interface and the dielectric. In addition, some mechanisms are also affected by temperature. Here they can be distinguished: (1) Schottky or thermionic emission, (2) direct tunneling, (3) Fowler-Nordheim tunneling, and (4) trap-assisted tunneling. Figure 3.9 summarizes these transport mechanisms.

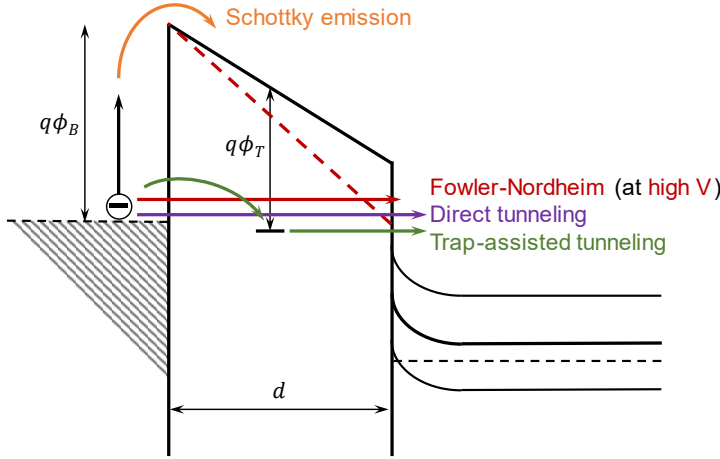


**Figure 3.9.** Representation of the energy band diagram of electrode-limited charge transport mechanisms in a MOS structure. The energy barriers of the electrode-dielectric interface ( $q\phi_B$ ) and the traps in the dielectric ( $q\phi_T$ ) are also indicated.

• **Schottky or thermionic emission**

In this conduction mechanism, electrons obtain enough thermal energy to surpass the energy barrier at the interface and be easily injected into the dielectric. Due to image force of the electrons leaving the metal, the actual barrier is lowered in what is called the Schottky effect. This is described by:

$$J_{Sch}(T, E) = \frac{4\pi qm^*}{h^3} (k_B T)^2 e^{\left[ \frac{-q(\phi_B - \sqrt{qE/4\pi\epsilon_r\epsilon_0})}{k_B T} \right]}, \quad (3.4)$$

where  $J$  is the current density,  $q$  is the electron charge,  $k_B$  is the Boltzmann's constant,  $m^*$  is the effective electron mass in the dielectric,  $h$  is the Planck's constant,  $T$  is the absolute temperature,  $q\phi_B$  is the Schottky barrier height,  $E$  is the electric field across the dielectric,  $\epsilon_r$  is the dielectric constant, and  $\epsilon_0$  is the permittivity of vacuum.

- **Direct tunneling**

According to quantum mechanics, once the electrons reach the electrode-barrier interface their associated wavefunction will penetrate the dielectric film, so that there is a non-zero probability of electrons existing at the other side. This effect is known as tunneling. In contrast with the Fowler-Nordheim mechanism (see below), in the case of direct tunneling electrons see the full thickness of the dielectric they must tunnel through. Its expression is:

$$J_{DT}(E) = \frac{q^2}{8\pi h [\phi_B^{1/2} - (\phi_B - Ed)^{1/2}]^2} E^2 e^{\left\{ -\frac{8\pi\sqrt{2qm^*}}{3hE} [\phi_B^{3/2} - (\phi_B - Ed)^{3/2}] \right\}}, \quad (3.5)$$

where  $d$  is the dielectric thickness.

- **Fowler-Nordheim tunneling**

If the thickness of the dielectric is too large, direct tunneling is highly diffculted. However, the potential barrier being lowered at high electric fields means that tunneling can take place through a triangular barrier, effectively reducing the thickness of the dielectric. The expression for this mechanism is:

$$J_{FN}(E) = \frac{q^3 E^2}{8\pi h q \phi_B} e^{\left[ \frac{-8\pi(2qm_T^*)}{3hE} \phi_B^{3/2} \right]}, \quad (3.6)$$

where  $m_T^*$  is the effective mass of electrons due to the reduced dielectric thickness.

- **Trap-assisted tunneling**

In the case of defective dielectrics, electron tunneling takes place from an intra-band state created by the defects, acting as trapping sites. This reduces the length to be tunneled from the whole dielectric to the distance from the trap to the semiconductor, thus aiding the process:

$$J_{TAT}(E) = \frac{qN_t}{2\tau} e^{\left( -\frac{8\pi\sqrt{2qm^*}}{3hE} \phi_t^{3/2} \right)}, \quad (3.7)$$

where  $N_t$  is the density of traps,  $\tau$  is the time between tunneling events (capture and emission times added together), and  $\phi_t$  is the potential of the traps.

▪ Bulk-limited mechanisms

In these mechanisms, conduction is limited by the dielectric material properties, which induce the circulation of a lower number of electrons than those supplied by the electrode. It is highly dependent on the trap energy level in the dielectric, although other parameters such as density of traps, electron mobility and permittivity are also crucial. At low applied voltages all these mechanisms resemble an ohmic-like conduction, hence appearing their differences at higher electric fields. Three main mechanisms can be distinguished: (1) Poole-Frenkel conduction, (2) hopping conduction, (both represented in Figure 3.10) and (3) space-charge-limited current.

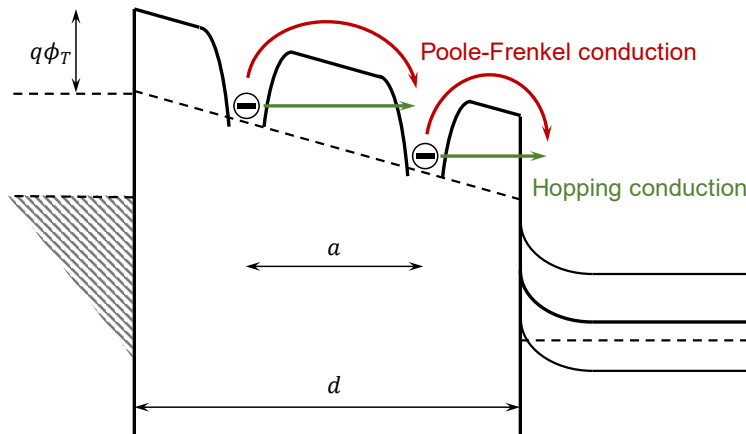


**Figure 3.10.** Representation of the energy band diagram of Poole-Frenkel and hopping conduction mechanisms in a MOS structure. The energy barrier of the traps in the dielectric ( $q\phi_T$ ) and mean hopping distance ( $a$ ) are also indicated.

• **Poole-Frenkel conduction**

This process is similar to the Schottky emission, with the difference of occurring inside the dielectric instead of at the electrode-dielectric interface. In this case, the electrons need to overcome the energy barrier of the traps to reach the conduction band. While moving across the dielectric, carrier trapping and de-trapping processes occur until the semiconductor is reached. The applied electric field reduces the energy required for de-trapping. This conduction is modelled by:

$$J_{PF}(T, E) = q\mu N_C E e^{\left[ \frac{\phi_t - \sqrt{q^3 E / (\pi \epsilon_r \epsilon_0)}}{k_B T} \right]}, \quad (3.9)$$

where  $\mu$  is the electronic drift mobility and  $N_C$  is the density of states of the conduction band.

- **Hopping conduction**

In parallel with the existence of a tunneling effect in the electrode-limited mechanisms, tunneling may also take place between trap levels, allowing electrons to jump or “hop” between sites within the dielectric. In this case, electrons cannot acquire enough thermal energy to overcome the potential barrier. This is expressed by:

$$J_H(T, E) = qanve^{\left( \frac{qaE - E_a}{k_B T} \right)}, \quad (3.10)$$

where  $a$  is the mean hopping distance,  $n$  is the concentration of electrons in the conduction band of the dielectric,  $v$  is the frequency of thermal vibration of the electrons at the trapping sites, and  $E_a$  is the activation energy (energy difference between the trap states to the bottom of the conduction band).

- **Space-charge-limited conduction**

When the number of injected electrons is higher than those that can move through the dielectric, charge accumulates and creates an additional barrier. At low voltage ( $V < V_{TR}$ ), injected electrons are fewer than the thermally-generated free electrons ( $n_0$ ) inside the dielectric. In addition, injected electrons require a longer time to travel through it than to be relaxed. Consequently, an ohmic conduction is observed. Once the voltage is higher than the transition value ( $V_{TR} < V < V_{TFL}$ ) to reduce transit time below the relaxation time, electrons move through the dielectric with the limitation of the traps. Above the trap-filled-limit ( $V > V_{TFL}$ ), all traps are essentially filled and the electrons accumulate in the dielectric, which creates a spatially distributed charge that further limits the injection. To describe this mechanism, the following equations are used:

$$J_{ohm} = qn_0\mu \frac{V}{d}, \text{ for } V < V_{TR}, \quad (3.11)$$

$$J_{TFL} = \frac{9}{8}\mu\epsilon_r\epsilon_0 \frac{N_C}{g_n N_t} e^{\left( \frac{-E_a}{k_B T} \right)} \frac{V^2}{d^3}, \text{ for } V_{TR} < V < V_{TFL}, \text{ and} \quad (3.12)$$

$$J_{SCLC} = \frac{9}{8}\mu\epsilon_r\epsilon_0 \frac{V^2}{d^3}, \text{ for } V > V_{TFL}, \quad (3.13)$$

where  $g_n$  is the degeneracy of the energy states in the conduction band.

### 3.3.2.2. Electroluminescence

To characterize the emission of light emitting devices, two different electroluminescent measurements are performed, employing the experimental setup described in the previous section. Instead of using the oculars, the microscope optical path is switched to a mirror that collects the light and sends it to the measuring system. A representation of this setup with the different measuring systems (explained below) is presented in Figure 3.11.

The first step is measuring the integrated EL, which requires the usage of a *Hamamatsu R928* GaAs photomultiplier tube (PMT) to collect all the light in the wavelength range from 300 to 900 nm. A script controls the voltage and current applied to the devices through the *Agilent* system and records their values together with the EL emission. With this data, an electrical threshold for emission can be obtained. In addition, the analysis of the EL- $I$  relation gives information on the excitation mechanism and the efficiency of emission.

Afterwards, the spectral distribution of this EL emission is acquired. For this, the PMT detector is substituted by a monochromator coupled to a liquid nitrogen-cooled CCD camera. The *Agilent* system is used in this case to excite the devices with constant current [over the threshold previously obtained and checking that voltage values are as expected

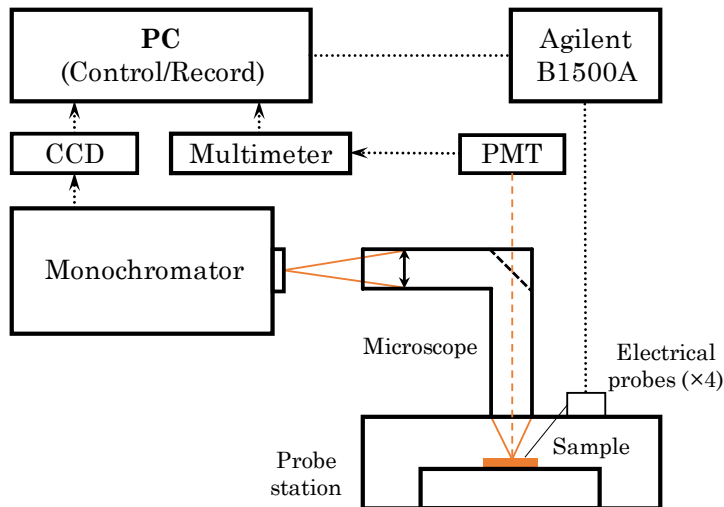


**Figure 3.11.** Scheme of the measurement setup for electrical measurements and EL, with the option for PMT or CCD characterization.

from  $I(V)$  measurements], while the emission of the devices is collected and integrated usually for 30 s. When light reaches the CCD camera, it is separated in wavelength and thus the spectrum of emission can be recorded. With the spectrum, the different luminescent centers present in the device can be distinguished and quantified, and their intensity ratio and purity can be determined.

#### 3.3.2.3. Photovoltaic characterization

The other kind of devices studied in this Doctoral Thesis correspond to solar cells or photovoltaic devices, that is, devices composed of semiconductor materials that absorb light and generate charge carriers (electron-hole pairs), which can be extracted from the device. This yields an electrical current as a result.

The experimental setup for these measurements is included in a *Bentham PVE300* commercial system. This system comprises a box that is closed during measurements, to avoid external light interferences, with two light sources and an electrical measuring system. The first light source is a solar simulator class B, whose irradiance matches that of the Sun at sea level ( $1 \text{ kW m}^{-2}$ ), although atmospheric absorption bands are not simulated. The other light source is comprised of two lamps (Xenon and quartz) that are used at different measuring wavelengths after going through a monochromator. The electrical system is formed by two probes and a conducting chuck where the devices are placed and fixed via vacuum. The probes are connected to an *Agilent B1500A* with two medium-power SMUs outside the box.

Using the Agilent system, an  $I(V)$  curve is measured at small voltage steps in a small range close to 0 V, with and without the solar light being applied to the device. The difference in the curves obtained in dark and under light exposure allows determining important parameters such as photocurrent and photoconductivity, open-circuit voltage, short-circuit current, point of maximum efficiency, and fill-factor of the photovoltaic structure under study.

Last, employing the monochromated light sources, the spectral response (SR) and quantum efficiency of the devices can also be evaluated. In this case, the device is forced to constant 0 V (or the point of maximum efficiency) by the external electric circuit while incident light wavelength is swept in a proper range, and the extracted current at each wavelength is monitored. The value directly measured is the

## Materials and Methods

spectral response (in A/W), that is, the ratio of generated current per incident optical power at each wavelength. Only light of energies above the band gap of the absorbing semiconductor can be absorbed.

The photovoltaic process requires light absorption and carrier extraction before recombination to be completed. In this sense, quantum efficiency (%) can be referred to two concepts: external or internal quantum efficiency (EQE or IQE, respectively). Both indicate the ratio of carriers collected per number of photons, but EQE considers all photons that irradiate the device (both the transmitted, absorbed and reflected ones) and IQE only those that are absorbed. Consequently, IQE is always larger than EQE in the visible range. As the number of carriers that are recombined before extraction is difficult to calculate, the IQE is usually calculated from the EQE using the device absorptance ( $A$ ), following:

$$IQE = \frac{EQE}{A} = \frac{EQE}{1-T-R}, \quad (3.20)$$

It should be noted that usually devices are opaque and thus there is no transmission ( $T = 0$ ). In addition, EQE can be estimated from the spectral response by calculating the number of photons irradiating at each wavelength from their energy, following:

$$EQE(\lambda) = SR(\lambda) \cdot \frac{hc}{q\lambda} = SR(\lambda) \cdot \frac{1239.5 [eV \cdot nm]}{\lambda [nm]}, \quad (3.21)$$

## References

- [1] H. Beh, D. Hiller, M. Bruns, A. Welle, H. W. Becker, B. Berghoff, C. Sürgers, R. Merz, M. Zacharias, *Journal of Applied Physics* **122**, 025306, 2017.
- [2] S. Perkowitz, *Optical Characterization of Semiconductors*, Elsevier, 1993.
- [3] S. M. Sze, K. K. Ng, *Physics of Semiconductor Devices*, John Wiley & Sons, Inc., Hoboken, NJ, USA, 2006.
- [4] K. C. Kao, *Dielectric Phenomena in Solids*, Elsevier, 2004.
- [5] F.-C. Chiu, *Advances in Materials Science and Engineering* **2014**, 1, 2014.

- [6] E. Lim, R. Ismail, *Electronics (Basel)* **4**, 586, 2015.



# Electroluminescence of Rare Earth containing devices

---

In this Chapter, light emitting devices containing rare earth ions as optically-active dopants are presented. These ions constitute the perfect platform to understand the basic requirements and modelling of MOS-structured light emitting devices, since they exhibit a narrow emission in different parts of the spectrum. The work in this Doctoral Thesis has focused on three elements: europium, terbium and cerium. Their visible light emission matches the three colors required for an RGB light emitting device; red from Eu, green from Tb and blue from Ce; making them also great candidate materials for future displays that combine different intensities of these three colors to produce others.

As exposed in *Section 2.2.3. Rare Earth electronic transitions*, these elements are optically active when in a trivalent state. However, they can form different stable oxides when forming clusters, losing their narrow emission properties. For this reason, it is crucial to limit the amount of dopant in the devices to homogenously distribute these atoms throughout the host matrix. Indeed, this limitation on the dopant concentration has been achieved in this Doctoral Thesis via co-deposition and delta doping. The work can be separated into two blocks, differentiated by both the doping process and the host matrix of the rare earth ions: ZnO and Al/SiO<sub>2</sub>.

## 4.1. Rare earth-doped ZnO

ZnO has long been considered an adequate material for hosting optically active elements. Zinc oxide is a wide band gap semiconductor (3.4 eV), meaning that it is transparent to visible light, as well as easier to process than other semiconductors that are more expensive and hazardous. For these reasons, it has been studied as an alternative for the fabrication of rare earth-containing light emitting devices.

In this work, doping is done via co-deposition of the host material and the rare earth element desired. The process is thus simplified, as only one layer is required to be fabricated, allowing for a better control over deposition when compared to the deposition of consecutive thin layers (see delta doping in *Section 4.2. Electroluminescence from multilayered Al/Tb/AlSiO<sub>2</sub>*). In addition, this method results in a higher homogeneity of the deposited films.

Aiming at attaining RGB light emitting devices, samples and device structures of ZnO doped with Eu, Tb and Ce were fabricated at the *Center of Research on Ions, Materials and Photonics (CIMAP)*, at the University of Caen Normandy (UNICAEN), using RF sputtering. The deposition of the doped-ZnO was carried out by positioning pellets of the desired rare earths on top of the ZnO target. The device structures for LEDs were finalized with the deposition of circular ZnO contacts on top of the active layer via ALD deposition and a common bottom contact of Al deposited via electron beam evaporation.

### 4.1.1. The effect of high temperature annealing

Both the emissions of Tb<sup>3+</sup> and Eu<sup>3+</sup> had been independently reported previously,<sup>[1,2]</sup> as well as the energy transfer taking place in Tb and Eu co-doped ZnO.<sup>[3]</sup> Nevertheless, these works lacked an in-depth analysis of the effect of the high-temperature annealing process, and thus a careful investigation of the changes in the microstructure, and how this affected the luminescence, was still required.

The first approach to these devices studied the effect of the annealing after deposition on the microstructure of Tb and Eu co-doped ZnO layer, playing attention to the role of all elements, including the Si from the substrate. Thermal treatments were done from 700 °C to 1100 °C in N<sub>2</sub> atmosphere for 1 h using 150-nm thick samples. One additional sample with the conditions presenting the best PL emission and structure was finalized into an EL device and electro-optically characterized, reducing the thickness of the active layer to 65 nm.

A combined structural and compositional characterization in the form X-ray diffraction (XRD), transmission electron microscopy (TEM) and energy-dispersive X-ray spectroscopy (EDX) reveals that the matrix does not maintain a ZnO structure with all annealing treatments. As deposited samples present a ZnO diffraction pattern showing a distorted lattice and small grain sizes. At 700 °C, the rare earth

elements segregate through the grain boundaries to the bottom, close to the silica layer naturally present on top of the Si substrate. At 900 °C,  $\text{Zn}_2\text{SiO}_4$  silicate crystallizes at the bottom, being the signals of ZnO lost; and  $\text{Tb}_x\text{Eu}_y\text{Si}_v\text{O}_w$  apatite grains start to appear towards the top. Above 900 °C, Zn evaporates from the samples, favoring the formation of silica in the matrix and the increase in size of the apatite crystals, reaching the size of the whole layer thickness. These two materials are the only detected at 1100 °C.

Photoluminescence measurements performed with different excitation wavelengths on samples annealed at different temperatures reveal the luminescent behavior of the rare earth ions. First, for high energy excitation (266 nm) resonant with the ZnO conduction band, the ZnO band-to-band emission is present. This emission disappears with increasing annealing temperature as ZnO is lost. For low temperatures,  $\text{Tb}^{3+}$  emission is visible but not that of  $\text{Eu}^{3+}$ , consistent with the evenly distributed ions in the matrix and the easier excitation of Tb from ZnO than Eu. As temperature increases, the diffusion of rare earth ions reduces the emission of  $\text{Tb}^{3+}$  due to the proximity between ions, resulting in non-radiative recombination processes (cross-talking). In contrast, the formation of the apatite grains favors the emission of  $\text{Eu}^{3+}$ , in addition to improving the energy transfer of  $\text{Tb}^{3+}$  to  $\text{Eu}^{3+}$  and reducing the visible radiation of  $\text{Tb}^{3+}$  available for collection. The direct excitation of  $\text{Eu}^{3+}$  ions by using a 532 nm shows that they are optically active starting at 800 °C, improving their emission as temperature increases with the ZnO quality first and with the increase in size of the apatite grains later. Last, a direct excitation of  $\text{Tb}^{3+}$  using 488 nm for a sample annealed at 1100 °C remarks the process of energy transfer to  $\text{Eu}^{3+}$  since no emission from  $\text{Tb}^{3+}$  ions can be detected whereas  $\text{Eu}^{3+}$  emission remains visible.

Following these observations, a light emitting device has been fabricated with layers annealed at 700 °C, as the uniform distribution of the rare earth ions and the presence of a thin silica layer could be beneficial for the operation of these devices. Indeed, the electroluminescence from both ions can be detected and the emission is visible to the naked eye. The analysis of this and other similar devices was completed in Paper II.

This work was presented as a poster in the European Materials Research Society (EMRS) Fall Meeting 2019. A journal article was published in *Applied Surface Science* **556**, 149754 (2021).



**Paper I: Influence of post annealing treatments on the luminescence of rare earth ions in ZnO:Tb,Eu/Si heterojunction (DOI: [10.1016/j.apsusc.2021.149754](https://doi.org/10.1016/j.apsusc.2021.149754))**





## Full Length Article

## Influence of post annealing treatments on the luminescence of rare earth ions in ZnO:Tb,Eu/Si heterojunction



C. Guillaume<sup>a,\*</sup>, J.L. Frieiro<sup>b</sup>, O. Blázquez<sup>b</sup>, C. Labbé<sup>a</sup>, J. López-Vidrier<sup>b</sup>, B. Garrido<sup>b</sup>, S. Hernández<sup>b</sup>, B. Liu<sup>c</sup>, L. Khomenkova<sup>d,e</sup>, C. Frilay<sup>a</sup>, F. Lemarié<sup>a</sup>, C. Leroux<sup>f</sup>, D. Pelloquin<sup>f</sup>, X. Portier<sup>a</sup>

<sup>a</sup> CIMAP, CEA, UMR CNRS 6252, ENSICAEN, Normandie Université, 6 Boulevard du Maréchal Juin, 14050 Caen, France

<sup>b</sup> MIND-IN2UB, Departament d'Enginyeria Electrònica i Biomèdica, Universitat de Barcelona, Martí i Franques 1, E-08028 Barcelona, Spain

<sup>c</sup> Shenyang National Laboratory for Materials Science (SYNL), Institute of Metal Research (IMR), Chinese Academy of Sciences (CAS), No. 72, Wenhua Road, Shenyang District, Shenyang 110016, China

<sup>d</sup> V. Lashkaryov Institute of Semiconductor Physics of the NAS of Ukraine, 45 Prospect Nauky, 03028 Kyiv, Ukraine

<sup>e</sup> National University of "Kyiv-Mohyla Academy", 2 Skovorody str., 04070 Kyiv, Ukraine

<sup>f</sup> CRISMAT, UMR CNRS 6508, ENSICAEN, Normandie Université, 6 Boulevard du Maréchal Juin, 14050 Caen, France

## ARTICLE INFO

## ABSTRACT

## Keywords:

Magnetron sputtering  
ZnO thin film  
(Tb, Eu) co-doping  
Annealing  
Photoluminescence  
Electroluminescence

(Tb, Eu) co-doped ZnO films with about 3 at.% total doping rate were grown by magnetron sputtering on Si substrate. Post annealing treatments were performed at 973–1373 K in continuous nitrogen flow to investigate the transformation of microstructural and optical characteristics by means of X-ray diffraction, transmission electron microscopy, photoluminescence and electroluminescence. For annealing temperatures lower than 1073 K, segregation of Eu and Tb was observed mainly at the film/substrate junction. For temperatures higher than 1173 K, additional phases appeared, namely, Zn<sub>2</sub>SiO<sub>4</sub> and rare earth silicates. For the highest temperature investigated (1373 K), only silica and rare earth silicates remained in the film due to Zn evaporation. PL measurements indicated a very intense Eu emission associated with the presence of rare earth silicate inclusions. Energy transfer from Tb towards Eu was evidenced in this secondary phase. At last, based on these preliminary works, a (Tb, Eu) co-doped ZnO/Si electroluminescent structure was produced and showed very promising results paving the way for very thin ZnO based light emitting diodes.

## 1. Introduction

ZnO is a well-known wide band-gap (3.3–3.4 eV) semiconductor suitable for many applications in the optoelectronic industry such as optical sensors and light emitting diodes (LEDs) but also in other emerging fields [1]. Indeed, its attractive physical properties combined with the fact that the ZnO growth is relatively simple at various scales using different growth techniques (sol gel [2], MOCVD [3], PLD [4], MBE [5], ALD [6], sputtering [7] methods for bulk and films and various chemical synthesis approaches where Zn salts are combined with bases) make this material the object of many studies during the last decades. In addition, relevant doping can lead to interesting optical functionalities which are currently achieved with more expensive and/or hazardous materials such as indium tin oxide [8] or gallium nitride [9].

Rare earth (RE) doping is often linked to optical functionalities such

as light emitting diodes for lighting or associated to energy conversion (down conversion, down shifting or up conversion) in photovoltaic structures. The photoluminescence (PL) effect is due to internal *d-f* electronic transitions in the RE elements and when they are present in a transparent matrix such as ZnO, optical properties may be exploitable. Among these lanthanides, much attention is paid to terbium (Tb) and europium (Eu). Most of the time, these lanthanides have predominantly a 3<sup>+</sup> valence state in ZnO. Tb ions can also have a 4<sup>+</sup> valence, but this latter does not lead to a radiative recombination [10]. Eu ions can possess a 2<sup>+</sup> oxidation state (EuO and EuSiO<sub>3</sub> phases) upon high annealing temperature, leading to an UV broad band emission [11]. Eu<sup>2+</sup> has been found in ZnO, but its PL signature is inefficient by contrast to that of the Eu<sup>3+</sup> counterpart [12].

In previous works, Tb doped ZnO films revealed that an energy transfer from ZnO host to Tb<sup>3+</sup> is possible and allows an optimal

\* Corresponding author.

E-mail address: [clement.guillaume@ensicaen.fr](mailto:clement.guillaume@ensicaen.fr) (C. Guillaume).

<https://doi.org/10.1016/j.apsusc.2021.149754>

Received 29 September 2020; Received in revised form 17 March 2021; Accepted 2 April 2021

Available online 8 April 2021

0169-4332/© 2021 Elsevier B.V. All rights reserved.

emission of  $Tb^{3+}$  upon an annealing close to 873 K [12,13]. Energy transfer from ZnO host to  $Eu^{3+}$  is also explained by transfer mechanisms via  $Zn_i$  and  $V_{Zn}$  defects [14] and annealing treatment at temperatures close to 873 K is improving this RE emission as well [15]. However, these energy transfers are often qualified in the literature as non-efficient [15,16]. Recently, a study of ZnO:Tb (3 at.%), Eu (<1 at. %)/Si and ZnO:Tb (3 at.%), Eu (<1 at. %)/alumina films of about 800 nm thick and annealed at 1173 K has been performed [17]. The authors demonstrated the formation of Tb oxide at the grain boundaries between the ZnO columns (columnar growth) within the film and the formation of zinc silicate and rare earth silicate at the bottom of the film in the case of the Si substrate. No aluminate phase was observed in the annealed structure grown on the alumina substrate. Two families of PL peaks were identified: a broader one coming from the Tb oxide inclusions, and sharper ones originating from the rare earth silicates. An energy transfer from Tb towards Eu was also mentioned.

Regarding ZnO:Tb, Eu films, a PL study on anneal treatments up to 1373 K was carried out revealing a very intense emission of  $Eu^{3+}$  upon the anneal treatment at the highest temperature. A possible explanation is given by an efficient energy transfer from  $Tb^{3+}$  to  $Eu^{3+}$  in a matrix of Willemite ( $Zn_2SiO_4$ ) [7]. As mentioned in previous works performed on ZnO:RE layers, most of the lanthanides tend to diffuse out of the ZnO matrix upon annealing and create secondary phases inside the film at high temperatures (from 1173 K) [18]. This diffusion process occurs from a few hundreds of degrees Celsius. But only a few studies dealt with the behavior of Tb and Eu doped ZnO thin films (about 150 nm thick) deposited on Si and exposed to extreme temperatures (up to 1373 K). The purpose of this work is to bring more insight on the various phases formed in doped ZnO films upon severe post anneal treatments and their associated luminescence properties. A complete study of the evolution of microstructural and optical properties with the annealing temperature for (Tb, Eu)-co-doped ZnO/Si junction is presented in this work. X-ray diffraction, transmission electron microscopy and energy dispersive X Ray spectroscopy are used for microstructural characterizations and PL results are analyzed to understand the origin of the observed emissions as well as their evolution with the annealing temperature value. A special attention is focused on the microstructural evolution of the film and their consequences in the PL response for the highest annealing temperatures (1273 K and 1373 K) for which secondary phases are obtained. A very recent microstructural study has been carried out on RE silicate inclusions in similar films (annealed at 1373 K) and the RE distribution in the oxyapatite cell is discussed [19].

The efficiency of PL emission of rare earths in ZnO is usually low, but ZnO, being a rather good conducting oxide, offers another perspective such as the electrical excitation of RE doped ZnO-based junctions [20]. Indeed, due to the presence of a significant amount of RE dopants uniformly distributed at the level of the junction upon moderate thermal treatments, ZnO:Tb, Eu/Si junction could be an interesting structure for electroluminescence (EL). In this paper, a LED structure based on Tb and Eu doped ZnO/Si materials is also considered to determine whether a 150 nm doped ZnO film with only a few at.% doping grown on an Si substrate could be feasible. If this is the case, in principle, by producing a stack of three layers respectively doped with different RE elements providing red, green and blue emissions, a white LED structure could be achieved and could pave the way to a cheap structure for lighting functionalities.

## 2. Experimental details

The films were elaborated by a bottom-up radio frequency magnetron sputtering setup equipped with two separate targets and temperature controlled 2-inch wafer holders. All the films were grown on (001) oriented 2 in. Si substrates. Film deposition was performed using argon plasma, a chamber vacuum pressure of 15  $\mu$ bar, a power density fixed at 1.95 W  $cm^{-2}$  and a substrate temperature value of 373 K. The holder/target distance was set at 7 cm. The target was composed of a pure 4 in.

ZnO target on the top of which 4  $Tb_4O_7$  and 10  $Eu_2O_3$  calibrated pellets were placed. Several preliminary experiments were carried out in order to correlate the number of pellets with the corresponding doping rate and the above mentioned configuration gave rise to 1.6 at.% and 1.3 at.% for Tb and Eu concentrations, respectively. These values were obtained by energy dispersive X Ray (EDX) spectroscopy measurements with a JSM6400 JEOL scanning electron microscope for as deposited films of about 1.5  $\mu$ m thick to make sure that the excited volume by the electron beam came only from the film and not from the substrate. Except for this specific measurement, all the films discussed in the structural and PL sections were 150 nm thick and the film dedicated to the electroluminescence experiment was 65 nm thick.

Wafers were cut in regular squared pieces (about 1 cm  $\times$  1 cm) and annealing treatments of the films were performed in a conventional furnace at  $T_A = 973$ –1373 K with a step of 100 K during 1 h in a continuous nitrogen flow. The samples were left in the furnace for the cooling down to room temperature.

Structural and microstructural investigations were conducted using X-ray diffraction and transmission electron microscopy (TEM) techniques. X-ray diffraction diagrams were acquired with a D8 Bruker Discover diffractometer, using a Cu ( $\lambda_{K\alpha1} = 1.5406$  Å) source, in Bragg Brentano configuration ( $\theta$ - $2\theta$ ). TEM observations in various modes were performed with a double corrected (probe and imaging) JEOL ARM200F microscope equipped with a cold FEG (Field Emission Gun) source operated at 200 kV. With this microscope, a point to point resolution of the order of 1.0 Å could be reached in high resolution mode (HRTEM). In addition, it was equipped with a scanning system (STEM) which offered the possibility to take chemical contrast images (resolution of 0.78 Å) owing to a high angle annular dark field (HAADF) detector as well as STEM EDX chemical mapping at a nanometer scale owing to a CENTURIO JEOL EDX spectrometer. The thin foils for TEM observations were prepared by a focused ion beam system (FEI HELIOS NanoLab 660) and prior to the thinning with a gallium beam, the top surface of the film was protected with a thin carbon film (a few tens of nm thick) and two platinum layers, one deposited electronically and the final one grown with the ion beam (a few microns thick in total).

Regarding optical properties, three laser sources were chosen for photoluminescence measurements. A laser diode at 266 nm, an argon laser at 488 nm and a frequency-doubled Nd:YAG laser at 532 nm wavelength have been used. The power density values were 2.6 W  $cm^{-2}$  and 50.9 W  $cm^{-2}$  for the first two lasers, respectively. For the third one, the beam went through the objective of a microscope with a  $\times 50$  magnification. The beam diameter was estimated at 0.87  $\mu$ m. The density power was close to 410 kW  $cm^{-2}$ . Such a power density represents approximately a factor of 1.6  $10^5$  compared to the laser used for  $\lambda_{excitation} = 266$  nm (2.6 W  $cm^{-2}$ ). Considering this high power density, preliminary measurements for low power densities were carried out by incrementing, using filters, from low power densities up to 410 kW  $cm^{-2}$ . These latter measurements showed that there was no local annealing effect of the beam on the excited part of the film. Finally, note that cathodoluminescence results were also obtained, but the very low signal recorded did not permit to present and analyse properly these data for all the annealing temperature values.

For electroluminescent experiments, electrical contacts were produced by the Department of biomedical and electronic engineering at the University of Barcelona (MIND-IN2UB). Top transparent and highly conductive contacts were composed of ZnO cylinders of 100 nm height and 0.5 mm in diameter, deposited on the ZnO:Tb, Eu film via atomic-layer-deposition (ALD) with a substrate temperature of 473 K. The bottom contact deposited on Si was a 200 nm thick layer of Al. Current-voltage characteristic  $I(V)$  and electroluminescent spectra were realized using an Agilent B1500A semiconductor device analyzer for  $I(V)$  measurements. Electroluminescence spectra of the device were acquired through the microscope channel, in optical mode with a CCD camera.

### 3. Structural properties

#### 3.1. X-ray diffraction characterizations

To have a clearer picture of the various phase contributions, we have presented the XRD results by separating the data in three different angle ranges. Fig. 1 shows XRD diagrams of ZnO:Tb (1.6 at.%), Eu (1.3 at.%) films for various annealing temperatures ( $T_A$ ) and focused on the peak position corresponding to the (0002) planes of ZnO (from  $2\theta = 33.5^\circ$  up to  $35^\circ$ ). The reference value for bulk ZnO is indicated by the green vertical straight line. A significant difference (about  $0.48^\circ$ ) is observed between the angular position of the (0002) peak for the as-deposited film and that of the reference. This shift means an increase of the c parameter of about 1.3%. It can be noted that the (0002) peak of the as-deposited film is relatively broad. For the films annealed at 973 K and 1173 K, the angular deviations are about  $-0.07^\circ$  and  $+0.08^\circ$ , respectively, revealing a variation in the c parameter of about  $+0.19\%$  and  $-0.23\%$ , respectively. For  $T_A = 1273$  K, the (0002) peak intensity falls down and disappears, in favor of a rhombohedral structure with the parameters  $a = b = 13.95 \text{ \AA}$  and  $c = 9.32 \text{ \AA}$ , consistent with Willemite  $\text{Zn}_2\text{SiO}_4$  and the appearance of the corresponding (41-50) planes. Interestingly, for the highest temperature (1373 K) the ZnO and  $\text{Zn}_2\text{SiO}_4$  signatures have disappeared. The average grain size of the films, calculated using the Scherrer equation following the [0002] axis, increases with  $T_A$  from 21 nm for the as-deposited film, up to 23 nm for the 973 K annealed film and 40 nm for 1173 K.

Fig. 2(a) and 2(b) are XRD diagrams of the same annealed ZnO:Tb, Eu films for the angular ranges from  $20.5^\circ$  up to  $33.5^\circ$  and from  $36^\circ$  up to  $60^\circ$ , respectively. For  $T_A = 1173$  K, new peaks appear which are consistent with the above mentioned zinc silicate phase ( $\text{Zn}_2\text{SiO}_4$ ). Another secondary phase is also detected by the presence of other peaks at  $2\theta = 21.82^\circ$ ;  $29.00^\circ$ ;  $31.82^\circ$ ;  $32.98^\circ$ ;  $39.90^\circ$ ;  $44.48^\circ$ ;  $48.72^\circ$ ;  $51.39^\circ$  and  $56.47^\circ$ . These peaks are in good agreement with a RE silicate namely  $\text{Tb}_x\text{Eu}_y\text{Si}_z\text{O}_w$  in accordance with an apatite related phase. For the highest annealing temperature  $T_A = 1373$  K, very sharp and intense peaks associated to this so called apatite related phase prevail whereas the peaks assigned to the  $\text{Zn}_2\text{SiO}_4$  phase have disappeared. More details on this phase are given in the next section (TEM results).

TEM observations have been carried to confirm at a nanoscale these previous results and to bring more details on the identification and localization of the RE silicate phase whose growth is generated upon thermal treatment from 1173 K but more obviously at  $T_A = 1373$  K.

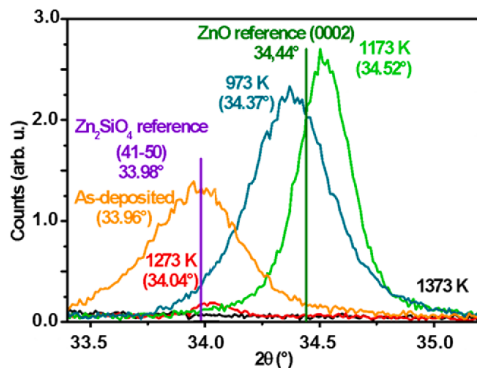


Fig. 1. XRD patterns focused on the (0002) peak of ZnO recorded with Bragg-Brentano configuration ( $\theta$ - $2\theta$ ) of the ZnO:Tb, Eu films versus  $T_A$ .

#### 3.2. Transmission electron microscopy observations

(Tb, Eu)-co-doped ZnO films, annealed at 973 K, 1273 K and 1373 K have been observed by TEM. Fig. 3 summarizes some TEM images for the film annealed at 973 K. They correspond to cross sectional views of the film along a [110] direction of the Si substrate allowing the electron beam to be parallel to the film/substrate interface. Fig. 3(a) and 3(b) are bright field and high resolution (HR) TEM images, respectively. The Tb and Eu co-doped films have a typical columnar structure of wurtzite ZnO as shown in Fig. 3(a) by the elongated vertical dark contrasts (Bragg contrasts). The HRTEM image (Fig. 3(b)) is focused on the bottom part of the film, where two amorphous sublayers of a few nanometers thick with very different contrasts. The bottom layer with the brighter contrast (about 3 nm thick) on the top of the substrate is a silica layer. The other thinner layer with a darker contrast located on top of the silica is enriched with Tb and Eu as demonstrated by the EDX chemical analysis. Fig. 3(c) is a chemical profile of Tb and Eu along the orange line indicated in Fig. 3(b). It clearly shows the RE enrichment over a thickness of about 4 nm at the bottom of the film just above the silica layer. Fig. 3(d) shows an image taken in STEM HAADF mode with chemical contrasts. Except for the bottom part of the film (discussed previously), the uniform contrast across all the film suggests an homogeneous distribution of the species. However, the STEM EDX Tb and Eu chemical maps in Fig. 3(e) and 3(f) give more insight. The higher contrast at the bottom of the film clearly visible for both maps confirm the segregation of the RE elements mainly at the bottom of the film over a thickness of about 3–4 nm. This RE-enriched layer contains up to 5 at.% of Tb and 3 at.% of Eu. It results from the post-annealing diffusion of RE ions at the film/substrate interface. This diffusion created a RE depleted zone, just above the REs enriched layer at the bottom of the film [Fig. 3(e-f)]. In the lower part of the film, diffusion forces linked to the potential well of the junction and/or the field of the space charge region of the junction stimulates the segregation of dopants towards the substrate during annealing [9]. Moreover, the lower part of the film close to the substrate has a lower grain size than the upper part of the film favoring REs diffusion owing to the grain boundaries [21].

Fig. 4(a) is a cross-sectional view (bright field TEM image) of the ZnO:Tb, Eu film annealed at 1273 K, along the [110] direction of the Si substrate. One can observe major changes compared to the film annealed at 973 K. For instance, one can notice the presence of a mostly crystallized phase at the bottom part of the film as evidenced by the darker Bragg contrasts in some regions and covering the whole film (no columns anymore). Furthermore, the chemical maps in Fig. 4(c-g) show that this region of the film is composed of Zn, O and Si elements and it contains a small amount of RE ions (0.6 at.% and 0.8 at.% for Tb and Eu, respectively). The presence of Si within the whole film (with about 16.0 at.%) is confirmed by Fig. 4(e). The formed phase in this bottom region has been identified by the analysis of various Fast Fourier Transformed (FFT) of high resolution TEM images as being  $\text{Zn}_2\text{SiO}_4$  with a rhombohedral structure, the R-3 space group and the following lattice parameters  $a = b = 13.95 \text{ \AA}$  and  $c = 9.32 \text{ \AA}$ . This result is in agreement with the XRD data. In the upper part of the film, large grains of about 100 nm size with a darker contrast are clearly visible. The chemical analysis of these inclusions reveals a high content of Eu (7.3 at.%) and Tb (12.2 at.%), as well as Si and O but a low content of Zn (Fig. 4(c-g)). The darker contrast in Fig. 4(a) is thus partly explained by the Bragg contrast (due to a crystalline phase) but also by a significant presence of RE (high Z value) in these inclusions.

A typical bright field TEM image of the Tb and Eu silicate phase is presented in Fig. 5(a), showing two Tb and Eu rich grains (grains 1 and 2). Fig. 5(b) is an HRTEM image of a region of grain 1. From different zone axes and their corresponding Fast Fourier Transforms (FFTs), as presented in Fig. 5(c) obtained from the high-resolution image of grain 1, a microstructural description can be made with a hexagonal apatite parent structure for the  $\text{Tb}_x\text{Eu}_y\text{Si}_z\text{O}_w$  phase, in agreement with the XRD data. Taking EDX data into account, the  $\text{Tb}_{12} \text{Eu}_{7.3} \text{Si}_{16} \text{O}_{62.0}$

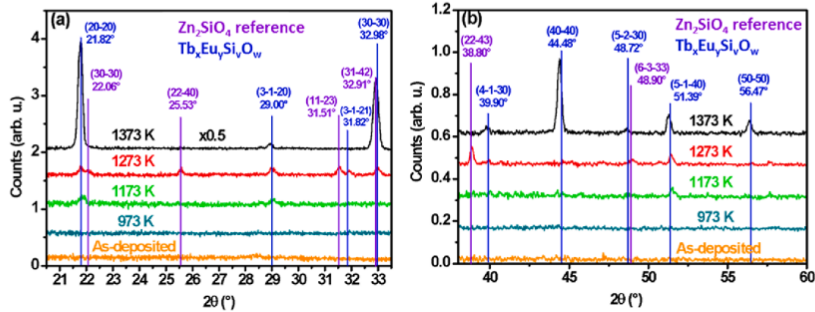


Fig. 2. XRD patterns of the ZnO:Tb,Eu films for various  $T_A$  values and for the angular ranges from 20.5° to 33.5° (a) and from 36° to 60° (b).

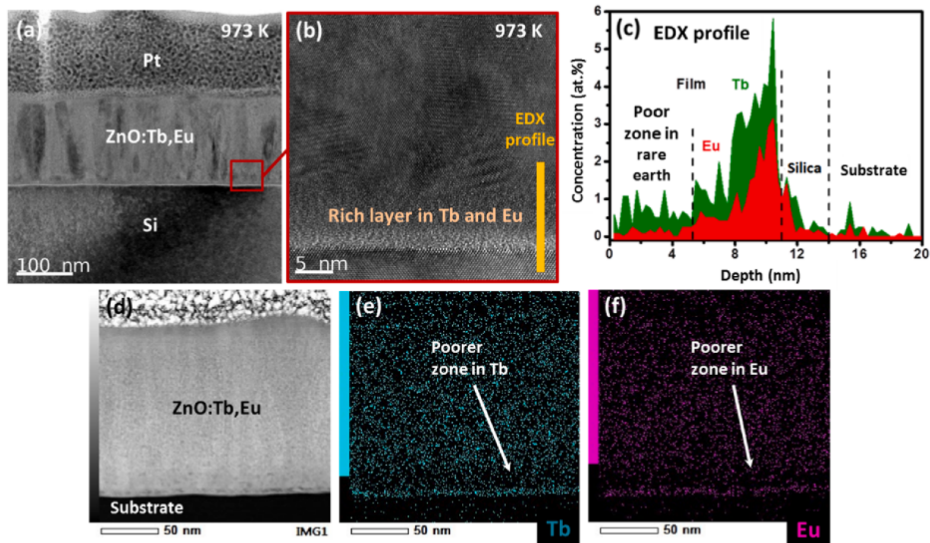


Fig. 3. (a) Conventional TEM image and (b) in high-resolution mode, of the ZnO:Tb,Eu, film annealed at 973 K. (c) Chemical profile of Tb and Eu along the orange line in (b). (d) STEM HAADF image and chemical maps for the Tb (e) and Eu (f) elements. (For interpretation of the references to colour in this figure legend, the reader is referred to the web version of this article.)

stoichiometry can be proposed for these inclusions. Note that several EDX measurements were carried out on various inclusions and the results were very similar considering the errors (about 1 at.% for heavier elements and up to 10% for lightest elements such as Oxygen).

Similar TEM observations have been realized for the film annealed at 1373 K. In the TEM image in Fig. 6(a), the region of the film observed is composed of a larger grain than those observed at 1273 K with well-defined facets and showing an hexagonal shape. It covers the entire thickness of the film (about 140 nm) and reaches >200 nm for its largest dimension lying in the film. Several grains of this kind have been observed in the same TEM foils allowing the observation of several microns. In the vicinity of this grain, an amorphous phase with a bright contrast is present. The data from the EDX maps shown in Fig. 6(d) and 6 (e) give the following stoichiometry:  $Si_{1.3}O_2$  which is close to silica (considering the uncertainty for O) for the amorphous phase with an additional 0.7 at.% of Zn, 1.1 at.% of Tb and 1.3 at.% of Eu. Moreover, crystallized  $Zn_2SiO_4$  is also formed in the film (not visible in the region

shown), in small proportion compared to the film annealed at 1273 K. As for the film annealed at 1273 K, the chemical analysis shows within the faceted grain, a significant amount of Tb of 11.0 at.% and Eu of 8.6 at.% as well as Si and O with 18.5 at.% and 61.0 at.%, respectively. These results reveal the evaporation of Zn upon extreme anneal treatment.

Similarly to the previous annealing temperature, the  $Tb_2Eu_2Si_6O_{19}$  phase is identified from the FFT in Fig. 7(c) obtained from the HREM image of a part of the grain (Fig. 7(a)) shown in Fig. 7(b). Again, these data are consistent with an hexagonal structure crystallizing with the following cell parameters  $a \approx b \approx 9.4 \text{ \AA}$  and  $c \approx 6.9 \text{ \AA}$  close to an apatite-type structure. The phase stoichiometry is in favor of a Tb and Eu silicate with the following chemical formula:  $Tb_{11.0}Eu_{8.6}Si_{18.5}O_{61.0}$ . Note that a distortion of this hexagonal lattice is detected with the variation of the RE content (at 1373 K) as reported in another work on RE silicate  $RE_2Si_2O_7$  depending on the nature of the RE [22]. A more detailed study has been developed on the RE silicate microstructure in similar ZnO:Tb, Eu films annealed at 1373 K in which the Eu and Tb ion distribution in

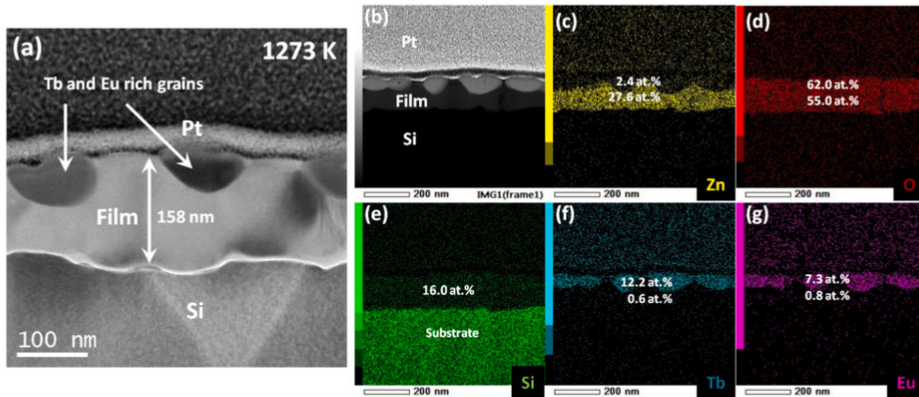


Fig. 4. (a) Bright field TEM Image of the ZnO:Tb,Eu film for  $T_R = 1273$  K. (c-g) Chemical maps of Zn (c), O (d), Si (e), Tb (f) and Eu (g), corresponding to the STEM HAADF image in figure (b).

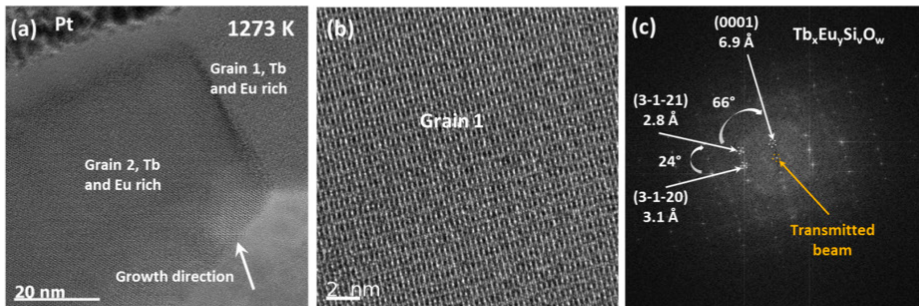


Fig. 5. (a) Bright field TEM image of the ZnO:Tb,Eu film annealed at 1273 K showing two grains of a Tb and Eu rich phase localized at the upper part of the film. (b) HRTEM Image of grain 1, identified in Fig. 5(a). (c) Fast Fourier Transform of grain 1.

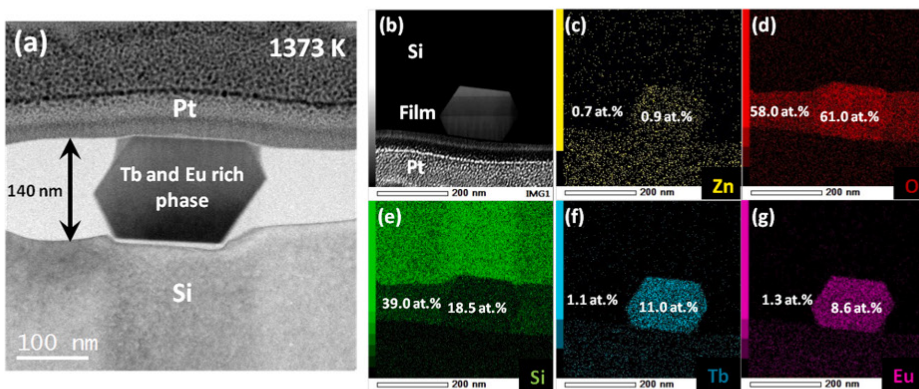


Fig. 6. (a) Bright field TEM image for the ZnO:Tb,Eu film for  $T_A = 1373$  K. (c-g) Chemical maps of Zn (c), O (d), Si (e), Tb (f) and Eu (g), corresponding to the STEM HAADF image in figure (b).

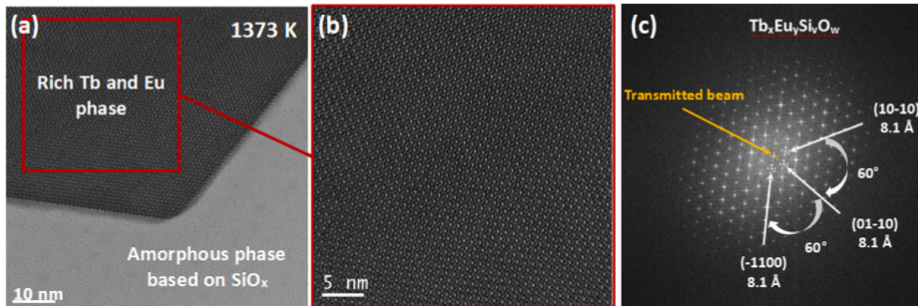


Fig. 7. (a) HRTEM image of the ZnO:Tb,Eu film for  $T_A = 1373$  K. (b) Enlarged HRTEM Image from the squared region in red of the grain in figure (a). (c) Fast Fourier Transform associated to the image in figure (b). (For interpretation of the references to colour in this figure legend, the reader is referred to the web version of this article.)

the atomic cell is discussed [19]. By comparison, the stoichiometry of the grains formed in the film annealed at  $T_A = 1373$  K is slightly different from that obtained for the film annealed at 1273 K ( $Tb_{12.2}Eu_{7.3}Si_{16.0}O_{62.0}$ ). With the raise of  $T_A$  from 1273 K to 1373 K, the stoichiometry of this phase leads to a [Tb]/[Eu] ratio value evolving from 1.67 down to 1.28. This latter value is close to 1.23 corresponding to the value of this ratio for the as-deposited film with an homogeneous distribution of the REs in the film. We conclude that for the extreme  $T_A$  value, the [Tb]/[Eu] ratio for the inclusions approaches the initial

dopant ratio.

### 3.3. Summary of the structural properties

The results demonstrate the diffusion of Tb and Eu and their segregation in an amorphous layer of a few nanometers thick at the film/substrate interface just above the native silica layer for  $T_A = 973$  K. The formations of zinc silicate ( $Zn_2SiO_4$ ) and apatite related ( $Tb_xEu_ySi_uO_w$ ) inclusions are observed from  $T_A = 1173$  K. These phases resulting from

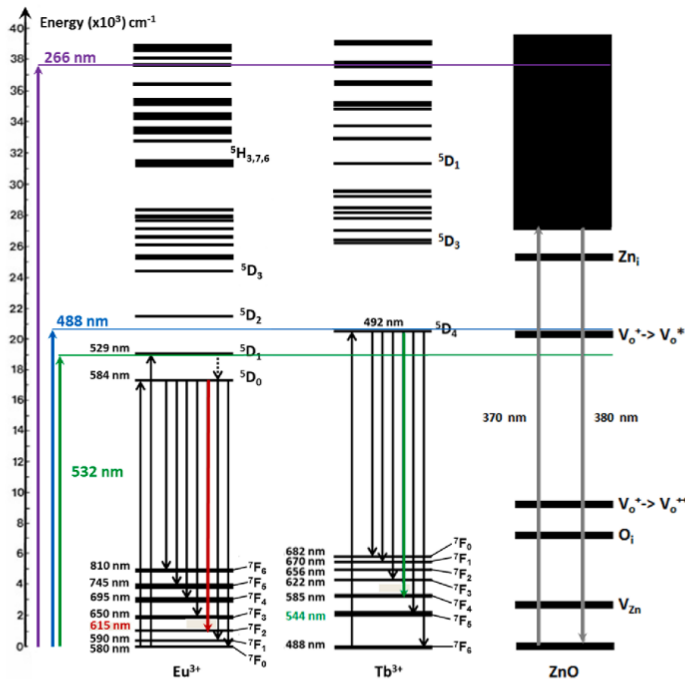


Fig. 8. Energy diagram of  $Eu^{3+}$  and  $Tb^{3+}$  (in  $LaCl_3$ ), with the 532 nm (green), 488 nm (blue) and 266 nm (purple) excitations [25]. The energy diagram of ZnO defects is also presented for comparison [26,27]. (For interpretation of the references to colour in this figure legend, the reader is referred to the web version of this article.)

the diffusion of Si in the film supplant the main ZnO phase at lower  $T_A$  values. For  $T_A > 1173$  K, the  $Tb_xEu_ySi_zO_w$  phase becomes dominant within the film with an increasing grain size of a few hundred nanometers, while  $Zn_2SiO_4$  tends to disappear in favor of silica and zinc evaporates almost completely from the film during annealing at the highest annealing temperature [23]. The [Tb]/[Eu] ratio decreases from 1.67 down to 1.28 for 1273 K and 1373 K, respectively. This last value is close to the initial [Tb]/[Eu] value (1.23) for the as-grown state of the film.

#### 4. Photoluminescence properties

In this part, the PL properties of the ZnO:Tb,Eu films are studied for different laser excitations and different  $T_A$  values. A particular attention is paid to the emission of the Tb and Eu-based phases as well as to the interaction between these two dopants.

Although the positions of the Tb and Eu energy levels may fluctuate slightly from one matrix to another, an energy diagram is recalled in Fig. 8, for the trivalent ions of  $Tb^{3+}$  and  $Eu^{3+}$  in a  $LaCl_3$  matrix [24]. The energy bands of ZnO are also specified. The three laser excitation wavelengths (532 nm, 488 nm and 266 nm) used are also displayed by colored arrows in order to highlight possible resonant levels with these excitations.

Regarding the possible  $Eu^{3+}$  positions in ZnO, some authors showed that  $Eu^{2+}$  can replace  $Zn^{2+}$  ions in the ZnO matrix and it is possible to excite  $Eu^{2+}$  via the  $Zn_i$  defects [28]. Other authors evoked the  $Eu^{3+}$  localization in an interstitial position in the ZnO matrix [29,30]. In addition, the significant difference in ionic radius between  $Zn^{2+}$  (0.74 Å) and  $Eu^{3+}$  (0.91 Å) makes a substitution of  $Eu_{Zn}$  difficult [31]. As far as  $Tb^{3+}$  is concerned, the same types of positions (substitution of Zn [32,33], interstitial site, and grain boundaries) and activations as for  $Eu^{3+}$  are reported, via ZnO defects such as  $Zn_i$  [34] or surface defects [31]. Indeed,  $Tb^{3+}$  has an ionic radius close to 0.92 Å, close to that of  $Eu^{3+}$ , and much larger than that of  $Zn^{2+}$  (0.74 Å). Thus, as for  $Eu^{3+}$ , the introduction of  $Tb^{3+}$  in ZnO is possible but subject to an instability which explains the diffusion phenomena and segregation of these REs outside the structure of ZnO during heat treatments.

##### 4.1. Laser excitation above the ZnO conduction band

The PL measurements of the ZnO:Tb (1.6 at.%), Eu (1.3 at.%) films as a function of the  $T_A$  are presented in Fig. 9, for a 266 nm excitation wavelength. Fig. 9(a) shows the PL response for all  $T_A$  in the spectral range from 360 nm up to 460 nm, whereas Fig. 9(b) and 9(c) display PL spectra in the 450 nm – 750 nm spectral range for low (973, 1073 and 1173 K) and high ( $T_A$  1273 and 1373 K) values, respectively.

##### 4.1.1. Indirect excitation of RE via ZnO defects

For an excitation upwards of the ZnO gap, Fig. 9(a) shows the presence of the excitonic peak emission for  $T_A = 1173$  K (high intensity) and 1273 K (low intensity). For the lowest  $T_A$  values, no emission is observed. For the highest  $T_A$  values at 1273 K and more clearly at 1373 K, the exciton peak collapses. As demonstrated in the previous section, the ZnO:Tb,Eu film reacts with the Si substrate to form zinc silicate ( $Zn_2SiO_4$ ) and also Tb,Eu silicate ( $Tb_xEu_ySi_zO_w$ ). A concomitant disappearance of ZnO has also been noticed. It is therefore not surprising to see a drop of the excitonic emission of ZnO. For  $T_A = 1373$  K (black curve), a wide band is visible from 380 nm to 460 nm, and even until 550 nm in Fig. 9(c). This latter cannot be associated with ZnO defects at such a  $T_A$  value since ZnO structure has totally disappeared. This broad emission band could come from the divalent ion  $Eu^{2+}$  and its associated levels  $4f^65d$  for which the emission wavelength is very sensitive to the crystal field [35,36]. This emission of  $Eu^{2+}$  could also have its origin in the formation of a metastable silicate of the  $EuSiO_3$  type.

The PL intensity in the spectral range from 550 to 750 nm, corresponding to the defects in ZnO [Fig. 9(b)], is very low but observable for

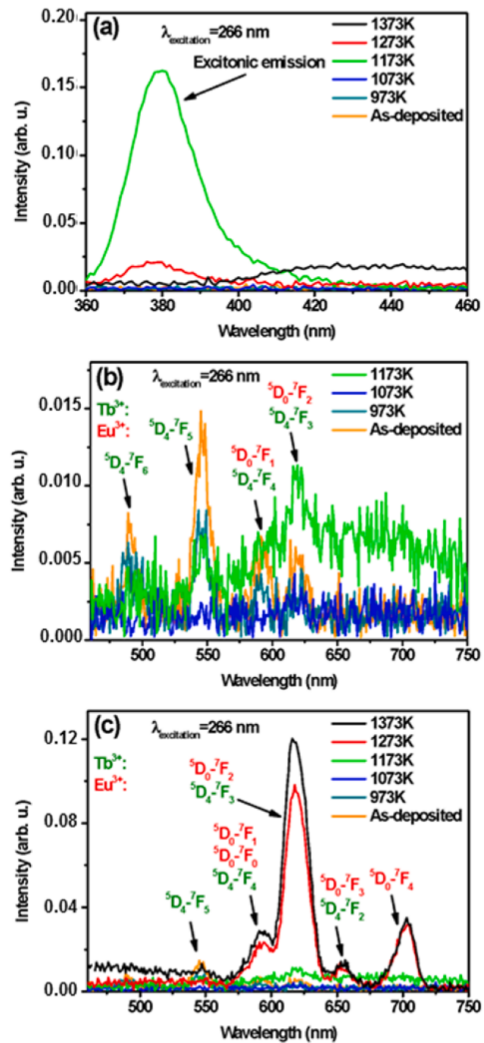


Fig. 9. PL spectra of ZnO:Tb (1.6 at.%), Eu (1.6 at.%) film for a laser excitation at 266 nm, in the spectral range (a) from 360 to 460 nm and (b) from 450 to 750 nm for the lower annealing temperatures and (c) for all  $T_A$ .

the film annealed at 1173 K. The main PL peaks at 545 nm and 620 nm are those originating from the  $Tb^{3+}$  and  $Eu^{3+}$  ions, respectively (see Fig. 8). In this spectral range, the PL intensity is dominated by the  $Tb^{3+}$  emission for the as-deposited and 973 K annealed films [Fig. 9(b)] while it mainly comes from the  $Eu^{3+}$  ions for the highest annealing temperatures (Fig. 9(c)).

This particular behavior of the PL intensity with high thermal budgets is explained as follows. The annealing generates the formation of the  $Tb_xEu_ySi_zO_w$  phase and its presence seems to be at the origin of this high intensity of PL of  $Eu^{3+}$  ions. However, it is possible that zinc silicate ( $Zn_2SiO_4$ ) with Tb and Eu doping to the extent of 1 at.% for each RE, contributes in some extent to the emission of  $Tb^{3+}$  and  $Eu^{3+}$  [37].

However, the volume occupied by this phase tends to decrease drastically with the evaporation of Zn. At  $T_A = 1373$  K, this phase is almost completely replaced by a silica phase with about 1 at.% of Tb and 1 at.% Eu doping [38], as noticed from XRD and TEM data, while the emission of  $\text{Eu}^{3+}$  remains dominant with an increase of about 20% (from  $T_A = 1273$  K to 1373 K). The  $\text{Tb}_x\text{Eu}_y\text{Si}_z\text{O}_w$  phase whose grain size has increased with  $T_A$  (Fig. 4(a) and 6(a)) seems to be the main reason of this PL intensity evolution of  $\text{Eu}^{3+}$ .

Fig. 10(a) connects the integrated PL intensities of  $\text{Tb}^{3+}$  and  $\text{Eu}^{3+}$  emissions from 475 up to 750 nm with the structural evolution of the matrix containing the emitting REs, with respect to  $T_A$ . In Fig. 10(b), only the intensities at 545 nm ( $\text{Tb}^{3+}$ ) and 620 nm ( $\text{Eu}^{3+}$ ) are plotted as a function of  $T_A$ . Note that for  $T_A = 1173$  K, the PL signatures of the ZnO defects are still visible. We have subtracted these signals to keep only the integrated PL intensities of the REs.

The plot in Fig. 10(a) shows a slight decrease in the integrated intensity from 373 K up to 1073 K followed by an abrupt increase from 1073 K up to 1373 K. Fig. 10(b) discriminates the evolution of the two PL peak intensities of Tb and Eu: the intensity of the main emission peak of  $\text{Tb}^{3+}$  (545 nm) decreases with  $T_A$  and the main emission peak of  $\text{Eu}^{3+}$  (620 nm) increases suddenly for  $T_A > 1173$  K. Note that the  ${}^5\text{D}_4\text{-}{}^7\text{F}_3$  transition of  $\text{Tb}^{3+}$  can also contribute to the intensity of the peak at 620 nm but in a much lesser extent.

#### 4.1.2. From $T_A = 373$ K to 1073 K

The visible emission is governed by the signal from  $\text{Tb}^{3+}$  and more particularly, for the as-deposited film and with the  $T_A$  increase until 1073 K, this intensity decreases (Fig. 10(b)). It does not appear any  $\text{Eu}^{3+}$  emission for such  $T_A$  values. The ZnO matrix is not conducive to an excitation of  $\text{Eu}^{3+}$  [12,39].

For the lowest  $T_A$  values down to 1073 K (blue field in Fig. 10(a)), the REs are mainly located within the host matrix. An homogeneous RE distribution, more particularly for the as-deposited film, would favor the emission of  $\text{Tb}^{3+}$ . At low  $T_A$ , the  $\text{Tb}^{3+}$  could be more excited via the ZnO defects than in the case of  $\text{Eu}^{3+}$ . On the other hand, with the increase of  $T_A$ , the REs tend to diffuse from the ZnO matrix via the grain boundaries first and then towards the film/substrate interface [40]. The PL intensity of  $\text{Tb}^{3+}$  tends to decrease with the annealing temperature, probably in relation with the RE diffusion phenomena observed in TEM toward the bottom part of the film until  $T_A = 1073$  K (from 373 K up to 1073 K) leading to a quenching of the PL intensity of  $\text{Tb}^{3+}$ . This quenching is possibly induced by resonant non-radiative energy transfers [41] between  $\text{Tb}^{3+}$  ions due to their proximity. They excite each other and increase the probabilities of non-radiative recombinations due to the segregation of the species in an amorphous environment. An oxidation

of  $\text{Tb}^{3+}$  to  $\text{Tb}^{4+}$  can also be considered as mentioned by some authors [10]. These  $4^+$  valence ions are known in the literature to not lead to a radiative emission and could be responsible for the disappearance of the luminescence of  $\text{Tb}^{3+}$  linked to its wide and strong absorption band in the visible region.

#### 4.1.3. $T_A = 1173$ K

We note that for  $T_A = 1173$  K, the emission of the main peak of  $\text{Tb}^{3+}$  is observable at 545 nm. However, another peak around 620 nm of the same intensity is also observed (Fig. 9(b)) which is normally a less intense peak for  $\text{Tb}^{3+}$ . This difference in intensity may be due to a change in the environment around  $\text{Tb}^{3+}$  favoring both the emissions of the  ${}^5\text{D}_4\text{-}{}^7\text{F}_5$  and  ${}^5\text{D}_4\text{-}{}^7\text{F}_3$  transitions of  $\text{Tb}^{3+}$ . But it is more likely that this emission is associated with the  ${}^5\text{D}_0\text{-}{}^7\text{F}_2$  transition of  $\text{Eu}^{3+}$  at 620 nm which is the main peak intensity of  $\text{Eu}^{3+}$ . This last hypothesis is supported by shorter distances between REs by diffusion of  $\text{Tb}^{3+}$  and  $\text{Eu}^{3+}$  towards the interfaces with the increase of  $T_A$  which leads to an activation of  $\text{Eu}^{3+}$  by an efficient energy transfer from  $\text{Tb}^{3+}$  to  $\text{Eu}^{3+}$  [42]. More importantly, it is most probable that the silicate phase described in the structural properties sections and containing relatively high amount of REs ( $\text{Tb}_x\text{Eu}_y\text{Si}_z\text{O}_w$ ) starts to form and leads to the emission of the REs in a favorable crystal field. The atomic arrangement in the lattice imposes certain specific and periodic distances between Tb and Eu which are in favor of an energy transfer from Tb towards Eu. These distances are discussed in a forthcoming paper [19].

#### 4.1.4. $T_A > 1173$ K

For  $T_A = 1273$  K and 1373 K, the disappearance of ZnO and the increasing presence of the  $\text{Tb}_x\text{Eu}_y\text{Si}_z\text{O}_w$  phase (increasing grain size) are clearly demonstrated in the previous structural study. In this phase, Tb and Eu are in relatively large quantities and the proximity of these two REs (with precise and periodic distances in the oxyapatite lattice) within the crystallized inclusions leads to an emission of  $\text{Eu}^{3+}$  about 10 times more intense than its  $\text{Tb}^{3+}$  counterpart. This configuration suggests an efficient energy transfer from  $\text{Tb}^{3+}$  to the benefit of  $\text{Eu}^{3+}$  within these  $\text{Tb}_x\text{Eu}_y\text{Si}_z\text{O}_w$  crystallites.

#### 4.1.5. Direct or indirect excitation of RE

Unfortunately, the low RE emissions in ZnO ( $T_A < 1073$  K) do not allow PLE measurements to successfully determine and confirm the origin of the RE excitation. Therefore, it is difficult to claim whether there is a dominant indirect excitation of RE via ZnO host matrix (via ZnO defects) or a direct excitation of RE upon optical stimulation. Cathodoluminescence experiments (not shown) did not permit either to discriminate an excitation process, because of the high energy

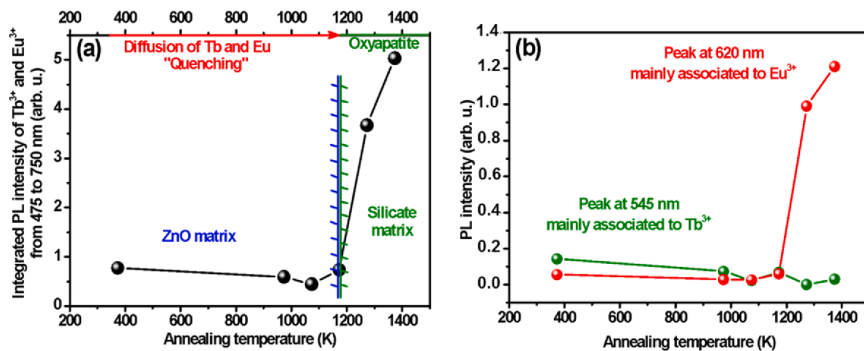


Fig. 10. (a) Plot of integrated PL from 475 to 750 nm and (b) emission intensities at 545 nm and 620 nm versus  $T_A$  based on the PL spectra in Fig. 9(b and c) for an excitation at 266 nm.

excitation. However, we can notice that a direct excitation of  $Tb^{3+}$  and  $Eu^{3+}$  at 266 nm is possible, as we can see it in the energy diagram of  $Tb^{3+}$  and  $Eu^{3+}$  in  $LaCl_3$  (Fig. 8) and according to the work of Pavitra et al. [43]. The absorption of  $Tb^{3+}$  occurs at the 4f-5d band. For Eu ions, an absorption band also exists in the blue/UV spectral region linked to  $Eu^{2+}$  which can lead to broad emission bands between 250 and 550 nm. Another sharper absorption band between 200 nm and 350 nm is associated with the charge transfer from  $O^{2-}$  to  $Eu^{3+}$ , which can cause emission of  $Eu^{3+}$ . Energy transfers between the bands of  $Eu^{2+}$  and those of  $Eu^{3+}$ - $O^{2-}$  are also possible [35].

At last, the  $Tb_xEu_ySi_zO_w$  phase seems to create a favorable mechanism involving an absorption at 266 nm and a transfer of this energy to the energy states of  $Tb^{3+}$ ,  $Eu^{3+}$  and possibly  $Eu^{2+}$  in a lesser extent, for which the emissions are observed [44].

#### 4.2. Laser excitations below the ZnO conduction band

To further investigate the RE excitation process, a 532 nm excitation source was also used to characterize the PL emission of the films and more specifically the emission of  $Eu^{3+}$  with the variation of  $T^{\circ}_A$ . Indeed, according to the energy diagram of  $Tb^{3+}$  and  $Eu^{3+}$  in Fig. 8, it appears, at a first glance, that for this excitation wavelength, only the transition from the fundamental level  ${}^7F_0$  of the  $Eu^{3+}$  to the  ${}^5D_1$  level can be directly excited [45].

The result of the PL measurements for the ZnO:Tb, Eu films as a function of  $T^{\circ}_A$  are presented in Fig. 11. The spectral range detection is limited by our experimental system from 570 nm up to 850 nm.

We can observe the unique emission of  $Eu^{3+}$  due to the direct excitation at 532 nm.  $Tb^{3+}$  is unlikely playing a role in the emission of the PL spectra in Fig. 11(a, b). Surprisingly, the emission of  $Eu^{3+}$  increases overall with  $T^{\circ}_A$  and reaches a maximum at 1073 K. For higher  $T^{\circ}_A$  values, its intensity decreases gradually and seems to remain stable for  $T^{\circ}_A = 1273$  K and 1373 K with a better signature (sharper peaks) of the  $Eu^{3+}$  emission.

The  $Eu^{3+}$  ions present in ZnO for the  $T^{\circ}_A$  values < 1173 K are therefore optically active even in the as-deposited film. Because of the diffusion and segregation processes,  $Eu^{3+}$  ions are mostly located at the bottom of the film in solid solution without forming secondary phases and a small amount is still present in the matrix. This result has been shown by XPS profiles for ZnO:Eu films annealed at 1073 K [12]. All  $Eu^{3+}$  ions contribute to the signal and the rising in the emission intensity of  $Eu^{3+}$  with  $T^{\circ}_A$  is most probably induced by the improvement of the crystalline quality of the ZnO matrix which reduces the non-radiative recombination mechanisms by the passivation of defects.

Beyond, for  $T^{\circ}_A = 1173$  K, 1273 K and 1373 K, the overall PL intensity saturates and decreases slightly. This decrease in intensity could be due to the lower volume of the REs rich inclusions compared to the

whole volume of the film. Furthermore, for these annealing temperatures, the peaks are better defined revealing the different contributions of the sub-energy levels of the same multiplet. The observation of this fine structure of the emission is rarely achievable at room temperature, since the difference between these energy levels is less than the thermal energy,  $k_B T = 25$  meV. The power density of  $410 \text{ kW.cm}^{-2}$  and the relatively high emission intensity may explain the observation of these peaks. Observing a change in the shape of these narrow peaks as a function of  $T^{\circ}_A$  seems to indicate a modification of the local environment around the  $Eu^{3+}$  and particularly, a different and better crystallized environment. Indeed, the environment of these ions went from a ZnO matrix (in the grains and/or at grain boundaries) for the lowest  $T^{\circ}_A$  values, to a silicate matrix such as the  $Tb_xEu_ySi_zO_w$  phase offering better conditions for the emission of RE elements. The slight decrease of the integrated intensity could also originate from the stoichiometry evolution between the inclusions formed at the highest temperatures. The amount of Tb in the inclusions for 1373 K is less than that observed for those formed upon annealing at 1273 K. Consequently, the energy transfer from Tb toward Eu is thus reduced.

#### 5. Highlight of an energy transfer from $Tb^{3+}$ to $Eu^{3+}$

This part comes back on the energy transfer mechanism between  $Tb^{3+}$  and  $Eu^{3+}$  in the  $Tb_xEu_ySi_zO_w$  phase in order to highlight it in more detail. Indeed, from an excitation at 488 nm (with a power density of  $50.9 \text{ W.cm}^{-2}$ ), it is possible to excite  $Tb^{3+}$  from the fundamental level  ${}^7F_6$  to the  ${}^5D_4$  excited level only. The  $Eu^{3+}$  excitation seems to be unlikely in this configuration [46].

PL measurements using an excitation at 488 nm have been performed for the ZnO:Tb, Eu film annealed at 1373 K. The PL spectrum of this sample is presented in Fig. 12.

Despite the direct excitation of  $Tb^{3+}$ , no signal associated with this RE is recorded between 500 and 750 nm, not even the main emission of  $Tb^{3+}$  which is usually located around 545 nm, as it can be observed in Fig. 9(b). On the other hand, a strong emission of  $Eu^{3+}$  is observed. It is centered mainly at about 620 nm and 700 nm. It occurs from the  ${}^5D_4$ - ${}^7F_4$  (585 nm) and  ${}^3D_4$ - ${}^7F_5$  (544 nm) transitions of  $Tb^{3+}$  to the  ${}^7F_0$ - ${}^5D_0$  (580 nm) and  ${}^7F_0$ - ${}^5D_1$  (535 nm) transitions of  $Eu^{3+}$  [7,47]. Such a total energy transfer, apparently very efficient in the  $Tb_xEu_ySi_zO_w$  phase from  $Tb^{3+}$  to  $Eu^{3+}$  was similarly observed (not shown) in a film containing 4.4 times more  $Tb^{3+}$  than  $Eu^{3+}$ .

#### 5.1. Summary of the PL properties

In ZnO, the RE ions PL emissions are globally weak caused by a low solubility of RE elements in this matrix [48]. The  $Tb^{3+}$  emission is the only RE emission observed in ZnO but it decreases when increasing  $T^{\circ}_A$

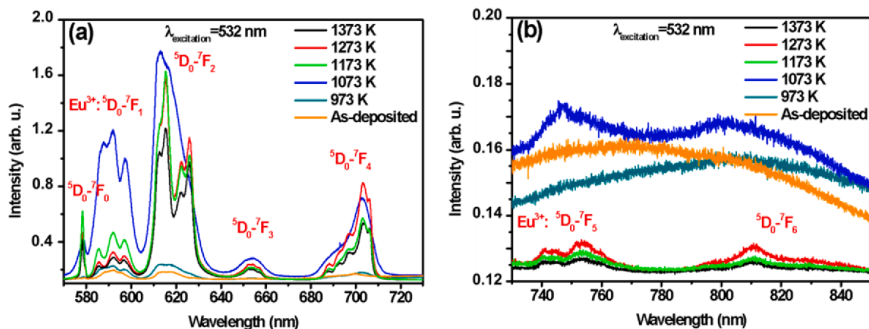


Fig. 11. PL spectra from 570 nm to 730 nm (a) and from 730 nm to 850 nm (b) of ZnO:Tb, Eu films annealed at various  $T^{\circ}_A$  for a laser excitation at 532 nm.

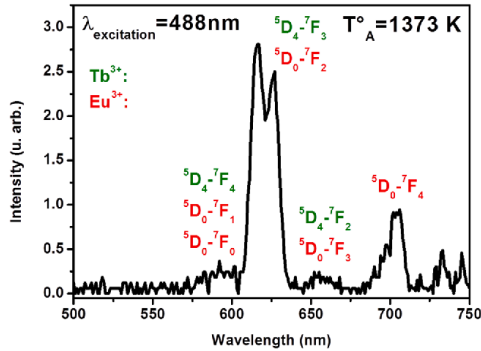


Fig. 12. PL spectrum of the ZnO:Tb, Eu film annealed at 1373 K for a laser excitation at 488 nm.

with the out-diffusion of the RE from ZnO grains. From  $T_A = 1173$  K, the  $Tb_xEu_ySi_vO_w$  phase is forming, giving rise to a dominant  $Eu^{3+}$  PL emission. The energy transfer from  $Tb^{3+}$  to  $Eu^{3+}$  was confirmed by direct excitation of  $Tb^{3+}$  at 488 nm showing an efficient and total energy transfer from  $Tb^{3+}$  to  $Eu^{3+}$  in the  $Tb_xEu_ySi_vO_w$  phase by contrast in ZnO matrix.

6. Light emitting diode

Considering the results presented above, a LED device has been achieved from the ZnO:Tb, Eu/Si(n) structure annealed at 973 K. Indeed, for this  $T_A$  value, in addition to the rather good quality of ZnO, the presence of a significant amount of REs at the ZnO/Si junction and just above the thin silica layer is potentially favorable for an emitting volume via electrical excitation. For higher  $T_A$ , the relatively important volume of resistive silica and the inhomogeneous distribution of  $Tb_xEu_ySi_vO_w$  inclusions in the film make difficult the elaboration of such a LED device.

The ZnO:Tb, Eu layer used for the LED structure has a thickness of 65 nm. Al and ZnO materials have been used to obtain ohmic contacts on Si and ZnO:RE, respectively. The forward bias voltage is defined as shown in the diagram in Fig. 13(a). A typical diode behavior is observed for this device in Fig. 13(b).

In Fig. 14, the EL spectra show quite intense electroluminescence spectra of  $Tb^{3+}$  and  $Eu^{3+}$  obtained for various current values from 100  $\mu A$  up to 1 mA in forward bias voltage.  $Eu^{3+}$  emission is the most intense suggesting an energy transfer between the REs. Note that these RE emissions are visible to the naked eye. RE excitation mechanism has been investigated and discussed in a recent published paper [49].

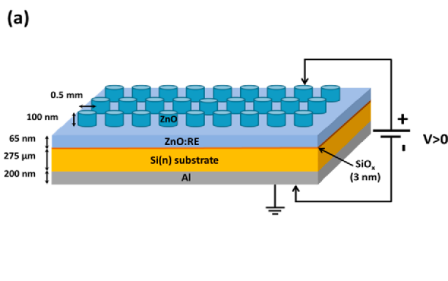


Fig. 13. LED device based on the ZnO:Tb, Eu/Si(n) heterojunction annealed at 973 K in forward bias voltage (a) and the corresponding I(V) diode behavior (b).

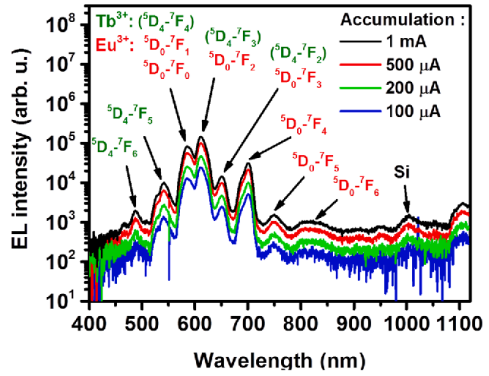


Fig. 14. Electroluminescence spectrum of the ZnO:Tb, Eu/Si(n) junction annealed at 973 K.

7. Conclusion

ZnO films (150 nm thick) with Tb (1.6 at%) and Eu (1.3 at%) codoping rates have been produced successfully by radiofrequency magnetron sputtering on (100) oriented Si substrates and the effects of post annealing treatment at extreme temperatures have been studied. The thermal treatment induced an RE out-diffusion from the matrix, an accumulation of RE at the film/substrate interface is observed. The annealing and the RE out-diffusion participated to an improvement of the crystalline quality of the ZnO matrix between the as-deposited films and those annealed for  $T_A < 973$  K. Regarding the PL properties, a weak emission of RE in ZnO has been noticed. It is explained by an unstable insertion of Tb and Eu into the ZnO matrix, due to their ionic diameters greater than  $Zn^{2+}$ . Therefore, they diffuse more easily at grain boundaries and at the film interfaces upon thermal treatments. For low  $T_A$  values ( $< 1173$  K), only  $Tb^{3+}$  is able to emit (for an excitation at 266 nm). However, a quenching phenomenon appeared when it diffuses and segregates at the bottom of the film without formation of secondary phases.  $Eu^{3+}$  is optically active by direct excitation at 532 nm.

For higher  $T_A$  values up to 1373 K, the Si substrate reacted with the RE doped ZnO films, zinc silicate ( $Zn_2SiO_4$ ) and  $Tb_xEu_ySi_vO_w$  apatite related inclusions of a few hundreds of nanometers were identified by XRD and TEM observations. Zinc silicate volume decreased with increasing temperature as the zinc evaporates, leaving only RE silicate and silica phases in the film.  $Tb_xEu_ySi_vO_w$  phase is considered as the main emitting phase of our films. The PL spectrum is dominated by the  $Eu^{3+}$  signal. The presence of  $Eu^{2+}$  is also observed in PL (excitation at 266 nm) for  $T_A = 1373$  K, as well as a weak  $Tb^{3+}$  emission (excitation at

266 nm). Contrary to what was mentioned in previous works [7], it is most probable that zinc silicate doped with Tb and/or Eu plays a minor role in this emission because the RE contents in this phase is low (<1 at. %) and furthermore, this phase mostly disappears at 1373 K, with the concomitant Zn evaporation. A direct laser excitation of  $\text{Eu}^{3+}$  at 532 nm induced the higher emission intensity for  $\text{Eu}^{3+}$  in the  $\text{Tb}_x\text{Eu}_y\text{Si}_z\text{O}_w$  phase. And for a direct excitation at 488 nm of  $\text{Tb}^{3+}$ , a total energy transfer to  $\text{Eu}^{3+}$  is attested in the  $\text{Tb}_x\text{Eu}_y\text{Si}_z\text{O}_w$  phase. The  $\text{Tb}_x\text{Eu}_y\text{Si}_z\text{O}_w$  phase obtained for the highest  $T_A$  is thus very interesting in terms of emission intensity for  $\text{Tb}^{3+}$  and  $\text{Eu}^{3+}$  and for the efficient energy transfer from  $\text{Tb}^{3+}$  to  $\text{Eu}^{3+}$ . Therefore, this phase would be of considerable interest for an electroluminescent device. Unfortunately, in our case, the quality of the film is deteriorated upon high post annealing temperatures (presence of  $\text{Tb}_x\text{Eu}_y\text{Si}_z\text{O}_w$  inclusions embedded in a silica matrix) such that these films seem irrelevant for good conducting abilities. Finally, the films annealed at 973 K appear as a good candidate for electroluminescent applications. Indeed, for this temperature, we have a good structural quality of the matrix combined with a moderate diffusion of REs at the film/substrate interface. We have clearly shown that the presence of a relatively high concentrations of REs at the junction interface between *n*-type ZnO:RE and doped Si (without formation of secondary phases) can give rise to interesting excitation phenomena by injections of carriers.

#### Declaration of Competing Interest

The authors declare that they have no known competing financial interests or personal relationships that could have appeared to influence the work reported in this paper.

#### Acknowledgements

The authors would like to thank the "Agence Nationale de la Recherche (ANR)" in the framework of the "Investissements d'Avenir" with the reference "ANR-11-EQPX-0020" for the financial support that allowed the use of the JEOL ARM200F microscope and the acquisition of an FEI FIB system (HELIOS Nanolab 660) for TEM sample preparations. This work was also financially supported by the Spanish Ministry of Economy and Competitiveness (Project No. TEC2016-76849-C2-1-R). J. L.F. acknowledges the subprogram "Ayudas para la Formación de Profesorado Universitario" (No. FPU16/06257) from the Spanish Ministry of Education, Culture and Sports for economical support. All the TEM results reported in this article fall within the scope of the CNRS Research Foundation IRMA (FR 3095).

#### References

- [1] M.A. Borysiewicz, ZnO as a functional material, a review, *Crystals* 9 (2019) 505, <https://doi.org/10.3390/cryst9100505>.
- [2] L. Znaidi, G.J.A. Soler Illia, S. Benyahia, C. Sanchez, A.V. Kanaev, Oriented ZnO thin films synthesis by sol-gel process for laser application, *Thin Solid Films* 428 (1-2) (2003) 257–262, [https://doi.org/10.1016/S0040-6090\(02\)01219-1](https://doi.org/10.1016/S0040-6090(02)01219-1).
- [3] N.W. Emanetoglu, C. Goda, Y. Liu, S. Liang, Y. Lu, Epitaxial ZnO piezoelectric thin films for saw filters, *Mater. Sci. Semicond. Process* 2 (3) (1999) 247–252, [https://doi.org/10.1016/S1369-8001\(99\)00022-0](https://doi.org/10.1016/S1369-8001(99)00022-0).
- [4] A. Fouchet, W. Praelier, B. Mercey, L. Méchin, V.N. Kulkarni, T. Venkatesan, Investigation of laser-ablated ZnO thin films grown with Zn metal target: A structural study, *J. Appl. Phys.* 96 (6) (2004) 3228–3233, <https://doi.org/10.1063/1.1772891>.
- [5] D.M. Bagnall, Y.F. Chen, M.Y. Shen, Z. Zhu, T. Goto, T. Yao, Room temperature excitonic stimulated emission from zinc oxide epilayers grown by plasma-assisted MBE, *J. Cryst. Growth* 184–185 (1998) 605–609, [https://doi.org/10.1016/S0022-0248\(98\)0127-9](https://doi.org/10.1016/S0022-0248(98)0127-9).
- [6] J. Lim, C. Lee, Effects of substrate temperature on the microstructure and photoluminescence properties of ZnO thin films prepared by atomic layer deposition, *Thin Solid Films* 515 (7-8) (2007) 3335–3338, <https://doi.org/10.1016/j.tsf.2006.09.007>.
- [7] C. Davesne, A. Ziani, C. Labbé, P. Marie, C. Frilay, X. Portier, Energy transfer mechanism between terbium and europium ions in zinc oxide and zinc silicates thin films, *Thin Solid Films* 553 (2014) 33–37, <https://doi.org/10.1016/j.tsf.2013.11.122>.
- [8] S.L. Ou, D.S. Wu, S.P. Liu, Y.C. Fu, S.C. Huang, R.H. Horng, Pulsed laser deposition of TiO<sub>2</sub>/AZO transparent conduct layers for GaIn LED applications, *Optics Express* 19 (2011) 16244–16251, <https://doi.org/10.1364/OE.19.016244>.
- [9] M.S. Kang, C.-H. Lee, J.B. Park, H. Yoo, G.-C. Yi, Gallium nitride nanostructures for light-emitting diode applications, *Nano Energy* 1 (3) (2012) 391–400, <https://doi.org/10.1016/j.nanoen.2012.03.005>.
- [10] R.K. Verma, K. Kumar, S.B. Rai, Inter-conversion of Tb<sup>3+</sup> and Tb<sup>4+</sup> states and its fluorescence properties in MO-Al<sub>2</sub>O<sub>3</sub>: Tb (M = Mg, Ca, Sr, Ba) phosphor materials, *Solid State Sci.* 12 (2010) 1146–1151, <https://doi.org/10.1016/j.solidstatesciences.2010.04.004>.
- [11] C. Panatarani, I. Wuled Lenggoro, K. Okuyama, The crystallinity and the photoluminescent properties of spray pyrolyzed ZnO phosphor containing Eu<sup>2+</sup> and Eu<sup>3+</sup> ions, *Journal of Physics and Chemistry of Solids* 65 (11) (2004) 1843–1847, <https://doi.org/10.1016/j.jpcs.2004.06.008>.
- [12] C. Davesne, Elaboration et caractérisation de films de ZnO dopé pour des applications optoelectroniques, PhD thesis, Université de Caen Basse Normandie, 2014. <https://hal.archives-ouvertes.fr/tel-01142121/file/These%20Christian%20DAVESNE.pdf>.
- [13] J. Zhang, H. Feng, W. Hao, T. Wang, Luminescent properties of ZnO sol and film doped with Tb<sup>3+</sup> ion, *Materials Science and Engineering: A* 425 (1-2) (2006) 346–348, <https://doi.org/10.1016/j.msea.2006.03.082>.
- [14] S.M. Ahmed, P. Szymanski, L.M. B-Nadi, M.A. El-Sayed, Energy-Transfer Efficiency in Eu-Doped ZnO Thin Films: The Effects of Oxidative Annealing on the Dynamics and the Intermediate Defect States, *ACS Applied Materials & Interfaces* 6 (3) (2014) 1765–1772, <https://doi.org/10.1021/am404662k>.
- [15] Y. Terai, K. Yamaoka, K. Yoshida, T. Tsuji, Y. Fujiwara, Photoluminescence properties of Eu-doped ZnO films grown by sputtering assisted metalorganic chemical vapor deposition, *Physica E* 42 (10) (2010) 2834–2836, <https://doi.org/10.1016/j.physe.2010.03.012>.
- [16] M. Korsunskaya, L. Borokovska, L. Khomenkova, O. Gudyymenko, V. Kladko, O. Kolomyys, V. Stréchuk, Z. Tsybrii, C. Guillaume, C. Labbe, X. Portier, O. Melnichuk, L. Melnichuk, Transformations in the photoluminescent, electrical and structural properties of Tb<sup>3+</sup> and Eu<sup>3+</sup> co-doped ZnO films under high-temperature annealing, *Journal of Luminescence* 217 (2020) 116739, <https://doi.org/10.1016/j.jlumin.2019.116739>.
- [17] N. Korsunskaya, L. Borokovska, L. Khomenkova, T. Sabov, O. Oberemok, O. Dubikovskyi, Z.Y. Zhuchenko, A. Zolotovskiy, I.N. Demchenko, Y. Stryanyy, C. Guillaume, C. Labbe, X. Portier, Redistribution of Tb and Eu ions in ZnO films grown on different substrates under thermal annealing and its impact on Tb-Eu energy transfer, *Appl. Surf. Sci.* 528 (2020) 146913, <https://doi.org/10.1016/j.apsusc.2020.146913>.
- [18] S.M.C. Miranda, M. Peres, T. Monteiro, E. Alves, H.D. Sun, T. Geruschke, R. Vanden, K. Lorenz, Rapid thermal annealing of rare earth implanted ZnO epitaxial layers, *Optical Materials* 33 (7) (2011) 1139–1142, <https://doi.org/10.1016/j.optmat.2010.10.009>.
- [19] Ch. Leroux, C. Guillaume, Ch. Labbe, X. Portier, D. Pelloquin, Identification of (Tb, Eu)<sub>3</sub>(Si<sub>3</sub>A<sub>6</sub>)<sub>2</sub>Oxy-Apatite Structures as Nanometric Inclusions in Annealed (Eu, Tb)-Doped ZnO/Si Junctions: Combined Electron Diffraction and Chemical Contrast Imaging Studies, *Inorganic Chemistry* (2021), <https://doi.org/10.1021/acs.inorgchem.0c03361>.
- [20] M. Huang, S. Wang, G. Wan, X. Zhang, Y. Zhang, K. Ou, L. Yi, Effect of co-doped Tb<sup>3+</sup> ions on electroluminescence of ZnO:Eu<sup>2+</sup> LED, *Materials in Electronics* 29 (9) (2018) 7213–7219, <https://doi.org/10.1007/s10854-018-8709-9>.
- [21] S. Hayamizu, H. Tabata, H. Tanaka, T. Kawai, Preparation of crystallized zinc oxide films on amorphous glass substrates by pulsed laser deposition, *J. Appl. Phys.* 80 (1996) 787–791, <https://doi.org/10.1063/1.362887>.
- [22] J. Felsche, Polymorphism and crystal data of the rare-earth disilicates of type RE<sub>2</sub>Si<sub>2</sub>O<sub>7</sub>, *J. Common Met.* 21 (1) (1970) 1–14, [https://doi.org/10.1016/0022-5088\(70\)90159-1](https://doi.org/10.1016/0022-5088(70)90159-1).
- [23] X.Q. Zhao, C.R. Kim, J.Y. Lee, C.M. Shin, J.H. Heo, J.Y. Lee, H. Ryu, J.H. Chang, H.C. Lee, C.S. Son, B.C. Shin, W.J. Lee, W.G. Jung, S.T. Tan, J.L. Zhao, X.W. Sun, Effects of thermal annealing temperature and duration on hydrothermally grown ZnO nanorod arrays, *Appl. Surf. Sci.* 255 (11) (2009) 5861–5865, <https://doi.org/10.1016/j.apsusc.2009.01.022>.
- [24] G.H. Dieke, H.M. Crosswhite, The Spectra of the Doubly and Triply Ionized Rare Earths, *Appl. Opt.* 2 (1963) 675–686, <https://doi.org/10.1364/AO.2.000675>.
- [25] G.H. Dieke, Spectra and energy levels of rare earth ions in crystals, Interscience, 1968.
- [26] S. Venpatil, J. Mitra, P. Dawson, One-step synthesis of ZnO nanosheets: A blue-white fluorophore, *Nanoscale Research Letters* 7 (2012) 470, <https://doi.org/10.1186/1556-276X-7-470>.
- [27] C. Guillaume, Croissance, photoluminescence et électroluminescence de films de ZnO dopé terres rares, PhD thesis, Université de Caen Basse Normandie, 2020. <https://tel.archives-ouvertes.fr/tel-02499705/document>.
- [28] Y. Zhang, Y. Liu, L. Wu, E. Xie, J. Chen, Photoluminescence and ZnO → Eu<sup>3+</sup> energy transfer in Eu<sup>3+</sup>-doped ZnO nanospheres, *J. Phys. Appl. Phys.* 42 (8) (2009) 085106, <https://doi.org/10.1068/0022-3727/42/8/085106>.
- [29] P. Chen, X. Ma, D. Yang, ZnO: Eu thin films: Sol-gel derivation and strong photoluminescence from 5<sup>D</sup><sub>0</sub>–7<sup>F</sup><sub>0</sub> transition of Eu<sup>3+</sup> ions, *J. Alloys Compound* 431 (1-2) (2007) 317–320, <https://doi.org/10.1016/j.jallcom.2006.05.078>.
- [30] S. Zhao, F. Shu, Y. Li, C. Liu, W. Shan, Y. Cui, L. Yang, Synthesis and Luminescence Properties of ZnO: Eu<sup>3+</sup> Nano Crystalline via a Facile Solution Method, *J. Nanosci. Nanotechnol.* 12 (3) (2012) 2607–2611, <https://doi.org/10.1166/jnn.2012.5761>.
- [31] R.S. Ningthoujam, N.S. Gajbhiye, A. Ahmed, S.S. Umre, S.J. Sharma, Re-Dispersible Li<sup>+</sup> and Eu<sup>3+</sup> Co-Doped Nanocrystalline ZnO: Luminescence and EPR Studies,

- J. Nanosci. Nanotechnol. 8 (6) (2008) 3059–3062, <https://doi.org/10.1166/jnn.2008.152>.
- [32] A. Hastir, R.L. Opila, N. Kohli, Z. Onuk, B.o. Yuan, K. Jones, Virpal, R.C. Singh, Deposition, characterization and gas sensors application of RF magnetron-sputtered terbium-doped ZnO films, *J. Mater. Sci.* 52 (14) (2017) 8502–8517, <https://doi.org/10.1007/s10853-017-1059-9>.
- [33] N.S. Singh, S.D. Singh, S.D. Meetei, Structural and photoluminescence properties of terbium-doped zinc oxide nanoparticles, *Chin. Phys. B.* 23 (5) (2014) 058104, <https://doi.org/10.1088/1674-1056/23/5/058104>.
- [34] V. Kumar, O.M. Ntwaeaborwa, H.C. Swart, Deep level defect correlated emission and Si diffusion in ZnO:Tb<sup>3+</sup> thin films prepared by pulsed laser deposition, *J. Colloid Interface Sci.* 465 (2016) 295–303, <https://doi.org/10.1016/j.jcis.2015.12.007>.
- [35] X. Liu, W. Xie, Y. Liu, J. Feng, X. Tang, J. Lin, Y. Dai, Y.u. Xie, L. Yan, Multichannel Luminescence Properties of Mixed-Valent Eu<sup>2+</sup>/Eu<sup>3+</sup> Coactivated SrAl<sub>3</sub>BO<sub>7</sub> Nanocrystalline Phosphors for Near-UV LEDs, *Inorg. Chem.* 56 (22) (2017) 13829–13841, <https://doi.org/10.1021/acs.inorgchem.7b01938>.
- [36] C.L. Heng, J.T. Li, Z. Han, P.G. Yin, An Abnormal Photoluminescence Enhancement in (Eu, Yb) Co-doped SiO<sub>2</sub> Thin Film, *Integr. Ferroelectr.* 151 (1) (2014) 179–186, <https://doi.org/10.1080/10584587.2014.901125>.
- [37] Q.Y. Zhang, K. Pita, C.H. Kam, Sol-gel derived zinc silicate phosphor films for full-color display applications, *J. Phys. Chem. Solids.* 64 (2) (2003) 333–338, [https://doi.org/10.1016/S0022-3697\(02\)00331-1](https://doi.org/10.1016/S0022-3697(02)00331-1).
- [38] G.H. Mhlongo, M.S. Dlamini, O.M. Ntwaeaborwa, H.C. Swart, K.T. Hillie, Luminescent properties and quenching effects of Pr<sup>3+</sup> co-doping in SiO<sub>2</sub>:Tb<sup>3+</sup>/Eu<sup>3+</sup> nanophosphors, *Opt. Mater.* 36 (4) (2014) 732–739, <https://doi.org/10.1016/j.optmat.2013.10.031>.
- [39] W. Jia, K. Monge, F. Fernandez, Energy transfer from the host to Eu<sup>3+</sup> in ZnO, *Opt. Mater.* 23 (1–2) (2003) 27–32, [https://doi.org/10.1016/S0925-3467\(03\)00054-5](https://doi.org/10.1016/S0925-3467(03)00054-5).
- [40] H. Akazawa, H. Shinjima, Concentration effect of H/OH and Eu<sup>3+</sup> species on activating photoluminescence from ZnO:Eu<sup>3+</sup> thin films, *J. Appl. Phys.* 114 (15) (2013) 153502, <https://doi.org/10.1063/1.4825121>.
- [41] G. Chen, F. Song, X. Xiong, X. Peng, Fluorescent Nanosensors Based on Fluorescence Resonance Energy Transfer (FRET), *Ind. Eng. Chem. Res.* 52 (33) (2013) 11228–11245, <https://doi.org/10.1021/ie303485n>.
- [42] L. Luo, F.Y. Huang, G.S. Dong, H.H. Fan, K.F. Li, K.W. Cheah, J. Chen, Strong luminescence and efficient energy transfer in Eu<sup>3+</sup>/Tb<sup>3+</sup>-codoped ZnO nanocrystals, *Opt. Mater.* 37 (2014) 470–475, <https://doi.org/10.1016/j.optmat.2014.07.008>.
- [43] E. Pavitra, G.S.R. Raju, Y.H. Ko, J.S. Yu, A novel strategy for controllable emissions from Eu<sup>3+</sup> or Sm<sup>3+</sup> ions co-doped SrY<sub>2</sub>O<sub>4</sub>:Tb<sup>3+</sup> phosphors, *Phys. Chem. Chem. Phys.* 14 (32) (2012) 11296, <https://doi.org/10.1039/c2cp41722g>.
- [44] B. Kaleli, M. Kulakei, R. Turan, Mechanisms of light emission from terbium ions (Tb<sup>3+</sup>) embedded in a Si rich silicon oxide matrix, *Opt. Mater.* 34 (11) (2012) 1935–1939, <https://doi.org/10.1016/j.optmat.2012.05.036>.
- [45] Y.-C. Li, Y.-H. Chang, Y.-F. Lin, Y.-S. Chang, Y.-J. Lin, Synthesis and luminescent properties of Ln<sup>3+</sup> (Eu<sup>3+</sup>, Sm<sup>3+</sup>, Dy<sup>3+</sup>)-doped lanthanum aluminum germanate LaAlGe<sub>2</sub>O<sub>7</sub> phosphors, *J. Alloys Compound.* 439 (1–2) (2007) 367–375, <https://doi.org/10.1016/j.jallcom.2006.08.269>.
- [46] A.K. Bedyal, D.D. Ramteke, V. Kumar, H.C. Swart, Excitation wavelength and Eu<sup>3+</sup>/Tb<sup>3+</sup> content ratio dependent tunable photoluminescence from NaSrBO<sub>3</sub>:Eu<sup>3+</sup>/Tb<sup>3+</sup> phosphor, *J. Mater. Sci. Mater. Electron.* 30 (12) (2019) 11714–11726, <https://doi.org/10.1007/s10854-019-01533-4>.
- [47] T. Ishizaka, R. Nozaki, Y. Kurokawa, Luminescence properties of Tb<sup>3+</sup> and Eu<sup>3+</sup>-doped alumina films prepared by sol-gel method under various conditions and sensitized luminescence, *J. Phys. Chem. Solids.* 63 (4) (2002) 613–617, [https://doi.org/10.1016/S0022-3697\(01\)00201-3](https://doi.org/10.1016/S0022-3697(01)00201-3).
- [48] M. Huang, S. Wang, G. Wan, X. Zhang, Y. Zhang, K. Ou, L. Yi, Ou and Lixin Yi, Effect of co-doped Tb<sup>3+</sup> ions on electroluminescence of ZnO:Eu<sup>3+</sup> LED, *Journal of Materials Science: Materials in Electronics.* 29 (9) (2018) 7213–7219, <https://doi.org/10.1007/s10854-018-8709-9>.
- [49] J.L. Friero, C. Guillaume, J. López-Vidrier, O. Blázquez, S. González-Torres, C. Labbé, S. Hernández, X. Portier, B. Garrido, Towards a white LED based on rare earth-doped ZnO, *Nanotechnology.* 31 (2020), 465207, <https://doi.org/10.1088/1361-6528/abade9>.

### 4.1.2. Devices for RGB electroluminescence

Once the best deposition conditions for the active layer had been determined, light emitting devices were fabricated. To this end, a 60-nm nominal thickness layer of rare earth doped-ZnO was used for all devices. With the aim of obtaining RGB and white emitting devices, a total of four devices were fabricated:

- ZnO doped with cerium, for blue emission.
- ZnO doped with terbium, for green emission.
- ZnO doped with terbium and europium for red emission.
- A three-layer stack of the previous three, 20-nm-thick each.

These layers were annealed at 700 °C in N<sub>2</sub> ambient for 1h. This would produce the best expected layers for electroluminescent devices, as indicated by the previous work, in terms of structure and optimized emission from the RE ions. The device structure was finalized by depositing Al as a common bottom contact on the back of the *n*-type Si substrate and circular-patterned ZnO deposited via ALD as top electrode. It is important to comment on the order of the three-stack layer: since the expected blue emission from Ce<sup>3+</sup> is sufficiently energetic to be absorbed by Tb<sup>3+</sup> and green emission from Tb<sup>3+</sup> is absorbed by Eu<sup>3+</sup>, the Ce-doped layer was deposited closer to the top transparent electrode and the Eu-doped layer at the bottom.

A quick test allowed determining that better EL emission was obtained when layers were deposited on top of *n*-type Si, in contrast to the same structures analyzed on *p*-type Si, as it can be seen in Figure 4.1. Both hot electrons and holes are capable of impact excitation of RE ions.<sup>[4]</sup> However, ZnO as the host material is *n*-type due to intrinsic defects and thus allows for good mobility of electrons. With electrons being majority carriers in *n*-type Si, it is easier to inject them from this substrate to ZnO than from *p*-type Si, with holes as majority carriers.

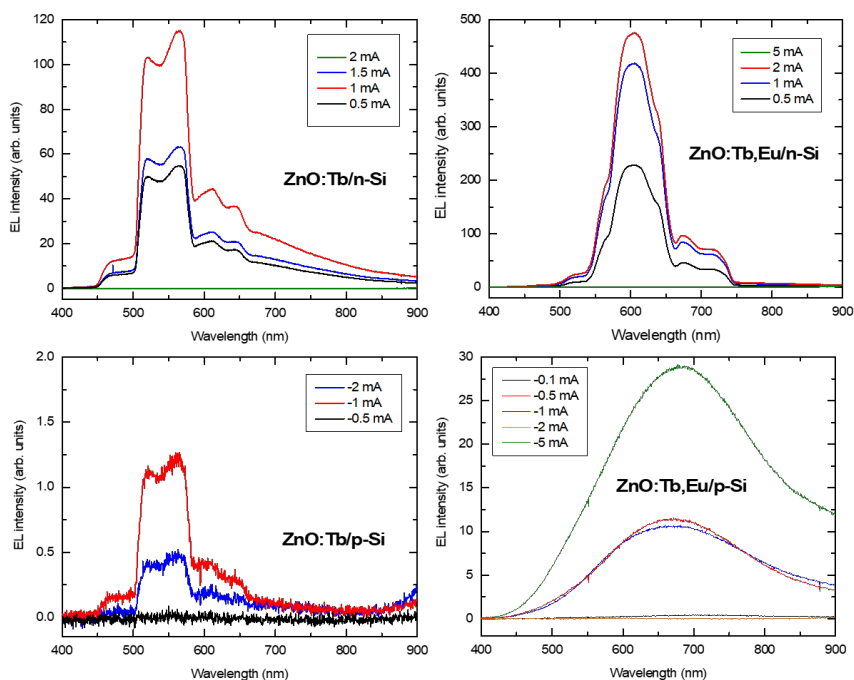


**Figure 4.1.** EL emission from the doped-ZnO devices under study, comparing the effect of the Si substrate doping. **(left)** Tb-doped ZnO, **(right)** Eu-doped ZnO. **(top)** Devices on *n*-type Si, **(bottom)** devices on *p*-type Si.

Transmission electron microscopy of the three-layered device shows a polycrystalline ZnO film with a thin layer of SiO<sub>x</sub> at the interface with the Si substrate, intentionally left for using as an electron accelerating layer. From EDX measurements, rare earth elements appear evenly distributed through their corresponding layers, except for the Eu-, Tb-co-doped layer where the dopants accumulate near the substrate, in agreement with the observations of the previous work for the employed annealing temperature.

The samples were first electrically characterized and modelled. Current-voltage measurements showed a clear rectification, as expected from a heterojunction. The data were fitted to find three regions of charge transport in accumulation conditions: (i) carrier extraction from ZnO inter-band traps and defects, (ii) a trap-assisted conduction through the traps, and (iii) Fowler-Nordheim tunneling. A detailed model of the energy band diagram at each device state was elaborated and applied to calculate the minimum voltage for FN onset for the four devices, in very good agreement with the data.

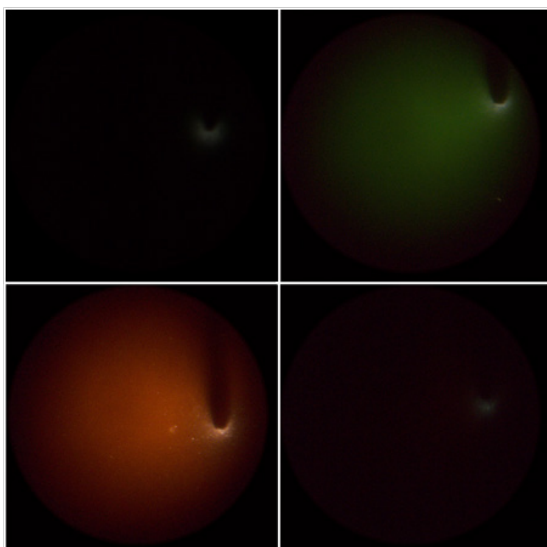


**Figure 4.2.** Images of the four RE-doped ZnO devices. Dopants, from left to right, and from top to bottom: Ce, Tb, Tb/Eu and the three-layer stack.

The electroluminescence emission from the devices was visible by the naked eye, as it can be seen in the images of Figure 4.2. The current threshold for emission was measured for all devices, and their efficiency was compared. The emission current threshold correlates well with the onset voltage for FN tunneling, meaning that it is in this regime where electrons have enough energy to excite the rare earth ions via impact excitation. The spectral analysis of the emission clearly yielded the emission peaks corresponding to  $\text{Tb}^{3+}$  and  $\text{Eu}^{3+}$  electronic transitions for the samples doped with Tb and Eu/Tb, respectively. For the latter, whereas  $\text{Eu}^{3+}$  emission is dominant, the emission of  $\text{Tb}^{3+}$  could also be detected. The sample doped with Ce showed two low-intensity broad emissions. The first one centered at  $\sim 500$  nm probably corresponds to  $\text{Ce}^{3+}$  transitions, whereas the second at  $\sim 650$  nm corresponds to ZnO defects. This fact can be explained by the clustering of Ce ions, attaining a  $\text{Ce}^{4+}$  electronic configuration which increases the probability of non-radiative recombination, while inducing more defects in ZnO due to an increase of oxygen vacancies. The three-layer stack shows the emission peaks of  $\text{Tb}^{3+}$  and  $\text{Eu}^{3+}$ , in agreement with the emission of the single-layered devices, demonstrating the viability of the structure for a white emitting device by combination of the various RE ions. The spectra were positioned in a CIE 1931 chromatic diagram, shedding light on the poor emission of  $\text{Ce}^{3+}$  and the color combination of the three single-layer devices into one.

This work was presented as a talk in the European Materials Research Society (EMRS) Spring Meeting 2020. A journal article was published in *Nanotechnology* **31**, 465207 (2020).



**Paper II: Toward RGB LEDs based on rare earth-doped ZnO (DOI: [10.1088/1361-6528/abadc9](https://doi.org/10.1088/1361-6528/abadc9))**



# Toward RGB LEDs based on rare earth-doped ZnO

J L Friero<sup>1,2,4</sup> , C Guillaume<sup>3</sup> , J López-Vidrier<sup>1,2</sup> , O Blázquez<sup>1,2</sup> , S González-Torres<sup>1,2</sup>, C Labbé<sup>3</sup>, S Hernández<sup>1,2</sup> , X Portier<sup>3</sup> and B Garrido<sup>1,2</sup> 

<sup>1</sup> MIND, Departament d'Enginyeria Electrònica i Biomèdica, Universitat de Barcelona, Martí i Franquès 1, 08028, Barcelona, Spain

<sup>2</sup> Institute of Nanoscience and Nanotechnology (IN<sup>2</sup>UB), Universitat de Barcelona, Barcelona 08028, Spain

<sup>3</sup> CIMAP Normandie Université, ENSICAEN, UNICAEN, CEA, UMR CNRS 6252, 6 Boulevard du Maréchal Juin, 14050, Caen, France

E-mail: [jfriero@elub.edu](mailto:jfriero@elub.edu)

Received 26 June 2020, revised 1 August 2020

Accepted for publication 10 August 2020

Published 26 August 2020



## Abstract

By using ZnO thin films doped with Ce, Tb or Eu, deposited via radiofrequency magnetron sputtering, we have developed monochromatic (blue, green and red, respectively) light emitting devices (LEDs). The rare earth ions introduced with doping rates lower than 2% exhibit narrow and intense emission peaks due to electronic transitions in relaxation processes induced after electrical excitation. This study proves zinc oxide to be a good host for these elements, its high conductivity and optical transparency in the visible range being as well exploited as top transparent electrode. After structural characterization of the different doped layers, a device structure with intense electroluminescence is presented, modeled, and electrically and optically characterized. The different emission spectra obtained are compared in a chromatic diagram, providing a reference for future works with similar devices. The results hereby presented demonstrate three operating monochromatic LEDs, as well as a combination of the three species into another one, with a simply-designed structure compatible with current Si technology and demonstrating an integrated red-green-blue emission.

Keywords: light emitting devices, electroluminescence, rare earths, RGB, ZnO

(Some figures may appear in colour only in the online journal)

## 1. Introduction

For decades now, zinc oxide (ZnO) has attracted much attention of a large part of the optoelectronics research community. This well-known transition metal oxide exhibits a wurzite structure, a direct bandgap with an energy of 3.4 eV and a large exciton binding energy (60 meV) [1], making this material suitable for many applications including thin film transistors, light emitters, detectors and gas sensors [2, 3]. Its high transparency to visible light (>80%) and good conductivity ( $\sim 100 \Omega^{-1} \text{cm}^{-1}$ ) have also made it a promising transparent

conductive oxide, boosted in many cases by the doping of elements like Al, which further increases its conductivity while maintaining a high transparency [4, 5]. In the context of light emission, it has been compared to gallium nitride (GaN), as they both arrange in the same crystalline structure and present very similar bandgap energy although they significantly differ in exciton binding energy, 25 meV for GaN, which in principle makes ZnO more suitable for light emission. The advantage of GaN over ZnO comes in the easier fabrication of *p*-type films, the tunability of the bandgap (and thus light emission energy) from the ultraviolet (UV) to the near IR when alloyed with In and/or Al (InAlGaN alloys) and the lower sensibility to defects and dislocations as non-radiative recombination centers [6]. Nevertheless, both the abundance of Zn compared

<sup>4</sup> Author to whom any correspondence should be addressed.

to Ga and higher exciton stability of ZnO at room temperature, together with its non-toxicity, still make ZnO relevant for optoelectronic applications.

In the case of ZnO, it is a semiconductor that intrinsically presents oxygen vacancies ( $V_o$ ) and zinc interstitials ( $Zn_i$ ) that act as donor impurities [7], being possible to control them during the fabrication or posterior annealing processes. This particularity is of special interest for producing good *n*-type ZnO layers, further enhanced by doping with group-III elements such as Al, Ga and In as substitutes for Zn sites or group-VII elements such as Cl and I, as substitutes for O ones. Nevertheless, reliable *p*-type layers remain a major challenge because of the self-compensation from those native donor defects. Some efforts have been done in this direction using group-I (substitutes for Zn) or group-V (for O) elements, or by alloying it with Mg [8, 9]. Therefore, the achievement of electroluminescence devices based on a ZnO *p-n* junction still has to overcome this issue.

Due to this last limitation, different strategies for producing ZnO-based light emitting devices (LEDs) have been researched, including defect engineering [10], nanostructuring [11] or the doping with already optically-active centers. In this context, rare earth (RE) elements have demonstrated over decades outstanding optical and electroluminescent (EL) properties [12]. Among all these, it is especially notable the intense, stable and narrow emission they present, the different RE species covering a wide range of the electromagnetic spectrum, spanning from the near-infrared (NIR) to UV [13]. Their hosting material specially affects the scattering of the emission, which is larger for polycrystalline and amorphous materials and weaker for crystalline matrices. RE elements are being employed by the industry for the fabrication of LEDs as part of phosphorescent stacks in an optical down conversion process. Additionally, the suitability of different host matrices [12, 14, 15], including ZnO [16–19], for hosting optically-active RE dopants has been extensively proven in the past, aiming at profiting from their emission after electrical excitation.

The emission process in RE is due to the electronic transitions within the inner *f*-shell of these elements (from the 4th or 5th levels for lanthanides and actinides, respectively), leading to photon emission with an energy dependent on those transitions. Initially, RE elements have their outer *f*-shell partially filled. In a  $C_{4v}$  configuration they have a +3-valence state as a result of the loss of the two electrons from the outer *s*-shell and one from the partially filled *f*-shell. This valence state is possible in ZnO-doped films when the RE ions occupy Zn sites [19]. In this configuration, excited lanthanide ions can relax through the predominant intra-*4f* (practically independent on the local environment) and *5d*-to-*4f* (quite sensitive to the matrix and local environment) electronic transitions [20–22], leading to intense narrow emission peaks.

Regarding research in the field of LEDs, of particular interest would result the finding of a red-green-blue (RGB) system able to be employed as full-color light source. Bearing this objective in mind, in this work we have studied three of these RE elements: europium (Eu), terbium (Tb) and cerium (Ce). In figure 1, the main electronic transitions involved in the

emission of these three elements are represented [16, 23, 24]. Please note that the most probable transitions, thus resulting in most intense emissions, are indicated in color referring to their apparent color: blue for  $Ce^{3+}$  (464 nm), green for  $Tb^{3+}$  (544 nm) and red for  $Eu^{3+}$  (616 nm).

Due to the precise conditions required for the optical activation of RE ions, the doping [17], fabrication process [25] or local environment [18, 26–28] become critical factors to obtain reliable devices that take profit of their luminescent properties. In this work, we have fabricated RE-doped ZnO layers by radiofrequency (RF) magnetron sputtering onto *n*-type Si substrates, with an atomic-layer-deposited (ALD) ZnO as top transparent electrode. Three different RE-species have been employed, Eu, Tb and Ce, for emitting, as discussed above, in the red, green and blue colors, respectively; with doping concentrations lower than 2 at.% for each dopant. The structural properties have been characterized by transmission electron microscopy (TEM) and energy dispersive x-ray (EDX) spectroscopy, allowing determining the spatial distribution of the RE-ions at the nanoscale. Electrical characterization has revealed different conduction mechanisms that can be related to the structural properties of the layers and the device configuration. Finally, all the studied devices exhibit EL as a consequence of the excitation of the RE-species. The obtained emissions are discussed in terms of the different RE species, the structural and electrical properties. The results here presented get us closer to achieving a tunable RGB-color LED fabricated with a base on abundant materials such as Si and Zn, taking advantage of the emission from RE ions as optical centers.

## 2. Materials and methods

The ZnO films were deposited from doped ZnO targets on an *n*-type (100)-oriented Si substrate via a 3-inch RF magnetron sputtering system, using a power density of  $0.96 \text{ W cm}^{-2}$ ,  $15 \mu\text{bar}$  of pressure, Ar flux of 2 sccm, and at a substrate temperature of  $400 \text{ }^\circ\text{C}$ . To avoid cross-contamination, three different ZnO targets nominally identical were used for each of the three different dopant species. Only two targets could be loaded in the chamber. Doping was obtained by placing RE oxide pellets ( $CeO_2$ ,  $Tb_4O_7$  or  $Eu_2O_3$ ) on the top of each ZnO target for the deposition of the films. Under these conditions, three 60 nm thick single-layer samples were deposited: (i) ZnO:Eu,Tb, (ii) ZnO:Tb, and (iii) ZnO:Ce. An additional sample containing the three RE species was fabricated by consecutively depositing 20 nm thick layers of the three mentioned films in a (iv) ZnO:Ce/ZnO:Tb/ZnO:Eu,Tb structure. For this three-layer structure, the sputtering chamber contained initially two targets which could not be activated simultaneously. First, a ZnO:Tb, Eu layer was deposited and then the ZnO:Tb layer using the second target. For the last ZnO:Ce layer, the chamber was opened to replace one of the two targets. The RE doping concentration was  $\sim 1.7$  at.% in ZnO:Ce,  $\sim 2$  at.% in ZnO:Tb, and 0.8 at.% of Eu and  $\sim 1.6$  at.% of Tb in ZnO:Eu,Tb, as determined by EDX measurements on  $2 \mu\text{m}$  thick layers in a scanning electron microscope. Afterwards, all

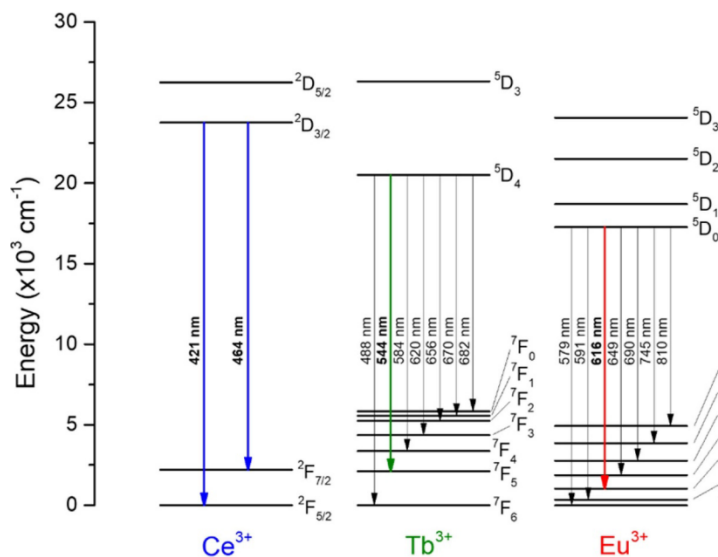


**Figure 1.** 5d-to-4f electronic transitions in the rare earth ions considered for this work ( $\text{Ce}^{3+}$ ,  $\text{Tb}^{3+}$  and  $\text{Eu}^{3+}$ ) and the wavelength corresponding to the resulting photons. The main transitions have been highlighted in the schematics in blue, green and red, respectively for  $\text{Ce}^{3+}$ ,  $\text{Tb}^{3+}$  and  $\text{Eu}^{3+}$ .

samples underwent an annealing process for 1 h at 700 °C in a  $\text{N}_2$  atmosphere.

Structural characterization by electron microscopy was done in sample (iv), as it can provide representative information of the deposition for the three films under investigation. The foils were prepared by focused ion beam (FIB, FEI HeliosNanolab 660), and their structure was analyzed at the nanoscale by conventional and high resolution TEM (HRTEM) using a double-corrected cold FEG ARM200F JEOL microscope, operated at 200 kV and equipped with a high-angle annular dark field detector and an EDX Centurio spectrometer. EDX profiles were acquired along a 75 nm straight line across the film with 120 probed spots and 1 s acquisition time per spot.

The top 100 nm thick ZnO electrode was deposited by means of ALD at a deposition temperature of 200 °C, resulting in a highly-conductive layer (conductivity  $> 100 \Omega^{-1} \text{cm}^{-1}$ ) with an optical transparency of  $\sim 85\%$  through the visible range [4]. Afterwards, circular contacts with 500  $\mu\text{m}$  diameter were patterned via conventional photolithography. Finally, a full-area deposition by electron beam evaporation of Al created the common bottom electrode to finalize the devices.

Current-voltage [ $I(V)$ ] measurements were carried out placing the devices within a Cascade Microtech Summit 11000 probe station coupled to an Agilent B1500A semiconductor device analyzer. A Faraday cage is used to isolate the devices from external electromagnetic noise. In all electrical measurements, a voltage was applied on the top ZnO contact while the bottom Al was grounded through the chuck of the system.

The voltage applied this way was swept in steps of 50  $\text{mV s}^{-1}$ . EL emission from the devices was collected by a microscope with a  $20\times$  NIR objective with a numerical aperture of 0.4, and it was spectrally resolved via a 1/4 m monochromator and a liquid nitrogen-cooled charge coupled device (CCD) in the 400 to 1000 nm range. Integrated EL was also collected by replacing the monochromator-CCD system by a GaAs photomultiplier tube, sensitive in the range from 350 to 900 nm.

### 3. Results

#### 3.1. Structural characterization

Figure 2 shows a HRTEM image (figure 2(a)) of sample (iv) and the EDX analysis performed (figure 2(b)) for the elements present in the sample along the growth direction, as indicated by the line in the HRTEM image. In figure 2(a), different regions on the sample can be clearly identified. From the bottom, it can first be found the *n*-type Si substrate with a  $\sim 5$  nm layer of native  $\text{SiO}_x$  on top, which was intentionally left unremoved before the deposition process to be used as electron energy barrier in electrical measurements. The deposited RE-doped ZnO films can be observed above the  $\text{SiO}_x$ . Please note here that there is no indication of the existence of any interface between each ZnO layer, despite the different steps for depositing all ZnO layers. However, non-uniform contrast zones are clearly visible suggesting local variations of the Bragg conditions due to local strains induced by the presence of dopants in the ZnO matrix. On top of the stack,

a carbon layer of a few nanometers and Pt were deposited in order to protect the top surface of the stack, before TEM sample preparation by FIB. The doped-ZnO total thickness was measured to be  $\sim 65$  nm and its polycrystalline nature can be clearly distinguished in the image by the different crystalline plane orientations present in the film. Some artifacts due to Moiré patterns can also be observed in the image.

To assess the composition of the layers upon annealing, EDX measurements were done along the vertical line indicated in figure 2(a). The atomic profiles corresponding to Pt (black), Si (grey), Ce (blue), Tb (green) and Eu (red) are plotted in figure 2(b). As shown in the TEM image, Si is only present at the bottom of the sample, whereas Pt is only present on top. To compare the concentration of each RE element for each sublayer, vertical lines have been drawn approximately where the profiles of the elements change, therefore suggesting the interface between the different sublayers. The intended nominal thickness for each sublayer was 20 nm. However, the actual thickness slightly differs; in particular, it can be observed in the TEM image that the Ce-doped layer is  $\sim 8$  nm thinner than the Tb-doped and Tb- and Eu-co-doped ones.

The EDX results also reveal the non-homogeneity of the RE ions within the layers but they allow positioning approximately the various interfaces between the sublayers. Despite the uncertainty of the measurements (about 1 at.%), fluctuation of the signals where each RE doping was nominally intended is indicative of their presence within the ZnO. This is particularly the case of Tb whose concentration reaches about 2 at.% in the middle of the structure. Thus, while Tb is uniformly distributed along the ZnO:Tb layer in the middle of the structure, the other two layers present a high agglomeration of the RE ions in certain zones: on one hand, Ce is accumulated at the top of the third layer, in a small region of  $\sim 5$  nm with a narrow depleted zone just below; on the other hand, in the first layer, Tb profile presents also a depleted region close to the interface with  $\text{SiO}_x$  where both Tb and Eu have accumulated very significantly in a region of  $\sim 8$  nm. Indeed, this latter fact was corroborated with a HRTEM image (see figure 2(c)), corresponding to the squared region in figure 2(a) of the bottom of the structure, where a thin ( $\sim 2$ – $3$  nm) amorphous layer enriched in Tb and Eu was identified on top of the  $\text{SiO}_x$  layer.

### 3.2. Electrical characterization

Initially, an electrical characterization via  $I(V)$  measurements was performed in order to understand the conduction regime governing each single-layer device. Figure 3 displays the  $I(V)$  curves for the ZnO:Ce (blue), ZnO:Tb (green), ZnO:Eu,Tb (red) and ZnO:Ce/ZnO:Tb/ZnO:Eu,Tb (orange) devices in a range from  $-8$  to  $10$  V. A sketch of the devices structure and their electrical connections during measurements is displayed in the inset at the bottom right corner of figure 3(a). At a first glance, figure 3(a) reveals a large rectification behavior in all four samples, exhibiting well-differentiated current level under forward and reverse biasing ( $V > 0$  and  $V < 0$ , respectively). This rectification is a consequence of the heterojunction formed by the different layers composing the device structure, and it is directly correlated with its energy band diagram. For

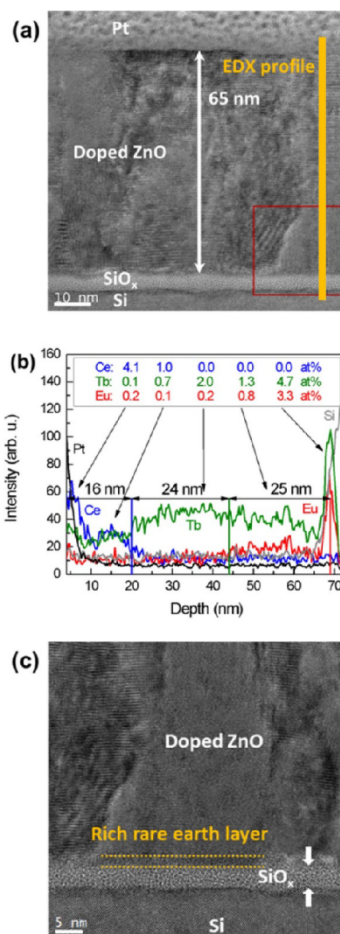


**Figure 2.** (a) TEM image corresponding to the deposited sample containing the ZnO:Ce/ZnO:Tb/ZnO:Eu,Tb stack, the total stack thickness measured being  $\sim 65$  nm. (b) EDX depth profiles for Pt, Si, Ce, Tb and Eu, obtained through 120 points measured along the 75 nm-vertical line indicated in (a). (c) HRTEM image of the bottom of the structure, corresponding to the red square in (a), where Tb and Eu have accumulated near the  $\text{SiO}_x$  layer.

forward bias, both ZnO:Tb and ZnO:Eu,Tb devices show a similar conduction behavior, resembled at one order of magnitude lower by ZnO:Ce/ZnO:Tb/ZnO:Eu,Tb and slightly different from the line-shape exhibited by ZnO:Ce. In addition, all four device structures present a pronounced change in the  $I(V)$  curve around 7 V, that could be associated with a change in the carrier transport through the structure as will be further covered.

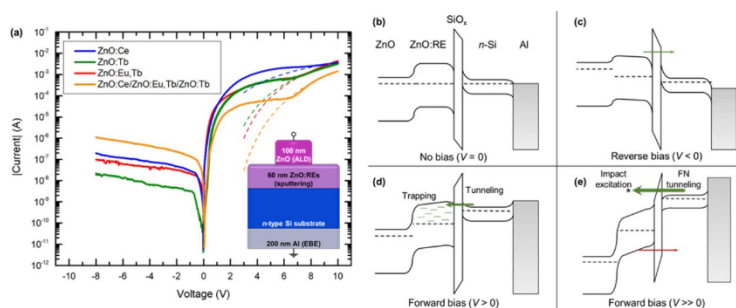


**Figure 3.** (a)  $I(V)$  curves corresponding to the devices with ZnO:Ce, ZnO:Tb and ZnO:Eu,Tb active layers, as well as the three-layer stack, in the range from  $-8$  to  $10$  V, respectively represented with a blue, green, red and orange line. Dashed lines present a Fowler-Nordheim fitting for each curve at high voltages. Inset sketch shows the structure of the devices under study. (b) Schematic energy band diagram for the device structure, with each layer labeled, under no applied bias. (c) Modified energy band diagrams under the application of reverse bias. (d), (e) Band diagrams under low and high forward biasing, respectively. Green and red arrows indicate the direction of the injected electrons and holes, respectively.

The observed trends can be explained in terms of the energy band diagrams of our devices. Bearing in mind our device configuration and the electronic band structure of the different layers, we have depicted in figures 3(b)–(e) the energy band diagrams for the device structure under four different bias conditions: (b) no bias, (c) reverse bias ( $V < 0$ ) and (d) forward bias ( $V > 0$ ) and (e) high forward bias ( $V \gg 0$ ). The top ZnO electrode and the *n*-type substrate present high electronic densities, with the energy Fermi level close to the bottom of the conduction band, whereas the RE-doped ZnO has been considered an intrinsic (or quasi-intrinsic) semiconductor, with the energy Fermi level practically in the middle of the band gap, as the introduction of RE dopants maintain the dielectric nature of the host matrices [29, 30]. Under no bias conditions (see figure 3(b)), the energy Fermi levels are aligned along the whole structure, having carriers blocked by two energy barriers at both sides of the  $\text{SiO}_x$  dielectric layer: a depletion region at the  $\text{SiO}_x$ -Si interface and an accumulation of electrons at the ZnO- $\text{SiO}_x$  interface. When the devices are set under reverse bias ( $V < 0$ ), the current rapidly increases up to 1 V. From this point the extracted current starts to be limited (see figure 3(a)). Below 1 V, the applied voltage is too weak for promoting efficient tunneling but it contributes to the extraction of carriers from traps and defects, leading to a high current increase. Further increasing the applied voltage, as it can be seen in figure 3(c), maintains the dielectric barrier of  $\text{SiO}_x$  while increasing the depletion region in the Si substrate. This is partially compensated by an increase of the accumulation region in the ZnO layer. The overall result is that the barrier scales with the applied external voltage, allowing some electrons to tunnel through the barrier. As the applied bias increases in absolute value, the number of electrons with enough energy to tunnel also increases, thus resulting in the slight enhancement in the measured current in agreement with our experimental observations.

On the other hand, the devices present a rapid growth in current under forward bias ( $V > 0$ ). In this polarity, as it can be

seen in figure 3(d), the accumulation region at the ZnO- $\text{SiO}_x$  interface is reduced until it soon shifts to a depletion region. As well, the depletion region initially present at the  $\text{SiO}_x$ -Si interface is rapidly reduced with the applied voltage. The combination of these two effects taking place allows for a faster rate of electrons to tunnel through the  $\text{SiO}_x$  barrier from the Si substrate to the RE-doped ZnO. It should be noted here that the doped-ZnO layer is polycrystalline and considered quasi-intrinsic, thus it may contain a large number of inter-band gap traps due to defects. At very low voltages ( $V < 1.6$  V) charge transport is again associated to carrier extraction from traps and defects (as previously identified for reverse bias conditions). As voltage increases and tunneling through the dielectric is enabled ( $1.6 \text{ V} < V < 7 \text{ V}$ ), a similar behavior to ohmic transport is observed due to a hopping mechanism of the electrons through the traps in the doped ZnO band gap, being the current bulk-limited. With the increase in applied external voltage the traps are rapidly filled and current increases until reaching a trap-filled limit, after which the current becomes limited due to space charge.

From the  $I(V)$  curves, it is evident that there is a change in conduction above 7 V for all devices. High applied external voltages can induce an accumulation region at the  $\text{SiO}_x$ -Si interface, once the depletion region is completely compensated (see figure 3(e)), whilst the depletion region at the ZnO- $\text{SiO}_x$  interface increases. Under these conditions, the energy bands of  $\text{SiO}_x$  dielectric layer is also bent and electrons are thus able to tunnel through a reduced triangular barrier following a Fowler-Nordheim (FN) mechanism. Assuming that FN is the main conduction mechanism in this regime, the  $I(V)$  curves at high voltages should follow:

$$I = a V^2 e^{(b/V)},$$

where  $a$  and  $b$  are constants. Indeed, we have fitted all  $I(V)$  curves by this mechanism (see dashed lines in figure 3(a)),

**Table 1.** Calculation of the minimum external voltage required to enter the FN tunneling regime.

Device	Flat-band voltage (V)	SiO <sub>2</sub> bending voltage (V)	Series resistance ( $R_s$ , in FN) (k $\Omega$ )	Voltage drop (due to $R_s$ ) (V)	Minimum voltage for FN (V)
ZnO:Ce			1.21	3.32	8.62
ZnO:Tb			1.79	1.13	6.43
ZnO:Eu,Tb	2.15	3.15	1.51	0.7	6.00
ZnO:Ce/ZnO:Tb/ ZnO:Eu,Tb			10.9	0.79	6.09

showing and excellent agreement with the experimental data.

In order to estimate the minimum voltage for FN conduction, we have taken into account the energy band diagram of the device structure in this range of voltages (see figure 3(e)) and evaluated its series resistance. To this end, some considerations have been made, treating the SiO<sub>x</sub> barrier as SiO<sub>2</sub>: (i) Flat band voltage can be calculated supposing that the Fermi level of *n*-Si is close to the conduction band and the ZnO-Fermi level in the middle of its band gap (at 1.70 eV from the bottom of the conduction band). Adding the electron affinity difference between ZnO and Si (4.50 and 4.05 eV, respectively), it results in a flat band voltage of 2.15 V. (ii) The minimum voltage required for overcoming the offset energy between Si and SiO<sub>2</sub> tunneling from the Si conduction band is equal to the difference in their electron affinities (4.05 eV for Si and 0.90 eV for SiO<sub>2</sub>), that is, 3.15 eV. (iii) Finally, the series resistance (and thus the voltage drop) can be numerically evaluated for each  $I(V)$  curve within the FN regime, using an iterative method. The resulting values from this procedure are summarized in table 1. Adding these three terms we can estimate the minimum voltages for FN conduction in each device as it appears in the last column of table 1. The FN fittings shown in figure 3(a) employ this value as lower limit for the fitting range.

As previously commented, the conduction under forward bias slightly differs for ZnO:Ce when compared to the other two films. This is probably due to the larger concentration of Ce with respect to the other two RE elements in their respective films, added to an easier oxidation process [31, 32]. These two facts could result in a combination of large clustering of Ce<sup>3+</sup> and oxidation to Ce<sup>4+</sup>, generating additional defect-related traps within the ZnO layer that require a larger external applied voltage to be filled. In addition, the clustering of Ce is in line with the EDX measurements, which showed an 8 nm thinner Ce film in the tri-layer system compared to the other two sublayers. Nevertheless, once the traps are filled FN dominates the conduction, in this case, for  $V > 8.62$  V. For devices with the ZnO:Ce/ZnO:Tb/ZnO:Eu,Tb stack, the deposition of multiple layers generates additional grain boundaries and/or strains due to the various doping rates from one layer to the adjacent ones, which can be directly related to the increase in the series resistance. While conduction is still dominated by FN at high voltages due to the presence of traps in the doped-ZnO layer, their higher series resistance hinders the conductivity by one order of magnitude.

### 3.3. Electroluminescence emission

In all devices, emission has only been observed under forward bias, in agreement with the higher charge injection under this condition, as determined by  $I(V)$  measurements. The complete analysis on the EL properties of the RE-doped ZnO devices is detailed in figure 4. Prior to spectrally resolving the EL of the devices, its integrated collection helped identifying the emission threshold and the relation of the emission with current, and thus the applied external voltage. For these measurements, the applied voltage was swept from 0 to 8 V in steps of 0.1 V·s<sup>-1</sup>. The results of this study are displayed in figure 4(a), following the color scheme of the devices analyzed in figure 3(a). Both ZnO:Tb and ZnO:Eu,Tb present again similar behaviors, with emission thresholds at 200–500  $\mu$ A. This threshold is increased to 1 mA in ZnO:Ce, thus indicating a less efficient emission. In the case of the multilayer device, the threshold is reduced to 10  $\mu$ A, pointing to a higher efficiency when close to the threshold that could be related to the increased series resistance maintaining FN as the main electron injection mechanism. It must also be noted that the obtained threshold currents of single-layer devices are in accordance with the change in conduction observed at around 7 V (see table 1).

So far, our results present a clear correlation between the emission and the conduction regime of the device. Considering electrons as majority carriers through the system (as suggested by the energy band diagrams in figures 3(c) and (d)), the excitation mechanism of the RE ions must be related to their injection into the doped-ZnO layer. Electrons, under forward bias, are injected from the *n*-type Si substrate into the doped-ZnO layer by tunneling through the dielectric SiO<sub>x</sub> barrier with an energy excess equal to the difference in energy between the substrate and the ZnO:RE conduction bands. Below the threshold for FN injection, electrons gain enough energy to tunnel but are then trapped by ZnO intra-band gap traps, thus not being able to excite the RE ions. Under large applied voltage, these hot electrons might gain additional energy due to the inclination of the ZnO conduction band and impact with the RE ions dispersed within the ZnO:RE layer, transferring their energy to excite the outer shell electrons of these elements, in a process called impact excitation [30]. Another (less probable) possibility includes a low injection of holes as minority carriers allowing the combination with electrons, thus creating excitons. The energy of this particle could be transferred to the RE ions thanks to the lattice [33]. Their later relaxation results in the emission of photons we detect as EL emission. In contrast and as previously discussed, under

reverse bias the injection of both electrons and holes is highly quenched, diminishing the possibility of RE excitation and resulting in non-observable EL emission.

EL emission from the devices is visible by the naked eye at high voltages. The insets in figure 4(a) show pictures of this visible emission from the devices while being electrically excited (each picture is marked with a symbol that matches the graph legend). These were acquired by setting a standard photographic-digital camera focusing through the microscope and collecting the image for 30 s while applying 2 mA of constant current to the devices. Both ZnO:Ce and the multilayered ZnO:Ce/ZnO:Tb/ZnO:Eu,Tb devices show a weak emission mainly located close to the contact point of the tip, whereas the other two exhibit a more homogeneous and intense emission, in agreement with the previous observations of the integrated EL curves. In addition, regarding the EL color exhibited by each device, Ce-doped ones present a white-blueish emission, Tb-doped devices a clear green one, and Eu,Tb-doped devices emit in orange-red. Finally, the multilayered devices present a white emission at the tip location.

The representation of the EL intensity data as shown in figure 4(b) allows comparing the devices in terms of their emission efficiency. According to this figure of merit, the multilayered device allows attaining an optical output at much lower currents. Nevertheless, all devices present a fast increase in efficiency that is afterwards saturated, in accordance with electron injection following the FN regime previously identified. In the case of ZnO:Ce, this regime has not yet been reached, thus resulting in the very low efficiency measured.

Once the threshold current for EL to occur was determined, the excitation mechanism has been identified and there are evidences that the emission could be seen by the naked eye, spectral measurements were carried out on each device by applying a fixed excitation current of 1 mA in substrate accumulation conditions. This current value corresponds to a high externally applied voltage where the high-voltage FN conduction mechanism is well established in all devices. In figure 4(c), the EL spectra for all four devices, measured under said conditions, are displayed.

Out of the three single-doped samples, ZnO:Ce shows a spectrum composed of two weak and wide features centered below 500 nm and around  $\sim 650$  nm, which would correspond to a combination of the electronic transitions listed in figure 1 for  $\text{Ce}^{3+}$  (421 and 464 nm) and the emission of ZnO defects, respectively. The broad emission band obtained instead of the well-defined electronic transitions could be related to the electronic states delocalization because of orbital distortion, caused by  $\text{Ce}^{3+}$  ions clustering, as well as additional interactions with  $\text{Ce}^{4+}$  ions, which we have previously attributed to affect the electrical properties [31, 32]. The combination of these two facts increases the probability of non-radiative processes, thus reducing the emission of the device. Oxidation of  $\text{Ce}^{3+}$  to  $\text{Ce}^{4+}$  is also compatible with the appearance of defects-related emission of ZnO, resulting from a larger concentration of oxygen vacancies in the film.

In contrast, both ZnO:Tb and ZnO:Eu,Tb devices show intense emission with narrow peaks corresponding to the

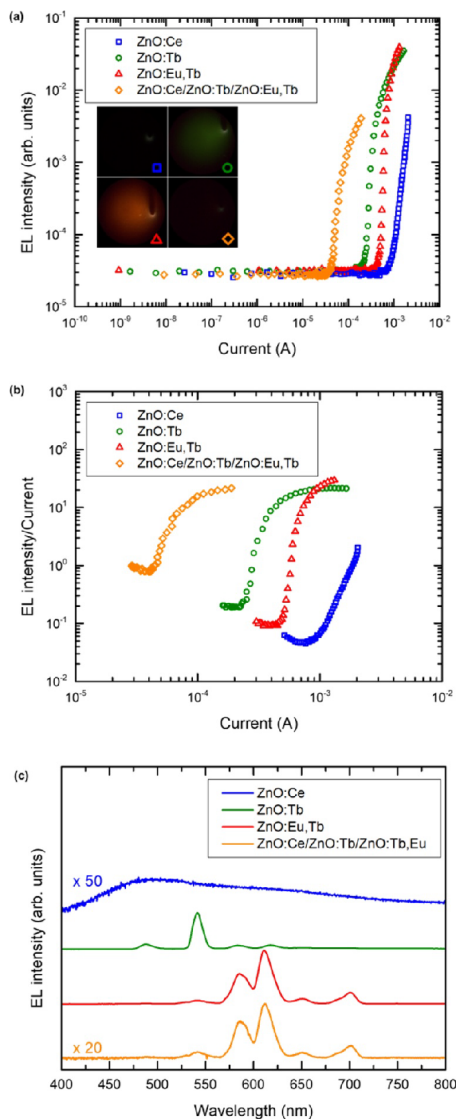


**Figure 4.** (a) Integrated electroluminescence of the four analyzed devices measured from 0 to 8 V. Pictures of the devices visible emission under electrical excitation are shown in the inset. (b) Representation of the integrated emission as emission efficiency, equivalent to an external quantum efficiency (EQE). (c) Corresponding electroluminescence spectra for the devices, collected during 30 s at 1 mA of applied current. The three graphs employ the same color code: ZnO:Ce in blue, ZnO:Tb in green, ZnO:Eu,Tb in red and ZnO:Ce/ZnO:Tb/ZnO:Eu,Tb in orange.

electronic transitions of  $Tb^{3+}$  and  $Eu^{3+}$  (see figure 1). The main emission of the Tb-doped sample is peaked at 541 nm, with three secondary peaks centered at 488, 584 and 617 nm, all four features constituting the expected emission of  $Tb^{3+}$  ions [34–36]. In the case of the ZnO:Eu,Tb device, other works in the literature have proved a higher efficiency of EL emission of  $Eu^{3+}$  ions for the co-doped films when compared to a device only containing Eu [34, 37]. Its EL exhibits its main emission peak at 611 nm, and three secondary peaks at 585, 651 and 700 nm, which is in agreement with the  $Eu^{3+}$  ions emission [38], although Tb is also optically active. Notwithstanding, the emission of  $Tb^{3+}$  ions appears to be quenched when compared to the emission of  $Eu^{3+}$  ones. On one hand, the main emission of  $Tb^{3+}$ ,  $^5D_4 \rightarrow ^7F_5$ , has a higher energy than the  $^7F_0 \rightarrow ^5D_0$  excitation transition of  $Eu^{3+}$ , and thus the energy involved in this emission may be partially transferred to  $Eu^{3+}$  ions and converted into an  $Eu^{3+}$  emission (the  $^5D_1$  and  $^5D_0$  electronic states might be populated). On the other hand, the remaining  $Tb^{3+}$ -related emission is masked by the emission of  $Eu^{3+}$ , as some of the main contributions almost overlap in wavelength (see figure 1). All these three emissions correspond well (in color and intensity) to the images of the devices shown in the insets of figure 4(a).

In agreement with the emission of the single-doped samples, the fourth one, combining all three layers, shows the characteristic emission peaks of  $Tb^{3+}$  and  $Eu^{3+}$  in the same positions as previously observed. This fact indicates that the optical activity of RE ions is still preserved when sputtered on a stack structure.  $Tb^{3+}$  ions emission can be detected by visually comparing the relative intensities between peaks at 541 and 611 nm with those in sample ZnO:Eu,Tb. Therefore, the layer sequence is optimal for obtaining a combined emission of the RE ions from one device, avoiding the  $Eu^{3+}$  absorption of  $Tb^{3+}$ -emitted photons that would take place if Eu was on top. Furthermore, it is worth noting that the emission of the combined-RE stack is 20 times less intense (as indicated) than that of the previously commented devices, which is a consequence of the reduction in thickness of the two emitting layers (as discussed during the structural characterization), and the presence of ZnO:Ce on top quenching the emission from the bottom layers. Last, the analyzed EL peaks have a FWHM of about 15 nm, in agreement with other reported works concerning RE-doped ZnO EL devices [14, 15, 22, 34].

### 3.4. Chromatic diagram

To complement the electro-optical study carried out in this work, the resulting EL emission from the investigated devices was analyzed under the CIE 1931 standard for reference. The position of the four obtained spectra are displayed in the chromatic diagram in figure 5: ZnO:Ce corresponds to yellow blue due mainly to the emission of ZnO defects. Emission from ZnO:Tb and ZnO:Eu,Tb well correspond to green and red-orange colors in the diagram, respectively. In addition, the device containing the three different layers exhibits an orange color closer to the white center of the diagram, in agreement with the presence of both  $Tb^{3+}$  and  $Eu^{3+}$  emissions.

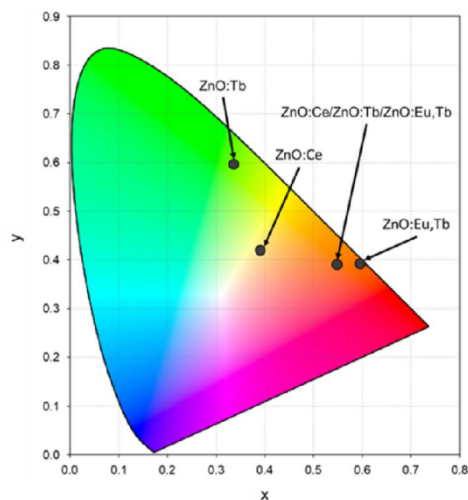


**Figure 5.** Location of the emission corresponding to each LED under study in the present work within the standard CIE 1931 chromatic diagram.

Indeed, from the chromatic diagram it becomes clear that blue emission from Ce ions has not yet been achieved or is highly quenched by the emission of ZnO-defects. If blue emission from  $Ce^{3+}$  could be added to the system, the position of the multilayered sample would become even closer to the center. Therefore, aiming at obtaining an efficient RE-based RGB LED, it is necessary to improve the deposition of a light-emitting  $Ce^{3+}$ -doped ZnO-based layer whose emission can provide the blue component expected to be combined with the intense green ( $Tb^{3+}$ ) and red ( $Eu^{3+}$ ) emissions hereby already demonstrated.

## 4. Conclusion

The devices hereby analyzed have proved the possibility of fabricating an RGB LED employing ZnO as host matrix for a low concentration of RE ions, using sputtering as the main deposition technique. For this purpose, three different RE elements have been explored, Ce, Tb and Eu, whose EL emission characteristics (determined by the electronic transitions when in a +3 valence state) respectively result in blue, green and red intense and narrow emissions.

Out of the three,  $Tb^{3+}$  and  $Eu^{3+}$  are optically active after the deposition and annealing processes underwent to achieve the device structure, and under the electrical excitation conditions employed for attaining EL devices emission; instead, Ce has only shown poor EL emission and only under high stress conditions. The analysis and characterization via TEM and EDX, as well as the electrical conduction mechanisms analysis, point toward the agglomeration of Ce ions in the

layer to be larger than in the case of Tb and Eu, affecting their local stoichiometry and therefore carrier transport and emission properties. Nonetheless, the results for Ce are still promising, and future test and characterization of the ZnO:Ce films controlling Ce-concentration and distribution are expected to improve their EL efficiency. The stack fabrication of the three films into a single device has also been tested, enabling the emission of the different optically-active centers present within the whole structure. As intended, their combined emission exhibits contribution from the three RE dopants, resulting in a shift toward the central region of the chromatic diagram.

Overall, the hereby presented results reinforce the suitability of ZnO as an adequate matrix to host optically-active RE ions with intense and narrow emission, useful for fabricating full-color light sources for general lighting and other optoelectronics applications.

### Acknowledgments

This work was financially supported by the Spanish Ministry of Economy and Competitiveness (Project No. TEC2016-76849-C2-1-R). JLF acknowledges the subprogram 'Ayudas para la Formación de Profesorado Universitario' (No. FPU16/06257) from the Spanish Ministry of Education, Culture and Sports for economical support. JL-V acknowledges financial support from a 'Juan de la Cierva' postdoctoral fellowship (JIC1-2017-33451) from the Spanish Ministry of Economy, Industry and Competitiveness. XP, CL, and CG are grateful to C Frilay for his expertise in the maintenance of the sputtering setup used for the growth of the ZnO films. They also thank F Lemarié for the TEM sample preparation by FIB.

### ORCID iDs

J L Frieiro  <https://orcid.org/0000-0002-6874-8811>  
 C Guillaume  <https://orcid.org/0000-0002-6732-1760>  
 J López-Vidrier  <https://orcid.org/0000-0003-0907-5853>  
 O Blázquez  <https://orcid.org/0000-0002-0921-2793>  
 S Hernández  <https://orcid.org/0000-0002-2226-1020>  
 B Garrido  <https://orcid.org/0000-0001-7961-6999>

### References

- [1] Özgür Ü, Alilov Y I, Liu C, Teke A, Reshchikov M A, Doğan S, Avrutin V, Cho S J and Morko H 2005 A comprehensive review of ZnO materials and devices *J. Appl. Phys.* **98** 1–103
- [2] Klingshirn C F 2007 ZnO: material, physics and applications *ChemPhysChem* **8** 782–803
- [3] Rogers D J, Teherani F H, Sandana V E, Razeghi M et al 2010 ZnO thin films and nanostructures for emerging optoelectronic applications Proc. SPIE 7605 L A Eldada and E-H Lee pp 76050K
- [4] Laube J, Nübling D, Beh H, Gutsch S, Hiller D and Zacharias M 2016 Resistivity of atomic layer deposition grown ZnO: the influence of deposition temperature and post-annealing *Thin Solid Films* **603** 377–81
- [5] Chen X L, Wang F, Geng X H, Zhang D K, Wei C C, Zhang X D and Zhao Y 2012 Natively textured surface Al-doped ZnO-TCO layers with gradual oxygen growth for thin film solar cells via magnetron sputtering *Appl. Surf. Sci.* **258** 4092–6
- [6] Rahman F 2019 Zinc oxide light-emitting diodes: a review *Opt. Eng.* **58** 1
- [7] Prucnal S et al 2017 Engineering of optical and electrical properties of ZnO by non-equilibrium thermal processing: the role of zinc interstitials and zinc vacancies *J. Phys. D: Appl. Phys.* **122** 035303
- [8] Janotti A and Van De Walle C G 2009 Fundamentals of zinc oxide as a semiconductor *Rep. Prog. Phys.* **72** 126501
- [9] Fan J C, Sreekanth K M, Xie Z, Chang S L and Rao K V 2013 p-Type ZnO materials: theory, growth, properties and devices *Prog. Mater. Sci.* **58** 874–985
- [10] Zeng H, Duan G, Li Y, Yang S, Xu X and Cai W 2010 Blue luminescence of ZnO nanoparticles based on non-equilibrium processes: defect origins and emission controls *Adv. Funct. Mater.* **20** 561–72
- [11] Duan L, Wang P, Wei F, Zhang W, Yao R and Xia H 2014 Electroluminescence of ZnO nanorods embedded in a polymer film *Solid State Commun.* **200** 14–16
- [12] Kenyon A J 2002 Recent developments in rare-earth doped materials for optoelectronics *Prog. Quantum Electron.* **26** 225–84
- [13] Khan L U and Khan Z U 2018 Rare earth luminescence: electronic spectroscopy and applications *Handbook of Materials Characterization* (Cham: Springer International Publishing) 345–404
- [14] Gaponenko N V et al 2001 Terbium photoluminescence in polysiloxane films *Mater. Sci. Eng. B* **81** 191–3
- [15] Heikenfeld J, Garter M, Lee D S, Birkhahn R and Steckl A J 1999 Red light emission by photoluminescence and electroluminescence from Eu-doped GaN *Appl. Phys. Lett.* **75** 1189–91
- [16] Luo Q, Wang L S, Guo H Z, Lin K Q, Chen Y, Yue G H and Peng D L 2012 Blue luminescence from Ce-doped ZnO thin films prepared by magnetron sputtering *Appl. Phys. A* **108** 239–45
- [17] Anand V, Sakthivelu A, Kumar K D A, Valanarasu S, Ganesh V, Shkir M, Kathalingam A and AlFaify S 2018 Novel rare earth Gd and Al co-doped ZnO thin films prepared by nebulizer spray method for optoelectronic applications *Superlattices Microstruct.* **123** 311–22
- [18] Komuro S, Katsumata T, Morikawa T, Zhao X, Isshiki H and Aoyagi Y 2000 1.54 Mm emission dynamics of erbium-doped zinc-oxide thin films *Appl. Phys. Lett.* **76** 3935–7
- [19] Llusçà M, López-Vidrier J, Antony A, Hernández S, Garrido B and Bertomeu J 2014 Up-conversion effect of Er- and Yb-doped ZnO thin films *Thin Solid Films* **562** 456–61
- [20] Röder R, Geburt S, Zapf M, Franke D, Lorke M, Frauenheim T, da Rosa A L and Rönning C 2019 Transition metal and rare earth element doped zinc oxide nanowires for optoelectronics *Phys. Status Solidi Basic Res.* **256** 1–12
- [21] Ishii M, Komuro S, Morikawa T and Aoyagi Y 2001 Local structure analysis of an optically active center in Er-doped ZnO thin film *J. Phys. D: Appl. Phys.* **89** 3679–84
- [22] Li J, Zalloum O H Y, Roschuk T, Heng C L, Wojcik J and Mascher P 2008 Light emission from rare-earth doped silicon nanostructures *Adv. Opt. Technol.* **2008** 295601
- [23] Umamaheswari D, Jamalajah B C, Sasikala T, Chengaiath T, Kim I G and Rama Moorthy L 2012 Photoluminescence and decay behavior of Tb 3+ ions in sodium fluoro-borate glasses for display devices *J. Lumin.* **132** 1166–70
- [24] Sorokina I T 2007 Crystalline mid-infrared lasers *Solid-State Mid-Infrared Laser Sources* vol 351 (Berlin, Heidelberg: Springer) pp 262–358
- [25] Jovanović D J, Antić Ž, Kršmanović R M, Mitić M, Siginević V, Bártová B and Dramićanin M D 2013

- Annealing effects on the microstructure and photoluminescence of Eu<sup>3+</sup>-doped GdVO<sub>4</sub> powders *Opt. Mater. (Amst)*. **35** 1797–804
- [26] Polman A 1997 Erbium implanted thin film photonic materials *J. Phys. D: Appl. Phys.* **82** 1–39
- [27] Takahei K, Taguchi A, Horikoshi Y and Nakata J 1994 Atomic configuration of the Er-O luminescence center in Er-doped GaAs with oxygen codoping *J. Phys. D: Appl. Phys.* **76** 4332–9
- [28] Ford G M and Wessels B W 1996 1.54  $\mu\text{m}$  electroluminescence from erbium doped gallium phosphide diodes *Mater. Res. Soc. Symp. - Proc.* **422** 345–50
- [29] Jambois O, Berencen Y, Hijazi K, Wojdak M, Kenyon A J, Gourbilleau F, Rizk R and Garrido B 2009 Current transport and electroluminescence mechanisms in thin SiO<sub>2</sub> films containing Si nanocluster-sensitized erbium ions *J. Phys. D: Appl. Phys.* **106** 063526
- [30] Ramírez J M et al 2012 Erbium emission in MOS light emitting devices: from energy transfer to direct impact excitation *Nanotechnology* **23** 125203
- [31] He X, Liu X, Li R, Yang B, Yu K, Zeng M and Yu R 2016 Effects of local structure of Ce<sup>3+</sup> ions on luminescent properties of Y<sub>3</sub>Al<sub>5</sub>O<sub>12</sub>: Ce nanoparticles *Sci. Rep.* **6** 1–11
- [32] Mishra S, Kshatri D S, Khare A, Tiwari S and Dwivedi P K 2016 SrS:Ce<sup>3+</sup> thin films for electroluminescence device applications deposited by electron-beam evaporation deposition method *Mater. Lett.* **183** 191–6
- [33] Luo L et al 2012 Efficient doping and energy transfer from ZnO to Eu<sup>3+</sup> ions in Eu<sup>3+</sup>-doped ZnO nanocrystals *J. Nanosci. Nanotechnol.* **12** 2417–23
- [34] Davesne C, Ziani A, Labbé C, Marie P, Frilay C and Portier X 2014 Energy transfer mechanism between terbium and europium ions in zinc oxide and zinc silicates thin films *Thin Solid Films* **553** 33–37
- [35] Blázquez O, López-Vidrier J, López-Conesa L, Busquets-Masó M, Estradé S, Peiró F, Hernández S and Garrido B 2016 Structural and optical properties of Al-Tb/SiO<sub>2</sub> multilayers fabricated by electron beam evaporation *J. Phys. D: Appl. Phys.* **120** 135302
- [36] Friero J L, Blázquez O, López-Vidrier J, López-Conesa L, Estradé S, Peiró F, Ibáñez J, Hernández S and Garrido B 2018 Green electroluminescence of Al/Tb/Al/SiO<sub>2</sub> devices fabricated by electron beam evaporation *Phys. Status Solidi* **215** 1700451
- [37] Borkovska L V et al 2019 Influence of annealing on luminescence and energy transfer in ZnO multilayer structure co-doped with Tb and Eu *Thin Solid Films* **692** 137634
- [38] Petersen J et al 2010 Correlation of structural properties with energy transfer of Eu-doped ZnO thin films prepared by sol-gel process and magnetron reactive sputtering *J. Phys. D: Appl. Phys.* **107** 1–7

## 4.2. Electroluminescence from multilayered Al/Tb/Al/SiO<sub>2</sub>

Silicon oxide has proven to be an excellent host for rare earth ions due to its optical properties that makes it a transparent material. In addition, it being an excellent dielectric material can also help in the excitation of the rare earth ions in the matrix by accelerating the electrical carriers via tunneling effects. Its only drawback is the low solubility of the rare earth ions in the matrix, allowing the formation of clusters that lose the light emission properties of the ions.<sup>[5]</sup>

With the aim of overcoming this limitation in mind, a previous study concluded that a *delta doping* approach can reduce cluster formation. In this fabrication method, very thin layers of the optically-active material and thicker layers of the host matrix are alternately deposited. Afterwards, an annealing treatment at high temperatures is employed to homogenize the structure. In addition, the inclusion of Al layers to the system also improved both the optical properties of the rare earth ions and the electrical properties of the system, which would be beneficial for electro-optical devices later fabricated.<sup>[6]</sup>

The work hereby presented integrates the best device structure from those previously tested into a light emitting device structure: a multilayer of Al/Tb/Al/SiO<sub>2</sub>. The device has been fully deposited in the electron-beam evaporation system available in the cleanroom of the Faculty of Physics of the University of Barcelona. Its main active layers are formed by 5×Al/Tb/Al/SiO<sub>2</sub> layers evaporated over a *p*-type Si wafer. The thickness of each layer was 0.8, 0.4 and 3 nm, respectively for Al, Tb and SiO<sub>2</sub>. The samples were annealed at 1100 °C in a N<sub>2</sub> atmosphere for 1 h, also previously found to be the optimal procedure. After that, ITO circular electrodes were deposited on top of the multilayers and annealed at 600 °C in N<sub>2</sub> for 1 h. Finally, the bottom of the Si wafer was metallized with Al to form a common bottom contact.

A first characterization via transmission electron microscopy determined that the actual thickness of the SiO<sub>2</sub> layers was of 5 nm, while the combination of the Al and Tb layers were 3-nm thick, indistinguishable with this technique. The aim was to deposit the thinnest layer possible of Tb, 0.4 nm. The real amount evaporated is probably higher (but not 1.5 times more), and thus the remaining thickness to the 3 nm measured is also due to extra Al. Composition of

#### 4.2. Electroluminescence from multilayered Al/Tb/Al/SiO<sub>2</sub>

the stack was analyzed via X-ray photoelectron spectroscopy (XPS), concluding that at least 45% of the Tb ions are in the form of Tb<sub>2</sub>O<sub>3</sub> (Tb<sup>3+</sup> valence) as desired. An additional sample with no Al layers showed that Tb ions are mainly bound to each other in clusters or to SiO<sub>2</sub> dangling bonds, because under the assumption that SiO<sub>2</sub> is stoichiometric no O should be available for Tb to form the oxide.

Next, the emission of the layers was checked via three methods: cathodoluminescence (CL), resonant and non-resonant PL. The first technique uses a 2 keV beam of electrons to excite the structure, allowing for the observation of the main emission peak of Tb transitions at 544 nm (<sup>5</sup>D<sub>4</sub> → <sup>7</sup>F<sub>5</sub>) as well as others at 489, 587 and 624 nm (<sup>5</sup>D<sub>4</sub> → <sup>7</sup>F<sub>i</sub>, i = 6, 4 and 3, respectively) and with a lower intensity at 415 and 437 nm (<sup>5</sup>D<sub>3</sub> → <sup>7</sup>F<sub>j</sub>, j = 5, 4; respectively). Photoluminescence in resonant conditions employed a 488-nm laser line to excite the Tb<sup>3+</sup> directly through the <sup>5</sup>D<sub>4</sub> → <sup>7</sup>F<sub>6</sub> transition, resulting in the emission of the lower energy peaks. Last, a He-Cd 325 nm emitting laser excited the sample in non-resonant conditions, via energy transfer from the matrix to the Tb ions, again obtaining the expected emission. These measurements confirmed that the ions are optically active with different efficiencies for their excitations. No emission was detected in samples with no Al, highlighting its importance in the structure.

The electrical analysis of the device structure revealed a Schottky conduction mechanism. In addition, it was corroborated that devices containing Al layers are more resistive than those without them, as these layers are presumed to be oxidized and thus impose additional insulating barriers. Nevertheless, the modelling of both devices showed a minor contribution of these layers, since conduction is mainly limited by SiO<sub>2</sub>. Finally, the EL of the devices was measured. In agreement with previous observations, samples missing the Al layers showed no emission. A first measurement of integrated EL emission determined that a threshold of 8.5 V and 2 μA was required for emission to take place. The emission intensity dependence on the increasing current followed a linear trend, which pointed towards a direct impact excitation mechanism, as expected from the literature.<sup>[7,8]</sup> Spectrally resolving the emission allowed discriminating the expected peaks for Tb ions with a low-intensity broad-background emission provided by defects emission from either the SiO<sub>2</sub> or the ITO contacts. The EL emission is compared to those obtained by CL and PL in Figure 4.3 allowing to clearly distinguish the peaks corresponding to Tb<sup>3+</sup> and to observe that EL yields wider signals, as it less efficient and thus transitions are less defined.

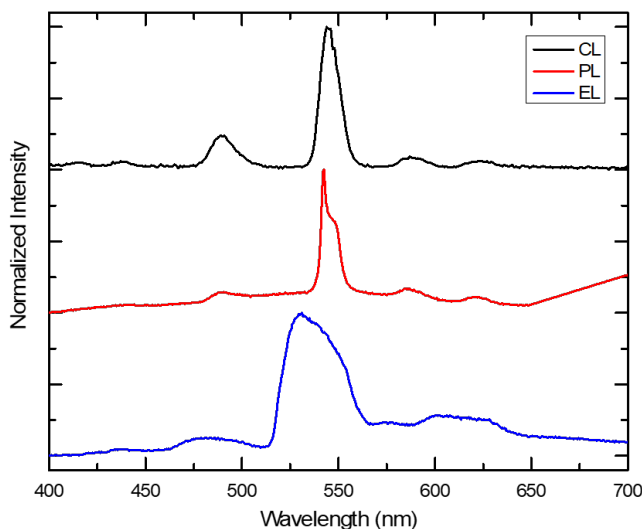


**Figure 4.3.** CL, PL and EL normalized emissions of Al/Tb/Al/SiO<sub>2</sub> devices, defining the emission peaks of Tb<sup>3+</sup> as expected from their electronic transitions.

Interestingly, the first hint of resistive switching in SiO<sub>2</sub> layers is also observed in these devices. Indeed, successive measurements of the EL showed a progressive reduction of the intensity (as it can be seen in the tracking of the intensity for the peak at 542 nm and the integrated emission in Figure 4.4), which could result in the total quenching of the emission. A monitorization of the electrical behavior under a constant applied current of 100  $\mu$ A showed that after 30 s, both EL and voltage drop in steps until device breakdown. This fact is easily associated with

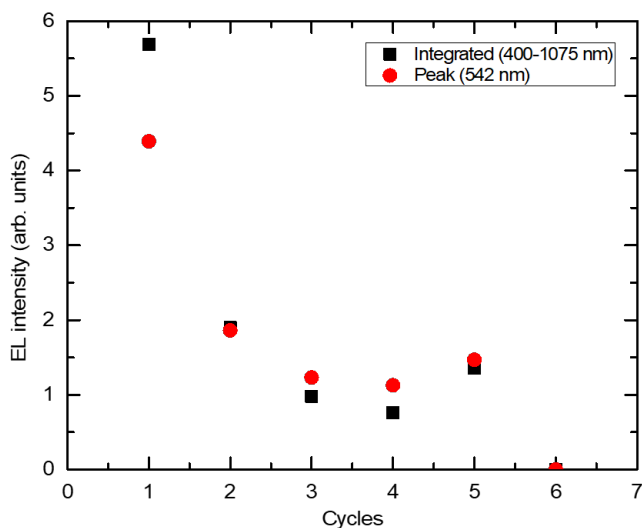


**Figure 4.4.** Decay of EL intensity with measuring cycles for both the peak emission at 542 nm and the integrated.

#### 4.2. Electroluminescence from multilayered Al/Tb/Al/SiO<sub>2</sub>

the movement of oxygen ions in the devices, creating low-resistance conduction paths, both reducing the amount of optically-active Tb ions and avoiding their excitation.

This work was presented as a poster in the European Materials Research Society (EMRS) Spring Meeting 2017. A proceedings paper was published in *Physica Status Solidi A* **215**, 1700451 (2018). It was also selected as the cover picture of the journal for Vol. 215, Issue 3, published on February 7<sup>th</sup>, 2018.



**Journal cover (Paper III): Physica Status Solidi A  
215, Issue 3 (2018) (DOI: [10.1002/pssa.201870005](https://doi.org/10.1002/pssa.201870005))**



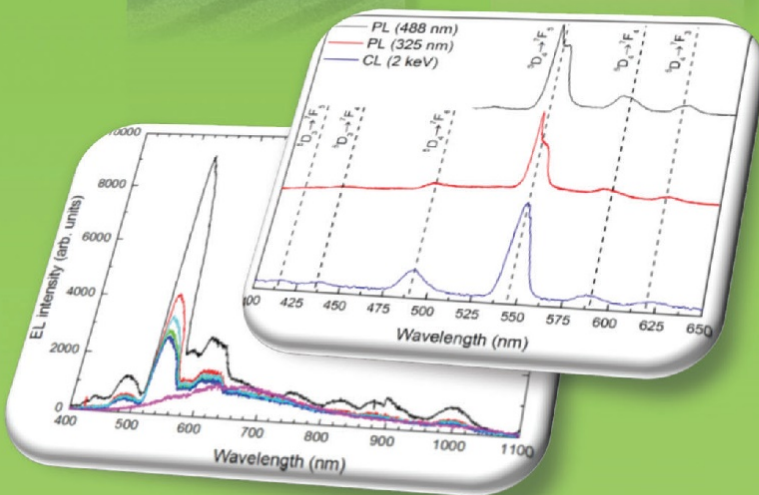
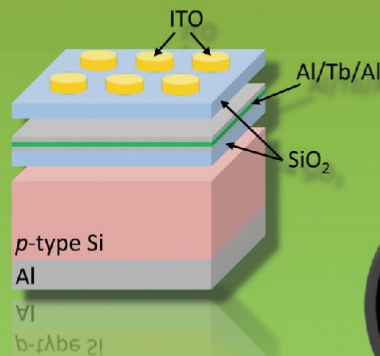
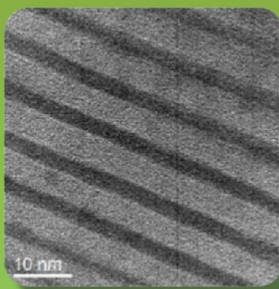
**Paper III: Green Electroluminescence of  
Al/Tb/Al/SiO<sub>2</sub> Devices Fabricated by Electron Beam  
Evaporation (DOI: [10.1002/pssa.201700451](https://doi.org/10.1002/pssa.201700451))**



Special Issue:

Nanoparticles in Dielectric Matrix: From Synthesis to Device Applications for Photonics, Electronics, and Biosensing

Guest-edited by Simona Boninelli



# Green Electroluminescence of Al/Tb/Al/SiO<sub>2</sub> Devices Fabricated by Electron Beam Evaporation

Juan Luis Friero, Oriol Blázquez, Julian López-Vidrier, Lluís López-Conesa, Sònia Estradé, Francesca Peiró, Jordi Ibáñez, Sergi Hernández,\* and Blas Garrido

In this work, the fabrication and the structural, optical and electrical properties of Al-Tb/SiO<sub>2</sub> nanomultilayers have been studied. The nanomultilayers were deposited by means of electron beam evaporation on top of p-type Si substrates. Optical characterization shows a narrow and strong emission in the green spectral range, indicating the optical activation of Tb<sup>3+</sup> ions. The electrical characterization revealed conduction limited by the electrode, although trapped-assisted mechanisms can also contribute to transport. The electroluminescence analysis revealed also emission from Tb<sup>3+</sup> ions, a promising result to include this material in future optoelectronic applications as integrated light-emitting devices.

## 1. Introduction

The invention of LEDs has opened the door for the field of optoelectronics, as the use of semiconductors allows scaling these light sources to the sizes of microelectronic devices employed today. Optoelectronic devices are designed to employ light in combination with (or instead of) electric currents, which introduces many advantages: separation of electronic devices (thus enabling the optimization of the chip layout), reduction of electromagnetic interference, cable length and weight, sustenance of precise signal timing, reduction of interconnect densities and energy saving (thanks to lower heat losses).<sup>[1–3]</sup>

These new devices need to be able to operate in concert with current electronic devices based on silicon technology, which requires of Si-based light collectors, transducers between electric and optical signals, light waveguides, and light emitters. For the latter, semiconductor materials doped with rare earth (RE) ions

have been widely studied in the last two decades due to their narrow and intense luminescence, as a potential alternative for more efficient devices than LEDs.<sup>[4–6]</sup>

Rare earth elements have their 4f electronic shell partially filled, and when they are optically active, they usually have an oxidation state +3 due to the loss of one 4f electron and the two 6s electrons. These elements have luminescent properties resulting from the intra-4f transitions (almost independent of the matrix) or 5d-to-4f ones (sensitive to the matrix).<sup>[7]</sup>

Erbium has been studied as dopant of different films like silica (SiO<sub>2</sub>), yielding emissions in the infrared part of the spectrum (≈1535 nm) when in an Er<sup>3+</sup> oxidation state, which makes it very useful for optical fiber telecommunication systems.<sup>[8,9]</sup> Other REs have been researched for their emission in the visible range, such as Ce<sup>3+</sup>,<sup>[8]</sup> Tb<sup>3+</sup>,<sup>[10–11]</sup> and Eu<sup>3+</sup>,<sup>[12]</sup> in the blue (460 nm), green (543 nm), and red (615 nm) parts of the spectra, respectively. In the Figure 1, the electronic levels, energies and transitions for a particular RE species (Tb<sup>3+</sup> ions as it will be later studied in this work<sup>[13]</sup>) are presented.

Fabrication of these materials has been exploited through many different techniques, such as plasma-enhanced chemical vapor deposition,<sup>[11]</sup> ion implantation,<sup>[14]</sup> liquid source chemical vapor deposition,<sup>[15]</sup> magnetron sputtering,<sup>[16]</sup> and sol-gel.<sup>[17]</sup> Some other techniques have also been attempted, but are less commonly employed, like atomic layer deposition.<sup>[18]</sup>

Following the approach to new RE light emitters, in this work it is described the fabrication and characterization of nanomultilayered (NML) structures composed of SiO<sub>2</sub>, Al and Tb<sup>3+</sup> ions, by means of electron beam evaporation (EBE). In a previous work, different combinations of these layers have been tested aiming at the best layer configuration that exhibits stronger emission.<sup>[19]</sup> The optical properties of the chosen configuration were studied by photoluminescence (PL) in samples annealed at different temperatures.<sup>[20]</sup>

The films employed in this work were deposited by using EBE, considering the optimum nanomultilayered structure as Al-Tb/SiO<sub>2</sub>, on top of a p-type Si substrate. The films used for the structural and optical characterization consist of 15 × Al/Tb/Al/SiO<sub>2</sub> layers, ending with a SiO<sub>2</sub> layer that serves as protection. For the electrical characterization, 5 × Al/Tb/Al/SiO<sub>2</sub> layers were fabricated, also on a p-type Si substrate, adding a full area bottom electrode of Al and top contact of indium tin oxide (ITO). The ITO contact also allows for electro-optical characterization, as it is a

J. L. Friero, O. Blázquez, Dr. J. López-Vidrier, Dr. L. López-Conesa, Dr. S. Estradé, Prof. F. Peiró, Dr. J. Ibáñez, Dr. S. Hernández, Prof. B. Garrido  
MIND-IN<sup>2</sup>UB, Department of Engineering: Electronics Universitat de Barcelona, Martí i Franquès 1, E-08028 Barcelona, Spain  
E-mail: shernandez@ub.edu

Dr. J. López-Vidrier  
IMTEK, Faculty of Engineering Albert-Ludwigs-University, Georges-Köhler-Allee 103, D-79110 Freiburg, Germany

Dr. J. Ibáñez  
Institute of Earth Sciences Jaume Almera ICTJA-CSIC, Lluís Soler i Sabarís s/n, E-08028 Barcelona, Catalonia, Spain

 The ORCID identification number(s) for the author(s) of this article can be found under <https://doi.org/10.1002/pssa.201700451>.

DOI: 10.1002/pssa.201700451

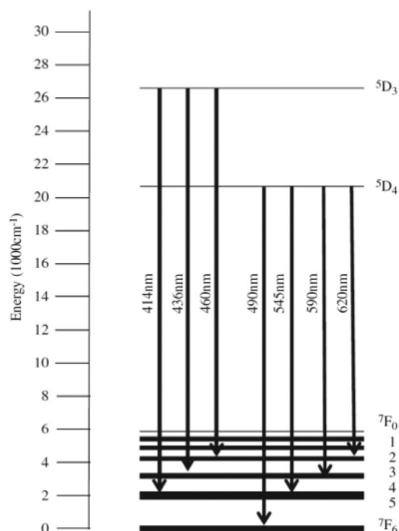


Figure 1. Electronic transitions of  $Tb^{3+}$ , taken from Ref. [13].

transparent conducting oxide (TCO). The average composition of the nanomultilayers was assessed by using X-ray photoelectron spectroscopy (XPS). Different techniques were employed to determine the optical properties of the Tb-films, such as PL and cathodoluminescence (CL). The electrical properties were studied through the different  $I(V)$  curves obtained. Finally, the electroluminescence (EL) of the NMLs was also measured in the accumulation regime. The results suggest the possibility of employing EBB for the fabrication of RE-doped materials that can be introduced into devices for optoelectronic applications in the future.

## 2. Experimental Section

Different combinations in nanomultilayer structures for  $SiO_2$ , Al and Tb were tested in a previous study, in order to achieve the optimal configuration for the optical activation of the  $Tb^{3+}$  ions.<sup>19,20</sup> All test samples and the ones here employed were fabricated by electron beam evaporation, and deposited on top of p-type Si substrates, which were cleaned with acetone, isopropyl alcohol, ethanol, and de-ionized water, and agitated ultrasonically during each process, before being introduced into the chamber.

The equipment employed for the deposition is a PFEIFFER VACUUM Classic 500 chamber with a Ferrotec GENIUS electron beam controller and a Ferrotec CARRERA high-voltage power supply. The base pressure in the chamber was  $1.6 \times 10^{-6}$  mbar and the temperature of the substrate was kept at  $100^\circ C$ . Acceleration voltages were 6 kV for  $SiO_2$  and Tb, and 10 kV for Al, with deposition rates of 1.0, 0.2, and  $0.2 \text{ \AA s}^{-1}$ , respectively.

The samples for the structural and optical characterization consisted of 15 stacks of Al/Tb/Al/ $SiO_2$ , with two 10-nm layers of  $SiO_2$  before and after them to prevent any atomic diffusion from or to the nanomultilayers. The nominal thickness of the Al, Tb,

and  $SiO_2$  layers were 0.8, 0.4, and 3 nm, respectively (see Figure 2 (a)). After deposition, the samples were submitted to an annealing process at  $1100^\circ C$  in  $N_2$  atmosphere for 1 h. An identical sample was also fabricated but with no Al, in order to observe the influence of this element. In the Figure 2(b) the cross-section of the nanomultilayers acquired by transmission electron microscopy (TEM) is shown, where the nanometric structure can be clearly seen: the bright layers with a thickness of 5 nm correspond to  $SiO_2$ , whereas the dark ones, with a thickness of 3 nm, are a stack of Al-Tb, as demonstrated by electron energy loss spectroscopy.<sup>20</sup> As revealed by the TEM image, this stack serves as delta doping system of Tb in a  $SiO_2$  matrix, allowing for obtaining nanometric separation between the different Tb layers, while isolating them in the growth direction and thus reducing possible clustering effects.

For the electrical and electro-optical characterization, new samples were fabricated consisting for 5 stacks of Al/Tb/Al/ $SiO_2$ , also annealed at  $1100^\circ C$  in  $N_2$  atmosphere for 1 h. After annealing, indium tin oxide (ITO) electrodes were deposited on top of the multilayers using a shadow mask, with circular shape with a radius of  $200 \mu m$ , and subsequently annealed at  $600^\circ C$  in  $N_2$  atmosphere for 1 h. Finally, a full area Al metallization was performed on the backside of the Si substrate for defining the bottom contact. This structure is schematically shown in Figure 2(c).

To determine the overall composition of the deposited films, XPS measurements were carried out using a PHI 5500 Multitechnique System, thus obtaining information regarding the Al influence on the Tb-related binding formation.

Photoluminescence measurements with two different excitation energies were employed for determining the optically active emission from  $Tb^{3+}$  ions. The 325-nm line from a HeCd laser or the 488-nm line from an  $Ar^+$  laser were used for the excitation of the  $Tb^{3+}$  ions. In the case of the HeCd laser, the spectra were analyzed using a Horiba Jobin Yvon LabRAM HR spectrometer, whereas the spectral analysis exciting with the  $Ar^+$  laser was done using a GaAs photomultiplier tube (PMT) coupled to a monochromator in a lock-in configuration. For the acquisition of CL spectra, a JEOL JSM-7100F scanning electron microscope coupled to a monochromator and a GaAs PMT was employed. In order to avoid damage on the surface, a defocused electron beam of  $80 \mu A$ , accelerated at 2 keV, was used for the measurements.

Electrical characterization of the samples was done by two contact measurements with an Agilent B1500 semiconductor device analyzer and a Cascade Microtech Summit 11000 probe station using a Faraday cage. The back-contact was grounded through the chuck, whereas the top ITO-contact was swept from  $-15$  to  $15$  V, with steps of  $50 \text{ mV s}^{-1}$ .

Emission from the sample obtained through electroluminescence (EL) was collected with a Seiva 888 L microscope. Whereas the integrated emission was recorded using the same GaAs PMT employed in the PL measurements, the spectral emission was captured by means of Princeton Instruments LN-cooled charge-coupled device via a  $1/4 m$  Oriel monochromator.

## 3. Results and Discussion

Measurements performed by XPS allowed determining the composition and the effect of the presence of Al atoms

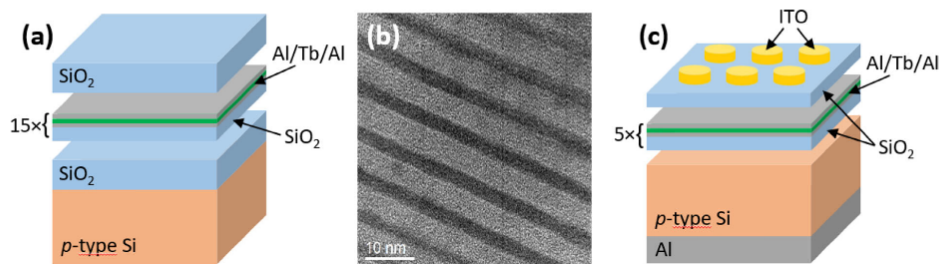


**Figure 2.** a) Sketch of the nominal deposited structure for structural and optical characterization purposes. b) HRTEM image of the deposited nanomultilayer structure. c) Sketch of the nominal deposited devices employed in the electrical and electro-optical characterization.

surrounding the Tb ions. In Table 1 we have summarized the obtained results. Whereas the sample with no Al showed stoichiometric SiO<sub>2</sub>, the sample containing Al showed an increase of the oxygen content. Thus, this observation implies that, on one hand, the Tb ions in the sample with no Al may be bound to other Tb ions or dangling bonds from SiO<sub>2</sub>, and, on the other hand, the sample with Al exhibits an oxygen excess that should be located in the Al/Tb/Al stack (the SiO<sub>2</sub> in the whole sample is stoichiometric). As aluminium is much more chemically reactive than terbium, the oxygen excess in the sample with Al is more likely to be bound to Al forming alumina (Al<sub>2</sub>O<sub>3</sub>). In order to have a minimum quote of the amount of Tb which is oxidized (i.e., prompt to be optically active), we considered that: (i) all the Si atoms are bound to O atoms, thus forming SiO<sub>2</sub>; (ii) all the Al atoms are in the form of alumina (Al<sub>2</sub>O<sub>3</sub>); and (iii) the remaining O content is bound to Tb atoms. Under these assumptions, and considering the atomic content in the Al/Tb/Al/SiO<sub>2</sub> sample (considering the whole film), we found that at least 45% of the Tb ions are in the form of Tb<sub>2</sub>O<sub>3</sub>. Thus, the addition of Al contributes to the oxidation of Tb ions, which should also influence their emission properties.<sup>[20]</sup>

Optical emission of the Al/Tb/Al/SiO<sub>2</sub> structure was first characterized by means of PL. Two different excitation lines were employed: a non-resonant excitation using  $\lambda = 325$  nm and a resonant excitation with  $\lambda = 488$  nm (see Figure 3).<sup>[12]</sup> The spectrum acquired under non-resonant conditions shows peaks at 489, 542, 584, and 621 nm; under resonant excitation, the same emission features were detected but the one at 489 nm, as it is close to the excitation wavelength. These emission bands are a consequence of the intra-4f electronic radiative transitions within Tb<sup>3+</sup> ions (<sup>5</sup>D<sub>4</sub> → <sup>7</sup>F<sub>J</sub>, with J = 6, 5, 4, and 3).<sup>[7,12]</sup>

Similar emission to the PL one was obtained when performing CL measurements by exciting the sample with an electron

beam of 2 keV, which allows an effective direct excitation of the Tb species by impact excitation. Figure 3 shows the emission spectrum collected with the characteristic peaks of Tb<sup>3+</sup> at 489, 544, 587, and 624 nm. These emission bands correspond to the <sup>5</sup>D<sub>4</sub> → <sup>7</sup>F<sub>J</sub> transitions as previously described. Blue emission bands also appear in the CL spectrum, corresponding to <sup>5</sup>D<sub>3</sub> → <sup>7</sup>F<sub>J</sub> (J = 5 and 4) transitions, with peaks at 415 and 437 nm. All these results are in good agreement with others found in the literature (see Ref. [21]).

The most intense emission at 544 nm in both PL and CL spectra corresponds to the green visible range, and it is split into two peaks, as a consequence of the Stark effect due to the local electric field.<sup>[7]</sup> These results evidence that the employed deposition technique and methodology, that takes advantage of the nanomultilayered deposition of different materials, produce optically active Tb<sup>3+</sup> species, emitting in the green spectral region.

The electrical properties of the fabricated devices were analyzed by acquiring the I(V) curves, grounding the Al bottom electrode through the chuck whereas the ITO contact on top was swept in two regimes: accumulation (negative bias) and inversion (positive bias). The obtained curves for each regime

**Table 1.** XPS evaluated atomic compositions for the Tb/SiO<sub>2</sub> and Al/Tb/Al/SiO<sub>2</sub> NMLs.

	Atomic content (%)			
	Si	O	Tb	Al
Tb/SiO <sub>2</sub>	33	65	2	–
Al/Tb/Al/SiO <sub>2</sub>	24	65	1	10

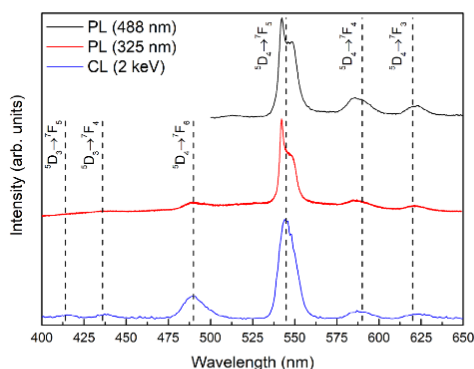


**Figure 3.** Normalized PL and CL measurements of the Al/Tb/Al/SiO<sub>2</sub> structure.

are displayed in Figure 4. The devices can reach intensities in the order of  $10^2 \mu\text{A}$  at  $-15 \text{ V}$  applied voltage. Higher voltages were not sustained by the ITO contacts as the current increased to mA. The curves show an almost symmetric behavior for both regimes, indicating non-rectifying characteristics.

As shown by structural characterization, the device is composed by layers of  $\text{SiO}_2$  and  $\text{Al}_2\text{O}_3$ , for which an insulating behavior, that is, limited movement of charges, is expected. Thus, considering the different transport mechanisms taking place in dielectric materials, we have assessed the electrical conduction of our devices. We found that the best agreement to the experimental data was obtained when considering an electrode-limited conduction mechanism based on Schottky emission. Thermionic emission of electrons is achieved when a potential barrier formed at a metal-insulator (or semiconductor-insulator) interface is overcome. Applying an external electric field the barrier can be lowered, easing the emission. This process can be modeled as:

$$J_{\text{Schottky}} = \frac{4\pi m^* q k_B^2 T^2}{h^3} \exp\left(-\frac{\varphi_b}{k_B T}\right) \exp\left(\frac{\beta}{k_B T} E^{1/2}\right), \quad (1)$$

where  $\varphi_b$  is the potential barrier height in (eV),  $q$  the elementary charge,  $E$  the applied electric field,  $k_B T$  the thermal energy,  $h$  the Planck's constant,  $m^*$  the effective mass of electrons, and  $\beta$  is defined as:

$$\beta = \sqrt{\frac{q^3}{4\pi\epsilon_0\epsilon_r}}, \quad (2)$$

where  $\epsilon_0$  and  $\epsilon_r$  are the absolute and relative permittivity, respectively.<sup>[22]</sup>

The fitting of the experimental  $I(V)$  curve to the Schottky emission model yields a relative dielectric constant of the dielectric layer of  $\epsilon_r = 18.86$ . However, in general, the obtained

permittivity value may differ from the experimentally determined values by means of other optical techniques, due to the heterogeneity of our samples. Actually, Poole–Frenkel mechanism is also in good agreement to the experimental data, however with a large dielectric constant ( $\epsilon_r > 300$ ). The presence of Al in the structure is the probable cause for the Schottky emission fitting best the data, because electrons must overcome the potential barrier generated by the  $\text{AlO}_x$  layers, as it has been previously reported.<sup>[23]</sup>

The  $I(V)$  characteristic of an identical device but without Al (Tb/SiO<sub>2</sub> multilayers) has also been analyzed. In Figure 4(c) there is a comparison of the current evolution at different voltages for both kinds of devices, with and without Al. It is evident that similar currents can be achieved for both devices, with and without Al in them, which implies that Al is not strongly influencing the electrical characteristic. Nevertheless, the sample with Al is slightly more resistive than the one with no Al (at high voltages), which could be due to either an increase of the total thickness or the fact that Al layers are presumably fully oxidized and thus become insulating (as we stated before). Another interesting feature is the fact that the slope of the two curves is also slightly different. Checking the conduction mechanisms, both curves follow a Schottky emission model at large voltages, but with a different dielectric constant: the sample without Al presents a dielectric constant of about 8.8, almost half of the one with Al. Consequently, Al is only slightly modifying the  $I(V)$  characteristic. Actually, the electrical conduction through the  $\text{SiO}_2$  barriers should be identical for both devices, just being different through the Al/Tb/Al or Tb layers, which modifies the effective dielectric constant while keeping the conduction mechanism.

The application of an electrical current to the device can also produce the excitation of  $\text{Tb}^{3+}$  ions, which can be de-excited by emitting their excess of energy in the form of light. No emission (or very weak) was found for the devices with no Al, which is in good agreement with PL measurements (see Refs. [19] and [20]). The total integrated emission collected by the PMT is shown in Figure 5 (a) and 5(b) as a function of the applied voltage and current circulating through the device, respectively. We observed that the threshold voltage for emission to take place is  $8.5 \text{ V}$ , whereas higher voltages produce an almost exponential increase of the integrated EL. Looking at the behavior of the EL with the injected current, we observe that it increases linearly with a threshold current for emission at  $\approx 2 \mu\text{A}$ , which establishes a direct relation between impinging electrons and resulting emitted photons. Thus, the linearity of the EL with the injected current at high voltage and injection (i.e., above the excitation threshold) is suggesting that electrons with high kinetic energy are responsible for the excitation of the Tb optical centers. In fact, such electro-optical characteristics are typical of an excitation mechanism governed mainly by direct impact excitation; however, energy transfer mechanisms from the matrix can also be contributing.<sup>[22]</sup>

The spectral analysis of the EL is displayed in Figure 6. The spectra were acquired for 30 s, applying  $-100 \mu\text{A}$  at  $-18 \text{ V}$ , in the range of  $400\text{--}1100 \text{ nm}$ . The spectra exhibit peaks at  $437$ ,  $483$ ,  $531$ , and  $576 \text{ nm}$ , over a broad low-intensity background. Whereas the former features correspond to  $^3\text{D}_4 \rightarrow ^7\text{F}_j$  transitions (with  $j = 6, 5, 4$ , and  $3$ ) from  $\text{Tb}^{3+}$  ions, in good agreement to PL and CL measurements (see Figure 3), the latter band is probably

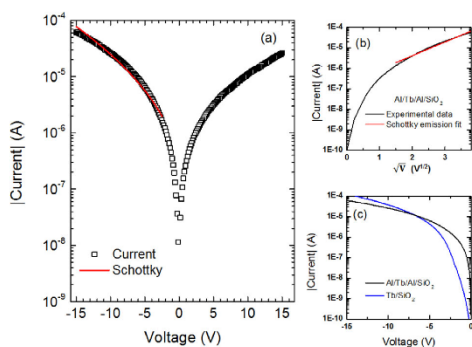


**Figure 4.** a)  $I(V)$  curve of a device containing Al/Tb/Al/SiO<sub>2</sub> multilayers, fit taking into account a Schottky-type conduction mechanism. b) Linearization for Schottky model in the range from  $-2.25$  to  $-15 \text{ V}$  for the device containing Al/Tb/Al/SiO<sub>2</sub> multilayers. c) Comparison of the  $I(V)$  curves of a devices containing Al/Tb/Al/SiO<sub>2</sub> and containing Tb/SiO<sub>2</sub> multilayers.

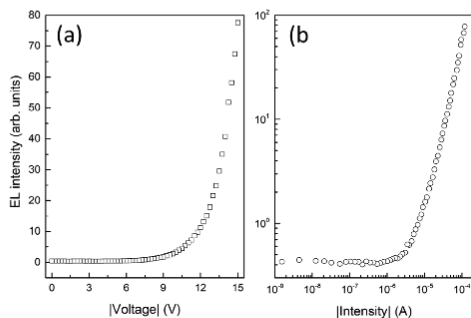


**Figure 5.** Integrated emission of the Al/Tb/Al/SiO<sub>2</sub> structure, obtained in accumulation, as a function of a) voltage and b) current, represented in absolute value.

originated in the deep defects in either the SiO<sub>2</sub> or the ITO contact.

Another interesting observation is the fact that there is an intensity reduction of the Tb emission at successive measurements, reaching total quenching of Tb emission beyond the fifth one (please see spectrum labeled as measurement #6 in Figure 6, where only the background contribution is observed). In order to study this effect, the time evolution of the EL and the applied voltage has been simultaneously monitored at a constant current, this time using a different (i.e., pristine) device (but virtually identical). The results of this particular device are presented in Figure 7. One can observe that the EL emission starts practically simultaneously with the current injection, within the employed time resolution (voltage also increases). Both EL and applied voltage remain constant for about 30 s, immediately after which there is a slight reduction in the voltage, together with a sudden reduction of the EL emission. For longer times, the device becomes even more conductive, inducing the total quenching of the device EL emission.

This EL quenching and voltage reduction could be related to some atomic rearrangement after high electron flux is injected.

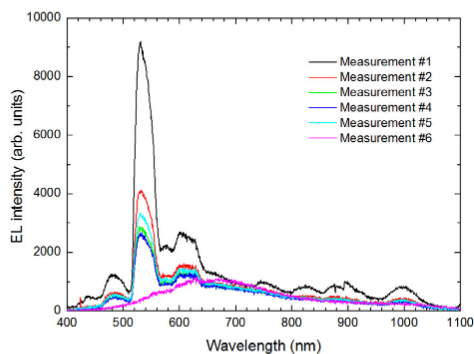


**Figure 6.** EL spectra successively acquired from the device at 100 μA and 30 s.

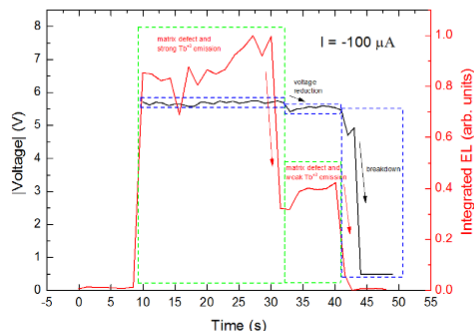


**Figure 7.** Evolution of voltage and EL as function of time for a device containing Al/Tb/Al/SiO<sub>2</sub> multilayers, at a constant current of 100 μA.

Indeed, it has been observed in oxide matrices that, under certain excitation conditions, a displacement of oxygen atoms takes place.<sup>[24,25]</sup> This, in turn, induces both the creation of alternative (oxygen vacancies-related) conduction paths and the probable reduction of Tb-O bonds, the latter reducing the concentration of optically active centers. In this frame, an increase of the thermal budget could improve the stability of the Tb<sub>2</sub>O<sub>3</sub> phase, making this material a potential candidate for future optoelectronics applications, in particular as integrated light-emitting devices.

#### 4. Conclusions

Al/Tb/Al/SiO<sub>2</sub> nanomultilayers have been fabricated by electron beam evaporation, alternatively depositing each layer. Optical characterization by means of PL and CL showed that Tb<sup>3+</sup> ions are optically active. Electrical characterization allowed inferring that the conduction mechanism governing the structure is a Schottky emission model, although thermal activated mechanisms cannot be discarded. The threshold voltage and current for EL to take place were determined by integrated EL measurement. As well, the spectral distribution of EL is related to a combination between Tb<sup>3+</sup> ions and matrix defect-related emission. The hereby presented results prove that the combination of electron beam evaporation and nanomultilayer structures are useful to obtain luminescent Al/Tb/Al/SiO<sub>2</sub> light-emitting systems.

#### Acknowledgements

This work was financially supported by the Spanish Ministry of Economy and Competitiveness (TEC2016-76849-C2-1-R and MAT2015-71035-R). O.B. also acknowledges the subprogram "Ayudas para Contratos Predoctorales para la Formación de Doctores" from the Spanish Ministry of Economy and Competitiveness for economical support.

#### Conflict of Interest

The authors declare no conflict of interest.

## Keywords

electron beam evaporation, luminescence, nanomultilayers, rare earth ions, terbium

Received: June 30, 2017

Revised: September 1, 2017

Published online:

- 
- [1] Efficient blue light-emitting diodes leading to bright and energy-saving white light sources, The Nobel Prize in Physics 2014 – Advanced Information, [online], Nobel Media AB, Available: [http://www.nobelprize.org/nobel\\_prizes/physics/laureates/2014/advanced.html](http://www.nobelprize.org/nobel_prizes/physics/laureates/2014/advanced.html), 2014; Accessed: 10/06/2017.
- [2] K. D. Hirschman, L. Tsybeskov, S. P. Duttagupta, P. Fauchet, *Nature* **1996**, *384*, 338.
- [3] G. T. Reed, G. Mashanovich, F. Y. Gardes, D. J. Thomson, *Nat. Photonics* **2010**, *4*, 518.
- [4] S. Yerci, R. Li, L. Dal Negro, *App. Phys. Lett.* **2010**, *97*, 081109.
- [5] A. J. Kenyon, *Prog. Quantum Electron.* **2002**, *26*, 225.
- [6] S. Jiang (Ed.), Proceedings of the SPIE VII Conference on Rare-Earth Doped Materials and Devices, 4990, **2003**.
- [7] J. Li, O. H. Zalloum, T. Roschuk, C. L. Heng, J. Wojcik, P. Mascher, *Adv. Opt. Technol.* **2008**, Article ID 295601.
- [8] A. J. Kenyon, P. F. Trwoga, M. Federighi, C. W. Pitt, *J. Phys.: Condens. Matter* **1994**, *6*, L319.
- [9] J. M. Ramírez, Y. Berencén, L. López-Conesa, J. M. Rebled, F. Peiró, B. Garrido, *Appl. Phys. Lett.* **2013**, *103*, 081102.
- [10] Y. Berencén, R. Wutzler, L. Rebohle, D. Hiller, J. M. Ramírez, J. A. Rodríguez, W. Skorupa, B. Garrido, *Appl. Phys. Lett.* **2013**, *103*, 111102.
- [11] S. Boninelli, G. Bellocchi, G. Franzò, M. Miritello, F. Iacona, *J. Appl. Phys.* **2013**, *113*, 143503.
- [12] H. Jeong, S.-Y. Seo, J.-H. Shin, *Appl. Phys. Lett.* **2006**, *88*, 161910.
- [13] A. J. Silversmith, D. M. Boye, K. S. Brewer, C. E. Gillespie, Y. Lu, D. L. Campbell, *J. Lumin.* **2006**, *121*, 14.
- [14] P. Ruterana, M. P. Chauvat, K. Lorenz, *Semicond. Sci. Technol.* **2015**, *30*, 044004.
- [15] J. L. Deschanvres, W. Meffre, J. C. Joubert, J. P. Senateur, F. Robaut, J. E. Broquin, R. Rimet, *J. Alloys Compd.* **1998**, *275*, 742.
- [16] T. Minami, T. Yamamoto, T. Miyata, *Thin Solid Films* **2000**, *366*, 63.
- [17] X. P. Zhao, J. B. Yin, *Chem. Mat.* **2002**, *14*, 2258.
- [18] L. Norin, E. Vanin, P. Soininen, M. Putkonen, in Conference on Lasers and Electro-Optics, Optical Society of America, May **2007**.
- [19] O. Blázquez, J. M. Ramírez, J. López-Vidrier, Y. Berencén, S. Hernández, P. Sanchis, B. Garrido, in SPIE Microtechnologies, pp. 95200K-95200 K, International Society for Optics and Photonics, June **2015**.
- [20] O. Blázquez, J. López-Vidrier, L. López-Conesa, M. Busquets-Masó, S. Estradé, F. Peiró, S. Hernández, B. Garrido, *J. Appl. Phys.* **2016**, *120*, 135302.
- [21] H. S. Ahmed, O. M. Ntwaeaborwa, M. A. Gusowski, J. R. Botha, R. E. Kroon, *Physica B: Condensed Matter* **2012**, *407*, 1653.
- [22] J. M. Ramírez, Ph.D. thesis, Dept. d'Electrònica, University de Barcelona, Barcelona, Spain, June **2015**.
- [23] C. J. Li, S. J. J. J. Chen, *Jap. J. App. Phys.* **2011**, *50*, 01BC08.
- [24] I. Valov, *ChemElectroChem* **2014**, *1*, 26.
- [25] E. W. Lim, R. Ismail, *Electronics* **2015**, *4*, 586.

### 4.2.1. Effect of Tb-doping on resistive switching

Following the conclusion of the previous work, the resistive switching properties shown by the devices were also analyzed. By comparing the cycling of Al/SiO<sub>2</sub> and Al/Tb/Al/SiO<sub>2</sub> layers, the study focused on the effect of the Tb doping. The suggested hypothesis was that the Tb ions present in the sample could reduce the movement of O ions during the cycling, retaining them in the active layer instead of them being lost, and consequently leaving the device in a permanent LRS. Indeed, a small increase in the endurance of the devices was observed for the devices containing RE ions. Nevertheless, none of them surpassed 50 RS cycles, which is a very minimal requirement for potential memories.

It was observed that the presence of Tb in the sample had three main effects (see Figure 4.5): (i) an accumulation of charge appears in cycles of the sample containing Tb, (ii) Tb<sub>x</sub>O<sub>y</sub> clusters slowly release oxygen during the reset, giving rise to a step-like process in which these clusters are continuously reduced and oxidized, and (iii) the diffusion length of O<sup>2-</sup> ions is reduced with the presence of Tb<sub>x</sub>O<sub>y</sub> clusters, meaning that a lower set voltage is required. Overall, an increase of two orders of magnitude in the resistance ratio between states was achieved in the sample containing Tb.

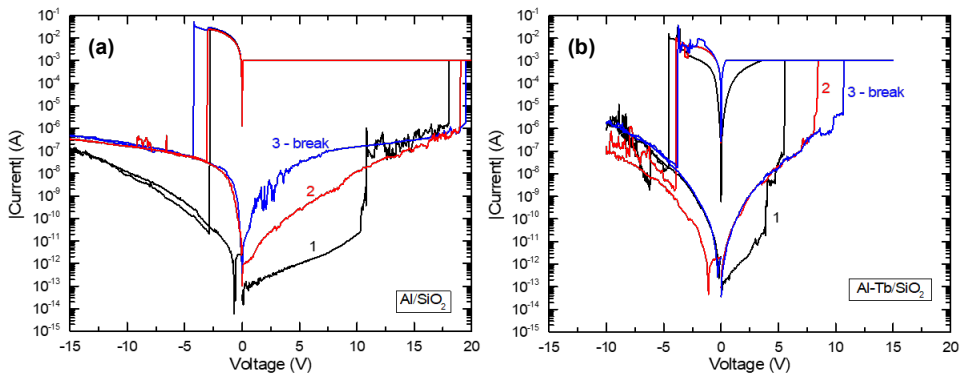


**Figure 4.5.**  $I(V)$  curves corresponding to resistive switching of (a) Al/SiO<sub>2</sub> and (b) Al-Tb/SiO<sub>2</sub> samples. Three different cycles are plotted and numbered, where labels 1 and 2 correspond to forming cycles (black and red, respectively), and label 3 (blue) states for a representative cycle for the rest of the measured  $I(V)$  curves until breakdown.

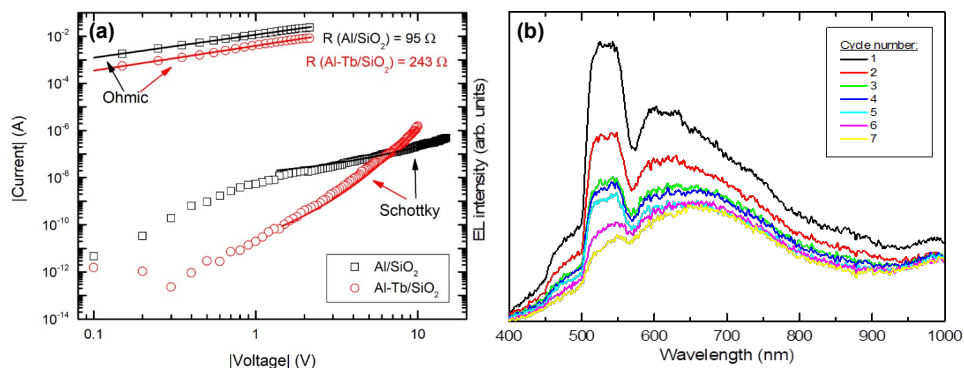


**Figure 4.6.** (a)  $I(V)$  curves in LRS and HRS from both Al/SiO<sub>2</sub> and Al-Tb/SiO<sub>2</sub> NMLs, with the corresponding fittings of the conduction mechanisms. (b) Electroluminescence of Al-Tb/SiO<sub>2</sub> samples measured between RS cycles in HRS. The reduction of intensity with each cycle suggests the formation of stronger CFs.

Further analysis of the behavior of the devices is presented in Figure 4.6, from where conclusions can be extracted. The conduction mechanisms for each state and device were also studied, finding a clear ohmic conduction governed the LRS in all cases, suggesting that CFs are formed by conductive Al and Si. In contrast, HRS seems governed by Schottky emission in both devices despite their difference in conductivity. This observation can be directly related to the presence of broken filaments in the sample, which act as tips for thermionic emission. It was also corroborated that the previously observed reduction in emission intensity also took place between RS cycles, which supports the previously explained theory of dielectric breakdown due to oxygen vacancies.

This work on the resistive switching properties of Al/SiO<sub>2</sub> devices doped with Tb was presented as a poster in the European Materials Research Society (EMRS) Spring Meeting 2018.

### 4.2.2. Replacement of Tb with Eu for red emission

Last, as part of the objective of obtaining an RGB light emitting device structure, a first attempt at the fabrication of Eu-based light emitting devices was made. A multilayer stack of SiO<sub>2</sub> and Eu layers following the *delta doping* approach was deposited via electron beam evaporation. The stack showed photoluminescence emission shown in Figure 4.7 corresponding to the expected electronic transitions of Eu<sup>3+</sup>, improving with the annealing temperature up to 700 °C where up to 5 transitions were visible. The emission from this element exhibited a more intense background emission when compared to Tb, which can be attributed not only to SiO<sub>2</sub> defects but also to the formation of EuO. Nevertheless, this is a good starting point towards the obtention of red-emitting rare earth-doped SiO<sub>2</sub> devices.

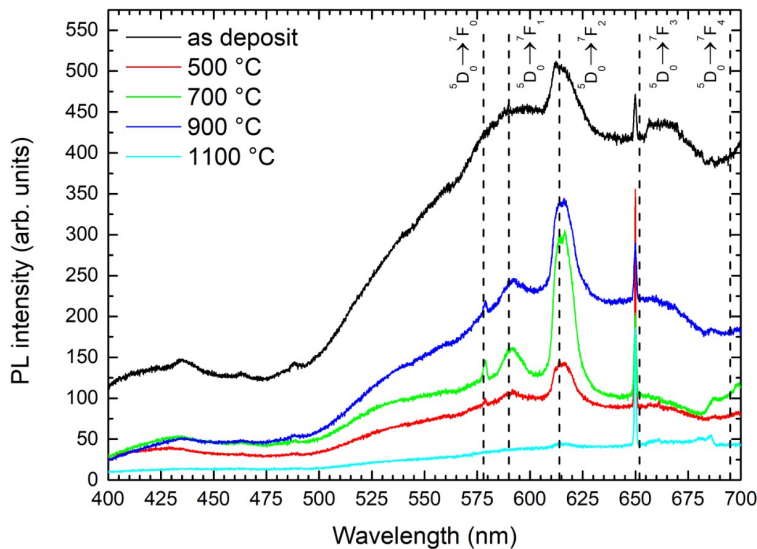


**Figure 4.7.** Photoluminescence of Eu/SiO<sub>2</sub> samples measured under 325-nm laser excitation. The study of different annealing temperatures yields 700 °C as the optimum one for enhanced Eu<sup>3+</sup> emission and reduced background emission from defects.

### References

- [1] J. Zhang, H. Feng, W. Hao, T. Wang, *Materials Science and Engineering: A* **425**, 346, 2006.
- [2] Y. Terai, K. Yamaoka, K. Yoshida, T. Tsuji, Y. Fujiwara, *Physica E: Low-dimensional Systems and Nanostructures* **42**, 2834, 2010.

- [3] C. Davesne, A. Ziani, C. Labbé, P. Marie, C. Frilay, X. Portier, *Thin Solid Films* **553**, 33, 2014.
- [4] K. Tanaka, S. Okamoto, *Applied Physics Letters* **85**, 923, 2004.
- [5] A. J. Kenyon, *Progress in Quantum Electronics* **26**, 225, 2002.
- [6] O. Blázquez, J. López-Vidrier, L. López-Conesa, M. Busquets-Masó, S. Estradé, F. Peiró, S. Hernández, B. Garrido, *Journal of Applied Physics* **120**, 135302, 2016.
- [7] G. Franzò, S. Coffa, F. Priolo, C. Spinella, *Journal of Applied Physics* **81**, 2784, 1998.
- [8] S. Bachir, J. C. Ronfard-Haret, K. Azuma, D. Kouyaté, J. Kossanyi, *Chemical Physics Letters* **213**, 54, 1993.

# Resistive switching of ZnO

---

Once light emitting devices have been studied, the next step is to analyze how resistive switching devices operate. These devices are composed of a simple MIM or MOS structure in which the intermediate layer can change its resistance via electrical operation. As a demonstrator, an ITO/ZnO/*p*-Si structure has been studied, aiming at a latter possible doping process with rare earth ions for combined electroluminescence emission.

Zinc oxide is presented as a good candidate for resistive switching due to it being an oxide highly defective when deposited by many different processes. Under these conditions, the possibility of creating a network of oxygen ions that are free to diffuse through the layer, leaving behind vacancy-based conductive filaments, is enhanced.

## 5.1. Resistive switching properties of ITO/ZnO/*p*-Si

In addition to the above mentioned, the selection of ZnO as the active layer enables the creation of transparent devices, using a non-toxic and abundant material that has been explored for many other applications. As well, ITO has been selected as the top contact for being the most employed material as a transparent conductive oxide and because its composition avoids the diffusion of metals from the electrode to the active layer, which can occur with metallic electrodes.<sup>[1]</sup> If this were to happen, a combination of the valence change and electrochemical metallization mechanisms would probably take place, making the modelling of the results very difficult and speculative. In addition, ITO acts as a reservoir of oxygen, enhancing the cycling endurance.<sup>[2]</sup>

Taking all of this into account, the fabricated devices consisted of 60 nm of ZnO deposited via RF magnetron sputtering on top of *p*-Si wafers. An annealing process at 450 °C in Ar atmosphere was carried out for 1 h, and afterwards the ITO top electrodes were deposited using photolithography patterning and electron beam evaporation, and

## Resistive switching of ZnO

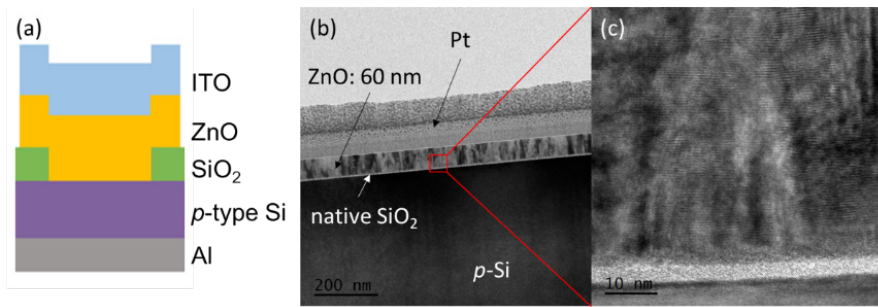


**Figure 5.1.** (a) Device structure for the ITO/ZnO/p-Si devices under study. (b) Cross section TEM image identifying the layers. (c) Zoom-in at the ZnO region, evidencing the polycrystalline nature of the layer.

treated again at 200 °C for 1 h in air. The bottom of the Si wafers was metallized with Al, forming a common bottom ground contact for all devices. The structure was analyzed via TEM imaging, included in Figure 5.1, finding that ZnO had a polycrystalline structure and that a native thin SiO<sub>2</sub> layer remained at the interface with the Si wafer. Through EDX, the composition of ZnO was found to contain 46 at.% of O and 54 at.% of Zn, being thus the layer defective in O as expected. This gives the film a characteristic *n*-type intrinsic doping.

Raman analysis of the devices further demonstrates the high crystallinity of the ZnO layer. As seen in Figure 5.2, up to fifth order of the A<sub>1</sub> (LO) mode at 573 cm<sup>-1</sup> can be seen.<sup>[3]</sup> In addition, analysis of highly stressed ZnO RS devices shows that the high crystallinity is maintained and only above the third order the intensity slightly decays, owing to a modification of the structure of nanosized dimensions.

These devices require an electroforming step to break the active ZnO layer for the first time and create the CFs for the RS cycling. For this process, an *I*(*V*) curve up to ~13 V is required, together with a current compliance of 5 mA. This creates a set of strong CFs throughout the device, allowing for successive cycling in a voltage range of ±1 V, with no needed compliance and with set and reset processes taking place at 0.4 and -0.4 V, respectively. A total of 100 uninterrupted cycles were performed under these conditions, exhibiting 5 orders of magnitude of resistance difference between the two resistance states.

After corroborating the operability of the devices, an endurance test was carried out. Using voltage pulses, a routine of set, read, reset and read operations was set up using 2, -0.2, -1 and -0.2 V, respectively. The device withstood a total of 1000 continuous cycles under these conditions, showing only 5 switching errors and a high stability of the states reached.

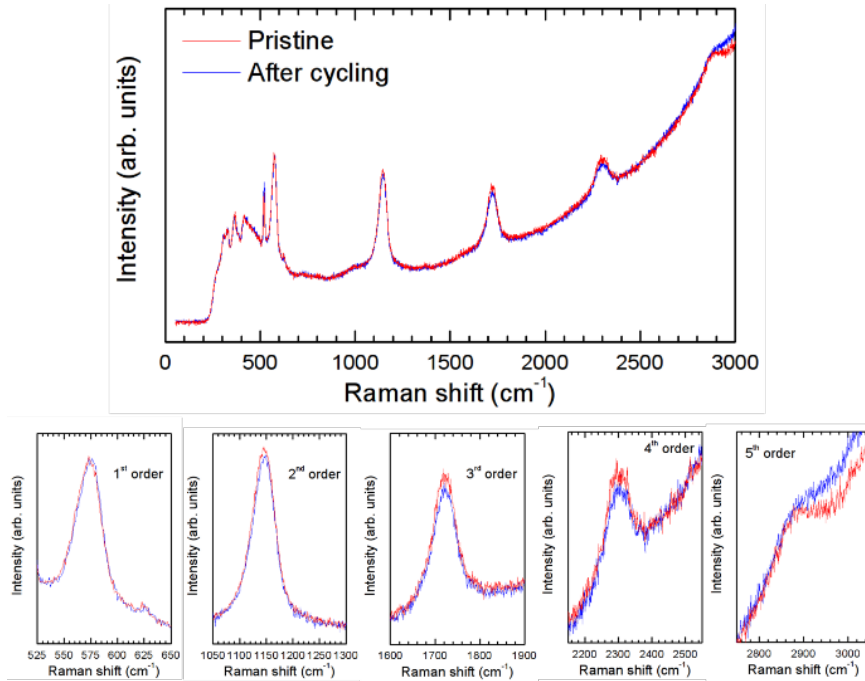


**Figure 5.2.** Raman analysis of a pristine and a RS cycled device. The  $A_1$  (LO) mode is detected up to the fifth order and intensity is only slightly lower for the stressed devices.

Last, a modelling of the resistive switching mechanism was performed analyzing the charge transport at each state. In the pristine state, no CFs are present in the active layer and thus the ZnO behaves as a low conductive semiconductor, being the conduction possible through tunneling processes between traps (TAT). In the LRS with CFs completely formed, a space charge-limited conduction (SCLC) can be clearly identified. Finally, in HRS, with part of the CFs dissolved, the ZnO acts once again as a barrier, resulting in a TAT process that evolves to a Fowler-Nordheim (FN) tunneling at higher voltages.

Under these conditions, and assuming that the part of the filaments that are re-oxidized in the HRS recover the composition of the pristine film, different parameters were calculated. First, using the pristine and LRS mechanisms, it was determined that conduction in the LRS takes place only in an equivalent area of  $1.4 \times 10^{-10} \text{ cm}^2$ , very low when compared to the total device area of  $2.1 \times 10^{-3} \text{ cm}^2$  defined by the top ITO contact. With CFs in ZnO devices typically having a diameter between 10 and 50 nm,<sup>[4]</sup> around 20 different paths are forming the network of CFs. Secondly, the trap-assisted tunneling presented in both the pristine and HRS states can be employed to first calculate the energy of the traps and then estimate the thickness of the ZnO gap, that is, the

length of the CFs re-oxidated in the reset process, resulting in 9 nm. This is in good accordance with the total thickness of the active layer, the increased conductivity of the HRS compared to the pristine state, and the possibility of FN tunneling when in HRS. This analysis was extended to a large number of cycles and devices. As shown in Figure 5.3, 92 % of HRS curves are very similar and the analysis of their CF gap corresponds to the  $9 \pm 1$  nm size obtained. Overall, this study clearly suggests that ZnO is a great candidate for high-endurance resistive switching devices.

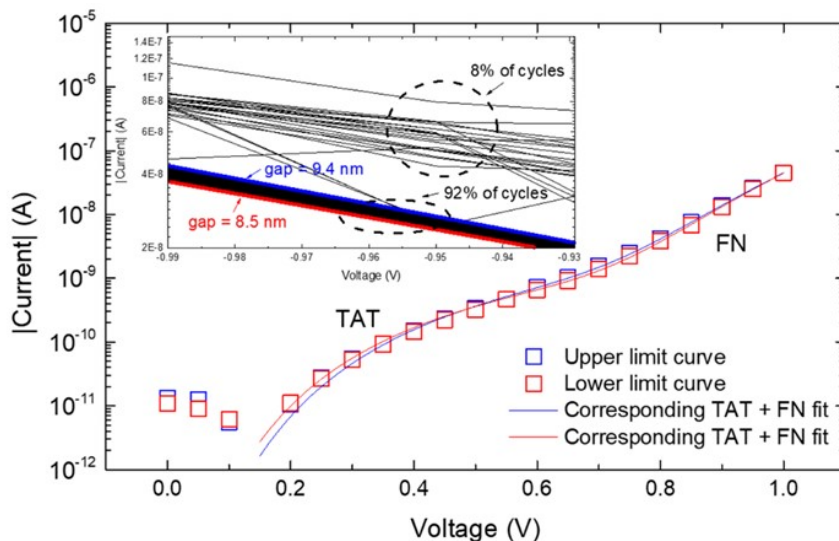


**Figure 5.3.** Reliability of ZnO RS devices. Inset shows HRS curves from different cycles and devices, concluding that 92 % of them lie within the upper and lower limits set.

This work was presented as a talk in the European Materials Research Society (EMRS) Spring Meeting 2018. A journal article was published in *Applied Surface Science* **556**, 149754 (2021).

**Paper IV: Resistive switching and charge transport mechanisms in ITO/ZnO/p-Si devices (DOI: [10.1063/1.5046911](https://doi.org/10.1063/1.5046911))**



## Resistive switching and charge transport mechanisms in ITO/ZnO/p-Si devices

O. Blázquez,<sup>1,2,a)</sup> J. L. Frieiro,<sup>1,2</sup> J. López-Vidrier,<sup>3</sup> C. Guillaume,<sup>4</sup> X. Portier,<sup>4</sup> C. Labbé,<sup>4</sup> P. Sanchis,<sup>5</sup> S. Hernández,<sup>1,2</sup> and B. Garrido<sup>1,2</sup>

<sup>1</sup>MIND, Department of Electronics and Biomedical Engineering, Universitat de Barcelona, Martí i Franquès 1, E-08028 Barcelona, Spain

<sup>2</sup>Institute of Nanoscience and Nanotechnology (IN2UB), Universitat de Barcelona, Av. Joan XXIII S/N, E-08028 Barcelona, Spain

<sup>3</sup>Laboratory of Nanotechnology, Department of Microsystems Engineering (IMTEK), Albert-Ludwigs-Universität Freiburg, Georges-Köhler-Allee 103, D-79110 Freiburg, Germany

<sup>4</sup>CIMAP Normandie Univ, ENSICAEN, UNICAEN, CEA, CNRS, 14050 Caen, France

<sup>5</sup>Nanophotonics Technology Center, Universitat Politècnica de València, Camino de Vera s/n, E-46022 Valencia, Spain

(Received 3 July 2018; accepted 14 October 2018; published online 29 October 2018)

The resistive switching properties of ITO/ZnO/p-Si devices have been studied, which present well-defined resistance states with more than five orders of magnitude difference in current. Both the high resistance state (HRS) and the low resistance state (LRS) were induced by either sweeping or pulsing the voltage, observing some differences in the HRS. Finally, the charge transport mechanisms dominating the pristine, HRS, and LRS states have been analyzed in depth, and the obtained structural parameters suggest a partial re-oxidation of the conductive nanofilaments and a reduction of the effective conductive area. *Published by AIP Publishing.* <https://doi.org/10.1063/1.5046911>

The poor energy efficiency of CMOS transistors and the fast scaling in memories are considered a serious drawback within the new era of big data and Internet of Things, which leads to the search of a new generation of ultra-low power nanodevices to overcome this important challenge that the electronics industry faces. Resistive switching (RS) memories or resistance random access memories (ReRAMs) have become a solution for the next generation of nonvolatile memories thanks to their low-power operation, high switching speed, and compatibility with the CMOS technology.<sup>1–4</sup> In these devices, the switching between the low resistance state (LRS) and the high resistance state (HRS), when an external electric field is applied, is due to either ionic movement leading to atomic rearrangement inside the active layer (valence change mechanism, VCM) or metallic diffusion from the electrode (electro-chemical metallization, ECM), thus inducing the formation and destruction of conductive nanofilaments (CNFs).<sup>5,6</sup> Different oxide compounds have been explored, such as TiO<sub>2</sub>, HfO<sub>2</sub>, SnO<sub>2</sub>, or ZnO, which have demonstrated promising results.<sup>7–12</sup> Among these metal oxides, ZnO has long attracted a great deal of attention because of its abundance and non-toxicity, giving rise to special interest also in gas sensing<sup>13,14</sup> or as a transparent conductive oxide (TCO) in light-emitting and photovoltaic devices. Hence, this broad range of applications of ZnO makes it a potential candidate for the field of transparent ReRAM devices.

Here, we report on the RS properties of sputtered ZnO within an indium tin oxide (ITO)/ZnO/p-Si device configuration. The selection of ITO as the top contact also provides advantages over the control of the switching mechanisms, as no metal diffusion from the electrodes should occur.<sup>15–18</sup> More than five orders of magnitude difference in current has been

observed between LRS and HRS, with stable switching, taking place at low voltages ( $\pm 1$  V) and with free current compliance. A cycling endurance beyond 1000 cycles has been demonstrated using pulse trains for performing the reading and the changes between the two resistance states. Finally, the obtained results are explained according to the charge transport mechanisms underlying the three different conduction states (pristine, LRS, and HRS), which sheds light on the CNF formation and destruction processes within ZnO. Whilst other publications only perform a fitting of the experimental data using different conduction models but without discussing the extracted physical parameters,<sup>19–21</sup> the hereby presented extended analysis of the  $I(V)$  curves of our devices allowed for the determination of structural parameters related to RS, such as the effective conductive area in LRS and the filament gap in HRS. The determination of these parameters has previously been carried out directly by transmission electron microscopy (TEM) techniques.<sup>22–24</sup> However, *in-situ* and *ex-situ* observation of the creation of those conductive paths and their interruption is a complex procedure, as well as the fact that sample preparation and/or the observation itself may modify the local structure.

Devices consisting of ITO/ZnO/p-type Si have been fabricated using a metal-oxide-semiconductor (MOS) configuration. For the oxide region, a 60-nm-thick layer was deposited on a *p*-type (100)-oriented silicon substrate by means of a 4-inch radiofrequency magnetron sputtering system from a pure ZnO target, using a power density value of 0.97 W cm<sup>-2</sup>, a 15  $\mu$ bar Ar pressure, and a substrate temperature of 400 °C. An annealing process at 450 °C for 1 h was carried out in a conventional furnace and under an Ar atmosphere. The top contact was achieved by deposition of ITO by electron-beam evaporation with subsequent annealing at 200 °C in air for 1 h. By using photolithography, devices with an effective area of 460  $\times$  460  $\mu$ m<sup>2</sup> were fabricated. A sketch of the device structure is presented in Fig. 1(a) with the different materials that

<sup>a)</sup>Author to whom correspondence should be addressed: oblazquez@el.ub.edu

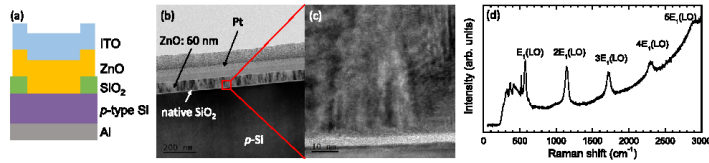


FIG. 1. (a) Sketch of the ZnO-based devices under study in this work. (b) TEM image of the deposited ZnO active layer, where the thickness of the layer can be measured to be  $\sim 60$  nm. (c) Zoom-in of the red-squared region in (b), where the polycrystalline nature of the layer can be identified. (d) Raman spectrum of a pristine device with the  $E_1(\text{LO})$  vibrational mode of ZnO and its overtones up to the 5<sup>th</sup> order, demonstrating its high crystalline quality.

compose each labelled layer. Energy-dispersive X-ray (EDX) analyses were performed on a  $2\text{-}\mu\text{m}$ -thick ZnO film grown with the same conditions than those used for the active layer presented, by employing an OXFORD Instruments equipment monitored with the INCA software and installed on a JEOL 6400 SEM microscope operating at 20 kV. Raman measurements were done at room temperature using a Horiba Jobin Yvon LabRam spectrometer, exciting the sample with the 325-nm line of a He-Cd laser. The electric characterization of the MOS devices was performed by means of an Agilent B1500 semiconductor device analyzer.

The ZnO active layer of the hereby presented resistive switching device has been characterized through diverse techniques. The TEM images of the ZnO layer are presented in Figs. 1(b) and 1(c). As it can be seen in Fig. 1(b), the ZnO active layer, deposited on top of the Si substrate, presents a thickness of  $\sim 60$  nm. A native  $\text{SiO}_2$  thin layer can be seen at the interface with the Si substrate. Pt layers were deposited via focused ion beam (FIB) to prepare the sample for TEM. The polycrystalline nature of the ZnO active layer can be easily identified in Fig. 1(c). The composition of the ZnO active layer has been analyzed by means of EDX, resulting in 46 at.% O and 54 at.% Zn, thus containing an expected oxygen deficiency due to the sputtering technique. A further analysis of the crystalline state of the ZnO layer has been carried out by means of Raman spectroscopy under near resonant conditions. In Fig. 1(d), it is displayed the spectra corresponding to a pristine device, where the  $E_1(\text{LO})$  mode is shown up to the fifth order; this, together with a low value of the half-width at half-maximum of  $\sim 13.7\text{ cm}^{-1}$  for the first peak, implies a high crystalline quality.<sup>25,26</sup>

The  $I(V)$  characteristics of the devices were studied by applying a voltage on the top electrode while grounding the bottom contact, sweeping the voltage from  $V = -1\text{ V}$  to  $V = +1\text{ V}$ , thus performing RS cycles. In Fig. 2(a), we show a representative  $I(V)$  curve out of more than 100 cycles, where the change from LRS to HRS is achieved at negative voltages, while the reverse change takes place at positive ones. Prior to it, an electroforming process was carried out by applying a positive ramp voltage and setting a current compliance at 5 mA. The voltage at which this electroforming process takes place lies around 12.5 V, leading the device to the LRS, as shown in the inset of Fig. 2(a). This state exhibits a much higher current than the pristine state, but without the need for using a limiting current compliance of the measuring system considering the explored range of voltages ( $\pm 1\text{ V}$ ): this state can thus be considered as a self-compliant LRS. The following step consists in applying a negative ramp voltage until

$-1\text{ V}$  in order to switch from LRS to HRS, leading to a considerable reduction in the current passing through the device, but being larger than the one observed in the pristine state. After applying another voltage sweep up to 1 V, the LRS state is again recovered. In this cycle, the *set* and *reset* processes occur around  $+0.4\text{ V}$  and  $-0.4\text{ V}$ , respectively.

At this point, the device was submitted to 100 consecutive self-compliant cycles by means of positive and negative ramp voltages in the range from  $-1\text{ V}$  to  $+1\text{ V}$  for *set* and *reset* steps, respectively [see the inset of Fig. 2(a)]. A current contrast of more than 5 orders of magnitude is observed between both states at a read voltage of  $V_{\text{read}} = -0.2\text{ V}$  (LRS is plotted in blue, HRS in red). In order to analyze better these parameters along the 100 cycles, Fig. 2(b) shows the cumulative probability of the currents at  $V_{\text{read}}$  for HRS and LRS. This plot confirms that both states are well defined and stable, with mean current values of  $\sim 10^{-11}\text{ A}$  and  $\sim 2 \times 10^{-6}\text{ A}$

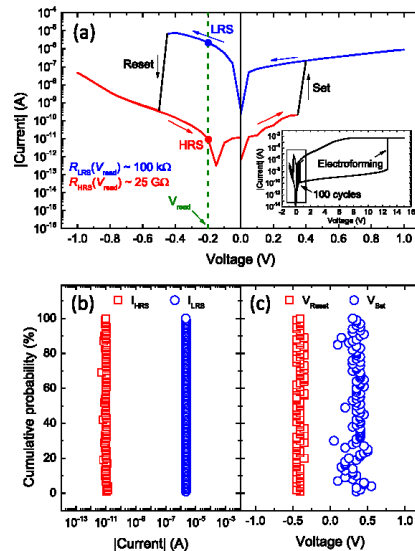


FIG. 2. (a)  $I(V)$  characteristics of one RS cycle, where the voltage sweep direction of each cycle is indicated by arrows. HRS and LRS are colored in red and blue, respectively, whereas the *set* and *reset* processes are displayed in black. The vertical green dashed line indicates the read voltage ( $V_{\text{read}}$ ) where the current is analyzed. In the inset, the electroforming process is shown, followed by the 100 cycles, as a reference scale. (b) and (c) represent the cumulative probability of the HRS and LRS currents at  $V_{\text{read}}$ , and the cumulative probability of the  $V_{\text{set}}$  and  $V_{\text{reset}}$ , respectively, averaged over the 100 cycles.

A for HRS and LRS, respectively. The cumulative probabilities of the switching voltages between both states ( $V_{\text{set}}$  and  $V_{\text{reset}}$ ) are shown in Fig. 2(c), which shows a clear variation between  $V_{\text{set}} = +0.1$  V and  $+0.6$  V (though always a positive voltage well below 1 V is required), whereas  $V_{\text{reset}}$  presents a small variation always taking negative values between  $-0.4$  V and  $-0.5$  V.

Taking into account the maximum  $V_{\text{set}}$  and  $V_{\text{reset}}$  values observed along the 100 cycles (in absolute value), the device was submitted to a specific pulse-voltage pattern, as shown in Fig. 3(a). In brief, the first pulse forces the *set* by applying  $+2$  V, followed by a second pulse at  $V_{\text{read}} = -0.2$  V to read the current of the LRS. The third pulse, at  $-1$  V, induces the *reset* towards HRS. Finally, the current at  $V_{\text{read}} = -0.2$  V is again monitored within this state. The duration of the *set* and *reset* pulses was kept at 50 ms, long enough to promote switching, as observed experimentally; on the contrary, reading times were set to a much faster value, 0.1 ms, limited by the experimental setup. The device presented an endurance of more than 1000 periods with 99.5% of success, whose cumulative probability is presented in Fig. 3(b). In this case, LRS presents the same current values than the observed ones when the device was submitted to voltage ramps via  $I(V)$  curves [see Fig. 2(b)], taking values centered again around  $\sim 2 \times 10^{-6}$  A. This confirms that the LRS is well defined under both excitation conditions. In contrast, HRS presents a larger current than the one obtained using  $I(V)$  curves. Whereas voltage ramps induced stable current intensity around  $\sim 10^{-11}$  A, pulse excitation increases the current intensity up to  $\sim 10^{-9}$  A. This difference in the current values within the HRS could be related to the short duration of the pulse during the *reset* process, which affects the atomic arrangement, as suggested by Marchewka *et al.* in TaO<sub>x</sub>-based ReRAMs.<sup>27</sup>

In order to shed light on the physics underlying the memristive behavior of the ZnO-based device under study, the charge transport mechanisms governing the different states (pristine, HRS and LRS) were determined in the substrate accumulation regime ( $V < 0$  range). Figure 4(a) presents the isolated  $I(V)$  curves corresponding to each of

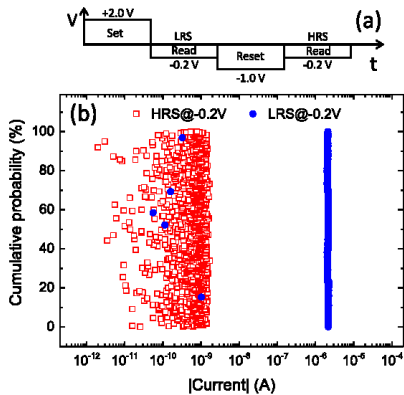


FIG. 3. (a) Scheme of the pulse-voltage pattern employed in the study. (b) Cumulative probability plot of HRS and LRS currents at  $V_{\text{read}}$  under the pulse schematics in (a), after more than 1000 periods.

these three states for the most representative cycle in Fig. 2(a), in the log-log representation. The three states present differentiated trends: the current intensity in the LRS exhibits a polynomial dependence on the applied voltage, whereas this dependence is exponential in the pristine state. In the HRS the situation is more complex and a combination of at least two mechanisms takes place.

In the pristine state, the trap-assisted tunneling (TAT) mechanism might presumably be the dominant conduction mechanism in our devices, as ZnO is an undoped material with intrinsic intra-band electronic states (due to its defective nature);<sup>28</sup> a sketch of the energy band diagram for the TAT mechanism is depicted in Fig. 4(b). Under these conditions, the electrical current depends exponentially on the applied voltage, which is given by the following expression:<sup>28</sup>

$$I = \frac{qn_t S}{2\tau} \exp\left(-\frac{8\pi\sqrt{2m^*}d\phi_t^{3/2}}{3hqV}\right), \quad (1)$$

with  $q$  being the elementary charge,  $n_t$  the trap areal density,  $S$  the area of the device,  $\tau$  the relaxation time between subsequent tunneling events,  $m^*$  the effective mass of electrons,  $d$  the thickness through which the electric field is applied,  $\phi_t$  the offset energy between the electrode Fermi level and the trap level, and  $h$  the Planck constant.

Regarding the LRS, the observed high current intensity suggests a large amount of injected carriers, which is compatible with the space charge-limited current (SCLC) theory [see Fig. 4(c)], exhibiting a quadratic dependence on the voltage.<sup>29</sup>

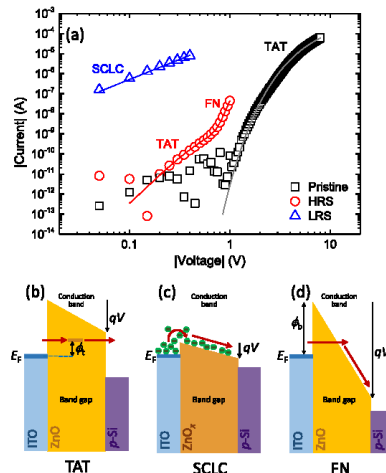


FIG. 4. (a) Log-log representation of the  $I(V)$  characteristics of pristine (black squares), HRS (red circles), and LRS (blue triangles) states. The fitting curves (in solid line) are also plotted together with the experimental data: trap-assisted tunneling (TAT) for pristine (in black), a combination of TAT and Fowler-Nordheim (FN) for HRS (in red) and space charge-limited current (SCLC) for LRS (in blue). All curves were acquired in substrate accumulation conditions ( $V < 0$ ). Sketches of the energy band diagram of TAT, SCLC, and FN charge transport mechanisms are depicted in (b), (c), and (d), respectively. Whereas TAT and FN mechanisms take place in the ZnO (pristine and HRS), the SCLC mechanism occurs in ZnO<sub>x</sub> (LRS).

$$I = \frac{9}{8} \mu \epsilon_0 \epsilon_r S \frac{V^2}{d^3}, \quad (2)$$

where  $\mu$  is the electron drift mobility, and  $\epsilon_0$  and  $\epsilon_r$  are the vacuum and relative permittivities, respectively. Finally, in the *reset* process, the conductivity of the devices dramatically decreases, reaching the HRS. Thus, the ZnO active layer becomes highly resistive and the intrinsic intra-band states are again relevant for the conduction. We observed that the current intensity dependence on the applied voltage exhibits two different trends, separated at a threshold voltage around 0.7 V [see Fig. 4(a)]. At voltages below this threshold, the TAT mechanism should again dominate charge transport, whereas Fowler-Nordheim<sup>30</sup> (FN) could be the main conduction mechanism at higher electric fields, due to the further lowering of the potential barrier. Therefore, a combination of both mechanisms can be considered as follows:

$$I = \frac{qn_t S}{2\tau} \exp\left(-\frac{8\pi\sqrt{2m^*}d\phi_t^{3/2}}{3hqV}\right) + \frac{q^2 S}{8\pi^2 h d^2 \phi_b} V^2 \exp\left(-\frac{8\pi\sqrt{2m^*}d\phi_b^{3/2}}{3hqV}\right), \quad (3)$$

where the first and second terms of the right side of the equation correspond to TAT and FN models, respectively; with  $\phi_b$  being the energy offset between the ITO electrode Fermi level and the ZnO conduction band [see Figs. 4(b) and 4(d)].

Under these considerations, we have fitted the experimental  $I(V)$  curves of the pristine, LRS and HRS states with the expressions from Eqs. (1), (2), and (3), respectively. This procedure allows us extracting physical parameters from the devices which are relevant to understand the RS mechanism within. Although obtaining these parameters is possible through other techniques, *in-situ* measurements often do not take into account sample damaging during preparation, whereas *ex-situ* ones can lead to many time-consuming attempts that do not often yield a specific result due to the difficulty of finding a CNF.

For the pristine state, we have fitted the experimental data using Eq. (1) taking into account that the current flows over the full device area through the 60-nm-thick ZnO layer, and using an electron effective mass for ZnO of  $0.3m_e$ ,<sup>31</sup> which results in  $\phi_t$  being around 0.20 eV. Considering this mechanism, the current is properly adjusted along more than six orders of magnitude, although some deviations are observed at voltages lower than 2 V. In fact, some other effects such as charge trapping can occur and, thus, the parameters that could be obtained from the pre-exponential factor are subjected to a large error.

Using Eq. (2), we have fitted the experimental data from LRS, obtaining an excellent agreement with the space charge-limited current (SCLC) conduction mechanism. From the fit, and assuming that for a stoichiometric ZnO<sub>x</sub> the electron drift mobility ranges between 18 and 140 cm<sup>2</sup> V<sup>-1</sup> s<sup>-1</sup> and the relative permittivity is above 8.3,<sup>32,33</sup> we have found that the effective device area that is contributing to the conduction should be equal to or below  $1.4 \times 10^{-10}$  cm<sup>2</sup>, much lower than the actual top ITO contact area ( $2.1 \times 10^{-3}$  cm<sup>2</sup>). This result suggests that the high current intensity observed in the LRS flows through filaments along the ZnO

semiconductor layer. Taking into account the maximum active surface evidenced by the conduction mechanism, the current density along the CNFs can be evaluated, obtaining a lower limit of  $J = 1.6 \times 10^4$  A cm<sup>-2</sup> at  $V_{\text{read}} = -0.2$  V. This current density is indeed excessively high, but still lower than the one observed in the TaO<sub>x</sub>/TiO<sub>2</sub>/TaO<sub>x</sub> structure, where values over  $10^7$  A cm<sup>-2</sup> were achieved.<sup>34</sup> Further assuming that, in the *set* process, out-diffusion of oxygen ions is forming CNFs with diameters of about 25 nm (typical diameters reported in the literature lie between 10 and 50 nm),<sup>11,12,35,36</sup> the found active surface corresponds to 20 CNFs. Thus, this result suggests the formation of a limited number of conduction paths, with nanoscale dimensions.

Finally, we could adequately fit the HRS  $I(V)$  curve to Eq. (3). Actually, the experimental current intensity for voltages below  $V = 0.7$  V is properly reproduced by considering only the TAT contribution. The fact that the TAT mechanism is dominant at low voltages suggests conduction through the ZnO defective states, in a similar way than in the pristine state. This assumption points out to CNFs being interrupted, presumably due to their partial re-oxidation. The overall current through the ZnO layer is limited by this gap region, which contributes to the HRS. Assuming that the current flows through a ZnO layer with similar structural and chemical composition than the one in the pristine state ( $\phi_b = 0.20 \pm 0.02$  eV), we found an effective thickness reduction of about 85% (effective thickness of  $9 \pm 1$  nm). The electric field along the gap of the interrupted CNFs is enhanced by, at least, this thickness variation, leading to a value of  $\sim 0.8$  MV cm<sup>-1</sup> at  $V = 0.7$  V (see, for instance, Ref. 37, where there is an enhancement of the electric field in Ga:ZnO nanofibers due to boundary effects). This electric field is enough to inject carriers with high kinetic energy to overcome the ITO-ZnO band offset ( $\phi_b$ ), making dominant the FN mechanism. Actually, the experimental data is well reproduced by the FN model, with a band offset energy of  $\phi_b = 0.57 \pm 0.04$  eV, which is below the energy that carriers have at voltages above 0.7 V. The application of voltages larger than 1 V will produce again the *set* process, presumably by promoting out-diffusion of oxygen atoms towards the electrode.

The modeling of the pristine state, LRS and HRS in ZnO-based devices has allowed determining the mechanism responsible for the conduction in each of them, as well as important structural parameters. In the literature, these three states have also been analyzed: (i) the pristine shows trap-assisted conduction typical of dielectric materials, like Poole-Frenkel or TAT, in good agreement with our observations.<sup>38,39</sup> On the other hand, (ii) the LRS typically exhibits a high conductance with an Ohmic or SCLC behavior; considering the effective areas reported so far,<sup>12</sup> the current density reaches values compatible with ZnO with a high density of oxygen vacancies, indicating that the CNF formation is due to the out-diffusion of O atoms and/or oxygen deficiency in the film grown by magnetron sputtering. Finally, (iii) the HRS at low voltages presents again conduction typical of dielectric materials assisted by traps, suggesting that the conductive paths are partially re-oxidized, thus inducing the interruption of the CNFs along 9 nm. At larger voltages (above 0.7 V), injected carriers from the ITO contact present enough energy to overcome the ITO-ZnO potential barrier, exhibiting a FN behavior.<sup>19</sup> The correlation between the

charge transport mechanisms through ZnO and its structural modification under external electrical stress helps anticipating the optimum operation conditions of ZnO-based memristors. In addition, subsequent cycles between positive and negative voltages can promote stable switching between the two states (HRS and LRS), maintaining the previously observed mechanisms.

The measurements and analyses have been extended to other cycles and devices with the same structure, finding similar results that lie within the error bars given for the extracted parameters. Further study on a stressed device and comparison with a pristine one (not shown) has provided proof of the modification of the ZnO structure, by comparing the resonant Raman  $E_1(\text{LO})$  overtones between both devices. As it has previously been suggested,<sup>40,41</sup> this fact is compatible with our hypothesis of oxygen out-diffusion in RS. Thus, the use of electrodes non-transparent to oxygen, ITO in our case, becomes an important factor in improving the endurance of these ZnO-based devices.

Here, we have demonstrated the RS properties of ITO/ZnO/*p*-type Si devices. A difference in current of more than 5 orders of magnitude is observed between LRS and HRS, with endurance beyond  $10^3$  cycles, while working at low voltages. The analysis of the intensity-voltage curves has shown the formation of CNFs at the *set* process due to out-diffusion of O atoms, which is responsible for the LRS. In the *reset* process, these CNFs are interrupted along 9 nm by their re-oxidation, recovering the ZnO defective layer in this region. The fact that this region is in the range of some nanometers propitiated the observed high stability of the RS cycle in these devices. Overall, ZnO, when combined with a *p*-type Si substrate and an ITO top electrode, is demonstrated as an excellent candidate for a future generation of RS memories, whose combination with other Si-based devices provides a large range of applications in transparent electronics.

This work was financially supported by the Spanish Ministry of Economy and Competitiveness (Project Nos. TEC2012-38540-C02-01 and TEC2016-76849-C2-1-R). O.B. also acknowledges the subprogram “Ayudas para Contratos Predoctorales para la Formación de Doctores” of the Spanish Ministry of Economy and Competitiveness for economical support. X.P., C.L., and C.G. are grateful to C. Frilay for his expertise in the maintenance of the sputtering kit used for the growth of the ZnO films.

<sup>1</sup>J. G. Baek, M. S. Lee, S. Seo, M. J. Lee, D. H. Seo, D.-S. Suh, J. C. Park, S. O. Park, H. S. Kim, I. K. Yoo, U.-J. Chung, and J. T. Moon, in *IEDM Technical Digest. IEEE International Electron Devices Meeting, 2004* (IEEE, 2004), pp. 587–590.

<sup>2</sup>R. Waser and M. Aono, *Nat. Mater.* **6**, 833 (2007).

<sup>3</sup>S. Kaeriyama, T. Sakamoto, H. Sumamura, M. Mizuno, H. Kawaura, T. Hasegawa, K. Terabe, T. Nakayama, and M. Aono, *IEEE J. Solid-State Circuits* **40**, 168 (2005).

<sup>4</sup>D. B. Strukov and K. K. Likharev, *Nanotechnology* **16**, 888 (2005).

<sup>5</sup>A. Mehonic, S. Cuffey, M. Wojdak, S. Hudziak, O. Jambois, C. Labbé, B. Garrido, R. Rizk, and A. J. Kenyon, *J. Appl. Phys.* **111**, 074507 (2012).

<sup>6</sup>A. Mehonic, A. Vrajitoarea, S. Cuffey, S. Hudziak, H. Howe, C. Labbé, R. Rizk, M. Pepper, and A. J. Kenyon, *Sci. Rep.* **3**, 2708 (2013).

<sup>7</sup>M. D. Pickett, G. Medeiros-Ribeiro, and R. S. Williams, *Nat. Mater.* **12**, 114 (2013).

<sup>8</sup>S. H. Jo, T. Chang, I. Ebong, B. B. Bhadviya, P. Mazumder, and W. Lu, *Nano Lett.* **10**, 1297 (2010).

<sup>9</sup>G. Vescio, A. Crespo-Yepes, D. Alonso, S. Claramunt, M. Porti, R. Rodríguez, A. Cornet, A. Cirera, M. Nafria, and X. Aymerich, *IEEE Electron Device Lett.* **38**, 457 (2017).

<sup>10</sup>I. Valov, *ChemElectroChem* **1**, 26 (2014).

<sup>11</sup>G. Martín, M. B. González, F. Campabadal, F. Peiró, A. Cornet, and S. Estradé, *Appl. Phys. Express* **11**, 014101 (2018).

<sup>12</sup>F. M. Simanjuntak, D. Panda, K.-H. Wei, and T.-Y. Tseng, *Nanoscale Res. Lett.* **11**, 368 (2016).

<sup>13</sup>J. Kim and K. Yong, *J. Phys. Chem. C* **115**, 7218 (2011).

<sup>14</sup>Q. Yuan, Y. Zhao, L. Li, and T. Wang, *J. Phys. Chem. C* **113**, 6107 (2009).

<sup>15</sup>J. W. Seo, J.-W. Park, K. S. Lim, J.-H. Yang, and S. J. Kang, *Appl. Phys. Lett.* **93**, 223505 (2008).

<sup>16</sup>S. Z. Rahaman, S. Maikap, H.-C. Chiu, C.-H. Lin, T.-Y. Wu, Y.-S. Chen, P.-J. Tzeng, F. Chen, M.-J. Kao, and M.-J. Tsai, *Electrochem. Solid-State Lett.* **13**, H159 (2010).

<sup>17</sup>F. M. Simanjuntak, D. Panda, T.-L. Tsai, C.-A. Lin, K.-H. Wei, and T.-Y. Tseng, *J. Mater. Sci.* **50**, 6961 (2015).

<sup>18</sup>F. M. Simanjuntak, O. K. Prasad, D. Panda, C.-A. Lin, T.-L. Tsai, K.-H. Wei, and T.-Y. Tseng, *Appl. Phys. Lett.* **108**, 183506 (2016).

<sup>19</sup>F. M. Simanjuntak, D. Panda, T.-L. Tsai, C.-A. Lin, K.-H. Wei, and T.-Y. Tseng, *Appl. Phys. Lett.* **107**, 033505 (2015).

<sup>20</sup>Q. Liu, W. Guan, S. Long, R. Jia, M. Liu, and J. Chen, *Appl. Phys. Lett.* **92**, 012117 (2008).

<sup>21</sup>Y. Shuai, S. Zhou, D. Bürger, M. Helm, and H. Schmidt, *J. Appl. Phys.* **109**, 124117 (2011).

<sup>22</sup>J.-Y. Chen, C.-L. Hsin, C.-W. Huang, C.-H. Chiu, Y.-T. Huang, S.-J. Lin, W.-W. Wu, and L.-J. Chen, *Nano Lett.* **13**, 3671 (2013).

<sup>23</sup>W. A. Hubbard, A. Kerelsky, G. Jasmin, E. R. White, J. Lođico, M. Mecklenburg, and B. C. Regan, *Nano Lett.* **15**, 3983 (2015).

<sup>24</sup>Q. Liu, J. Sun, H. Lv, S. Long, K. Yin, N. Wan, Y. Li, L. Sun, and M. Liu, *Adv. Mater.* **24**, 1844 (2012).

<sup>25</sup>X. Zhu, H.-Z. Wu, D.-J. Qiu, Z. Yuan, G. Jin, J. Kong, and W. Shen, *Optics Commun.* **283**, 2695 (2010).

<sup>26</sup>M. F. Cerqueira, M. I. Vasilevskiy, F. Oliveira, A. G. Rolo, T. Viseu, J. Ayres de Campos, E. Alves, and R. Correia, *J. Phys.: Condens. Matter* **23**, 334205 (2011).

<sup>27</sup>A. Marchewka, B. Roesgen, K. Skaja, H. Du, C.-L. Jia, J. Mayer, V. Rana, R. Waser, and S. Menzel, *Adv. Electron. Mater.* **2**, 1500233 (2016).

<sup>28</sup>M. Krzywiecki, L. Grządziel, A. Sarfraz, D. Iqbal, A. Szwajca, and A. Erbe, *Phys. Chem. Chem. Phys.* **17**, 10004 (2015).

<sup>29</sup>P. N. Murgatroyd, *J. Phys. D: Appl. Phys.* **3**, 151 (1970).

<sup>30</sup>R. H. Fowler and L. Nordheim, *Proc. R. Soc. A* **119**, 173 (1928).

<sup>31</sup>Ü. Özgür, Y. I. Alivov, C. Liu, A. Teke, M. A. Reshchikov, S. Doğan, V. Avrutin, S.-J. Cho, and H. Morkoç, *J. Appl. Phys.* **98**, 041301 (2005).

<sup>32</sup>E. M. Kaidashev, M. Lorenz, H. von Wenckstern, A. Rahm, H.-C. Semmelhack, K.-H. Han, G. Benndorf, C. Bundesmann, H. Hochmuth, and M. Grundmann, *Appl. Phys. Lett.* **82**, 3901 (2003).

<sup>33</sup>D. Gall, *J. Appl. Phys.* **119**, 085101 (2016).

<sup>34</sup>W. Lee, J. Park, S. Kim, J. Woo, J. Shin, G. Choi, S. Park, D. Lee, E. Cha, B. H. Lee, and H. Hwang, *ACS Nano* **6**, 8166 (2012).

<sup>35</sup>D.-H. Kwon, K. M. Kim, J. H. Jang, J. M. Jeon, M. H. Lee, G. H. Kim, X.-S. Li, G.-S. Park, B. Lee, S. Han, M. Kim, and C. S. Hwang, *Nat. Nanotechnol.* **5**, 148 (2010).

<sup>36</sup>B. J. Choi, A. C. Torrezan, J. P. Strachan, P. G. Kotula, A. J. Lohm, M. J. Marinella, Z. Li, R. S. Williams, and J. J. Yang, *Adv. Funct. Mater.* **26**, 5290 (2016).

<sup>37</sup>X. Sun, *SPIE Newsroom* **82**, 1096 (2006).

<sup>38</sup>C. Ha, Q. Wang, S. Bai, M. Xu, D. He, D. Lyu, and J. Qi, *Appl. Phys. Lett.* **110**, 073501 (2017).

<sup>39</sup>F. Gul and H. Efeoglu, *Superlattices Microstruct.* **101**, 172 (2017).

<sup>40</sup>O. Blázquez, G. Martín, I. Camps, A. Mariscal, J. López-Vidrier, J. M. Ramírez, S. Hernández, S. Estradé, F. Peiró, R. Serna, and B. Garrido, *Nanotechnology* **29**, 235702 (2018).

<sup>41</sup>G. Bersuker, D. C. Gilmer, D. Veksler, P. Kirsch, L. Vandelli, A. Padovani, L. Larcher, K. McKenna, A. Shluger, V. Iglesias, M. Porti, and M. Nafria, *J. Appl. Phys.* **110**, 124518 (2011).

### 5.1.1. Effect of terbium doping

Once the resistive switching properties of the base structure had been established, the next step involved the doping of the active ZnO layer with rare earth ions. This in theory could make possible the simultaneous light emission and resistive switching properties in a single device; indeed, in a single active layer.

Bearing this objective in mind, an analogous structure to that of section 5.1. *Resistive switching properties of ITO/ZnO/p-Si* was deposited, introducing Tb as a doping rare earth species. Indeed, the combination of ZnO and Tb<sup>3+</sup> ions for green electroluminescence has already been demonstrated in the previous *Chapter 4. Electroluminescence of Rare Earth containing devices*. Terbium was included in the structure by positioning pellets of Tb<sub>4</sub>O<sub>7</sub> on top of the ZnO sputtering target.

Unfortunately, whereas the resistive switching of ZnO presented before required voltage sweeps between -2 and 1 V, this low-voltage cycling was not always achieved, being only possible the cycling when between -4 and 10 V. The electroforming process employed is key for obtaining one operational state or the other in these devices, but in the case of the Tb-doped structures, low-voltage cycling was never achieved. As concluded in the previous chapter, Tb<sup>3+</sup> ions help in the cycling process by oxidizing and reducing, maintaining the network of oxygen ions readily available for the reset operation. This means that whenever a reset is to happen, it cannot be controlled to a very small portion of the filaments as oxygen is well distributed in the layer.

Resistive switching cycles are presented for these devices in Figure 5.4. As expected from cycling with Tb in the active layer, the overall endurance of the devices increased, as O is kept in the active layer and reset process can continue to occur for longer. When comparing voltage values, both structures need similar forming and reset voltages, being the set achieved at almost half the required voltage in the doped structure than in the undoped one. Additionally, less dispersion and a higher resistance ratio between HRS and LRS can be observed for doped devices, as  $I(V)$  curves tend to follow always similar paths. In the case of doped devices, LRS is more conductive and HRS is more resistive than in the undoped ones. This trend is also replicated when pulsed cycling is analyzed for both devices.

## Resistive switching of ZnO

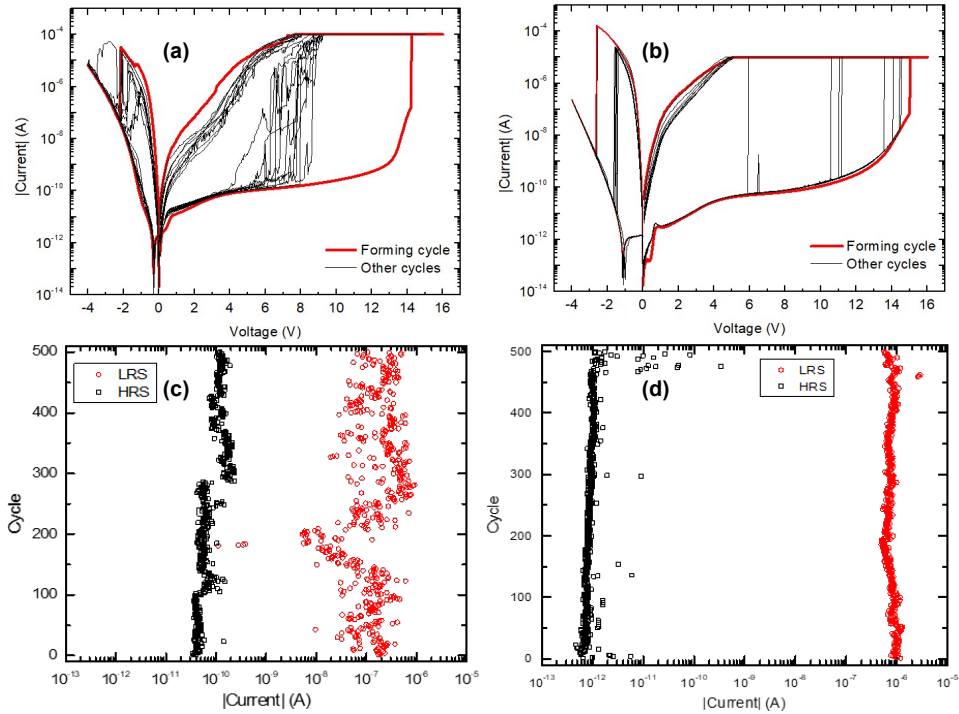


**Figure 5.4.** (a, b) High voltage RS  $I(V)$  curves of ZnO based devices. (c, d) Pulsed cycling of the same devices. (a, c) Undoped devices, (b, d) doped devices.

For a combined measurement of both light emission and resistive switching cycling, the light emitted by the devices was integrated and collected over the range of 185 to 850 nm while simultaneously performing an  $I(V)$  cycle. As it can be seen in Figure 5.5(a), light emission is obtained when the device is in the LRS, with a threshold for emission of  $\sim 10^{-5}$  A. No emission is observed while the device is in HRS. A peak of emission takes place when a set or reset process occurs, in correspondence with the sudden change in the current circulating through the device at that time.

Spectrally resolving this emission, the origin of the luminescence is revealed. For this, a continuous voltage measurement at each state is performed, while monitoring the current to avoid that a resistance change affects the analysis. No EL is observed when measuring the HRS, in accordance with the previous observation [Figure 5.5(b)]. Different measurements in the LRS have led to the same result: a wide emission through the visible and part of the infrared centered around  $\sim 640$  nm. This contrasts with the expected narrow emission of  $Tb^{3+}$  ions, meaning that the latter are not active under these conditions. Instead, this emission clearly corresponds to that of defective ZnO. Indeed, the

### 5.1. Resistive switching properties of ITO/ZnO/p-Si

presence of CFs when in the LRS, where EL emission exists, means that current circulates through O-defective ZnO paths. In addition, these CFs probably avoid most of the  $\text{Tb}^{3+}$  ions, and consequently these ions are not excited. In HRS, the electrons circulating have a very low energy that, again, is not enough to excite Tb.

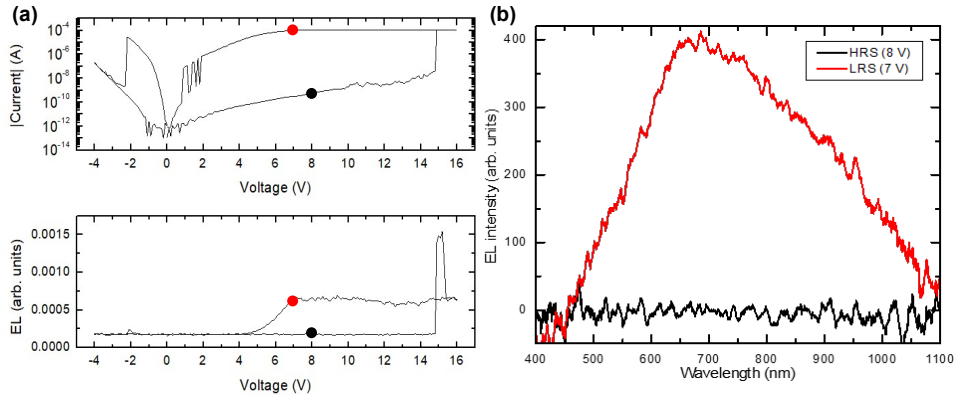


**Figure 5.5.** (a) Simultaneous monitoring of the  $I(V)$  cycle and the EL emission during a resistive switching cycle of a ZnO device doped with Tb. (b) EL emission spectrally resolved for HRS and LRS. Color circles on the left image serve as guide for the measurement conditions on the right.

Results from this work are promising, showing once again that combined emission and resistive switching is possible. Nevertheless, the expected luminescent centers are not activated with the cycling. For this reason, other studies on the same effect were carried out with other luminescent species, Si NCs, which will be addressed in *Chapter 6. Combined properties in Si NCs-containing devices.*

This work has been presented as a poster in the European Materials Research Society (EMRS) Spring Meeting 2019.

## 5.2. Electroforming under incident light

The last study performed with these ZnO-based structures allowed the observation of a useful phenomenon when these transparent devices are exposed to light during the electroforming process. Under light incidence, a progressive formation of CFs can be achieved, thus making the LRS desired for operation of the devices more controllable. This means that the devices can work between two states that not necessarily have to be the same for all devices but rather having the LRS selected within a range.

Under illumination with a 532-nm Nd:YAG laser, different devices were submitted to an  $I(V)$  curve with increasing stop voltage, from 2 V to 7 V, in steps of 1 V. In none of the cases a complete electroforming process, signaled by an abrupt change in current, took place. As a reference, this change occurs at 14 V for a pristine device in dark conditions. A control set of measurements in the same voltage range and in dark conditions, maintained the line-shape of a typical device brought to the 14-V electroforming process. This allows identifying an increase in current of up to 5 orders of magnitude when under illumination, correspondent to photogenerated electrons injected into ZnO.

The relevance of these different performed cycles lies in the aftermath. Indeed, if after the illuminated cycle, another  $I(V)$  measurement is done in the same voltage range in dark conditions, the observed conduction state will be different for all devices. All of them will have a higher conduction than the control device only cycled in dark, and the conductivity will increase with the stop voltage.

In addition, different charge transport mechanisms can be distinguished depending on the stop voltage. The three lowest stop-voltage curves maintain a highly pristine-like behavior, thus being the conduction limited by a Schottky barrier that is progressively reduced as the CFs grow. Conversely, the two highest stop-voltage curves correspond to a space-charge limited-current (SCLC) mechanism, in agreement with that found previously (*Section 5.1. Resistive switching properties of ITO/ZnO/p-Si*) for fully-formed CFs.

Last, the increase of CFs formation with voltage has also been demonstrated under pulsed conditions (Figure 5.6). Similar to the  $I(V)$  curves, different devices were submitted to a train of 10 write and read pulses with different write values in the range of 1 V to 10 V, all while

under illumination. A control device was submitted to the same pulses in dark conditions. The recorded read current averages showed that, in dark conditions, the device maintained the initial state up to 9 V, only performing the electroforming process when the 10-V pulses were reached. In contrast, devices under illumination deviated from the initial state starting at 5 V and reached the LRS at 8 V. Between these two values, increasing read currents showed the presence of intermediate resistance states.

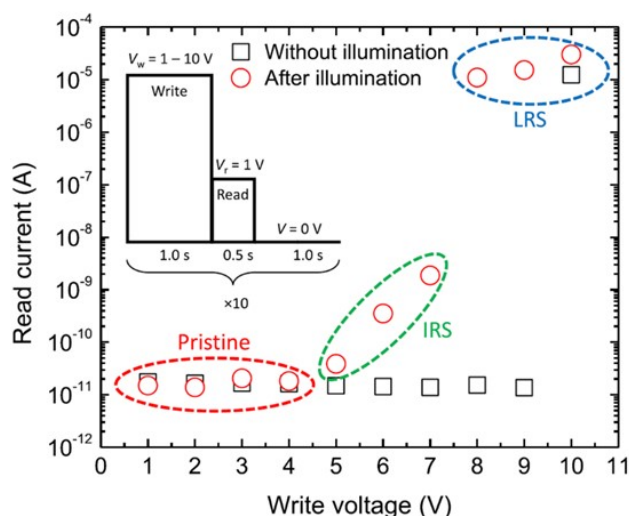


**Figure 5.6.** Read values of 10 pulsed voltage cycles for electroforming of ZnO-based RS devices. When done under illumination, intermediate resistance states appear at 5–7 V.

This work corroborates that a combination of applied electric field and circulating current are responsible for the electroforming process, and by extension the set and reset processes. Even if the creation of CFs during the electroforming process is abrupt when only a high voltage applied is possible (low current circulation in the pristine state), the contribution of additional current (e.g., due to photogenerated carriers) can lead to a change in its dynamics, paving the way for other operation modes within the same devices. These results clearly identify the usefulness of light-exposed transparent resistive switching devices, allowing for the initial selection of the device operation conditions.

This work has been presented as a poster in the European Materials Research Society (EMRS) Spring Meeting 2019 and the 2019 Annual Meeting of the Institute of Nanoscience and Nanotechnology of the UB (IN<sup>2</sup>UB); and as a talk in the European Materials Research Society (EMRS) Fall Meeting 2019. A journal article was published in *Applied Physics Letters* **115**, 261104 (2019).



**Paper V: Light-activated electroforming in ITO/ZnO/p-Si resistive switching devices (DOI: [10.1063/1.5125844](https://doi.org/10.1063/1.5125844))**



# Light-activated electroforming in ITO/ZnO/*p*-Si resistive switching devices

Cite as: Appl. Phys. Lett. **115**, 261104 (2019); doi: 10.1063/1.5125844

Submitted: 28 August 2019 · Accepted: 14 December 2019 ·

Published Online: 26 December 2019



O. Blázquez,<sup>1,2,a)</sup> J. L. Frieiro,<sup>1,2</sup> J. López-Vidrier,<sup>3</sup> C. Guillaume,<sup>4</sup> X. Portier,<sup>4</sup> C. Labbé,<sup>4</sup> S. Hernández,<sup>1,2</sup> and B. Garrido<sup>1,2</sup>

## AFFILIATIONS

<sup>1</sup>MIND, Department of Electronics and Biomedical Engineering, Universitat de Barcelona, Martí i Franquès 1, E-08028 Barcelona, Spain

<sup>2</sup>Institute of Nanoscience and Nanotechnology (IN<sup>2</sup>UB), Universitat de Barcelona, Av. Joan XXIII S/N, E-08028 Barcelona, Spain

<sup>3</sup>Laboratory of Nanotechnology, Department of Microsystems Engineering (IMTEK), Albert-Ludwigs-Universität Freiburg, Georges-Köhler-Allee 103, D-79110 Freiburg, Germany

<sup>4</sup>CIMAP Normandie Univ., ENSICAEN, UNICAEN, CEA, CNRS, 14050 Caen, France

<sup>a)</sup>Author to whom correspondence should be addressed: [oblazquez@el.ub.edu](mailto:oblazquez@el.ub.edu)

## ABSTRACT

We report on light-activated electroforming of ZnO/*p*-Si heterojunction memristors with transparent indium tin oxide as the top electrode. Light-generated electron-hole pairs in the *p*-type substrate are separated by the external electric field and electrons are injected into the active ZnO layer. The additional application of voltage pulses allows achieving different resistance states that end up in the realization of the low resistance state (LRS). This process requires much less voltage compared to dark conditions, thus avoiding undesired current overshoots and achieving a self-compliant device. The transport mechanisms governing each resistance state are studied and discussed. An evolution from an electrode-limited to a space charge-limited transport is observed along the electroforming process before reaching the LRS, which is ascribed to the progressive formation of conductive paths that consequently induce the growth of conductive nanofilaments through the ZnO layer.

Published by AIP Publishing. <https://doi.org/10.1063/1.5125844>

The interest in resistive random access memories (RRAMs) has arisen as a promising alternative to conventional flash memories.<sup>1,2</sup> The possibility to switch between two resistance states, namely, the high resistance state (HRS) and low resistance state (LRS), and retaining them without the necessity of any supplied voltage, opens a large range of potential applications in nonvolatile memories,<sup>3,4</sup> even in logic and neuromorphic computing.<sup>5,6</sup> The filamentary formation and partial destruction of conductive paths through a dielectric material have been established as the main mechanism of this resistive switching (RS) behavior, with electrochemical metallization (ECM) or valence change mechanism (VCM) being the most observed processes in metal oxides.<sup>7,8</sup> In both cases, the out-diffusion of ions by electrical stress plays a crucial role in this structural and chemical modification.<sup>9–11</sup> The first formation of these conductive nanofilaments (CNFs) takes place during the electroforming process, in which the LRS of the device is defined and it depends on the number and width of the CNFs.<sup>12</sup> In the case of polycrystalline materials, which usually present grain boundaries, these filamentary conductive paths are typically generated in these regions due to their initially defective nature.<sup>13</sup> The abrupt and spontaneous formation of these

nanostructures under electrical stress has been used to obtain well-differentiated resistance states, with the speed of the transition between them being on the order of picoseconds in some cases.<sup>14</sup> However, this abrupt transition can be a drawback due to the permanent damages that some devices may undergo and consequently requiring to set a current compliance to avoid this occurrence. So far, some studies have focused on the control of the formation of the CNFs by using different values of the current compliance, which modifies the conductivity of the LRS and even enhances the endurance and the retention of the resistance states.<sup>15,16</sup> Recently, light interaction has been proposed to modify the RS properties by either modulating the density of trapped electrons in heterojunctions<sup>17</sup> or decreasing the Schottky-like barriers at rectifying interfaces.<sup>18,19</sup> This effect has also been observed in solar cell-related materials such as perovskites, thus broadening their wealth of applications.<sup>20,21</sup> Beyond these effects, an additional electron injection can facilitate the formation of oxygen vacancies, as observed in amorphous SiO<sub>2</sub>.<sup>22</sup> This effect has also been employed to influence the RS properties, where an additional current injection from the substrate, by means of photoconductivity, induces a decrease in the required voltage to switch to the LRS.<sup>23</sup>

In this work, we present the control of the CNF formation in pristine indium tin oxide (ITO)/ZnO/*p*-Si devices. The application of light photogenerates additional carriers in the *p*-Si substrate, which in combination with the applied voltages helps achieving a progressive growth of the CNFs. The application of subsequent current-voltage [ $I(V)$ ] curves, progressively increasing the end-voltage, allowed controlling this CNF formation, thus achieving intermediate resistance states (IRS) at lower voltages, even without the necessity of setting a current compliance. Similar behavior has been observed using voltage pulses, recovering these IRS and achieving the same LRS.

Samples under study consist of an ITO/ZnO/*p*-Si metal-insulator-semiconductor (MIS) device structure. Before the ZnO deposition onto the *p*-type Si substrate, a 400-nm-thick thermal SiO<sub>2</sub> layer was grown and etched using standard photolithography to define squared windows ( $60 \times 60 \mu\text{m}^2$ ) in the field oxide. The ZnO layer was full-area deposited via radio frequency-magnetron sputtering, with a thickness of 60 nm, and subsequently annealed at 450 °C for 1 h under Ar flow. A second process of photolithography permitted the deposition of the ITO top electrode by electron-beam evaporation (EBE). Finally, full-area Al was deposited by EBE as the bottom electrode. The structural characterization was carried out via transmission electron microscopy and Raman scattering measurements, indicating that ZnO exhibits a polycrystalline structure, and the results were published in a previous study on the same devices (see Ref. 24). The electrical characterization of devices was performed using an Agilent B1500 semiconductor device analyzer and a Cascade Microtech Summit 11000 probe station, supplying the voltage on the top ITO electrode and keeping the bottom contact grounded. Light excitation consisted in illuminating the device through the top ITO contact by means of a Nd:YAG continuous wave laser working at 532 nm with a power density of  $\sim 300 \text{ mW cm}^{-2}$ .

Before the analysis of the effect of light on the electroforming process, a complete  $I(V)$  cycle in a pristine device under dark conditions was carried out, completing the electroforming and the first reset [see Fig. 1(a)]. An abrupt increase in the current can be observed around  $\sim 14 \text{ V}$ , resulting in a switch to the LRS (a current compliance of 1 mA is required to avoid permanent damage to the device). The reset of the resistance state was carried out at negative voltages, obtaining an irregular curve in the range between  $-1.0 \text{ V}$  and  $-2.5 \text{ V}$  until the reset was completed. Successive  $I(V)$  characteristics were acquired in different but equivalent devices before, under, and after illumination to study the effect of light in the electroforming process. Cycling was done in a sequence with an end-voltage that was increased in each cycle up to 7 V. For comparison, a series of  $I(V)$  curves measured in the dark using another device were also recorded. In Fig. 1(b), the  $I(V)$  curves corresponding to the measurements without and under illumination are plotted. In the dark, the same  $I(V)$  characteristics were obtained in all cases, not reaching yet the electroforming and keeping the device in the pristine state to further study the effect of a combined application of light and voltage. These curves agree with the completed cycle under dark conditions obtained in the previously analyzed pristine device [see Fig. 1(a)]. Regarding the curves obtained under illumination, a clear increase in 5 orders of magnitude in current was obtained, with this effect being mainly ascribed to the injection into ZnO of electrons photogenerated within the *p*-Si substrate (although some electrons can also be promoted to the ZnO conduction band by direct absorption of photons at the ZnO/Si interface). After acquiring each curve under illumination, another curve was recorded in the dark

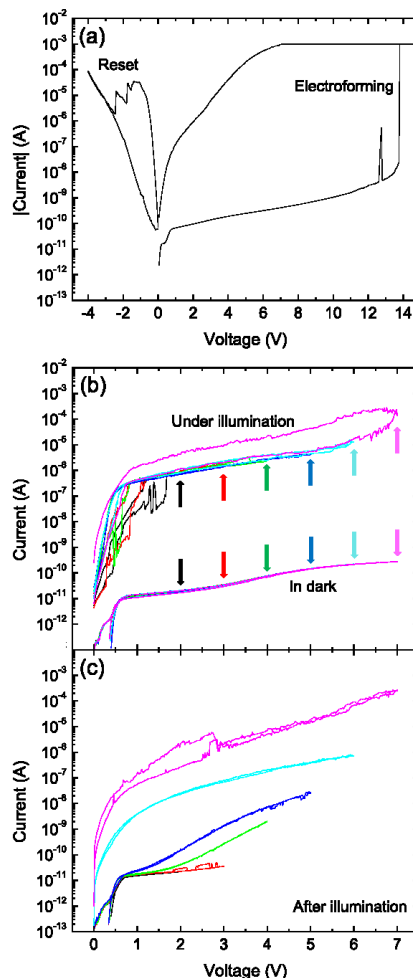


FIG. 1. (a) Complete first cycle of a device, acquired in the dark, showing the electroforming and first reset processes. (b) Sequence of  $I(V)$  characteristics increasing the end-voltage from 2 V to 7 V in the dark and under illumination. The colored arrows in (b) indicate the maximum voltage of each curve of the same color for the sake of a better comparison. (c) Curves obtained in the dark measured immediately after the acquisition of the corresponding curves under illumination shown in (b).

to observe possible permanent modifications in the  $I(V)$  characteristics [Fig. 1(c)]. In contrast to the curves in the dark obtained prior to illumination, where no modification of the  $I(V)$  characteristics was observed [see Fig. 1(b)], the curves acquired in the dark after

illumination present a clear variation, making the device more conductive and therefore exhibiting distinct resistance states. Curves until 2 V and 3 V present a similar line shape, consistent with the curves in the preillumination condition (at voltages lower than 0.75 V, displacement current dominates and charge accumulation takes place). However, the postilluminated  $I(V)$  characteristics at increasing end-voltage show a progressive increase in the current, with the illumination being responsible for this modification. As a consequence, charge accumulation no longer occurs, which suggests that illumination induces a modification of the charge transport mechanism through the device.

Analyzing more in detail the evolution of the postilluminated  $I(V)$  curves [see Fig. 1(c)], the first two curves (end-voltage of 2 V and 3 V) exhibit displacement current at voltages below 0.75 V, as well as accumulated charge in backward curves with a remnant voltage around 0.4 V. In addition, the pristine state presents asymmetrical  $I(V)$  characteristics with a clear limitation of the current at positive voltages, which can be ascribed to a Schottky-like conduction mechanism. However, this current limitation is altered in the two following curves acquired after illumination (end-voltage of 4 V and 5 V), which could be related to initial structural modifications caused by oxygen out-diffusion within the ZnO layer, therefore inducing an increase in conductivity. The two last curves (end-voltage of 6 V and 7 V) exhibit a totally different line shape, free of displacement current and accumulated charge, suggesting again another transport mechanism. This behavior can be ascribed to the existence of CNFs connecting directly both electrodes.

A similar experiment was carried out but using voltage pulses instead of  $I(V)$  sweeps. In this case, a train of 2 pulses was performed. The first pulse acted as writing voltage ( $V_w$ ) with 1 s of duration, whose amplitude was varied from 1 V to 10 V; the second one was meant for reading the current of each resistance state for 0.5 s, which was set at  $V_r = 1$  V in all cases. This sequence of two pulses was repeated 10 times with 1 s of separation between each one, its schematics being represented in the inset of Fig. 2. As proceeded using  $I(V)$  curves, this sequence was applied before, during and after illumination for each  $V_w$ . To analyze the influence of light, another device was submitted to the same pulsed sequence but only in the dark. In Fig. 2, the average current at  $V_r$  along the 10 pulses is plotted as a function of the different supplied  $V_w$  for both operation conditions, following the already described pulsed sequence. As observed, the reference device, biased in the dark, exhibits a constant value of the read current around  $10^{-11}$  A for all  $V_w$  except at 10 V, when it shows a sudden increase in the current up to  $10^{-5}$  A. In the case of experiments under illumination, the same values of the read current around  $10^{-11}$  A are obtained at low  $V_w$  ( $V_w \leq 4$  V), after illuminating the devices. In contrast, a gradual increase in the read current in the range from 5 V to 8 V takes place, achieving a value of  $\sim 10^{-5}$  A, which matches with the current obtained in the nonilluminated device at 10 V. This progressive current increase brings the device into intermediate resistance states (IRS), in good agreement with our observation when performing voltage sweeps.

To further elucidate the influence of light on the RS properties of the devices, it is interesting to study the charge transport mechanism evolution that the devices undergo when progressively switching from higher to lower resistance states. In order to analyze better this evolution, the  $I(V)$  curves of the different resistance states were fitted

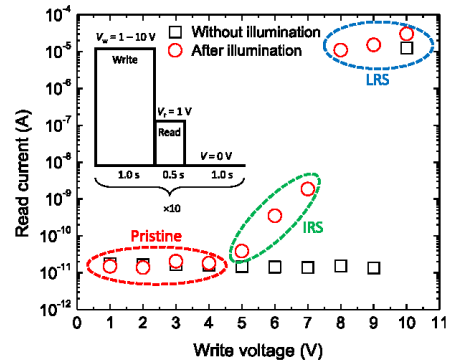


FIG. 2. Representation of the average value of read current, along 10 pulses, obtained in the dark at  $V_r = 1$  V, as a function of the different write voltage  $V_w$ , without (black squares) and after (red circles) illumination. Three different regions can be observed in the second case: pristine, intermediate resistance states (IRS), and low resistance state (LRS). In the inset, a scheme of the applied voltage pulse train is illustrated.

according to the most general dependence of current on voltage in heterostructures,

$$I(V) = AV^\alpha \cdot \exp(BV^\beta), \quad (1)$$

with  $A$  and  $B$  being constants and  $\alpha$  and  $\beta$  the potential dependence of the pre-exponential and exponential factors, respectively. The exponential factor is related to the conduction in materials with potential barrier profiles (like dielectrics or semiconductors), whereas the pre-exponential one is typically associated with conduction in materials with large carrier density, influenced by the profile of the electric field (like in degenerated semiconductors or metals). The curves and their corresponding fits are plotted in Fig. 3(a), where the resulting fitting parameters are also indicated. In the case of the three first curves, where the device is in intermediate states close to the HRS, only exponential contribution ( $\alpha = 0$  and  $\beta \neq 0$ ) is found. The value of  $\beta$  decreases when the end-voltage increases, which is consistent with a combination of a lower effect of the Schottky barrier on charge transport and the initial and progressive formation of CNFs. In contrast, the  $I(V)$  curves corresponding to the LRS show a value of  $\alpha \approx 2$ . This value is in agreement with a previous work carried out in the dark conditions on these same devices, where the space charge-limited current mechanism (SCLC) was determined to be dominant within the LRS in the accumulation regime ( $V < 0$ ).<sup>24</sup> Please note that, in the present work, curves are taken in the inversion regime ( $V > 0$ ), but the symmetry of the curves when the CNFs are formed suggests similar behavior in both polarities. Regarding the obtained value of  $\beta \approx 0.5$  in the LRS, it could be ascribed to the Poole-Frenkel correction proposed by Murgatroyd, where the reduction of the effective trap level depth due to the external electric field is taken into account;<sup>25</sup> nevertheless, this contribution only affects at low voltages, with  $I \propto V^2$  being the dominant dependence.

In contrast to some studies reported in the literature that have only observed differences in the RS properties of ZnO when the device

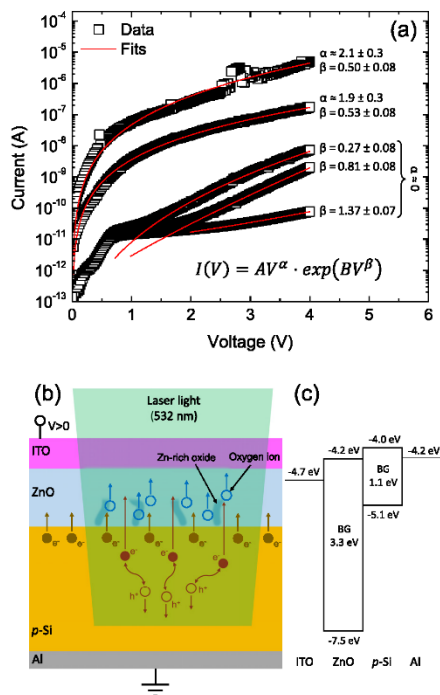


**FIG. 3.**  $I(V)$  curves recorded after illumination with their corresponding fits following the general expression indicated in the inset. (b) Scheme of the device depicting the formation of CNFs due to the diffusion of the oxygen ions (blue circles) toward the top electrode when it is biased at positive voltage. The photogenerated electron-hole pairs formed within the Si substrate (red circles) enhance electron injection into the ZnO, which facilitates the formation of the CNFs. (c) Energy band diagram of the device structure, showing the band offset and bandgap (BG) energies corresponding to the involved materials.

is under illumination, but involving no permanent modifications after that,<sup>18,26–28</sup> the hereby analyzed devices exhibit different resistance states after being illuminated. These results demonstrate that light strongly influences the formation of the CNFs during the electroforming process, obtaining different resistance states by adequately combining the applied voltage and the extra current induced via photoconduction. Indeed, the performed electrical characterization already gives information about the role of the device structure in its RS properties. In particular, the rectifying behavior observed in the inversion regime suggests the presence of a Schottky-like barrier at the interface between the ZnO layer and the *p*-Si substrate, whereas the remnant voltage around 0.4 V in this same pristine state confirms the existence of accumulated charge at this interface. On the one hand, some studies reported that, under illumination, the trapping and detrapping of optically generated charges in this region could influence on the RS behavior, for instance by inducing lower

resistance states or lower set voltages.<sup>17,18</sup> On the other hand, other authors proposed that the increase in the number of injected electrons due to carrier photogeneration in the substrate, together with electron trapping at intrinsic defects within the active layer, contributes to the creation of oxygen vacancies, crucial for the formation of the CNFs in metal oxides.<sup>25</sup> As a consequence of any of these hypotheses, the voltage at which the switch to the LRS is achieved, i.e., the voltage at which the CNFs are generated, is significantly reduced by the application of light.

It has been previously reported that the generation and stability of the CNFs depend not only on the applied voltage (i.e., the external electric field) but also on the current circulating through the material.<sup>23</sup> Indeed, the electron flow is responsible for breaking Zn-O bonds in order to free  $O^{2-}$  ions, whose diffusion toward the electrodes induces the formation of vacancy sites within the ZnO lattice that constitute the CNF. The fact that the ZnO presents polycrystalline morphology suggests that the breaking of Zn-O bonds takes place at grain boundaries, as has been reported in the literature, producing there the local formation of Zn-rich regions.<sup>13</sup> In this regard, the utilization of light permits injecting an additionally photogenerated current from the substrate into the oxide material which, combined with the applied voltage, induces the structural changes into the ZnO layer [see Fig. 3(b)]. In the dark, the applied voltage is the main responsible for the electroforming process due to the low current that the device presents, typically requiring high voltages to switch to the LRS. At this high voltage, loosely bound oxygen ions move toward the ITO, thus inducing the sudden switch to a lower resistance state due to a high electrical stress of the material, achieving high currents. Therefore, this abrupt increase in current resulting from the formation of the CNFs can induce an undesired overshoot of current in the device, even working at lower voltages with short duration voltage pulses, and using a suitable compliance, which can lead to permanent damage within the structure. In contrast, the additional current injected from the Si substrate [following the energy band schematics in Fig. 3(c)] when illuminated allows achieving sufficient electrical stress at lower voltages, thus providing gradual oxygen ions drift without triggering the sudden formation of the whole CNF, even when forming a considerably large number of them. However, during illumination, the increase in current may induce some defects at the ZnO/ITO interface and/or deeper into the ITO contact.

We have hereby shown that, in the ITO/ZnO/*p*-Si devices under study, the progressive and stable CNF generation during the electroforming can be achieved by means of two different approaches: the progressive increase in the end-voltage in consecutive  $I(V)$  curves and the usage of voltage pulses (which reduce the required electroforming voltages from 10 V to 5 V), which avoid the constant stress of the device under illumination and thus prevent a sudden switch to the LRS. These presented protocols therefore give the possibility to control the formation of the CNFs, permitting to tune the resistance into intermediate states and thus obtaining a quasianalog behavior, thanks to the adequate addition of light to the applied voltage.

This work was financially supported by the Spanish Ministry of Economy and Competitiveness (Project Nos. TEC2012-38540-C02-01 and TEC2016-76849-C2-1-R). O.B. also acknowledges the subprogram “Ayudas para Contratos Predoctorales para la Formación de Doctores” from the Spanish Ministry of Economy and Competitiveness for economical support. J.L.F. acknowledges

the subprogram “Ayudas para la Formación de Profesorado Universitario” (No. FPU16/06257) from the Spanish Ministry of Education, Culture and Sports for economical support. X.P., C.L., and C.G. are grateful to C. Frilay for his expertise in the maintenance of the sputtering setup used for the growth of the ZnO films.

## REFERENCES

- <sup>1</sup>R. Waser and M. Aono, *Nat. Mater.* **6**, 833 (2007).
- <sup>2</sup>P. Nardi, S. Balatti, S. Larentis, D. C. Gilmer, and D. Ielmini, *IEEE Trans. Electron Devices* **60**, 70 (2013).
- <sup>3</sup>M.-J. Lee, C. B. Lee, D. Lee, S. R. Lee, M. Chang, J. H. Hur, Y.-B. Kim, C.-J. Kim, D. H. Seo, S. Seo, U.-I. Chung, I.-K. Yoo, and K. Kim, *Nat. Mater.* **10**, 625 (2011).
- <sup>4</sup>M. H. R. Lankhorst, B. W. S. M. M. Ketelaars, and R. A. M. Wolters, *Nat. Mater.* **4**, 347 (2005).
- <sup>5</sup>Z. Wang, S. Joshi, S. E. Savel'ev, H. Jiang, R. Mitya, P. Lin, M. Hu, N. Ge, J. P. Strachan, Z. Li, Q. Wu, M. Barnell, G.-L. Li, H. L. Xin, R. S. Williams, Q. Xia, and J. J. Yang, *Nat. Mater.* **16**, 101 (2017).
- <sup>6</sup>J. Borghetti, G. S. Snider, P. J. Kuekes, J. J. Yang, D. R. Stewart, and R. S. Williams, *Nature* **464**, 873 (2010).
- <sup>7</sup>R. Waser, R. Dittmann, G. Staikov, and K. Szot, *Adv. Mater.* **21**, 2632 (2009).
- <sup>8</sup>I. Valov, *ChemElectroChem* **1**, 26 (2014).
- <sup>9</sup>A. Mehonic, M. Buckwell, L. Montesi, L. Garnett, S. Hudziak, S. Fearn, R. Chater, D. McPhail, and A. J. Kenyon, *J. Appl. Phys.* **117**, 124505 (2015).
- <sup>10</sup>O. Blázquez, G. Martín, I. Camps, A. Mariscal, J. López-Vidrier, J. M. Ramirez, S. Hernández, S. Estradé, P. Peiró, R. Serna, and B. Garrido, *Nanotechnology* **29**, 235702 (2018).
- <sup>11</sup>C. Chen, S. Gao, F. Zeng, G. S. Tang, S. Z. Li, C. Song, H. D. Fu, and F. Pan, *J. Appl. Phys.* **114**, 014502 (2013).
- <sup>12</sup>T. Ninomiya, K. Katayama, S. Muraoka, R. Yasuhara, T. Mikawa, and Z. Wei, *Jpn. J. Appl. Phys., Part 1* **52**, 114201 (2013).
- <sup>13</sup>P. Zhuge, S. Peng, C. He, X. Zhu, X. Chen, Y. Liu, and R.-W. Li, *Nanotechnology* **22**, 275204 (2011).
- <sup>14</sup>B. J. Choi, A. C. Torrezan, J. P. Strachan, P. G. Kotula, A. J. Lohn, M. J. Marinella, Z. Li, R. S. Williams, and J. J. Yang, *Adv. Funct. Mater.* **26**, 5290 (2016).
- <sup>15</sup>Y.-L. Wu, C.-W. Liao, and J.-J. Ling, *Appl. Phys. Lett.* **104**, 242906 (2014).
- <sup>16</sup>X. Chen, W. Hu, S. Wu, and D. Bao, *Appl. Phys. Lett.* **104**, 043508 (2014).
- <sup>17</sup>M. Ungureanu, R. Zazpe, F. Golmar, P. Stolar, R. Llopis, P. Casanova, and L. E. Hueso, *Adv. Mater.* **24**, 2496 (2012).
- <sup>18</sup>B. Sun, J. Wu, X. Jia, F. Lou, and P. Chen, *J. Sol-Gel Sci. Technol.* **75**, 664 (2015).
- <sup>19</sup>A. Sawa, T. Fujii, M. Kawasaki, and Y. Tokura, *Appl. Phys. Lett.* **85**, 4073 (2004).
- <sup>20</sup>Z. Chen, Y. Zhang, Y. Yu, M. Cao, Y. Che, L. Jin, Y. Li, Q. Li, T. Li, H. Dai, J. Yang, and J. Yao, *Appl. Phys. Lett.* **114**, 181103 (2019).
- <sup>21</sup>J. Zhao, S. Li, W. Tong, G. Chen, Y. Xiao, S. Lei, and B. Cheng, *Adv. Electron. Mater.* **4**, 1800206 (2018).
- <sup>22</sup>D. Z. Gao, A.-M. El-Sayed, and A. L. Shluger, *Nanotechnology* **27**, 505207 (2016).
- <sup>23</sup>A. Mehonic, T. Gerard, and A. J. Kenyon, *Appl. Phys. Lett.* **111**, 233502 (2017).
- <sup>24</sup>O. Blázquez, J. L. Frieiro, J. López-Vidrier, C. Guillaume, X. Portier, C. Labbé, P. Sanchis, S. Hernández, and B. Garrido, *Appl. Phys. Lett.* **113**, 183502 (2018).
- <sup>25</sup>P. N. Murgatroyd, *J. Phys. D* **3**, 151 (1970).
- <sup>26</sup>J. Park, S. Lee, and K. Yong, *Nanotechnology* **23**, 385707 (2012).
- <sup>27</sup>B. K. Barnes and K. S. Das, *Sci. Rep.* **8**, 2184 (2018).
- <sup>28</sup>D. Liang, X. Li, J. Wang, L. Wu, and P. Chen, *Solid-State Electron.* **145**, 46 (2018).

**References**

- [1] C. Schindler, M. Weides, M. N. Kozicki, R. Waser, *Applied Physics Letters* **92**, 122910, 2008.
- [2] L. Shi, D. Shang, J. Sun, B. Shen, *Applied Physics Express* **2**, 101602, 2009.
- [3] R. Cuscó, E. Alarcón-Lladó, J. Ibáñez, L. Artús, J. Jiménez, B. Wang, M. J. Callahan, *Physical Review B* **75**, 165202, 2007.
- [4] F. M. Simanjuntak, D. Panda, K. H. Wei, T. Y. Tseng, *Nanoscale Research Letters* **2016 11:1 11**, 1, 2016.



# Combined properties in Si NC-containing devices

---

After the promising results found with ZnO as the base material for combined resistive switching properties with light interaction, a second platform was tested. Indeed, while the first yielded good results, these were far from being completely applicable to devices, as light emission was poor and not from the expected luminescent centers (ZnO defects instead of rare earth dopants) and light absorption only significantly influenced the electroforming process.

To analyze all the possibilities that offer the combination of these different applications, the new base active layer selected was SiO<sub>2</sub> with embedded Si NCs. Resistive switching of SiO<sub>x</sub> had already been proven,<sup>[1]</sup> whilst the resistive switching of SiO<sub>2</sub> was complicated, as it presents a high bonding energy that difficult the liberation of O<sup>2-</sup> ions to create the required vacancies.

Hence, with this screening of the available options for an already CMOS-compatible material, the inclusion of Si NCs hypothetically solved two issues at once. First, the presence of Si NCs would introduce defective SiO<sub>x</sub> regions in the surrounding areas to the NCs where the resistive switching process could begin and propagate throughout the layer. Second, Si NCs show both light emission and absorption properties, thus no other optically active centers would be required.

The devices for these experiments were fabricated via PECVD in collaboration with the *IMTEK* at the *University of Freiburg*, where the growth of Si NCs by the multilayer approach was first reported.<sup>[2,3]</sup> Although only one type of device has been employed for this research, a total of sixteen different structures were investigated mainly due to the poor (or lack of) resistive switching effect (only four of them exhibited it). The difference between the structures lay in the presence of different interlayers and their thickness, whereas parameters like layer composition or required annealing temperature for Si NCs formation were already well-known.<sup>[4,5]</sup>

In addition, the fabrication of Si NCs following the multilayer approach was also tried out via electron beam evaporation in the cleanroom facilities of the *University of Barcelona*, in contrast to chemical-vapor deposition used at *IMTEK*. This would provide a second source of samples should it be required.

## 6.1. Si NCs embedded in SiO<sub>2</sub> by electron beam evaporation

Since first reported, the fabrication of Si NCs by the multilayer approach has been proven by different techniques, including electron beam evaporation.<sup>[6]</sup> This work presents the fabrication of Si NCs within the same evaporation system using SiO<sub>2</sub> and Si targets, the latter being evaporated in an O<sub>2</sub> atmosphere.

The first analysis performed via XPS demonstrated the composition of both intended layers of the multilayer system. The obtained SiO<sub>2</sub> layer results in a stoichiometry close to that of pure SiO<sub>2</sub>, with 34 at.% of Si and 66 at.% of O. The deconvolution of the peaks indicated the existence of Si<sup>4+</sup>, Si<sup>3+</sup>, Si<sup>2+</sup>, and Si<sup>1+</sup>, but no Si<sup>0</sup>. Furthermore, only one peak corresponding to the Si-O bonding was found for O. In contrast, when analyzing the SRO layer, Si<sup>0</sup> is present together with the other states, indicating the appearance of Si-Si bonding. The O peak analysis confirmed this by showing, in addition to the Si-O bonding, a new state corresponding to O-O. By employing TEM, the real thickness of the layers was compared to the nominal one for different values, thus calibrating the deposition. For samples annealed at 1200 °C, the presence of Si NCs was also observable.

The crystalline signal of Si NCs was easily identified for samples under two conditions of the tested parameters, that is, annealing temperature for the post-deposition processing and thickness of the SRO layer. Indeed, a minimum of annealing temperature of 1000 °C and layer thickness of 4.3 nm are required for the signal of Si NCs to be detected by Raman scattering (517 cm<sup>-1</sup>), with amorphous Si and/or SiO<sub>2</sub> also being observable. The NCs size for samples annealed at 1200 °C and with thicknesses of the SRO of 4.3 and 4.7 nm were also determined using a phonon confinement model,<sup>[5]</sup> respectively resulting in 3.9 and 4.2 nm, in good agreement with similar systems fabricated by other methods.

### 6.1. Si NCs embedded in SiO<sub>2</sub> by electron beam evaporation

Last, in contrast to bulk Si, Si NCs can be optically characterized via photoluminescence emission. Emission is not detected for as-deposited samples, whereas in annealed samples the PL intensity increases up to 1200 °C. In addition, the emission intensity increases and becomes narrower as the thickness of the SRO layers decreases. Two different contributions could be detected, corresponding to the emission of the Si NCs (900 nm) and Si-SiO<sub>2</sub> interface defects (750 nm). These contributions were time-resolved to shed light on their origin, each presenting two dynamic ranges and thus being fitted to:

$$I_{PL} = A_1 e\left[-\left(\frac{t}{\tau_1}\right)^{\beta_1}\right] + A_2 e\left[-\left(\frac{t}{\tau_2}\right)^{\beta_2}\right], \quad (6.1)$$

where  $A$  is the amplitude,  $\tau$  the decay time and  $\beta$  the stretching parameter; each dynamic being numerated.

Both contributions presented a first fast emission, which can be related to SiO<sub>2</sub> defects (such as O vacancies). The occurrence of stretched exponentials for the second dynamic range is due to a distribution of NCs in size, to their interaction with each other and disorder. According to a core-shell model, the high energy emission is originated at the shell, where lower  $\beta$  corresponds to defects at the Si-SiO<sub>2</sub> interface, and lower  $\tau_2$  to a high disorder. As for the low energy emission, related thus to the core,  $\tau_2$  increases with the thickness of the SRO layers, due to a larger distribution of sizes of NCs.

This work demonstrates the usefulness of electron beam evaporation for the fabrication of Si NCs-based optoelectronic devices, being it a simpler technique that can yield high quality results.

The results hereby introduced have been presented as a poster at the European Materials Research Society (EMRS) Spring Meeting 2018 and the 2018 Annual Meeting of the Institute of Nanoscience and Nanotechnology of the UB (IN<sup>2</sup>UB). A journal article was published in *Physica Status Solidi A* **216**, 1800619 (2019).



**Paper VI: Size-Controlled Si Nanocrystals Fabricated  
by Electron Beam Evaporation (DOI:  
[10.1002/pssa.201800619](https://doi.org/10.1002/pssa.201800619))**



# Size-Controlled Si Nanocrystals Fabricated by Electron Beam Evaporation

Oriol Blázquez, Lluís López-Conesa, Julià López-Vidrier, Juan Luis Frieiro, Sonia Estradé, Francisca Peiró, Jordi Ibáñez, Sergi Hernández,\* and Blas Garrido

Multilayers consisting of silicon nanocrystals (Si NCs) and SiO<sub>2</sub> are successfully fabricated by electron beam evaporation, using pure Si and SiO<sub>2</sub> targets in an oxygen-rich atmosphere for alternately depositing silicon-rich oxide (SRO) layers and SiO<sub>2</sub> barriers, respectively. A post-deposition annealing process is carried out at different temperatures in order to achieve the Si precipitation in the form of nanocrystals. The stoichiometry of the layers is determined by X-ray photoelectron spectroscopy, which confirms the controlled silicon oxidation in order to attain SRO layers. Transmission electron microscopy and Raman-scattering measurements confirm the presence of crystalline Si-nanoprecipitates. Photoluminescence spectra from the Si NC samples can be deconvoluted into two contributions, whose dynamics suggest that two different luminescent centers are responsible for the optical emission of the samples.

applications, which drastically decreases the probability of electron-hole radiative recombination. As it is well known, nanostructuring Si results in the quantization and energy increase of its allowed electronic states, properties that strongly depend on the nanostructure size.<sup>[1–3]</sup> The consequent tunability of the band gap of Si nanocrystals (Si NCs) has been widely investigated in order to employ their optical properties in light-emitting,<sup>[4–7]</sup> photovoltaic<sup>[8–10]</sup> devices or memory applications.<sup>[11,12]</sup> Matrix-embedded Si NCs are one of the most employed configurations, being SiO<sub>2</sub> the most usual dielectric matrix. By controlling the stoichiometry of silicon oxide (i.e., the Si excess), a high-temperature annealing process can be carried out which promotes the precipitation of the Si excess in the form of Si NCs.

## 1. Introduction

Since the middle of the last century, silicon has been one of the most important semiconductor materials studied by researchers thanks to its abundance, non-toxicity, and good electrical properties, thus being widely employed in the electronics industry. However, its indirect band gap is the main drawback for optical

On one hand, the control of the Si NC size has been achieved by the Si NCs/SiO<sub>2</sub> multilayers (MLs) approach, where the stoichiometric SiO<sub>2</sub> layers play the role of barrier against Si diffusion, thus limiting the growth of the Si NCs along the vertical direction.<sup>[1]</sup> In addition, several works on the effect of the annealing temperature ( $T_a$ ) and the thickness of the SiO<sub>2</sub> barriers have been carried out to determine the optimal structure for optoelectronic applications.<sup>[13,14]</sup> On the other hand, the fabrication of these nanostructures has basically been achieved by means of either chemical-vapor deposition,<sup>[3,15]</sup> sputtering,<sup>[16]</sup> or Si implantation in SiO<sub>2</sub>.<sup>[17]</sup> The electron-beam evaporation (EBE) technique has also been employed to generate multilayered Si NCs/SiO<sub>2</sub> structures. However, whereas the SiO<sub>2</sub> layers can be easily EBE-deposited, the silicon-rich oxide (SRO) layers are typically achieved via either thermal evaporation<sup>[18]</sup> or EBE<sup>[19]</sup> of SiO targets. So far, the possibility to fabricate Si NCs evaporating both SiO<sub>2</sub> and SRO layers employing the same EBE technique has not been explored yet. In the case of SRO, using pure Si target provides an alternative technique-compatible strategy; indeed, this has proved useful to synthesize colloidal Si NCs by placing the pure Si target in deionized water, followed by a thermal treatment via ultra-short pulsed laser ablation.<sup>[20]</sup>

In this work, we present the fabrication, entirely carried out by means of the EBE technique, as well as the structural and optical characterization of Si NCs embedded in a SiO<sub>2</sub> matrix. For this, a ML approach was employed by alternating the deposition of SRO layers and SiO<sub>2</sub> barriers, respectively using pure Si and SiO<sub>2</sub> targets in an oxygen-rich atmosphere.

O. Blázquez, Dr. L. López-Conesa, J. L. Frieiro, Dr. S. Estradé, Prof. F. Peiró, Dr. S. Hernández, Prof. B. Garrido  
MIND, Departament d'Enginyeria Electrònica i Biomèdica  
Universitat de Barcelona  
Martí i Franquès 1, E-08028 Barcelona, Spain  
E-mail: shernandez@ub.edu

O. Blázquez, Dr. L. López-Conesa, J. L. Frieiro, Dr. S. Estradé, Prof. F. Peiró, Dr. S. Hernández, Prof. B. Garrido  
Institute of Nanoscience and Nanotechnology (IN2UB)  
Universitat de Barcelona  
Av. Joan XXIII S/N, E-08028 Barcelona, Spain

Dr. J. López-Vidrier  
Laboratory for Nanotechnology  
Department of Microsystems Engineering (IMTEK)  
University of Freiburg  
Albert-Ludwigs-University Freiburg  
Georges-Köhler-Allee 103, D-79110 Freiburg, Germany

Dr. J. Ibáñez  
Institute of Earth Sciences Jaume Almera  
ICTJA-CSIC  
Lluís Solé i Sabarís s/n, 08028 Barcelona, Catalonia, Spain

DOI: 10.1002/pssa.201800619

## 2. Results and Discussion

First, we study the stoichiometry of SiO<sub>2</sub> and SRO layers deposited by e-beam and annealed at 1200 °C by X-ray photoelectron spectroscopy (XPS). For this analysis, due to the limited depth resolution of the experimental set-up (during the sputtering process), bulk SiO<sub>2</sub> and SRO samples were employed for determining their composition, and thus the equivalent of the ML samples. Figure 1 shows the Si2p and O1s XPS signals, whose areas under the curve were determined and corrected for the sensitivity factor of each atomic specimen. From this analysis, atomic concentrations of Si (34%) and O (66%) were determined for the SiO<sub>2</sub> sample, which confirms its stoichiometry. In contrast, the SRO layer presents a clear substoichiometry with atomic values of Si (42%) and O (58%), corresponding to SiO<sub>1.4</sub>, which confirms that Si is partially oxidized when it is evaporated from a pure Si target with an O<sub>2</sub> line. Exploring in more detail the Si2p spectra of both SiO<sub>2</sub> and SRO layers, deconvolution via different pseudo-Voigt fits was performed in order to determine the contribution of the different oxidation states of Si. In the case of the SiO<sub>2</sub> sample [see Figure 1 (a)], the main contribution corresponds to the Si<sup>4+</sup> state (103.7 eV), with a decreasing contribution of the other oxidation

states as the oxidation number decreases, namely Si<sup>3+</sup> (102.6 eV), Si<sup>2+</sup> (101.4 eV), and Si<sup>1+</sup> (100.1 eV), progressively. No contribution of Si<sup>0</sup> is observed, which is in agreement with the stoichiometry of this layer. On the other hand, Figure 1(b) shows the Si2p signal of the SRO layer, exhibiting a broader spectrum than the SiO<sub>2</sub> layer. In this case, the distribution of the different oxidation states of silicon is clearly changed, decreasing the Si<sup>4+</sup> (103.7 eV) contribution and increasing the Si<sup>3+</sup> (102.5 eV), Si<sup>2+</sup> (101.3 eV), and Si<sup>1+</sup> (100.0 eV) ones. In contrast to the SiO<sub>2</sub> layer, the SRO layer shows the metallic Si<sup>0</sup> (98.6 eV) contribution, indicating Si-Si bonds due to the lack of oxygen. Regarding the O1s analysis of the SiO<sub>2</sub> presented in Figure 1(c), a single pseudo-Voigt function was fitted at 532.0 eV, indicating that oxygen is only bound to Si atoms in a single configuration (-O-). However, the SRO layer exhibits an O1s broader spectrum [see Figure 1(d)], which suggests that part of the oxygen presents different bonds. The main contribution is centered at 532.1 eV and it is again attributed to oxygen bound to Si atoms in single configuration (-O-), like within the SiO<sub>2</sub> layer. The other contribution displays a higher energy (533.6 eV) and it can be directly correlated with the substoichiometry of the layer. In this case, peroxy configuration (-O-O-) is sensitive to be formed in the regions where Si excess is present.<sup>[21]</sup> In Table 1, the binding

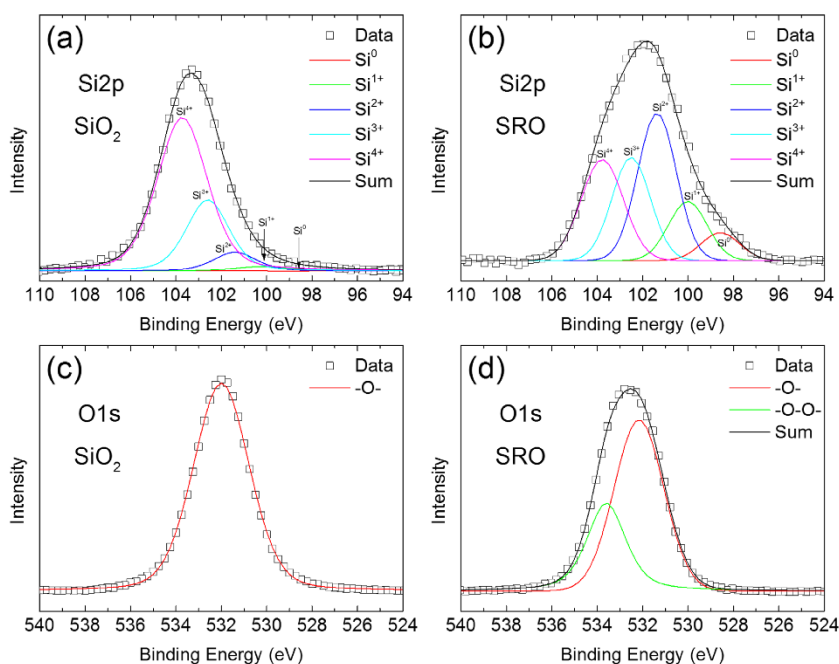


**Figure 1.** XPS analysis corresponding to bulk deposition of both SiO<sub>2</sub> and SRO, after annealing at 1200 °C, employed for the fabrication of the multilayered structure. a) and b) present the Si2p signal of SiO<sub>2</sub> and SRO, respectively, deconvoluted by means of pseudo-Voigt fits related to the different oxidation states of Si. c) and d) show the spectra of the O1s for both layers, SiO<sub>2</sub> and SRO, respectively. In this case, (c) displays a single pseudo-Voigt fit (-O-), whereas (d) is deconvoluted into two pseudo-Voigt contributions related to (-O-) and (-O-O-) oxygen configurations.

**Table 1.** Peak positions corresponding to the different contributions of Si2p and O1s, obtained fitting the XPS spectra acquired from SiO<sub>2</sub> and SRO layers.

	SiO <sub>2</sub>		SRO	
	Si2p	O1s	Si2p	O1s
Peak position (eV)	-	-	98.6	-
	100.1	532.0	100.0	532.1
	101.4	-	101.3	533.6
	102.6	-	102.5	-
	103.7	-	103.7	-
Integrated area (arb. units)	7.25	34.90	4.92	17.54
Atomic concentration (%)	34	66	42	58

energy, integrated area and resulting atomic concentration of each contribution are summarized.

Transmission electron microscopy (TEM) images of the test sample annealed at 1200 °C were analyzed in order to match the nominal thicknesses with the measured Si NC sizes. In Figure 2(a), an energy-filtered TEM (EFTEM) image of this sample is exhibited, filtering the energy around the Si plasmon peak ( $\approx 17$  eV). The image clearly confirms the ML structure even at this high annealing temperature, where the brightest zones correspond to a higher Si concentration. In the stack near the Si substrate (the first layers at the bottom of the image), the SiO<sub>2</sub> barriers are kept constant at a measured thickness of 2.7 nm, while the measured thickness of the SRO layers varies from 3.5 to 4.7 nm. In the second stack (layers at the top of the image), the SiO<sub>2</sub> barriers exhibit thickness values that vary from 2.3 to 3.5 nm, with constant SRO layers of a measured thickness of 3.5 nm. Thanks to this test sample, nominal and real thicknesses were correlated. Indeed, the increase in nominal thickness clearly corresponds to an increase in the real (measured) thickness. This relation between nominal and measured SiO<sub>2</sub> and SRO thicknesses is plotted in Figure 2(b), displaying a linear trend. This study has allowed calibrating our deposition set-up and determining the real thickness of the

SRO layers ( $L_{\text{SRO}}$ ). High-resolution TEM (HRTEM) images were also acquired in the center of this first stack to determine whether Si NC formation was achieved during the annealing process. In Figure 2(c), different Si lattice planes (highlighted by red lines) are observed and attributed to the Si NC formation, providing an unequivocal proof that the Si nanoaggregates contain a non-negligible crystalline phase. It is important to note that only crystalline planes parallel to the electron-beam can be observed, which substantially reduces the number of visible Si NCs.

Raman measurements were performed at room temperature on samples deposited on fused silica substrates. In Figure 3(a), the Raman spectra corresponding to the sample with the largest SRO thickness ( $L_{\text{SRO}} = 4.7$  nm), annealed at different  $T_a$ , are plotted. Two different features can be clearly distinguished from the spectra: a broad band from 300 to 500  $\text{cm}^{-1}$ , with its maximum around 470  $\text{cm}^{-1}$ , related to disorder-activated acoustical and optical modes in amorphous Si and amorphous SiO<sub>2</sub>, and a peak centered around  $\approx 517$   $\text{cm}^{-1}$ , attributed to the crystalline Si transversal-longitudinal optical (TO-LO) phonon mode. The first band is observed in all the spectra, whereas the crystalline feature appears only after an annealing beyond 1000 °C. This last feature indicates the formation of crystalline aggregates under these particular thermal annealing conditions. Despite the fact that the precipitation of the Si excess within the SRO layers and the formation of amorphous Si nanoclusters already takes place at temperatures as low as 700–800 °C, a higher  $T_a$  is necessary for the crystallization of these nanoaggregates.<sup>[13,22]</sup> In this regard, the presence of the crystalline Si peak in the spectra corresponding to samples annealed at  $T_a > 1000$  °C confirms the presence of a Si crystalline phase, which totally agrees with the lattice planes observed by HRTEM [see Figure 2(c)].

The Raman spectra from the samples annealed at 1200 °C and containing different  $L_{\text{SRO}}$  are displayed in Figure 3(b), showing the above-mentioned contributions. However, in this case, the peak related to crystalline Si is only observed for  $L_{\text{SRO}}$  equal or thicker than 4.3 nm, with no observation of thinner SRO layers. In fact, the observed contribution from the SiO<sub>2</sub>, either coming

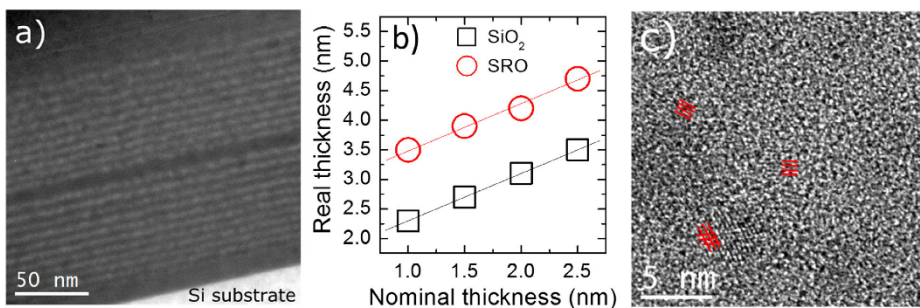


**Figure 2.** a) EFTEM image obtained after filtering around the Si plasmon peak ( $\approx 17$  eV) with a 3 eV energy window. Bright regions in the image correspond to Si-rich oxide (SRO) regions. b) Relation between nominal and real deposition thicknesses of SiO<sub>2</sub> and SRO layers. c) HRTEM image in the center of the first stack. Si lattice planes can be observed (highlighted by red lines) for some crystalline nanoaggregates.

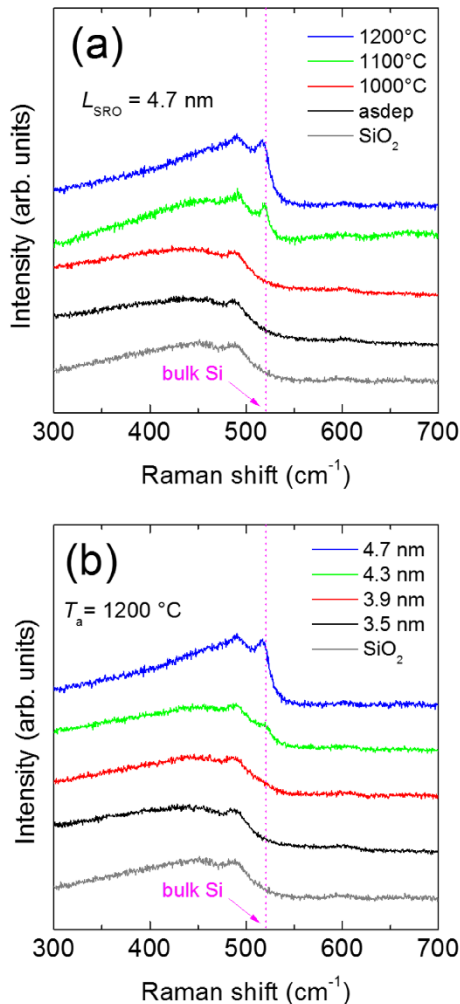


**Figure 3.** a) Raman spectra corresponding to the samples with 4.7-nm-thick SRO layers for both the as-deposited samples and the ones annealed at different  $T_a$ . b) Raman spectra corresponding to the samples with different SRO thicknesses annealed at  $T_a = 1200^\circ\text{C}$ . In both figures, the pink dotted vertical line indicates the peak position of the bulk crystalline Si signal. In addition, the Raman spectrum of the  $\text{SiO}_2$  substrate (gray lines) is added for comparison.

from the surroundings or from the substrate, could be masking the crystalline contribution. Another possible explanation might be ascribed to the fact that a critical Si mass is necessary to achieve the formation of crystalline aggregates.<sup>[23]</sup> Analyzing this

crystalline feature using the phonon confinement model described in Ref. [24] in samples with  $L_{\text{SRO}} = 4.3\text{ nm}$  and  $L_{\text{SRO}} = 4.7\text{ nm}$  [see Figure 3(b)], we have found a crystalline Si NC size of 3.9 and 4.2 nm, respectively. In addition, by comparing the total Si-cluster size from TEM and the Si-crystalline size from the Raman analysis, we conclude that there is an almost full crystallization of the precipitated Si, in good accordance with previous results in a similar system.<sup>[24]</sup> These results are in excellent agreement with HRTEM images, where crystalline nanoaggregates are observed with sizes around 4 nm [see Figure 2(c)].

Photoluminescence measurements were carried out on EBE-grown Si NCs/ $\text{SiO}_2$  samples deposited on Si substrates, exciting them with the 532-nm line of a continuous wave Nd:YAG laser. In Figure 4(a), the PL spectra from the samples with  $L_{\text{SRO}} = 3.9\text{ nm}$  and annealed at different temperatures are shown. In the case of the as-deposited sample, no emission is observed, which is in agreement with the fact that the precipitation of the Si excess in the form of nanoaggregates has not taken place yet. In contrast, annealed samples exhibit PL emission with a broad spectrum in the red-infrared part of the spectrum. The intensity of this PL emission increases with the annealing temperature, achieving its maximum at  $1200^\circ\text{C}$ . A similar evolution has been found for the samples with different  $L_{\text{SRO}}$ , indicating that the optimum annealing temperature for obtaining improved optical emission matches with the one for having high crystalline quality, as demonstrated from the Raman study.

The PL spectra of the samples with different  $L_{\text{SRO}}$  and annealed at  $1200^\circ\text{C}$  are shown in Figure 4(b). In this case, the PL intensity decreases as the  $L_{\text{SRO}}$  increases, exhibiting also a broader lineshape. Considering that the PL lineshape from Si NCs is constituted by a combination of Gaussian contributions (see, e.g., Refs. [19,25]), our spectra could be deconvolved using only two Gaussian functions in the energy domain, one of them centered at higher energies (around 750 nm) and another centered at lower energies (around 900 nm). The deconvolution of the PL spectra for samples with  $L_{\text{SRO}} = 3.5\text{ nm}$  and  $L_{\text{SRO}} = 4.7\text{ nm}$  is displayed in Figure 4(c), exhibiting excellent accordance between the experimental spectra and the Gaussian fits. In Figure 4(d), the band gap energy corresponding to each contribution as a function of  $L_{\text{SRO}}$  is plotted for all samples annealed at  $T_a = 1200^\circ\text{C}$ . The peak energy of both contributions decreases for larger  $L_{\text{SRO}}$  values, which is consistent with the reduction of quantum confinement of carriers in larger Si NCs. However, this trend is more accentuated in the case of the lower-energy contribution (green circles). In addition, the deconvolved peak at lower energies displays an overall intensity which is almost independent on  $L_{\text{SRO}}$ , in contrast to the intensity of the higher-energy contribution (blue squares), exhibiting a pronounced intensity quenching at larger  $L_{\text{SRO}}$  [see Figure 4(e)]. Considering the peak energy values and the intensity behavior reported in the literature for Si NCs with similar sizes,<sup>[1–3,25]</sup> our observations suggest that the low-energy contribution is directly related to Si NCs emission via radiative electron-hole recombination, whereas the high energy contribution could be associated to highly localized defect levels at the Si- $\text{SiO}_2$  interface, in good agreement with Ref. [25].

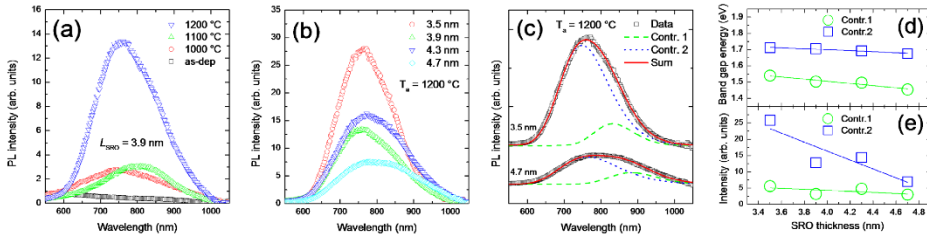


**Figure 4.** PL spectra corresponding to the samples with (a) constant  $L_{\text{SRO}} = 3.9$  nm and annealed at different temperatures, and (b) different  $L_{\text{SRO}}$  and annealed at  $1200^\circ\text{C}$ . (c) Example of the two-contribution spectra deconvolution carried out on the samples with  $L_{\text{SRO}} = 3.5$  (thinnest sample) and  $L_{\text{SRO}} = 4.7$  nm (thickest one), both annealed at  $1200^\circ\text{C}$ . (d) Peak energy corresponding to each PL contribution from the samples annealed at  $1200^\circ\text{C}$ , as a function of  $L_{\text{SRO}}$ . (e) Evolution of PL intensity of each contribution from the samples annealed at  $1200^\circ\text{C}$ , as a function of  $L_{\text{SRO}}$ .

In order to obtain more information about the origin of both contributions, PL dynamics were studied by exciting the samples with a  $\text{Nd}^{3+}:\text{YAG}$  5-ns-pulsed laser. To perform time-resolved PL spectroscopy, the monochromator was set at two different wavelengths, 850 and 650 nm, which have been selected to separately maximize each PL contribution. The PL time decay of the samples annealed at  $1200^\circ\text{C}$  for different  $L_{\text{SRO}}$ , at 850 and 650 nm, is shown in **Figure 5**(a) and (b), respectively. At both wavelengths, the behavior of the PL dynamics suggests two different time evolutions, which could be fitted by the

combination of two stretched exponential decay functions, following the typical analysis for Si NCs:<sup>[26]</sup>

$$I_{\text{PL}} = A_1 \exp\left[-\left(\frac{t}{\tau_1}\right)^{\beta_1}\right] + A_2 \exp\left[-\left(\frac{t}{\tau_2}\right)^{\beta_2}\right] \quad (1)$$

The first term in Equation (1) represents the PL decay with faster dynamics, characterized by its decay time  $\tau_1$ , stretching parameter  $\beta_1$  and amplitude  $A_1$ ; the second term describes the

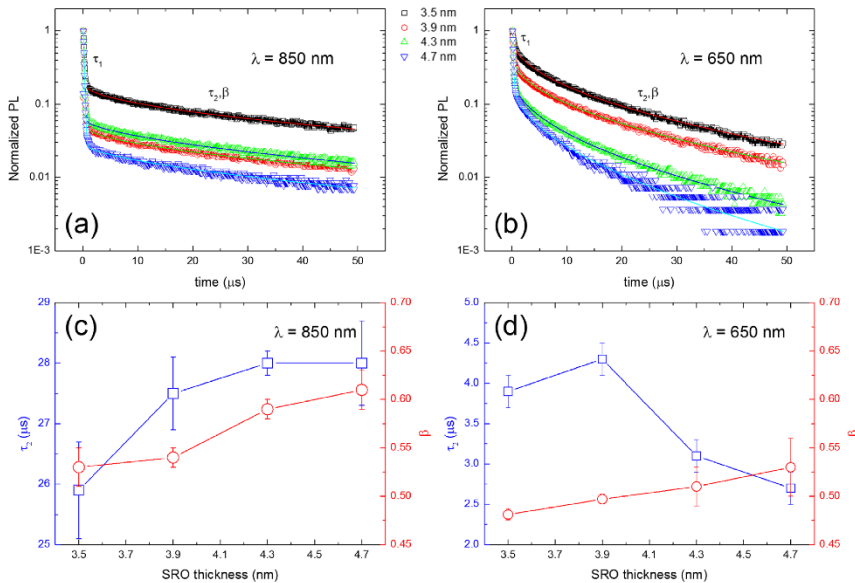


**Figure 5.** Time evolution of the PL intensity corresponding to the samples containing different  $L_{\text{SRO}}$  and annealed at  $1200^\circ\text{C}$ , measured at (a) 850 nm and (b) 650 nm. The corresponding fits to the fast and slow components are also displayed. (c) and (d) plot the slow decay time,  $\tau_2$ , and stretching parameter,  $\beta$ , corresponding to the same samples in (a) and (b).

slower PL decay, with its own decay time  $\tau_2$ , amplitude  $A_2$ , and stretching parameter  $\beta_2$ . In all cases, the faster contribution exhibits a stretching parameter  $\beta_1 = 1$  (i.e., equivalent to a single exponential) and a decay time of  $\tau_1 = (140 \pm 10)$  ns, which matches with time response limitations of our experimental set-up. Hence, there are luminescent centers with decay time faster than this value (and thus not measurable by our equipment), which are typically attributed to emission related to  $\text{SiO}_2$  matrix defects (probably due to oxygen vacancies).<sup>[27–29]</sup>

The slow decay time  $\tau_2$  exhibits a different behavior depending on the observation wavelength. Comparing Figure 5 (a) and (b), one can observe that the low-energy contribution at 850 nm presents decay times  $\tau_2$  lower than the high-energy one at 650 nm, which suggests a different nature of the luminescent centers. In addition, the time evolution of PL at 850 nm shows a lower stretching parameter than the curves at 650 nm. In order to study these parameters in detail, the evolution of  $\tau_2$  and  $\beta$  as a function of  $L_{\text{SRO}}$  are represented for both contributions [Figures 5(c) and (d)]. The Figure 5(c) shows that the contribution at 850 nm has an increase of  $\tau_2$  for larger  $L_{\text{SRO}}$ , obtaining a constant value at  $L_{\text{SRO}}$  larger than 4.3 nm, whereas the  $\beta$  value slowly increases with  $L_{\text{SRO}}$ . Analyzing both parameters ( $\tau_2$  and  $\beta$ ) for the high-energy contribution [see Figure 5(d)], one can see that  $\tau_2$  exhibits values around one order of magnitude lower than the low-energy contribution, as well as decreasing at thicker  $L_{\text{SRO}}$ . Again, the stretching parameter  $\beta$  exhibits the same evolution as a function of  $L_{\text{SRO}}$  than in the low-energy contribution, in which a clear increase of its value is observed, despite still keeping lower values.

The results concerning the excitonic recombination dynamics can be further discussed in terms of their time evolution. In particular, the stretched exponential behavior exhibited by both low- (850 nm) and high-energy (650 nm) contributions [see Figure 5(a) and (b), respectively] already gives relevant information about the emission centers that yield the observed luminescence. The stretched exponential function has typically been ascribed to i) a dispersion in excitonic recombination times originated by a broad NC size distribution, each NC size population exhibiting different characteristic decay times;<sup>[30,31]</sup> ii) the interaction between neighboring NCs that induce effects related to electron-phonon coupling;<sup>[32,33]</sup> or iii) the degree of dispersion from the electron and hole motion due to disorder within the material.<sup>[34,35]</sup> In these three different but correlated frames, the stretching parameter  $\beta$  can be interpreted as a dispersion from the ideal case ( $\beta = 1$ ) of size mono-population of non-interacting (i.e., separated enough) Si NCs. These characteristics allow explaining the observed PL results so far. Indeed, and as can be seen in Figure 5(c) and (d), the high-energy contribution presents remarkably lower  $\beta$  values than the low-energy one. This occurrence could be attributed to highly localized defect levels at the Si-SiO<sub>2</sub> interface, with a larger degree of disorder than in the case of the high-energy contribution, in agreement with the core-shell model. This assumption is supported by the shorter recombination times ( $\tau_2$ ), by about one order of magnitude, which might indicate exciton instability because of insufficient carrier confinement due to high disorder. Finally, Figure 5(c) and (d) show how  $\tau_2$  clearly increases for the low-energy contribution at thicker SRO

layers until saturating at the thickest  $L_{\text{SRO}} = 4.7$  nm, since even thicker barriers will not propitiate the precipitation and crystallization of larger NCs, but instead the broadening of the NC size distribution centered around a saturated NC mean size.<sup>[36]</sup> In the case of the high-energy component of PL, we observed the opposite trend compared to the low-energy one, with a reduction of the radiative time  $\tau_2$  at larger NCs, in agreement with previous reports in similar samples, which indicates luminescence from the amorphous phase at large NCs.

### 3. Conclusions

To summarize, the results obtained from the different structural and optical techniques employed in this study revealed the presence of two different optically active luminescent centers within our EBE-fabricated samples: size-dependent excitonic recombination typically reported for Si quantum dots (low-energy PL contribution) and highly localized disorder-based emission (high-energy PL component) tightly related to the NC amorphous shell and/or NC/SiO<sub>2</sub> matrix interface defects. Therefore, by means of the EBE deposition of alternated SiO<sub>2</sub> and oxidized Si (i.e., the SRO) nanolayers and after a proper high-temperature annealing treatment, we have shown that we are able to tune the luminescence yielded by Si NCs. This has been achieved by controlling the deposited SRO thickness and annealing conditions, which results in the modulation of the two PL emission components. Consequently, the adequacy of the EBE technique to prepare high-quality and light-emitting Si nanostructures has been proved, which paves the way for easy-manufacturing Si NC-based optoelectronic devices.

### 4. Experimental Section

Multilayers of SRO/SiO<sub>2</sub> were deposited onto either *p*-type (100)-Si or fused silica substrates by means of electron-beam evaporation. The employed system was a PFEIFFER VACUUM Classic 500 with a Ferrotec GENIUS electron-beam controller equipped with a Ferrotec CARRERA high-voltage power supply. Before the deposition, the substrates were successively cleaned with acetone, isopropyl alcohol, ethanol, and deionized water, being agitated ultrasonically in each process. The MLs were grown depositing alternatively SiO<sub>2</sub> and SRO layers, by respectively evaporating SiO<sub>2</sub> and Si targets, both at a rate of  $0.5 \text{ \AA s}^{-1}$ . The base pressure in the chamber was  $2 \times 10^{-6}$  mbar and the substrate was kept at 100 °C. An O<sub>2</sub> line (1.5 sccm), equivalent to  $6 \times 10^{-5}$  mbar, was introduced in the chamber during the whole process, avoiding a possible substoichiometry of the SiO<sub>2</sub> and promoting a partial oxidation of the Si (SRO). In order to control the deposition of SRO and SiO<sub>2</sub> layers, nominal and final thicknesses were compared by fabricating a test sample, which consists of two multilayer stacks separated by 10-nm-thick SiO<sub>2</sub> as a reference layer. The first stack (close to the substrate) presents a variation of the SRO layers keeping constant the SiO<sub>2</sub> barriers thickness at 2.0 nm, whereas for the other one the SiO<sub>2</sub> barrier thickness was varied while keeping constant the SRO layers thickness at 2.0 nm. For the study of the optical properties of EBE-prepared Si NCs, different samples were deposited with SRO nominal layers ranging from 1.0 to 2.5 nm with a constant SiO<sub>2</sub> barrier with a nominal thickness of 1.5 nm. This multi-layered structure was repeated five times, adding a 10-nm of SiO<sub>2</sub> as buffer and capping

layers. All ML samples underwent an annealing process inside a tubular furnace for 1 h in N<sub>2</sub> atmosphere, at different annealing temperatures ranging from 1000 to 1200 °C.

In order to determine the stoichiometry of the SRO and SiO<sub>2</sub> layers, an XPS analysis was carried out using a PHI 5500 Multitechnique System. Bulk samples of both materials, SRO and SiO<sub>2</sub>, were required due to the impossibility of the system to distinguish each individual layer in a multilayered structure with nanometer-thick layers. XPS measurements were carried out in 200-nm thick samples (either SRO or SiO<sub>2</sub>) at a depth of about 50 nm, in order to ensure that information only from the bulk of the samples is acquired, with negligible contribution from their surfaces. The structural characterization was carried out by means of TEM. A conventional mechanical polishing method was employed in cross-section geometry with a subsequent low angle Ar<sup>+</sup> ion milling up to the electron transparency of the sample. TEM images were acquired by a JEOL 2010F microscope, operated at 200 kV and equipped with a field emission gun coupled to a Gatan imaging filter with 0.8 eV energy resolution. EFTEM in scanning mode and HRTEM were employed to analyze the ML structure and the Si NC formation, respectively. The crystallinity of the Si NCs deposited onto fused silica substrate was analyzed by Raman measurements in backscattering configuration with a Horiba Jobin-Yvon LabRam spectrometer, exciting the samples with the 532-nm line of a Nd:YAG laser at room temperature, keeping the power density on the sample at  $\approx 5 \times 10^4 \text{ W cm}^{-2}$ . The optical properties were determined measuring the photoluminescence emission of the films grown onto Si substrate in a range between 550 and 1050 nm, exciting the samples with the 325-nm line of a He-Cd laser, using a power density of  $8 \times 10^3 \text{ W cm}^{-2}$ , and collecting the emitted light with the same experimental setup; the PL intensity of all spectra was corrected by the spectral response of the system. Finally, time-resolved PL measurements were carried out by exciting the samples with the third harmonic line (355 nm) of a BRILLIANT Nd<sup>3+</sup>:YAG 5-ns-pulsed laser at a peak power density of  $10^8 \text{ W cm}^{-2}$ , while inspecting their emission at 650 and 850 nm, in order to understand the origin of the different luminescence contributions.

## Acknowledgements

This work was financially supported by the Spanish Ministry of Economy and Competitiveness (TEC2016-76849-C2-1-R and MAT2015-71035-R). O.B. also acknowledges the subprogram "Ayudas para Contratos Predoctorales para la Formación de Doctores" from the Spanish Ministry of Economy and Competitiveness for economical support. J.L.F. also acknowledges the subprogram "Ayudas para la Formación de Profesorado Universitario" from the Spanish Ministry of Education, Culture and Sports for economical support.

## Conflict of Interest

The authors declare no conflict of interest.

## Keywords

electron beam evaporation, multilayered silicon nanocrystals, photoluminescence, Raman scattering, transmission electron microscopy

Received: July 31, 2018

Revised: October 24, 2018

Published online:

- [1] M. Zacharias, J. Bläsing, P. Veit, L. Tsybeskov, K. Hirschman, P. M. Fauchet, *Appl. Phys. Lett.* **1999**, *74*, 2614.
- [2] J. Heitmann, R. Scholz, M. Schmidt, M. Zacharias, *J. Non. Cryst. Solids* **2002**, *299–302*, 1075.
- [3] J. Heitmann, F. Müller, M. Zacharias, U. Gösele, *Adv. Mater.* **2005**, *17*, 795.
- [4] N. Lalic, J. Linnros, *J. Appl. Phys.* **1996**, *80*, 5971.
- [5] S. Chan, P. M. Fauchet, *Appl. Phys. Lett.* **1999**, *75*, 274.
- [6] J. López-Vidrier, Y. Berencén, S. Hernández, O. Blázquez, S. Gutsch, J. Laube, D. Hiller, P. Löper, M. Schnabel, S. Janz, M. Zacharias, B. Garrido, *J. Appl. Phys.* **2013**, *114*, 163701.
- [7] J. López-Vidrier, S. Gutsch, O. Blázquez, D. Hiller, J. Laube, R. Kaur, S. Hernández, B. Garrido, M. Zacharias, *Appl. Phys. Lett.* **2017**, *110*, 203104.
- [8] I. Perez-Wurfl, X. Hao, A. Gentle, D.-H. Kim, C. Conibeer, M. A. Green, *Appl. Phys. Lett.* **2009**, *95*, 153506.
- [9] D. Di, I. Perez-Wurfl, G. Conibeer, M. A. Green, *Sol. Energy Mater. Sol. Cells* **2010**, *94*, 2238.
- [10] C. Conibeer, M. Green, R. Corkish, Y. Cho, E. C. Cho, C. W. Jiang, T. Fangsuwannarak, E. Pink, Y. Huang, T. Puzzer, T. Trupke, B. Richards, A. Shalav, K. Lung Lin, *Thin Solid Films* **2006**, *511–512*, 654.
- [11] S. Tiwari, F. Rana, H. Hanafi, A. Hartstein, E. F. Crabbé, K. Chan, *Appl. Phys. Lett.* **1996**, *68*, 1377.
- [12] T. Z. Lu, M. Alexe, R. Scholz, V. Talalae, R. J. Zhang, M. Zacharias, *J. Appl. Phys.* **2006**, *100*, 014310.
- [13] J. López-Vidrier, S. Hernández, D. Hiller, S. Gutsch, L. López-Conesa, S. Estradé, F. Peiró, M. Zacharias, B. Garrido, *J. Appl. Phys.* **2014**, *116*, 133505.
- [14] J. López-Vidrier, Y. Berencén, S. Hernández, B. Mundet, S. Gutsch, J. Laube, D. Hiller, P. Löper, M. Schnabel, S. Janz, M. Zacharias, B. Garrido, *Nanotechnology* **2015**, *26*, 185704.
- [15] Y. Lebour, P. Pellegrino, S. Hernández, A. Martínez, E. Jordana, J.-M. Fedeli, B. Garrido, *Phys. E* **2009**, *41*, 990.
- [16] K. Ma, J. Y. Feng, Z. J. Zhang, *Nanotechnology* **2006**, *17*, 4650.
- [17] M. Perálvarez, J. Barreto, J. Carreras, A. Morales, D. Navarro-Urrios, Y. Lebour, C. Domínguez, B. Garrido, M. Perálvarez, C. Domínguez, C. Domínguez-Horna, *Nanotechnology* **2009**, *20*, 1.
- [18] A. Martínez, S. Hernández, P. Pellegrino, O. Jambois, P. Miska, M. Grün, H. Rinnert, M. Vergnat, V. Izquierdo-Roca, J. M. Fedeli, B. Garrido, *Phys. Status Solidi C* **2011**, *8*, 969.
- [19] D. C. Gunduz, A. Tankut, S. Sedani, M. Karaman, R. Turan, *Phys. Status Solidi C* **2015**, *12*, 1229.
- [20] S. Alkis, A. K. Okyay, B. Ortaç, *J. Phys. Chem. C* **2012**, *116*, 3432.
- [21] A. Mehonic, M. Buckwell, L. Montesi, L. Garnett, S. Hudziak, S. Fearn, R. Chater, D. McPhail, A. J. Kenyon, *J. Appl. Phys.* **2015**, *117*, 124505.
- [22] S. Hernández, A. Martínez, P. Pellegrino, Y. Lebour, B. Garrido, E. Jordana, J. M. Fedeli, *J. Appl. Phys.* **2008**, *104*, 044304.
- [23] M. Zacharias, P. Streitenberger, *Phys. Rev. B* **2000**, *62*, 8391.
- [24] S. Hernández, J. López-Vidrier, L. López-Conesa, D. Hiller, S. Gutsch, J. Ibáñez, S. Estradé, F. Peiró, M. Zacharias, B. Garrido, *J. Appl. Phys.* **2014**, *115*, 203504.
- [25] J. Ibáñez, S. Hernández, J. López-Vidrier, D. Hiller, S. Gutsch, M. Zacharias, A. Segura, J. Valenta, B. Garrido, *Phys. Rev. B* **2015**, *92*, 035432.
- [26] M. Greben, P. Khoroshy, X. Liu, X. Pi, J. Valenta, *J. Appl. Phys.* **2017**, *122*, 034304.
- [27] J. A. Rodríguez, M. A. Vásquez-Agustín, A. Morales-Sánchez, M. Aceves-Mijares, *J. Nanomater.* **2014**, *2014*, 1.
- [28] O. Blázquez, J. López-Vidrier, L. López-Conesa, M. Busquets-Masó, S. Estradé, F. Peiró, S. Hernández, B. Garrido, *J. Appl. Phys.* **2016**, *120*, 135302.

- [29] G. R. Lin, C. J. Lin, K. C. Yu, *J. Appl. Phys.* **2004**, *96*, 3025.
- [30] J. Linnros, N. Lalic, A. Galeckas, V. Crivickas, *J. Appl. Phys.* **1999**, *86*, 6128.
- [31] M. Dovrat, Y. Goshen, J. Jedrzejewski, I. Balberg, A. Sa'ar, *Phys. Rev. B* **2004**, *69*, 1.
- [32] S. L. Brown, R. Krishnan, A. Elbaradei, J. Sivaguru, M. P. Sibi, E. K. Hobbie, *AIP Adv.* **2017**, *7*, 055314.
- [33] S. L. Brown, J. B. Miller, R. J. Anthony, U. R. Kortshagen, A. Kryjevski, E. K. Hobbie, *ACS Nano* **2017**, *11*, 1597.
- [34] L. Pavesi, M. Ceschini, *Phys. Rev. B* **1993**, *48*, 17625.
- [35] L. Pavesi, *J. Appl. Phys.* **1996**, *80*, 216.
- [36] J. López-Vidrier, S. Hernández, A. M. Hartel, D. Hiller, S. Gutsch, P. Lôper, L. López-Conesa, S. Estradé, F. Peiró, M. Zacharias, B. Garrido, *Energy Proc.* **2011**, *10*, 43.

## 6.2. Resistance state read through light emission

As presented before, the selection of a SiO<sub>2</sub>-Si NCs active layer for resistive switching aimed at taking advantage of both the presence of defective SiO<sub>x</sub> areas, where resistive switching could be initiated, and the optical properties of Si nanostructures. A possible combination of electrical and optical properties in one resistive switching device paves the way to a new generation of *optical memristors* that can be written or read either electrically or optically. This expands their range of applications into the field of optoelectronics, with the added benefits of using light signals.

The basic device structure fabricated for this work consisted of Si NCs MLs deposited on top of a Si substrate and with ZnO as a top transparent electrode. Whereas the number of SRO layers that would become nanostructured Si was maintained at five, the presence or absence of other layers were tested in different combinations to find the best resistive switching conditions. These included a top SiO<sub>2</sub> layer capping the MLs and a Si<sub>3</sub>N<sub>4</sub> thin layer between the substrate and the MLs, which favors minority carriers injection from the substrate into the MLs.<sup>[4]</sup> Of the four possible devices, the best resistive switching conditions occur when the Si<sub>3</sub>N<sub>4</sub> is present, but not the SiO<sub>2</sub> capping layer. The MLs and the Si<sub>3</sub>N<sub>4</sub> were deposited via PECVD, whereas photolithographically-patterned ALD-deposited ZnO was employed as top electrode.

The first test carried out with the devices was their resistive switching performance. The devices present a highly resistive pristine state in accordance with SiO<sub>2</sub> being the dielectric, which is broken through the electroforming process at 9.5 V. A current compliance is set at 100 μA to avoid a permanent LRS. The device has a bipolar behavior, as expected from the valence change mechanism taking place, that is, O ions being liberated leaving behind a network of SiO<sub>x</sub> conductive filaments. Thus, the reset process takes place for negative polarity at around -8 V. Finally, the HRS is observed to be less resistive than the pristine state of the device, owing to a partial re-oxidation of the CFs rather than it being complete. A difference of two orders of magnitude in current (or resistance) is maintained for most of the cycles.

## 6.2. Resistance state read through light emission

Once the resistive switching cycle has been established, and bearing in mind the optical properties of Si NCs, different devices were set to either LRS or HRS. The electroluminescence of the devices was measured at different constant voltages applied below the reset and set process values, monitoring the current to avoid a change of state. Electroluminescence emission is observed under certain conditions: either in HRS and large applied voltage in inversion or accumulation, or in LRS in accumulation. A clear difference is already observed between both conditions, the first resulting in a peak-like emission, whereas a broad band is obtained in LRS. This points towards different origins for the emissions, e.g., different luminescent centers.

Indeed, an in-depth analysis of each emission revealed that that of HRS corresponds to a peak centered at 900 nm, in perfect agreement with  $\sim 4$ -nm-size Si NCs (as observed for these samples via TEM). In contrast, the emission at LRS can be deconvoluted into two emissions, one also corresponding to Si NCs at 900 nm, and a broader one centered at 670 nm, which can be attributed to the emission of ZnO defects.<sup>[7]</sup> This has been corroborated by measuring the emission in Figure 6.1(a) of a reference device in a similar structure that does not include the Si NCs MLs, where only a wide emission centered at  $\sim 700$  nm is observed. An ideal reading condition for the devices can be set to 6 V, where no emission can be observed at LRS, and high intensity NIR occurs at HRS, clearly distinguishing the state of the device. Accumulation conditions ( $V < 0$ ) are not recommended, since the emission exhibits a low intensity for both states until reaching values close to the reset voltage.

Finally, the emissions were correlated with the VCM and the state of the device. In pristine conditions, a very high intensity emission from Si NCs is observed, as recombination processes take place within them. As shown in Figure 6.1(b), the emission of the pristine and HRS are very similar, with only a difference in intensity. This owes to the same luminescent centers being active for both states, i.e. Si NCs, with some of them losing the quantum confinement in HRS due to the remaining CFs. In HRS charges partially travel through the dielectric as low resistance paths connecting the electrodes are unavailable, permitting again the recombination in the Si NCs and thus a higher intensity emission from them.

## Combined properties in Si NC-containing devices

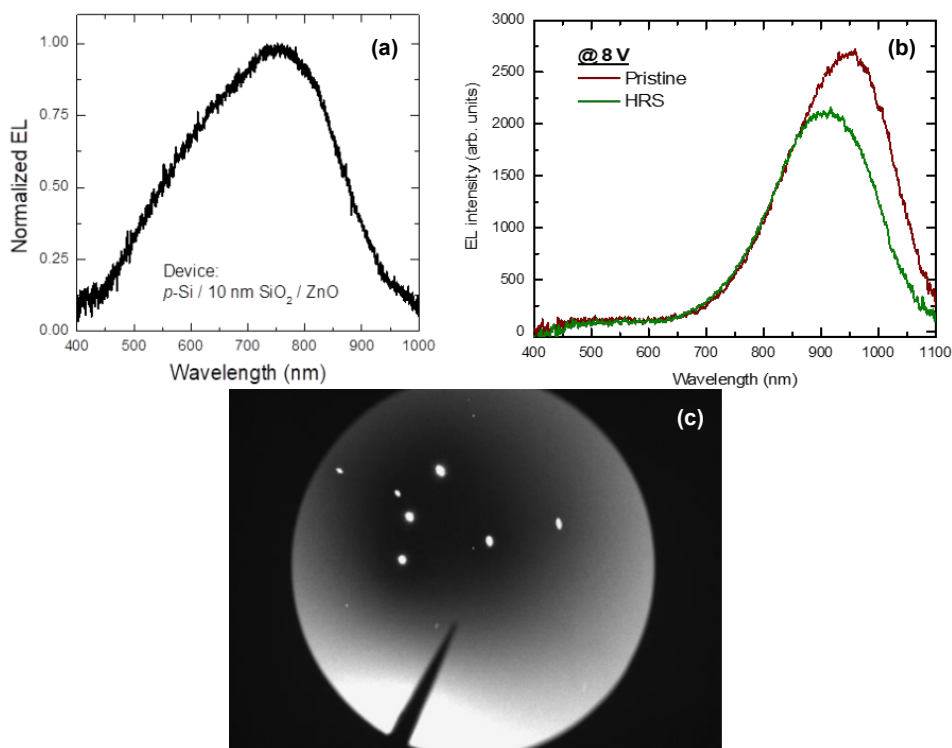


**Figure 6.1.** (a) EL emission of a reference device not containing Si NCs MLs. (b) Comparison of EL emission in pristine and HRS conditions of devices with Si NCs MLs. (c) Image of a device containing Si NCs MLs emitting light in spot-like conditions when in LRS.

When CFs are formed and the device is in LRS, a high current is injected to the device through the ZnO contact, which allows for the emission of its defects. Figure 6.1(c) displays the spot-like emission of these devices in LRS, owing to a higher density of carriers circulating through the CFs beneath the visible ZnO top electrode. Only a low number carriers travelling the distance (through the dielectric) are able to yield a low intensity emission of the Si NCs. It should also be noted here that the CFs are probably formed between Si NCs, since their interface with the SiO<sub>2</sub> corresponds to defective zones where O is more likely to be liberated. This would also reduce the amount of Si NCs available for emission, as quantum confinement would be lost for those that become part of a CF.

This work paves the way for resistive switching devices to be included in the next generation of optoelectronics. Indeed, the procedure and device presented can be considered novel, since as of the writing of the correspondent journal article, only two other works could

## 6.2. Resistance state read through light emission

be found to report the combination of these two properties, although with not so clear performance.<sup>[8,9]</sup>

A journal article was published in *Journal of Applied Physics* **126**, 144504 (2019), selected as part of the Editor's Pick collection. In addition, the results hereby introduced have been presented as a talk at the European Materials Research Society (EMRS) Spring Meeting 2019 and Fall Meeting 2019, and as a poster at the 2019 Annual Meeting of the Institute of Nanoscience and Nanotechnology of the UB (IN<sup>2</sup>UB). It was also recognized with a Graduate Student Award at the EMRS Fall Meeting 2019, Symposium A.



**Paper VII: Silicon nanocrystals-based  
electroluminescent resistive switching device (DOI:  
[10.1063/1.5119299](https://doi.org/10.1063/1.5119299))**



# Silicon nanocrystals-based electroluminescent resistive switching device

Cite as: *J. Appl. Phys.* **126**, 144501 (2019); doi: [10.1063/1.5119299](https://doi.org/10.1063/1.5119299)

Submitted: 10 July 2019 · Accepted: 15 September 2019 ·

Published Online: 8 October 2019



J. L. Friero,<sup>1,2,a)</sup>  J. López-Vidrier,<sup>3,b)</sup>  O. Blázquez,<sup>1,2</sup>  D. Yazicioğlu,<sup>3</sup>  S. Gutsch,<sup>3</sup>  J. Valenta,<sup>4</sup>   
S. Hernández,<sup>1,2</sup>  M. Zacharias,<sup>3</sup>  and B. Garrido<sup>1,2</sup> 

## AFFILIATIONS

<sup>1</sup>MIND, Departament d'Enginyeria Electrònica i Biomèdica, Universitat de Barcelona, Martí i Franquès 1, 08028 Barcelona, Spain

<sup>2</sup>Institute of Nanoscience and Nanotechnology (IN<sup>2</sup>UB), Universitat de Barcelona, Av. Diagonal 645, 08028 Barcelona, Spain

<sup>3</sup>Laboratory of Nanotechnology, IMTEK, Faculty of Engineering, Albert-Ludwigs Universität Freiburg, Georges-Köhler-Allee 103, 79110 Freiburg, Germany

<sup>4</sup>Faculty of Mathematics and Physics, Charles University, Ke Karlovu 3, 121 16 Prague 2, Czech Republic

<sup>a)</sup>[jfriero@el.ub.edu](mailto:jfriero@el.ub.edu)

<sup>b)</sup>[julia.lopezvidrier@imtek.uni-freiburg.de](mailto:julia.lopezvidrier@imtek.uni-freiburg.de)

## ABSTRACT

In the last few years, the emergence of studies concerning the resistive switching (RS) phenomenon has resulted in the finding of a large amount of materials being capable of acting as an active layer in such devices, i.e., the layer where the change in resistance takes place. Whereas the normal operation consists of the electrical readout of the modified resistance state of the device after electrical writing, electro-optonic approaches seek the involvement of light in these devices, be it either for the active Set or Reset operations or the readout. We propose in this work silicon nanocrystal multilayers (Si NC MLs) as an active material for being used in RS devices, taking advantage of their outstanding optical properties. The resistance states of Si NC MLs were obtained by electrical excitation, whose readout is carried out by electrical and electro-optical means, thanks to a distinguishable electroluminescence emission under each state. To achieve this, we report on an adequate design that combines both the Si NC MLs with ZnO as a transparent conductive oxide, whose material properties ensure the device RS performance while allowing the electro-optical characterization. Overall, such an occurrence states the demonstration of a Si NCs-based electroluminescent RS device, which paves the way for their future integration into photonic integrated circuits.

© 2019 Author(s). All article content, except where otherwise noted, is licensed under a Creative Commons Attribution (CC BY) license (<http://creativecommons.org/licenses/by/4.0/>). <https://doi.org/10.1063/1.5119299>

## I. INTRODUCTION

Although the resistive switching (RS) phenomenon had been known for many years, it was in 2008 when the first fully operational RS device was realized.<sup>1</sup> Materials presenting the RS phenomenon, typically dielectrics, exhibit inner structural modification after an electric field is applied through the two sandwiching electrodes, resulting in controlled changes in resistivity under certain electrical polarities.<sup>2</sup> This novel property allows dielectric materials to act, when embedded in the proper device structure, as resistive random-access memory (RRAM) devices that operate between at least two well-defined states, thus performing as digital memories.<sup>3</sup> Indeed, the occurrence of RS between two well-defined resistance states is widely accepted to be caused by the formation of a conductive

filament (CF) across the dielectric material which, according to the most established models, takes place via either the atomic diffusion from the metallic electrodes toward the dielectric (electrochemical metallization, ECM)<sup>4</sup> or the generation of oxygen vacancies due to oxygen atom diffusion from the oxide-based dielectric toward the electrodes (valence change mechanism, VCM).<sup>5,6</sup> The cyclic generation and destruction of the CF has been investigated in a wealth of dielectric and semiconductor materials, aiming not only at the full understanding of the fundamental properties of the RS phenomenon but also at the determination of the optimum conditions for long-lasting performance (that is, improved properties of a RRAM device).<sup>7,8</sup> Heterogeneous materials such as Si suboxides are of high interest, since they are compatible with current electronic technologies. Within

this context, previous works have been led by the group of Kenyon by employing a TiN/SiO<sub>2</sub>/TiN structure devoted to understanding the role of the dielectric/electrode interfaces in the CF formation and destruction processes,<sup>9,10</sup> and to demonstrate that the presence of Si nanoinclusions might as well contribute to the switching operation of the dielectric layer.<sup>11</sup>

The improved electronic properties yielded by nanostructured silicon in comparison to its bulk counterpart have led, during the last few decades, to the in-depth investigation of their underlying fundamentals, in order to optimize their performance to be applied in the electronics and optoelectronics fields. In particular, the quantum confinement effect, that is, the spatial confinement of the carrier wavefunctions within the nanostructure, induces the relaxation of the band-to-band transition selection rules as well as an increase of the Si bandgap energy that can be controlled by decreasing the particle size.<sup>12,13</sup> Within the whole range of Si nanostructures, matrix-embedded Si nanocrystals have provided, thanks to their versatility and robustness, a model platform for examining the structural, optical, and electrical properties of semiconductors at the nanoscale level. Several works have been published that pursued the determination of the physical mechanisms governing the optical<sup>14–16</sup> and electrical<sup>17–19</sup> performance of SiO<sub>2</sub>-embedded Si NCs, aiming at their applications as an active emitting layer in light-emitting diode (LED) structures.<sup>20–22</sup> Indeed, it is the size-dependence of the Si NC properties what makes this material system of great interest and, consequently, the adequate control of NCs size and shape has focused much effort. Within this context, arranging the NCs along multilayers (MLs) has led to excellent control by depositing nanometer-thin Si-rich oxide (SiO<sub>x</sub>) layers between stoichiometric SiO<sub>2</sub> barriers, the latter efficiently limiting the Si excess diffusion from the SiO<sub>x</sub> layers during the postdeposition high-temperature annealing. The final process induces the precipitation and crystallization of the Si excess into ordered arrays of Si NC superlattices.<sup>23,24</sup>

Recently, new attempts on semiconductor and electronics industries to be adapted to the needs of the field of photonics, aiming at fast light-based and material-free interconnections, constitute the development of the novel concept of “optical memristor” as a requisite for the future in RRAM industry. The ability to optically write or read (or both) the resistance state in a RS memory will increase the overall device operation speed and provide a direct signal conversion, while making this new technology fully-compatible with the photonic integrated circuits (PICs). Although not fully exploited, some reports on the optical memristor field exist. Mehonic *et al.* published on the effect of light writing of SiO<sub>x</sub>-based RRAM devices, the generated photoconductivity inducing permanent state switching until light incidence was stopped, thus demonstrating the possibility of achieving light-triggered resistance switching.<sup>25</sup> Furthermore, the group of Leuthold has worked on optically-read electrically-written memristors within a waveguide (WG) structure, where surface plasmon polariton generation at the interface between amorphous Si and the active WG material (Si) led to different optical losses (and thus different readout) of the light beam through the WG.<sup>26</sup> Another functionality which has not yet been fully explored is electroluminescence (EL), i.e., an active optical response to electrical stimuli in each resistance state after electrical writing. This occurrence has the advantage of having the electrical and optical source integrated

within the same device,<sup>27</sup> instead of requiring external laser sources for writing (light-triggered RRAM devices)<sup>25</sup> or reading (through WG structure).<sup>26,28,29</sup> Recent studies have reported on structures containing Si NCs/SiO<sub>2</sub> MLs as an active memristive layer, where not only the RS properties of Si NC MLs were inspected but also the role played by the number of Si NC/SiO<sub>2</sub> bilayers on the CF formation was addressed.<sup>30</sup> Given these demonstrations and their well-known EL properties, Si NC MLs become a great active layer candidate to develop “electroluminescent memristors.” Electroluminescence in Si NCs, be it governed by either bipolar carrier injection<sup>31,32</sup> or impact excitation,<sup>33,34</sup> can be strongly influenced by the formation of a CF through the nanostructures, which, in turn, may serve as a distinguishable signature between both resistance states. It is this different EL emission at each resistance state which can be exploited in PICs as an indicator of the device memory state, and its modulation paves the way to novel integrated optical RS devices for photonic applications.

In this work, we demonstrate ZnO/Si NCs-based devices as electroluminescent RRAM devices. For this, we embedded Si NC MLs as the dielectric material (I) into a metal-insulator-semiconductor (MIS) device design, where intrinsically *n*-type ZnO (M) serves as a top transparent conductive oxide (TCO), and *p*-type Si is employed as the substrate (S). Herein, we show that not only EL emission can be achieved in a controlled way from this MIS device system but also Si NCs provide a characteristic EL signal that allows distinguishing the resistance state of the device, desirable for optical resistance switching applications.

## II. EXPERIMENTAL DETAILS

Devices consisting of a MIS structure have been fabricated using Si NCs/SiO<sub>2</sub> MLs on top of a Si substrate, with a ZnO electrode as top transparent contact,<sup>35</sup> as sketched in Fig. 1(a). Plasma-enhanced chemical vapor deposition (PECVD) was the selected technique to deposit five Si-rich oxynitride (SRON)/SiO<sub>2</sub> bilayers on top of a *p*-type Si substrate, with nominal layer thicknesses of 4.5 nm and 1 nm, respectively, following the superlattice approach.<sup>24</sup> The stoichiometry of the SRON layer was held constant at SiO<sub>0.93</sub>N<sub>0.23</sub>, which corresponds to a Si excess of [Si]<sub>exc</sub> = 17 at. %. An additional 2-nm-thin Si<sub>3</sub>N<sub>4</sub> sublayer was inserted between the substrate and the first SRON sublayer, which was found to promote electron injection in inversion conditions due to the contained fixed positive charges as a consequence of its defective nature.<sup>35,36</sup> The ML samples underwent an annealing treatment at 1150 °C for 1 h under N<sub>2</sub> ambient in a quartz tube furnace, to promote the precipitation and crystallization of the Si excess within the SRON layers in the form of Si NCs. The material fabrication process was completed by passivating the samples with H<sub>2</sub> at 450 °C, in order to get rid of undesired dangling bonds. For more details on the ML deposition, the reader is kindly directed to Ref. 37.

A direct observation of the sample structure was done via energy-filtered transmission electron microscopy (EFTEM), using a JEOL 2010F instrument (field emission gun operating at 200 keV). To perform EFTEM, the instrument was equipped with a Gatan Image Filter (with a resolution of 0.8 eV), which

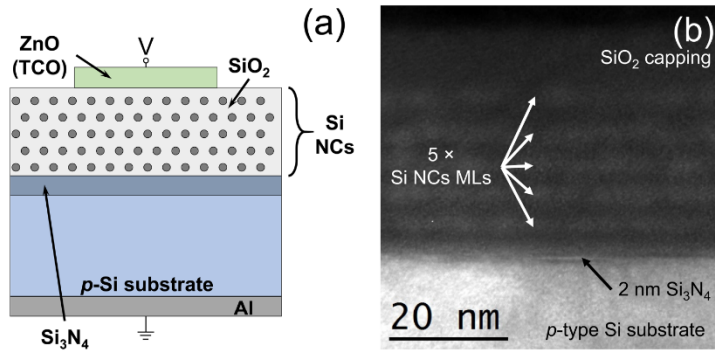


**FIG. 1.** (a) Sketch of the MIS device structure containing the Si NC MLs as the insulator (I) layer, and ZnO (*n*-type TCO) and Si substrate (*p*-type) as metal (M) and semiconductor (S) layers, respectively. For the electrical and electro-optical characterization, voltage was applied at the top electrode while the bottom was grounded. Thicknesses are not to scale. (b) EFTEM image of an equally-deposited sample, where the Si NCs can be identified in the ML structure, deposited over a Si substrate and with a capping of SiO<sub>2</sub> (which was later removed for device processing).

allowed filtering the signal around the Si plasmon energy ( $E_{Si} \sim 17$  eV). Prior to the TEM inspection, the samples were prepared by mechanical flat polishing and final low angle Ar<sup>+</sup>-ion milling. As it can be observed in Fig. 1(b), the real thickness of the final structure, measured by EFTEM, is in good agreement with the nominal thickness of  $\sim 30$  nm. The image also confirms that the Si NCs layers are clearly separated in the pristine state of the sample, with no percolation through them whatsoever (previous studies have shown that percolation appears for silicon excess above  $[Si]_{exc} = 38\text{--}44$  at. %<sup>38,39</sup>).

Aiming at the electroluminescence performance of the devices, ZnO (intrinsically *n*-type) was employed as top TCO (resistivity of 0.1  $\Omega$  cm and  $\sim 75\%$  transparency throughout the whole visible spectrum),<sup>40,41</sup> which was deposited on top of the MLs by means of atomic layer deposition (ALD) and afterwards photolithography-patterned to achieve 500- $\mu$ m-diameter circular contacts (total device area of  $\sim 2 \times 10^{-3}$  cm<sup>2</sup>). Finally, for the back contact, the Si substrate was full-area Al metallized via evaporation. Further details on the preparation of analogous devices can be found elsewhere.<sup>35,37</sup>

For the electrical characterization, the devices were loaded into a Cascade Microtech Summit 11000 probe station, properly screened from external electromagnetic noise by means of a Faraday cage. The current-voltage [ $I(V)$ ] characteristics were performed using an Agilent B1500 semiconductor device analyzer. Finally, EL spectra were acquired via a Princeton Instruments LN<sub>2</sub>-cooled CCD coupled to a monochromator (400–1100 nm range).

### III. RESULTS

#### A. RS cycle characterization

To attain knowledge on the RS behavior of Si NC MLs, the devices were submitted to full  $I(V)$  cycles, the voltage being applied at the ZnO top electrode, as shown in Fig. 1(a). In particular, Fig. 2 displays a representative set of ten  $I(V)$  cycles out of one of the several device structures measured, using 50 mV steps. Indeed, the curves exhibit easily-identifiable bipolar resistive

switching characteristics, which are described as follows: (1) a first sweep to positive voltages ( $V > 0$ ) on the pristine device structure (red curve) results in monotonous current increase until  $V = 9.5$  V, (2) at which a sudden increase in current takes place. This process is known as “electroforming,” and it is typically ascribed to the first formation of CFs through the dielectric layer.<sup>5</sup> Anticipating the electroforming process, we set the current compliance (CC) at 100  $\mu$ A, which was found to be the most adequate one to allow the CF formation while avoiding permanent damage to the device. This electroforming process was found to be very stable in all the measured devices, always occurring at a voltage of

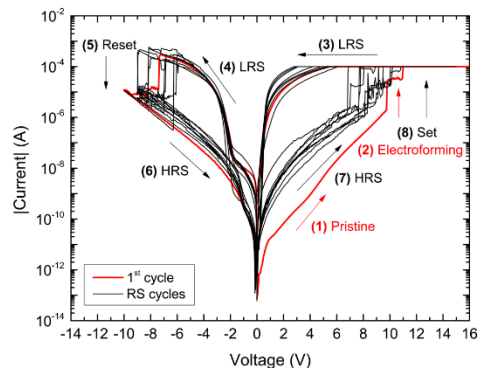


**FIG. 2.** Typical current (in absolute value) vs voltage curves of the Si NC ML structure under study, showing controlled bipolar RS cycles. In red, the first cycle, corresponding to the pristine state, the electroforming process ( $\sim 10$  V) and the first Reset of the device; in black, the following  $I(V)$  curves until completing 10 RS cycles. Current compliance of 100  $\mu$ A was employed for  $V > 0$ .

$10 \pm 0.5$  V. (3) The backwards voltage sweep down to  $V = 0$  V shows a very high conductivity in comparison to the pristine state, due to the inner structural modification within the MLs: the device lays now within the low resistance state (LRS). (4) Voltage is then increased toward negative polarity ( $V < 0$ ), exhibiting again low resistivity. Two different conduction regimes can be observed in LRS, while the device is under substrate accumulation conditions. The first regime, down to  $-2$  V, is due to the current displacement of the trapped charge in the structure, basically in defects present either in the ZnO electrode or in the active Si NCs MLs; in the second regime, beyond  $-2$  V, electron injection from the top electrode already dominates conduction. When  $-8$  V are reached, the current suddenly drops by almost two orders of magnitude. (5) This is called the “Reset” process, and it is attributed in the literature to the partial destruction of the CF.<sup>2,42</sup> Afterwards, the device lays within the high resistance state (HRS). (6) Again, the backwards voltage sweep down to  $V = 0$  V induces no modification of the resistive state of the device. (7) Last, following a positive voltage sweep, (8) the switch from HRS to LRS can be achieved through the recovery of the CF due to their reduction in the Set process, induced in our device beyond  $V = 8$  V. Note that the HRS is more conductive than the pristine state (hence the term “partial” is used for the destruction of the CF in the Reset process).<sup>5</sup>

Overall, the various RS cycles recorded showed Set and Reset voltage values spanning from 7 V to 10 V and from  $-6$  V to  $-9$  V, respectively, which states a nearly symmetric performance with a relatively low dispersion. This, added to the 2 orders of magnitude in the current difference between LRS and HRS at a read voltage of  $V_{\text{read}} = -4$  V (where conduction mechanisms are well established in both resistance states), makes this device structure a good candidate for controlled RS cycling,<sup>3</sup> where future improvements can be developed to reduce the voltage ranges of operation and the requirement of a CC. Finally, it must also be mentioned that, after multiple cycles, we have detected an increasing current level for the HRS both in negative and positive polarization, which can be related to the low overall endurance of the analyzed devices. No other trends have been observed neither in the LRS current levels nor in the Set and Reset voltages. Therefore, this occurrence indicates that the failure of the devices, always taking place in the form of an almost permanent LRS, could be attributed to the formation of CFs with lower reoxidation state after every new cycle.

## B. Electroluminescence emission

The well-known EL properties of  $\text{SiO}_2$ -embedded Si NCs make this material an adequate research platform to study the effect of the RS phenomenon on the light emission properties of the structure under study. In order to simultaneously characterize both properties that the active layer exhibits, device structures were submitted to the electroforming process and additional RS cycles following the process previously described in Sec. III A. The characterization of the EL emission was then performed by having each device in one of the two stable states (LRS and HRS) and applying a constant voltage while both monitoring the current (to check that the resistance state under study is maintained throughout the

measurement of the emission) and acquiring the emitted EL spectra. The voltage range analyzed was selected to include the Set and Reset processes previously observed in the electrical characterization and employing a voltage step of 1 V, resulting in respective ranges for HRS and LRS of  $-8$  V to 8 V and  $-6$  V to 7 V. It must be mentioned here that no clear dependence was found between the number of cycles applied and emission intensity.

In Figs. 3(a) and 3(b), all the spectra collected for one device in both resistance states (HRS and LRS, respectively) are shown, stating a clear difference in emission between the states and a dependence with the voltage applied. In terms of polarity, the structure shows no relevant emission when in substrate inversion conditions ( $V > 0$ ) in LRS. In any other case, when increasing the voltage applied to the structure, the EL also shows a monotonous increase in intensity. Regarding the wavelength dependence of the EL, each state presents a clearly different spectral line shape, whereas HRS shows a peak-like feature, a broad band appears at high applied voltages in LRS, under substrate accumulation ( $V < 0$ ) regime. This already indicates that EL from the device, strongly dependent on the resistance state, might arise from different luminescent centers. A more in-depth characterization of the resulting luminescence was performed for the EL spectra acquired for each resistance state both in the inversion [Fig. 3(c)] and accumulation [Fig. 3(d)] regimes, being the EL optical output read, respectively, at  $V_{\text{read}} = 7$  V and  $V_{\text{read}} = -6$  V. It is important to note that the EL spectra are reproducible when acquired at the mentioned  $V_{\text{read}}$  during several performed RS cycles and in different devices; this essentially means not only that the EL properties hereby shown do have a real sample-related origin (i.e., not related to artefacts), but also that RS cyclability, i.e., stable process reproducibility (see Fig. 2), is also extended to the EL domain.

As already mentioned above, Fig. 3 evidences distinct EL spectral line shape at different resistance states and applied polarities. On the one hand, the inversion regime exhibits, as it can be seen in Fig. 3(c), a clear EL emission, centered around 900 nm, only when the device is in the HRS. This emission is ascribed to radiative recombination of quantum-confined excitons within the Si NCs, as it is well established in the literature and has been previously published by some of the authors.<sup>33–35,43</sup> The emission band is asymmetric, exhibiting a shoulder at shorter wavelengths (higher energies), which can be ascribed to the excitation of several NC size populations. Nevertheless, considering the overall peak position around  $\sim 900$  nm ( $\sim 1.38$  eV), we can estimate a dominant NC mean size of  $\sim 4$  nm, as confirmed by TEM studies and previously reported for equivalent structures.<sup>37,44,45</sup> On the other hand, different EL spectrum line shapes can be found in substrate accumulation conditions, where emission is detected only in the LRS, as observed in Fig. 3(d). The clear broadband emission, from 500 to 1100 nm, resulting in LRS has been deconvolved, in the energy domain, into two Gaussian contributions: a lower energy contribution centered at  $\sim 930$  nm ( $\sim 1.33$  eV, red dotted line) and a broader and higher-energy band around  $\sim 730$  nm ( $\sim 1.70$  eV, magenta dashed line). After immediate comparison to the inversion regime, the lower-energy band can be attributed to quantum-confined emission from the main NC size population; in contrast, the most plausible origin for the higher-energy band is the emission of deep-level radiative defects within the top ZnO electrode, typically

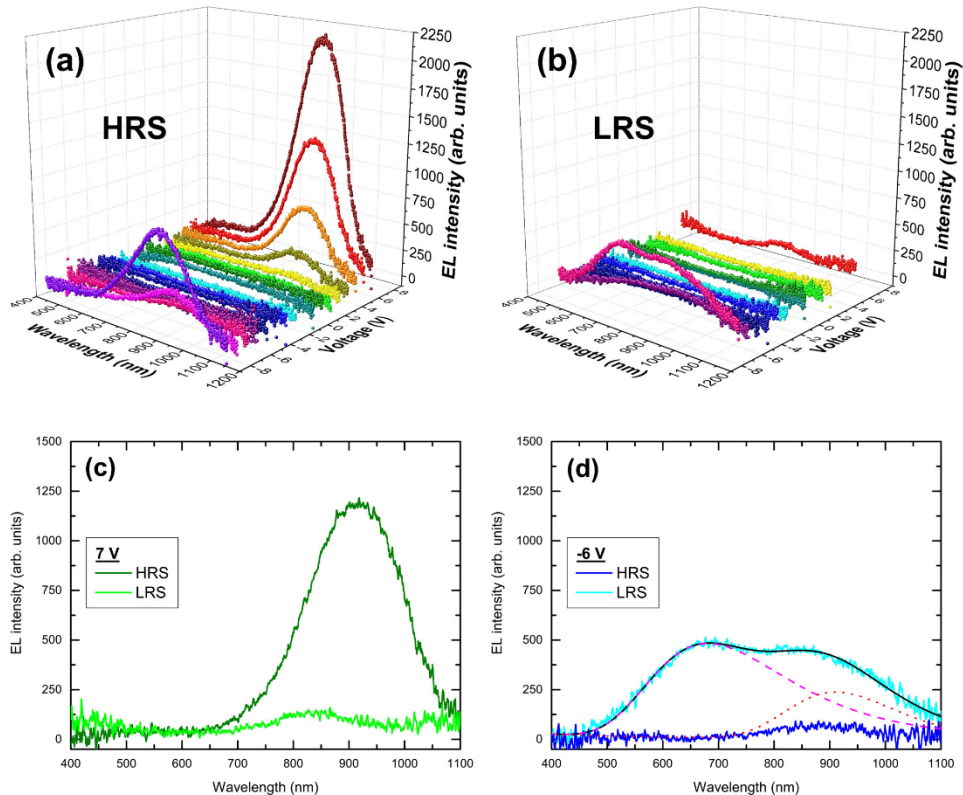


**FIG. 3.** 3-dimensional plots of EL spectra acquired under different  $V_{\text{read}}$ , spanning from  $-8\text{ V}$  to  $8\text{ V}$ , corresponding to HRS (a) and LRS (b). The  $V_{\text{read}}$  range was selected from the Set ( $8\text{ V}$ ) to its opposite value passed the Reset ( $-8\text{ V}$ ), in the case of HRS; and from the Reset ( $-6\text{ V}$ ) to the Set ( $7\text{ V}$ ), in the case of LRS. (c) and (d) correspond to the EL spectra yielded by the devices at both HRS and LRS under read conditions: substrate inversion ( $7\text{ V}$ ) and accumulation ( $-6\text{ V}$ ), respectively. For the accumulation regime, deconvolution of the main signal into different-origin contributions is represented with red dotted and magenta dashed lines.

donor-acceptor pairs generated at O vacancies and/or Zn interstitials,<sup>46</sup> as was recently reported in an analogous structure.<sup>43</sup>

From a technological point of view, RS-dependent EL emission means that a controlled direct transduction of the signal output is produced and, therefore, it can be employed for faster and more efficient communication between components in PICs. Therefore, to be employed in this kind of circuits, the signal would have to be detected by a different component of the PIC, which should be able to distinguish between a light-emitting state and a non-emitting one (if using binary logic). In a device structure such as the one we propose here, the operation regime can be described by the integrated EL emission observed in Fig. 4 (obtained after integrating

the EL spectra plotted in Fig. 3), by selecting a reading voltage that yields a large enough difference between the states. By analyzing both polarities in the graph, a good reading voltage may be selected for a maximum difference in emission between states at  $8\text{ V}$  (inversion regime). Nevertheless, this reading voltage lays well within the Set voltage range, thus implying a conflict in case the device suddenly changes its resistance state. To avoid this, the best voltage value must be kept below (in absolute values) the writing voltage ranges:  $-6\text{ V}$  to  $-9\text{ V}$  and  $7\text{ V}$  to  $10\text{ V}$ , for Reset and Set operations, respectively. After these considerations, the largest possible EL difference is yielded around  $6\text{ V}$ , thus making this the best possible reading voltage.

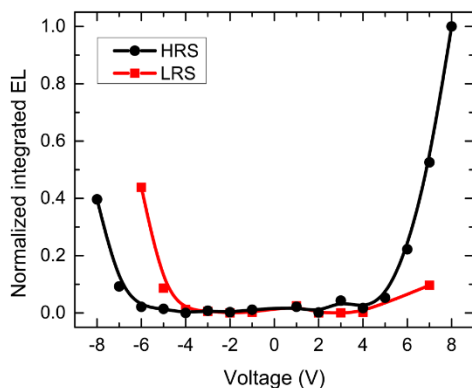


**FIG. 4.** Normalized EL emission intensity obtained by integrating the area under the curve of the spectra plotted in Fig. 3. Both states can be distinguished in accumulation and inversion regimes, but eliminating the Reset and Set voltage ranges, from  $-6$  V to  $-9$  V and from  $7$  V to  $10$  V, respectively; the largest difference between states is found at  $6$  V, making this the optimum reading voltage.

Up to this point we have shown how our ZnO/Si NCs-based RS device structures are capable of giving a distinguishable EL emission in different resistance states when employing reading conditions that have been established for  $6$  V, i.e., not forcing the device to a point where an undesired Set or Reset takes place, while keeping strong EL emission. In particular, quantum-confined Si NCs emission dominates in HRS, although these nanostructures exhibit non-negligible EL even in LRS; instead, a broad band extended to the visible, ascribed to the added emission of ZnO defects, is only observed in LRS. Indeed, the demonstration of such difference in emission between both resistance states makes (*n*) ZnO/Si NC MLs/(*p*)Si MIS structure a good candidate for the novel field of EL memristors.

#### IV. DISCUSSION

The results hereby presented demonstrate a relation between the RS behavior and the EL emission of the (*n*)ZnO/Si NC MLs/(*p*)Si structures under study. Indeed, it is possible to immediately identify the resistance state of the device only by monitoring its emission after electrical excitation at a particular reading voltage value. Four different emissions can be distinguished according to the resistance state and the electrical applied voltage polarity [see Figs. 3(a) and 3(b)], whose main emission features are summarized in Table I. Please note that the different characteristics of the Si NC-related emission poses a clear progress on the optical reading of the resistance state, by yielding a clearly-distinguishable EL emission. In addition, the selection of ZnO as top transparent electrode is far from unintended, and its luminescent centers extended through the visible range ( $>500$  nm) only in

**TABLE I.** Origin of the EL emission from tested structures as observed in Fig. 3, at each resistance state and under different applied voltage polarities.

Resistance state\ voltage polarity	Accumulation ( $V < 0$ )	Inversion ( $V > 0$ )
HRS (CF partially dissolved)	Si NCs (NIR, intense)	Si NCs (NIR, intense)
LRS (CF created)	Si NCs (NIR, weak) ZnO defects (visible)	No EL

LRS and under accumulation regime serve as complementary fingerprint to that of Si NCs.<sup>43</sup>

Going more in depth in this issue, the fact that distinct EL emission is yielded under different resistance states implies that a correlation exists between the structural modification of the layer containing the Si NCs and the electrical excitation of the different luminescent species within the whole system. Therefore, we intend to explain our observations by means of a simple model of the structure under study, as sketched in Fig. 5. With this aim, we will follow the RS cycle as presented in Fig. 2.

As observed by EFTM [Fig. 1(b)], after the fabrication process, the matrix-embedded Si NCs are arranged along multilayers due to their confined growth through the superlattice approach.<sup>24</sup> This is the so-called pristine state, and it presents periodical SiO<sub>2</sub> barriers between NCs that strongly influence charge transport.<sup>47,48</sup> In this state, positively biasing the top electrode (substrate inversion regime) results in the injection of substrate electrons into the dielectric [Pristine, Fig. 5(a)], giving as a result the emission of Si NCs-related EL. Regarding the possible EL excitation mechanisms, it is still controversial whether bipolar electron-hole injection<sup>31,32</sup> or hot electron impact<sup>34,48</sup> dominate NC excitation within ordered MLs. Under these conditions, being the Si substrate *p*-type, minority carrier (electron) injection from the substrate should be totally quenched, and thus no emission should be observed. Notwithstanding, the thin PECVD-deposited Si<sub>3</sub>N<sub>4</sub> sublayer between substrate and MLs acts as a reservoir of fixed positive charge which, by means of Coulombian attraction, enhances the injection probability of electrons, as recently reported on an analogous device structure.<sup>35</sup> As a result, Si NCs-related emission still takes place; and regarding the excitation mechanisms, hot electron impact is almost certainly the origin of emission, since hole injection from the ZnO electrode can be excluded.

High positive electrical polarity applied at the gate electrode attracts oxygen ions which move toward it, thus generating oxygen vacancies at the Si/SiO<sub>2</sub> interfaces,<sup>49</sup> such as those surrounding Si NCs; therefore, CFs are created through the Si NCs [electroforming, Fig. 5(b)]. The formation of CFs through the NCs is supported by previous observations,<sup>50</sup> and it creates a highly percolated Si NC network along the vertical direction in which carrier confinement is no longer possible. As a consequence, Si NC-related EL emission in LRS in the present electrical polarity is quenched. Please, note that (although it is difficult to confirm without direct observation) the possibility of the CFs being created entirely through the SiO<sub>2</sub> matrix (and not through the NCs) cannot be ruled out. As well, previous works on Si NCs suggest the existence of a SiO<sub>x</sub> shell

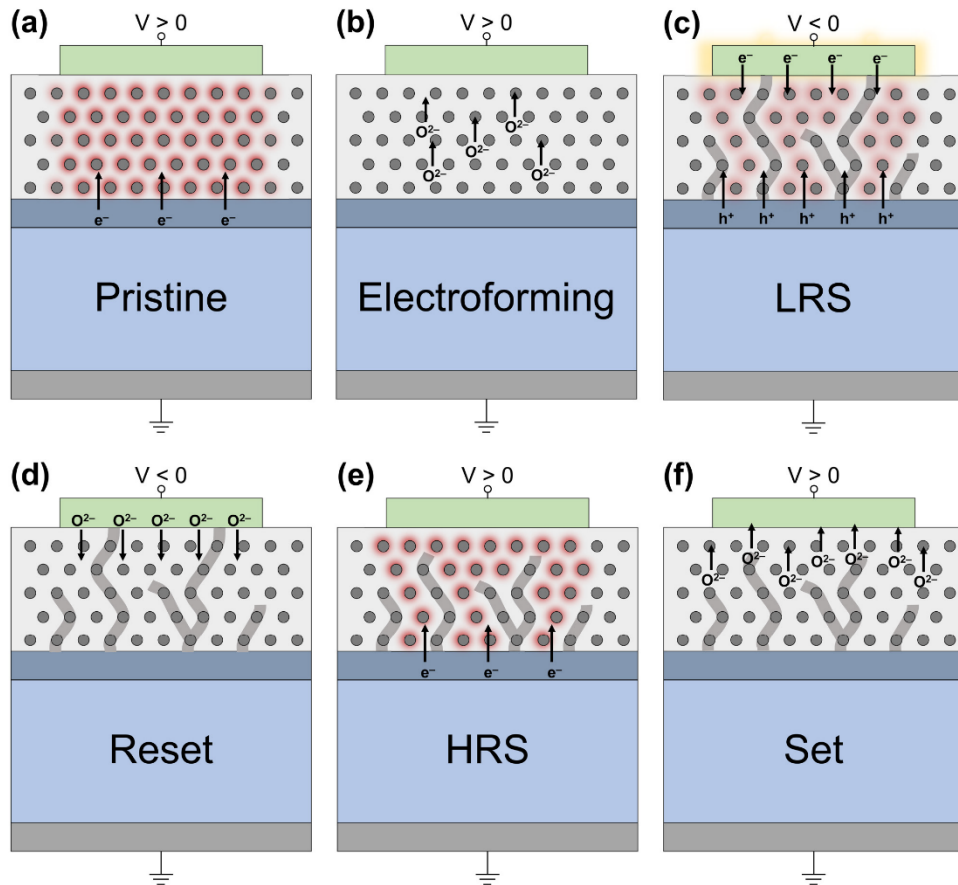


**FIG. 5.** (a) Excitation of the Si NCs in the pristine state. (b) At  $V > 0$ , CF formation takes place within the pristine device (electroforming) through oxygen ion attraction from the MLs toward the ZnO electrode. A nonemitting network of percolating Si NCs is obtained (LRS). (c) At  $V < 0$ , electron-hole pair formation, and thus EL emission, is attained within the Si NCs and the deep-level defect states in ZnO. (d) At high enough negative bias, CF partial reoxidation takes place via oxygen ions diffusing back from the ZnO into the MLs (HRS). Si NC-related EL emission is observed under these conditions. (e) At  $V > 0$ , the  $\text{Si}_3\text{N}_4$  thin layer enhances the minority carrier injection from the substrate, and therefore EL emission from Si NCs is still achieved. (f) Set process, where oxygen ions are again moved toward the ZnO electrode, similar to (a). Arrows indicate charge and ion transport. Luminescent species from which EL is observed, under each resistance state, are shadowed.

surrounding the NC crystalline core,<sup>51</sup> which could generate an additional path for CF formation. In any case, CF formation through oxide cannot modify the description of the phenomena hereby attempted. Regarding the bridging by multiple filaments in contrast to other general explanations that use only one, the model we present is just one possibility that requires of further structural

analysis. The observation of spot-like EL emission distributed along the ZnO electrode (not shown here) supports the assumption of multiple filaments being generated through the active layer, which we will explore in future works. Already in LRS, negative voltage polarity at the top electrode will induce substrate accumulation; under these conditions, electrons are injected from the top

electrode and holes from the Si substrate [Fig. 5(c)]. In spite of conduction through the CF being dominant in this resistance state, conduction along the rest of the device volume may be enough to excite a relevant population of NCs and thus contribute to EL, as experimentally observed [see Fig. 3(d)]. As well, electron-hole pairs can be generated within ZnO deep-levels by either direct electron impact or the injection of holes created at the ZnO/MLs interface, as previously reported.<sup>43</sup> In any case, the final result is the excitation of both luminescent species (Si NCs and ZnO defects) and their consequent EL emission. From a macroscopic point of view, the occurrence of emission coming from the ZnO electrode is supported by the observation of bright visible spots (even with the naked eye) on the surface of the device, which results in electrode damaging due to the high current density reached at the contact points between the CF and the ZnO produced during the Reset process, when current reaches a maximum value circulating through the CF; this damage is still observed after device operation. Through repeated visual inspection of the device, no increase of the damaged areas has been observed after it first takes place during the first cycle.

Under negative bias, and using high enough voltages, oxygen ions preferentially stored within the ZnO electrode diffuse back into the MLs due to electrical repulsion from the top electrode. As a consequence, oxygen vacancies will be filled and the CF partially reoxidizes next to the ZnO/MLs interface [Reset, Fig. 5(d)].<sup>42</sup> In this HRS and maintaining negative bias at the top electrode, electron-hole formation within the NCs takes place (as described above), which induces a clear Si NCs-related EL emission. After positive biasing, substrate inversion occurs, after which the injection of carriers into the MLs is reverted: only electrons are injected from the substrate [Fig. 5(e)]. Under the same conditions that applied for the pristine state, Si NC-related emission takes place. At this point, it is relevant to mention that, even when the electrical and EL properties of the pristine and HRS states should be equivalent, the former presents higher conductivity (see Fig. 2) and less intense EL under both applied polarities. This is due to the CFs being partially reoxidized after Reset, leaving some oxygen vacancies behind. Part of the injected current in the HRS is leaked through the remnants of the CF which contain non-confined Si NCs, and therefore a weaker EL intensity is expected from the rest of the unaltered Si NCs as only a part of the total current, and thus a lower current density, is circulating through them. A high applied positive polarity induces once more the movement of oxygen ions toward the top electrode. This process forms the CFs again and thus the device returns to the LRS [Set, Fig. 5(f)].

Finally, the hereby presented model, which is able to completely describe our observations, is in good agreement with most relevant reports on the topic. Some works have explored the behavior of Si oxides under resistive switching processes and their relation with Si NCs.<sup>11,30,50</sup> As well, the interaction of light in RS materials has also been explored, such as the case of light-activation of RS in the work of Mehonic *et al.*<sup>25</sup> and the reading of the RS state via optical absorption modulation in the work of Emboras *et al.*<sup>28</sup> Indeed, the occurrence of EL emission following (and thus being a consequence of) the RS cycle of a given dielectric material has been already reported only in few works, some of which include size-unconstrained matrix-embedded Si NCs.<sup>27,52</sup> Nevertheless, the

present work establishes a particular design, fabrication, and polarization method aiming at fully controlling and tuning the optical readout of the resistance state, making this unique combination of material and device structure a strong candidate for the next generation of light-integrating electronics.

## V. CONCLUSIONS

In summary, we have explored the RS and EL properties of Si NCs embedded into (*n*)ZnO/Si NC MLs/(*p*)Si device structures. It has been observed that the EL emitted at each resistance state (HRS and LRS) exhibits a distinguishable light emission after electrical excitation under both regimes (accumulation and inversion polarities). Of utter importance is not only the employed MIS design but also its particularities: whereas a Si<sub>3</sub>N<sub>4</sub> thin layer between substrate and the MLs enhances the electron injection probability from the substrate and thus electron-hole formation within the NCs, ZnO was employed as top transparent and EL-emitting electrode. The occurrence of additional light-emitting centers within the visible range (ZnO defects) to the well-known NIR Si NCs-related emission has demonstrated to allow for characteristic EL at each resistance state. In addition, the large difference in the EL emitted by the device structures under inversion electrical polarity for each resistance state allows for optically reading the resistance state of the device. As a consequence, the utilization of Si NCs within the present design could be the starting point for a new generation of EL memristors which can be exploited for the integration of photonics and electronics into the same physical location.

## ACKNOWLEDGMENTS

The authors thank Dr. L. López-Conesa and the group led by Professor F. Peiró for their help in the acquisition of the TEM images. This work was financially supported by the Spanish Ministry of Economy and Competitiveness (No. TEC2016-76849-C2-1-R) and the German Research Foundation (Nos. ZA191/27-3 and ZA191/33-1). J.V. is grateful for the funding through the Charles University center project (No. UNCE-SCI-010). J.L.F. acknowledges financial support from the subprogram "Ayudas para la Formación de Profesorado Universitario" (No. FPU16/06257) from the Spanish Ministry of Education, Culture and Sports for economical support. O.B. also acknowledges the subprogram "Ayudas para Contratos Predoctorales para la Formación de Doctores" from the Spanish Ministry of Economy and Competitiveness for economical support.

## REFERENCES

- <sup>1</sup>D. B. Strukov, G. S. Snider, D. R. Stewart, and R. S. Williams, "The missing memristor found," *Nature* 453(7191), 80–83 (2008).
- <sup>2</sup>I. Valov, "Redox-Based Resistive Switching Memories (ReRAMs): Electrochemical systems at the atomic scale," *ChemElectroChem* 1(1), 26–36 (2014).
- <sup>3</sup>D. S. Jeong, R. Thomas, R. S. Katiyar, J. F. Scott, H. Kohlstedt, A. Petaru, and C. S. Hwang, "Emerging memories: Resistive switching mechanisms and current status," *Rep. Prog. Phys.* 75(7), 076502 (2012).
- <sup>4</sup>I. Valov, R. Waser, J. R. Jameson, and M. N. Kozicki, "Electrochemical metallization memories—Fundamentals, applications, prospects," *Nanotechnology* 22(28), 289502 (2011).

- <sup>5</sup>R. Waser, R. Dittmann, C. Staikov, and K. Szot, "Redox-based resistive switching memories: nanoionic mechanisms, prospects, and challenges," *Adv. Mater.* **21**(25–26), 2632–2663 (2009).
- <sup>6</sup>O. Blázquez, G. Martín, I. Camps, A. Mariscal, J. López-Vidrier, J. M. Ramírez, S. Hernández, S. Estradé, F. Peiró, R. Serna *et al.*, "Memristive behaviour of Si-Al oxynitride thin films: The role of oxygen and nitrogen vacancies in the electroforming process," *Nanotechnology* **29**(23), 235702 (2018).
- <sup>7</sup>G. Niu, P. Calka, M. A. der Matur, F. Santoni, S. Guha, M. Frasciuke, P. Hamoumou, B. Guttier, E. Perez, C. Walczyk *et al.*, "Geometric conductive filament confinement by nanotips for resistive switching of HfO<sub>2</sub>-RRAM devices with high performance," *Sci. Rep.* **6**(1), 25757 (2016).
- <sup>8</sup>X. M. Kim, S. Han, and C. S. Hwang, "Electronic bipolar resistance switching in an anti-serially connected Pt/TiO<sub>2</sub>/Pt structure for improved reliability," *Nanotechnology* **23**(3), 035201 (2012).
- <sup>9</sup>A. Mehonic, M. S. Munde, W. H. Ng, M. Buckwell, L. Montes, M. Bosman, A. L. Shluger, and A. J. Kenyon, "Intrinsic resistance switching in amorphous silicon oxide for high performance SiO<sub>x</sub> ReRAM devices," *Microelectron. Eng.* **178**, 98–103 (2017).
- <sup>10</sup>M. S. Munde, A. Mehonic, W. H. Ng, M. Buckwell, L. Montes, M. Bosman, A. L. Shluger, and A. J. Kenyon, "Intrinsic resistance switching in amorphous silicon suboxides: The role of columnar microstructure," *Sci. Rep.* **7**(1), 9274 (2017).
- <sup>11</sup>A. Mehonic, S. Cuff, M. Wojdak, S. Hudziak, O. Jambois, C. Labbé, B. Garrido, R. Rizk, and A. J. Kenyon, "Resistive switching in silicon suboxide films," *J. Appl. Phys.* **111**(7), 074507 (2012).
- <sup>12</sup>F. Iacona, G. Franzò, and C. Spinella, "Correlation between luminescence and structural properties of Si nanocrystals," *J. Appl. Phys.* **87**(3), 1295–1303 (2000).
- <sup>13</sup>F. Iacona, G. Franzò, V. Vinciguerra, A. Irrera, and F. Priolo, "Influence of the spatial arrangement on the quantum confinement properties of Si nanocrystals," *Opt. Mater.* **17**(1–2), 51–55 (2001).
- <sup>14</sup>L. Khriachtchev, M. Räsänen, S. Novikov, and L. Pavesi, "Systematic correlation between Raman spectra, photoluminescence intensity, and absorption coefficient of silicon layers containing Si nanocrystals," *Appl. Phys. Lett.* **85**(9), 1511–1513 (2004).
- <sup>15</sup>D. Kovalev, H. Heckler, G. Polisski, J. Diener, and F. Koch, "Optical properties of silicon nanocrystals," *Opt. Mater.* **17**(1–2), 35–40 (2001).
- <sup>16</sup>K. Kúsová, P. Hapala, J. Valenta, P. Jelínek, O. Cibulka, L. Ondič, and I. Pelant, "Direct bandgap silicon: Tensile-strained silicon nanocrystals," *Adv. Mater. Interf.* **1**(2), 1300042 (2014).
- <sup>17</sup>D. J. DiMaria, D. W. Dong, C. Falcony, T. N. Theis, J. R. Kirtley, J. C. Tsang, D. R. Young, F. L. Pesavento, and S. D. Brorson, "Charge transport and trapping phenomena in off-stoichiometric silicon dioxide films," *J. Appl. Phys.* **54**(10), 5801–5827 (1983).
- <sup>18</sup>I. Balberg, E. Savir, J. Jedrzejewski, A. G. Nassiopoulou, and S. Gardelis, "Fundamental transport processes in ensembles of silicon quantum dots," *Phys. Rev. B* **75**(23), 235329 (2007).
- <sup>19</sup>I. Balberg, "Electrical transport mechanisms in three dimensional ensembles of silicon quantum dots," *J. Appl. Phys.* **110**(6), 061301 (2011).
- <sup>20</sup>G. Franzò, A. Irrera, E. C. Moreira, M. Miritello, F. Iacona, D. Sanfilippo, G. Di Stefano, P. G. Fallica, and F. Priolo, "Electroluminescence of silicon nanocrystals in MOS structures," *Appl. Phys. A* **74**(1), 1–5 (2002).
- <sup>21</sup>A. Irrera, D. Pacifici, M. Miritello, G. Franzò, F. Priolo, F. Iacona, D. Sanfilippo, G. Di Stefano, and P. G. Fallica, "Electroluminescence properties of light emitting devices based on silicon nanocrystals," *Physica E* **16**(3–4), 395–399 (2003).
- <sup>22</sup>A. Fojtík, J. Valenta, T. H. Stuchlíková, J. Stuchlík, I. Pelant, and J. Kočka, "Electroluminescence of silicon nanocrystals in p–i–n diode structures," *Thin Solid Films* **515**(2), 775–777 (2006).
- <sup>23</sup>M. Zacharias and P. Streitenberger, "Crystallization of amorphous superlattices in the limit of ultrathin films with oxide interfaces," *Phys. Rev. B* **62**(12), 8391–8396 (2000).
- <sup>24</sup>M. Zacharias, J. Heitmann, R. Scholz, U. Kahler, M. Schmidt, and J. Bläsing, "Size-controlled highly luminescent silicon nanocrystals: A SiO/SiO<sub>2</sub> superlattice approach," *Appl. Phys. Lett.* **80**(4), 661–663 (2002).
- <sup>25</sup>A. Mehonic, T. Gerard, and A. J. Kenyon, "Light-activated resistance switching in SiO<sub>2</sub> RRAM devices," *Appl. Phys. Lett.* **111**(23), 233502 (2017).
- <sup>26</sup>C. Hoessbacher, Y. Fedoryshyn, A. Emboras, A. Melikyan, M. Kohl, D. Hillerkuss, C. Hafner, and J. Leuthold, "The plasmonic memristor: A latching optical switch," *Optica* **1**(4), 198 (2014).
- <sup>27</sup>A. A. Zakhidov, B. Jung, J. D. Slinker, H. D. Abruña, and G. G. Malliaras, "A light-emitting memristor," *Org. Electron.* **11**(1), 150–153 (2010).
- <sup>28</sup>A. Emboras, I. Goykhman, B. Desiatov, N. Mazurski, L. Stern, J. Shappir, and U. Levy, "Nanoscale plasmonic memristor with optical readout functionality," *Nano Lett.* **13**(12), 6151–6155 (2013).
- <sup>29</sup>U. Koch, C. Hoessbacher, A. Emboras, and J. Leuthold, "Optical memristive switches," *J. Electroceramics* **39**(1–4), 239–250 (2017).
- <sup>30</sup>K. E. González-Flores, B. Palacios-Márquez, J. Álvarez-Quintana, S. A. Pérez-García, L. Licea-Jiménez, P. Horley, and A. Morales-Sánchez, "Resistive switching control for conductive Si-nanocrystals embedded in Si/SiO<sub>2</sub> multilayers," *Nanotechnology* **29**(39), 395203 (2018).
- <sup>31</sup>A. Marconi, A. Anopchenko, M. Wang, G. Pucker, P. Bellutti, and L. Pavesi, "High power efficiency in Si-Nc/SiO<sub>2</sub> multilayer light emitting devices by bipolar direct tunneling," *Appl. Phys. Lett.* **94**(22), 221110 (2009).
- <sup>32</sup>A. Anopchenko, A. Marconi, E. Moser, S. Prezioso, M. Wang, L. Pavesi, G. Pucker, and P. Bellutti, "Low-voltage onset of electroluminescence in nanocrystalline-Si/SiO<sub>2</sub> multilayers," *J. Appl. Phys.* **106**(3), 033104 (2009).
- <sup>33</sup>J. López-Vidrier, Y. Berencén, S. Hernández, O. Blázquez, S. Gutsch, J. Laube, D. Hiller, P. Löper, M. Schnabel, S. Janz *et al.*, "Charge transport and electroluminescence of silicon nanocrystals/SiO<sub>2</sub> superlattices," *J. Appl. Phys.* **114**(16), 163701 (2013).
- <sup>34</sup>J. López-Vidrier, Y. Berencén, S. Hernández, B. Mundt, S. Gutsch, J. Laube, D. Hiller, P. Löper, M. Schnabel, S. Janz *et al.*, "Structural parameters effect on the electrical and electroluminescence properties of silicon nanocrystals/SiO<sub>2</sub> superlattices," *Nanotechnology* **26**(18), 185704 (2015).
- <sup>35</sup>J. López-Vidrier, S. Gutsch, O. Blázquez, J. Valenta, D. Hiller, J. Laube, J. Blanco-Portals, L. López-Gomes, S. Estradé, F. Peiró *et al.*, "Effect of Si<sub>3</sub>N<sub>4</sub>-mediated inversion layer on the electroluminescence properties of silicon nanocrystal superlattices," *Adv. Electron. Mater.* **4**, 1700666 (2018).
- <sup>36</sup>Y. Berencén, J. M. Ramirez, O. Jambois, C. Domínguez, J. A. Rodríguez, and B. Garrido, "Correlation between charge transport and electroluminescence properties of Si-rich oxide/nitride/oxide-based light emitting capacitors," *J. Appl. Phys.* **112**(3), 033114 (2012).
- <sup>37</sup>A. M. Hartel, D. Hiller, S. Gutsch, P. Löper, S. Estradé, F. Peiró, B. Garrido, and M. Zacharias, "Formation of size-controlled silicon nanocrystals in plasma enhanced chemical vapor deposition grown SiO<sub>x</sub>N<sub>y</sub>/SiO<sub>2</sub> superlattices," *Thin Solid Films* **520**(1), 121–125 (2011).
- <sup>38</sup>S. Gutsch, D. Hiller, J. Laube, M. Zacharias, and C. Kübel, "Observing the morphology of single-layered embedded silicon nanocrystals by using temperature-stable TEM membranes," *Beilstein J. Nanotechnol.* **6**(1), 964–970 (2015).
- <sup>39</sup>J. Laube, S. Gutsch, D. Wang, C. Kübel, M. Zacharias, and D. Hiller, "Two-dimensional percolation threshold in confined Si nanoparticle networks," *Appl. Phys. Lett.* **108**(4), 043106 (2016).
- <sup>40</sup>J. Laube, D. Nübling, H. Beh, S. Gutsch, D. Hiller, and M. Zacharias, "Resistivity of atomic layer deposition grown ZnO: The influence of deposition temperature and post-annealing," *Thin Solid Films* **603**, 377–381 (2016).
- <sup>41</sup>H. Beh, D. Hiller, J. Laube, S. Gutsch, and M. Zacharias, "Deposition temperature dependence and long-term stability of the conductivity of undoped ZnO grown by atomic layer deposition," *J. Vac. Sci. Technol. A* **35**(1), 01B127 (2017).
- <sup>42</sup>O. Blázquez, J. L. Frieiro, J. López-Vidrier, C. Guillaume, X. Portier, C. Labbé, P. Sanchis, S. Hernández, and B. Garrido, "Resistive switching and charge transport mechanisms in ITO/ZnO/p-Si devices," *Appl. Phys. Lett.* **113**(18), 183502 (2018).
- <sup>43</sup>J. López-Vidrier, S. Gutsch, O. Blázquez, D. Hiller, J. Laube, R. Kaur, S. Hernández, B. Garrido, and M. Zacharias, "Modulation of the electroluminescence emission from ZnO/Si NCs/p-Si light-emitting devices via pulsed excitation," *Appl. Phys. Lett.* **110**(20), 203104 (2017).

- <sup>44</sup>J. López-Vidrier, S. Hernández, D. Hiller, S. Gutsch, L. López-Conesa, S. Estradé, F. Peiró, M. Zacharias, and B. Garrido, "Annealing temperature and barrier thickness effect on the structural and optical properties of silicon nanocrystals/SiO<sub>2</sub> superlattices," *J. Appl. Phys.* **116**(13), 133505 (2014).
- <sup>45</sup>J. López-Vidrier, S. Hernández, A. M. Hartel, D. Hiller, S. Gutsch, P. Löper, L. López-Conesa, S. Estradé, F. Peiró, M. Zacharias *et al.*, "Structural and optical characterization of size controlled silicon nanocrystals in SiO<sub>2</sub>/SiO<sub>2</sub>N<sub>y</sub> multilayers," *Energy Procedia* **10**, 43–48 (2011).
- <sup>46</sup>Y. Chen, D. M. Bagnall, H. Koh, K. Park, K. Hiraga, Z. Zhu, and T. Yao, "Plasma assisted molecular beam epitaxy of ZnO on c-plane sapphire: Growth and characterization," *J. Appl. Phys.* **84**(7), 3912–3918 (1998).
- <sup>47</sup>S. Gutsch, J. Laube, A. M. Hartel, D. Hiller, N. Zakharov, P. Werner, and M. Zacharias, "Charge transport in Si nanocrystal/SiO<sub>2</sub> superlattices," *J. Appl. Phys.* **113**(13), 133703 (2013).
- <sup>48</sup>D. Hiller, A. Zelenina, S. Gutsch, S. A. Dyakov, L. López-Conesa, J. López-Vidrier, S. Estradé, F. Peiró, B. Garrido, J. Valenta *et al.*, "Absence of quantum confinement effects in the photoluminescence of Si<sub>3</sub>N<sub>4</sub>-embedded Si nanocrystals," *J. Appl. Phys.* **115**(20), 204301 (2014).
- <sup>49</sup>A. X. Chu and W. B. Fowler, "Theory of oxide defects near the Si-SiO<sub>2</sub> interface," *Phys. Rev. B* **41**(8), 5061–5066 (1990).
- <sup>50</sup>J. Yao, L. Zhong, D. Natelson, and J. M. Tour, "In situ imaging of the conducting filament in a silicon oxide resistive switch," *Sci. Rep.* **2**(1), 242 (2012).
- <sup>51</sup>A. Zimina, S. Eisebitt, W. Eberhardt, J. Heitmann, and M. Zacharias, "Electronic structure and chemical environment of silicon nanoclusters embedded in a silicon dioxide matrix," *Appl. Phys. Lett.* **88**(16), 163103 (2006).
- <sup>52</sup>C. He, J. Li, X. Wu, P. Chen, J. Zhao, K. Yin, M. Cheng, W. Yang, G. Xie, D. Wang *et al.*, "Tunable electroluminescence in planar graphene/SiO<sub>2</sub> memristors," *Adv. Mater.* **25**(39), 5593–5598 (2013).

### 6.3. Resistance state read through light absorption

Following the range of interesting optical properties presented by Si NCs, and the possibility of resistive switching already being demonstrated, the interaction of the device structure with impinging light was analyzed. Other works have already shown that the use of resistive switching materials in optical waveguides can lead to an optical read of the state by modifying the propagation losses with the resistance state (and therefore, the material inner structure).<sup>[10]</sup> In this case, the work is aimed at observing a modification of the light absorbed by the device structure presented in the previous section, as it corresponds to a tandem Si-Si NCs solar cell.<sup>[11]</sup>

In order to characterize the device response, two light sources were employed, a 532-nm continuous-wave laser (with power densities from 0.1 to 200 mW cm<sup>-2</sup>) and a monochromated Xe lamp (with power densities of 0.5–2 mW cm<sup>-2</sup> in the 300–1100 nm spectral range). The photovoltaic response of devices and their dependence with the resistance state was first analyzed using the CW laser. Different devices were set to each state, pristine, HRS and LRS, and illuminated while monitoring the current at 0 V, as it can be observed in Figure 6.2.

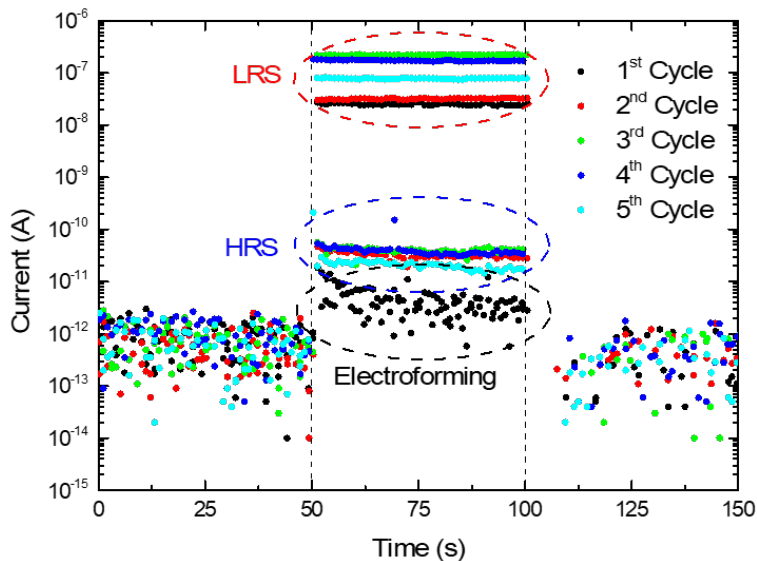


**Figure 6.2.** Readout of Si NCs containing RS devices at 0V when illuminated with a green CW laser, showing different current responses dependent of the state of the devices. Variations between cycles are negligible.

### 6.3. Resistance state read through light absorption

A sequence of darkness, illumination and darkness, for 50 s each, was employed to observe the response of each state and any remaining signal after illumination. The results show that devices in darkness present no current conduction as expected, but some conduction takes place while illuminated. With respect to the noise level of the measuring system observed in darkness,  $10^{-13}$  A, the current increases one, two or five orders of magnitude respectively for pristine, HRS and LRS, under illumination. No current is detected when returning to darkness, and the variation between cycles is negligible.

Indeed, light absorption is assumed to take place in the Si substrate or the Si NCs. The barriers of SiO<sub>2</sub> suppose a big drawback for carrier extraction. The fact that conductive paths in the form of CFs are present in the HRS and mainly the LRS, allow for the avoidance of these barriers and thus photogenerated carries are more easily extracted. The photocurrent that can be extracted scales with the power density reaching the device, and enough difference between the LRS and HRS can be detected even at the minimum laser power of  $2.4 \times 10^{-6}$  W. This fact is remarkable, as an electrical reading requiring of 3 V would already consume  $1.8 \times 10^{-4}$  W, meaning that an optical readout of the device saves energy when compared to the typically employed electrical readout.

Last, the origin of light absorption was also inspected. A reference device consisting of ZnO electrodes on top of a Si substrate was fabricated, and its spectral response compared to that of the resistive switching device at different states. Unfortunately, the lower power of the Xe lamp at some wavelengths limited the experiment. Spectral response could be obtained at 0 V only for the reference sample and the LRS state, whereas a voltage of 8 V was required for obtaining some photoconduction signal at the pristine and HRS states. Nevertheless, the compared spectra clearly identify both the Si substrate and the MLs as responsible in the absorption process. At high energies, the larger density of states of Si NCs compared to bulk Si contribute to a higher absorption in this range, resulting in an observed peak feature when these are present. In addition, a blue shift can be observed at lower energies, which agrees with the higher bandgap of Si NCs compared to bulk Si. Although the benefit in terms of optical readout of resistive switching devices is clear with these results, the overall efficiency of extraction hinders the device performance. Indeed, comparing the external quantum efficiency of the reference sample and the device in LRS, the efficiency is lower for the latter by three orders of magnitude.

## Combined properties in Si NC-containing devices

This can be mainly attributed to the barriers of SiO<sub>2</sub> in the MLs, which poses a drawback for extraction.

In any case, these results point towards another fact that should be considered together with the light emission readout of optical memristors: a very low power light absorption readout. These two combined concepts clearly demonstrate the usefulness of optical memristors as selective light emitters and detectors.

These results were presented as a talk at the European Materials Research Society (EMRS) Spring Meeting 2020 and as a poster at the 38th European Photovoltaic Solar Energy Conference and Exhibition, being a Poster Award Winner. A journal article was published in *Applied Physics Letters* **116**, 193503 (2020).

**Paper VIII: Photoelectrical reading in ZnO/Si NCs/p-Si resistive switching devices (DOI: [10.1063/5.0005069](https://doi.org/10.1063/5.0005069))**



# Photoelectrical reading in ZnO/Si NCs/p-Si resistive switching devices

Cite as: Appl. Phys. Lett. **116**, 193503 (2020); doi:10.1063/5.0005069

Submitted: 18 February 2020 · Accepted: 4 May 2020 ·

Published Online: 14 May 2020



J. López-Vidrier,<sup>1,2,a)</sup> J. L. Frieiro,<sup>1,2</sup> O. Blázquez,<sup>3</sup> D. Yazicioglu,<sup>4</sup> S. Gutsch,<sup>4</sup> K. E. González-Flores,<sup>5</sup> M. Zacharias,<sup>4</sup> S. Hernández,<sup>1,2</sup> and B. Garrido<sup>1,2</sup>

## AFFILIATIONS

<sup>1</sup>MIND, Department of Electronic and Biomedical Engineering, Universitat de Barcelona, Martí i Franquès 1, E-08028 Barcelona, Spain

<sup>2</sup>Institute of Nanoscience and Nanotechnology (IN<sup>2</sup>UB), Universitat de Barcelona, Av. Diagonal 645, E-08028 Barcelona, Spain

<sup>3</sup>Catalonia Institute for Energy Research (IREC), Jardins de les Dones de Negre 1, 2 pl., E-08930 Sant Adrià del Besòs (Barcelona), Spain

<sup>4</sup>Laboratory for Nanotechnology, IMTEK, Faculty of Engineering, University of Freiburg, Georges-Köhler-Allee 103, D-79110 Freiburg, Germany

<sup>5</sup>Centro de Investigación en Materiales Avanzados S.C. (CIMA), Unidad Monterrey-PIIT, Apodaca, NL M-66628, Mexico

<sup>a)</sup>Author to whom correspondence should be addressed: [jlopezv@ub.edu](mailto:jlopezv@ub.edu)

## ABSTRACT

The increasing need for efficient memories with integrated functionalities in a single device has led the electronics community to investigate and develop different materials for resistive switching (RS) applications. Among these materials, the well-known Si nanocrystals (NCs) have demonstrated to exhibit RS properties, which add to the wealth of phenomena that have been studied on this model material platform. In this work, we present ZnO/Si NCs/p-Si resistive switching devices whose resistance state can be electrically read at 0 V under the application of low-power monochromatic illumination. The presented effect is studied in terms of the inner structural processes and electronic physics of the device. In particular, the creation of conductive filaments through the Si NC multilayers induces a low-resistance path for photogenerated carriers to get extracted from the device, whereas in the pristine state charge extraction is strongly quenched due to the insulating nature of the NC-embedding SiO<sub>2</sub> matrix. In addition, spectral inspection of the generated photocurrent allowed unveiling the role of Si NCs in the reported effect. Overall, the hereby shown results pave the way to obtain memories whose RS state can be read under low-power conditions.

© 2020 Author(s). All article content, except where otherwise noted, is licensed under a Creative Commons Attribution (CC BY) license (<http://creativecommons.org/licenses/by/4.0/>). <https://doi.org/10.1063/5.0005069>

The resistive switching (RS) effect, which has been researched since the 1960s on resistive random-access memories (RRAMs) based on dielectric materials such as SiO<sub>2</sub>,<sup>1</sup> has attracted great interest because of its potential application in non-volatile memory storage devices. The working principle of RS is the reduction of the dielectric resistance by several orders of magnitude (low resistance state, LRS), by enabling barrier-free (quasi-Ohmic) charge transport after adequate application of an external electric field (and consequent current) through the material. The main property of this effect is, however, its reversibility, since proper polarity can recover a high resistance state (HRS).<sup>2</sup> In some metal oxides, conductive filaments (CF) are created mainly obeying two mechanisms, namely the diffusion of metal atoms from the electrodes toward the dielectric (electrochemical metallization, ECM)<sup>3</sup> and the vacancy generation by oxygen ion diffusion from

the dielectric toward the electrodes (valence change mechanism, VCM).<sup>4</sup> In addition, some groups have reported that light can also take part in RS, by either inducing stable CF formation (writing)<sup>5,6</sup> or reading the resistance state by means of electrical excitation (electroluminescence)<sup>7,8</sup> or optical transmittance (propagation losses in plasmonic waveguides),<sup>9</sup> in what is so far known as *optical memristor*. The study and development of these optical memristors can lead to a novel area of photonics-integrated memory devices.

The RS phenomenon has been widely studied in oxide materials, Si suboxides (SiO<sub>x</sub>) being particularly interesting for the electronics industry because of their compatibility with complementary metal-oxide-semiconductor technology. Here, the works led by the group of Kenyon have highlighted the importance of electrode/dielectric interfaces in the CF formation process,<sup>10,11</sup> other studies being focused on

the adequacy of certain metals to the diffusion characteristics within Si-based matrices.<sup>12</sup> After a high-temperature annealing treatment, Si nanocrystals (NCs) can be produced, in which quantum confinement allows for improved and size-controlled electronic properties with respect to bulk Si.<sup>13,14</sup> Because of the wealth of optical and electrical phenomena that Si NCs exhibit, this material has served for many years as an adequate research platform for the study of semiconductors; nevertheless, only a few works exist on the RS properties of Si NCs.<sup>8,15,16</sup> In this regard, the electro-optical properties of Si NCs can be coupled to their RS to perform proof-of-concept optical memristors. In particular, we hereby propose a Si NC-based RS device where the resistance state can be read at 0 V by exhibiting a clear photocurrent response in LRS when exposed to low-power illumination.

To perform the present study, size-controlled Si NC multilayers (MLs) were prepared via the superlattice approach,<sup>17,18</sup> by depositing  $5 \times \text{SiO}_{0.93}\text{N}_{0.23}$  [Si-rich Si oxynitride (SRON), 4.5 nm]/ $\text{SiO}_2$  (1 nm) bilayers on top of a (100) Si substrate (*p*-type, base resistivity of 1–20  $\Omega\text{cm}$ ) using plasma-enhanced chemical vapor deposition (PECVD). Afterwards, a high-temperature annealing treatment was carried out at 1150 °C for 1 h in a  $\text{N}_2$  ambient atmosphere, to induce phase separation, thus resulting in the precipitation of the Si excess (17 at. % at the selected stoichiometry) and its crystallization in the form of Si NCs. This process was followed by  $\text{H}_2$  defect passivation at 450 °C for 1 h, to get rid of the undesired dangling bonds. Prior to the ML deposition, a 2-nm-thick  $\text{Si}_3\text{N}_4$  interlayer was PECVD-deposited on top of the Si substrate, which improves the injection of minority carriers (electrons) from *p*-Si in substrate inversion conditions.<sup>19</sup> The device structure was achieved by depositing a 100-nm-thick ZnO layer on top of the MLs via atomic layer deposition (ALD) at 200 °C,<sup>20,21</sup> which acts as a transparent conductive electrode (almost negligible absorption throughout the visible range, conductivity  $\sigma > 100 \Omega^{-1}\text{cm}^{-1}$ ). A control sample was also fabricated containing neither the Si NC MLs nor the  $\text{Si}_3\text{N}_4$  interlayer (i.e., ZnO ALD-deposited on top of the *p*-Si substrate). Conventional photolithography was then used to circularly pattern the ZnO electrodes (area  $\sim 8 \times 10^{-3} \text{cm}^2$ ). Finally, the back contact was achieved by full-area Al deposition. The inset in Fig. 1(a) shows the schematic of the final device structure. Further details on material and device preparation can be found elsewhere.<sup>22–25</sup>

Electrical characterization [current–voltage  $I(V)$  and current–time  $I(t)$ ] of the devices was carried out at room temperature, in the dark and under illumination, using an Agilent B1500A semiconductor device analyzer connected to a probe station. The devices were polarized by applying voltage on the top ZnO electrode while grounding the Al-coated back contact. For measurements under monochromatic illumination, the devices were illuminated through the top ZnO electrode using either a 532-nm continuous wave laser (at power densities spanning from 0.1 to 200  $\text{mW cm}^{-2}$ ) or a Xe lamp coupled to a monochromator (reaching power densities of  $\sim 0.5$ –2  $\text{mW cm}^{-2}$  in the spectral range of 300–1100 nm). The spectral response (SR) was obtained by recording the current at each incident wavelength, once normalized by the corresponding optical power density.

To inspect the RS properties of the device structure, several devices were analyzed by means of  $I(V)$  sweeping at both positive ( $V > 0$ , substrate inversion regime) and negative ( $V < 0$ , substrate accumulation regime) voltages. As shown in Fig. 1(a) for one representative device of the set, the employed device design exhibits bipolar RS behavior. To obtain these characteristics, a particular  $I(V)$  protocol

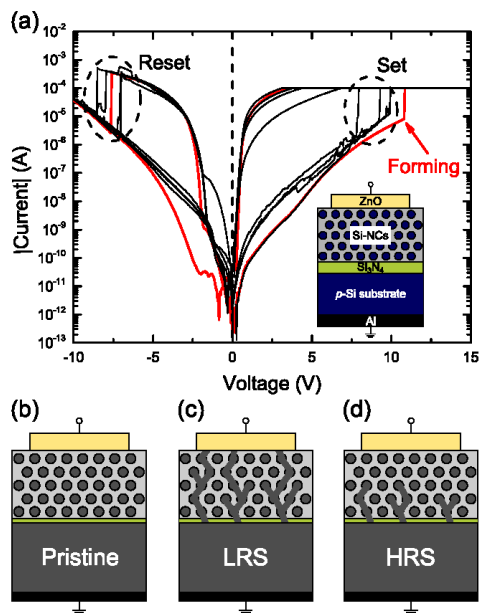


**FIG. 1.** (a)  $I(V)$  characterization corresponding to the device under test. The *electroforming* cycle and four subsequent cycles are plotted in red and black, respectively. The *set* and *reset* processes are highlighted using dashed circles. The inset shows a sketch of the device structure. (b)–(d) Schematics showing the CF formation across the Si NC MLs: pristine (b), LRS (c), and HRS (d) states.

must be followed, whose steps are described in the following, the pristine state of the device [Fig. 1(b)] being the starting point. First, an increasing positive voltage is applied, which induces a gradual increase in current until a sudden change takes place around  $\sim 11$  V, after which the device exhibits higher conductivity, reaching the LRS. This initial process is called *electroforming*, and it has been previously attributed, in Si-rich oxide-related materials,<sup>8,26</sup> to the diffusion of loosely bound  $\text{O}^{2-}$  ions within the  $\text{SiO}_2$  lattice toward the upper electrode (where a positive voltage has been applied); as a consequence, the generated O vacancies ( $\text{V}_{\text{O}}^{2+}$ ) constitute at least one high-conductivity path, a CF, improving the electrical conduction of the Si NCs/ $\text{SiO}_2$  multilayers [Fig. 1(c)]. In order to prevent excessive current to cause permanent damage to the device during this *electroforming* process, a current compliance of 100  $\mu\text{A}$  was employed. Already under substrate accumulation ( $V < 0$ ), the conductivity level is held high until reaching  $V \sim -7.5$  V, where a sudden decrease occurs, obeying to a partial reoxidation of the generated CFs during the *electroforming* process, i.e., the *reset* process [Fig. 1(d)]. The device lies now within the HRS, where current levels resemble those corresponding to the pristine state of the device. After this first RS cycle [red color in Fig. 1(a)], subsequent  $I(V)$  cycles exhibit similar processes, attaining the LRS (*set* process) at voltages between 8 V and 10 V, and HRS

(reset) at voltages between  $-6$  V and  $-9$  V; to attain lower set and reset voltages, a lower number of SRON/SiO<sub>2</sub> bilayers should be employed, as demonstrated in similar material systems in the literature.<sup>15</sup> Regarding the overall RS performance, our devices exhibit an evident conductivity variation between the LRS and the HRS, an  $I_{LRS}/I_{HRS}$  ratio of  $\sim 10^4$ – $10^5$  being measured at 3 V.

Please note that we have assumed the main CF generation taking place through the Si NCs. Indeed, this is the most plausible framework, since other works in the literature have demonstrated *in situ* creation of Si-rich regions in stoichiometric Si oxide after electric field application,<sup>27</sup> the group of Kenyon as well concluding that a CF is generated through Si-rich regions in SiO<sub>2</sub> thin films.<sup>26</sup> In addition, the suboxide region surrounding the Si NC is likely to contain O vacancy-related defects,<sup>28</sup> which might enhance the local probability of CF generation. One last comment must be made regarding the ZnO electrode. In contrast to the clear RS effect observed in devices containing sputtered ZnO,<sup>6,29</sup> ALD-deposited ZnO was found to exhibit a high conductivity ( $\sigma > 100 \Omega^{-1} \text{cm}^{-1}$ ).<sup>20,21</sup> As a consequence, no RS takes place on the ZnO/p-Si reference device, even at applied voltages higher than 40 V, and therefore, no contribution of the electrode on the CF formation through the Si NC multilayers is expected.

So far, the device structure has demonstrated to behave as a bipolar RS device, exhibiting a clear difference between both resistance states in both voltage polarities. Taking profit of the easy-identifiable RS states, we inspected the impact of controlled illumination on the electrical properties at each state, using visible light. For this, we measured the evolution of current with time without applying any voltage, i.e., at  $V = 0$  V, in the pristine, LRS, and HRS states from a single RS cycle in different devices. In Fig. 2(a), the  $I(t)$  transients corresponding to each state from a representative device, both in the dark and under illumination (532-nm laser,  $\sim 20 \text{ mW cm}^{-2}$ ), are plotted, where the change between dark and illumination is clearly indicated by vertical dashed lines. It is evident that the application of light induces an increase in current (photocurrent) in each resistance state, always well above the (dark) noise level (around  $\sim 10^{-13}$  A, which is the resolution of our experimental setup). Actually, under illumination conditions, the change in current is much more pronounced for the LRS, reaching a current increase up to five orders of magnitude with respect to dark conditions. Instead, when operating in the pristine or in the HRS states, the current only increases up to one or two orders of magnitude, respectively, from the noise level. Several devices under test showed the same behavior. In addition, the RS state of the device was read during five cycles on the same device hereby presented, only showing a slight random dispersion in LRS and HRS photocurrent, and thus confirming that this observed difference between the LRS and HRS is not stochastic.

The measured current under illumination is coming from photo-carrier generation promoted by the optical absorption of light either in the Si substrate or in the Si NCs (almost negligible absorption is expected in ZnO given its high transparency at the measured wavelength), whose extraction takes place thanks to the internal electric field created by the heterojunction (a negative flatband voltage around  $-2$  V exists, according to capacitance-voltage measurements carried out in the past and reported in Ref. 19). This inner electric field is sufficiently intense to allow photogenerated electrons to sweep toward the top ZnO electrode and photogenerated holes to be collected by the Si substrate, which induces the extraction of a non-negligible current.

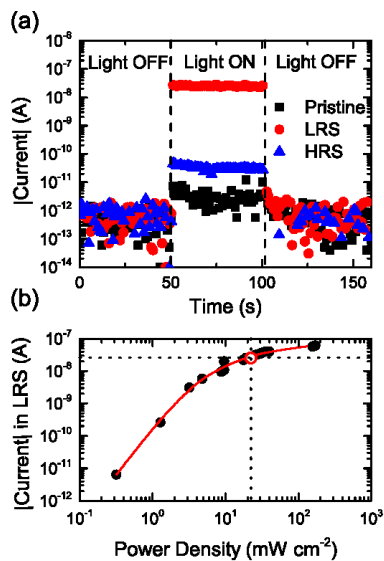


**FIG. 2.** (a) Time evolution of the current, at 0 V, corresponding to the device under study (from Fig. 1) under 532-nm laser excitation, for each RS state: pristine (black squares), LRS (red circles), and HRS (blue triangles). Vertical dashed lines indicate the time when light was switched on and off. (b) Laser power density dependence of the average current level of the device while in the LRS. The laser power conditions employed in (a) correspond to the red open circle. Black full circles represent the experimental data, whereas the red line serves as a guide to the eye.

Although this occurrence can take place in any of the resistance states under study, the SiO<sub>2</sub> barriers state a main drawback for the extraction of photogenerated carriers when the device lies in the pristine and HRS states (as confirmed by the low current levels reached under illumination). In contrast, the CFs present in the LRS notably enhance carrier extraction of the system, thus resulting in a clearly different electrical response between LRS and HRS under illumination, around  $\sim 3$  orders of magnitude. Finally, to push the device to its detection limit, we measured the generated photocurrent in the LRS under different laser power densities, whose results are plotted in Fig. 2(b). We could observe a sizeable signal even at values as low as  $\sim 0.3 \text{ mW cm}^{-2}$ , which corresponds to a power of  $2.4 \times 10^{-6}$  W after considering the device area (totally illuminated in our experiment). This optical power is about two orders of magnitude lower than the required one for reading the LRS only by electrical means [the power in LRS at a read value of 3 V is about  $\sim 1.8 \times 10^{-4}$  W, see Fig. 1(a)]. Furthermore, we could also extrapolate our measurements to pulsed excitation for evaluating the energy consumption of the reading process. Assuming that capacitive effects are not relevant in the LRS (at least in the ns-regime), and considering excitation pulses of a duration of 10 ns (in agreement with current works in RS devices),<sup>30</sup> the energy employed for the lowest-power consumption photoelectrical reading of the LRS would be  $2.4 \times 10^{-14}$  J, well below the pJ limit exhibited by other RS

systems in the literature employing only electrical means.<sup>30</sup> Overall, our results show that our RS system state can be photoelectrically read, which supposes a lower power consumption than if purely electrical means were to be considered.

To elucidate the photogeneration origin within the device structure, we proceeded with the spectral analysis of the electrical response of the LRS, at 0 V and using monochromatic excitation from 300 to 1100 nm [power density of  $\sim 0.5\text{--}2\text{ mW cm}^{-2}$ , above the device sensitivity limit, as shown in Fig. 2(b)]. The obtained SR, once adequately normalized to the energy of the incident photons, yields the external quantum efficiency [EQE =  $SR \times (h \times c) / (q \times \lambda)$ ,  $h$  being Planck's constant,  $c$  the speed of light in vacuum,  $q$  the elementary charge, and  $\lambda$  the associated wavelength to the incident photon], which represents, at each incoming wavelength, the number of extracted photocarriers per incident photon. Figure 3 plots the EQE spectrum (at 0 V) corresponding to the device under study in the LRS (red circles), and that from a control device only containing the *p*-Si substrate with ALD-deposited ZnO on top (black squares), which exhibits a direct electrical connection between these two materials. Given the low power density of the monochromatic source, no EQE spectrum could be obtained from the device under test, at 0 V, either in the pristine or HRS states; instead, the spectrum corresponding to the pristine state was acquired at 8 V for the sake of comparison (blue triangles). It is important to note that the EQE spectrum from the device under test still presents a sizeable EQE in the transparency region of Si NCs ( $\lambda > 1000\text{ nm}$ ),<sup>31</sup> arising from carrier photogeneration in the bulk Si substrate. When comparing the EQE of the device in the LRS to the Si NC-free reference device, three pieces of evidence immediately arise: the NC-based device in LRS exhibits (i) a much lower EQE (about three orders of magnitude), (ii) a change in the EQE line shape, and (iii) a blueshift of the EQE low-energy edge.

On the one hand, the limited photocurrent extracted from the devices containing Si NCs—observation (i)—could be ascribed to the presence of insulating layers ( $\text{SiO}_2$  and  $\text{Si}_3\text{N}_4$ ), which notably hinder

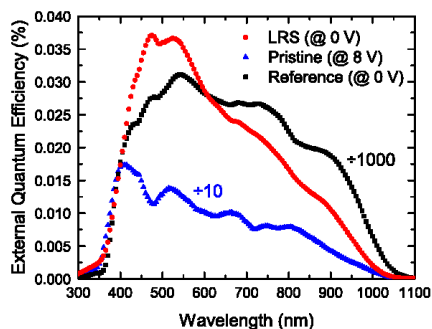


FIG. 3. External quantum efficiency spectra, obtained under illumination and at 0 V, corresponding to the device under study while in the LRS state (red circles), and acquired at 8 V while in the pristine state (blue triangles). The EQE corresponding to a ZnO/*p*-Si reference device, at 0 V, is provided as Si NC-free reference (black squares). The pristine state and reference EQE spectra are respectively divided by a factor 10 and 1000 to match with the signal level of the test device in the LRS.

the photogenerated carrier extraction; moreover, in the case of the LRS, the defective nature of the CF (or CFs)<sup>32</sup> might reduce the carrier diffusion length. Actually, the generated  $V_{\text{O}}^{2+}$  that constitutes the CF may generate a local region with mixing of those compounds (Si,  $\text{SiO}_x$ , and/or  $\text{SiN}_x$ ) that, together with its defective nature and its limited cross section, could be contributing to limit the overall carrier extraction. On the other hand, observations (ii) and (iii) suggest that the Si NC/ $\text{SiO}_2$  MLs contribute to carrier photogeneration in the LRS. The EQE line shape for the device containing the NCs—observation (ii)—presents a more pronounced feature at shorter wavelengths, which is compatible with the larger density of states in this range of energies for nanostructured Si.<sup>33,34</sup> Finally, the fact that there is a blueshift of the EQE edge at longer wavelengths—observation (iii)—also indicates a higher bandgap energy than bulk Si, compatible with carrier quantum confinement within Si NCs.<sup>13,14</sup> Indeed, the EQE spectrum at 8 V corresponding to the pristine state of the same NC-containing device confirms both observations (low-energy edge blueshift and more efficient high-energy photoresponse). Therefore, the three pieces of evidence are in agreement with Si NCs playing an important role in the electrical properties under illumination after *electroforming*, where the carriers are preferentially extracted through the CFs, i.e., the lower-resistance paths.

In summary, the clear influence of the Si NCs to the EQE of the device under study in the LRS must necessarily be linked to the CFs. Bearing in mind that carriers are mainly absorbed by either the Si NC MLs or the Si substrate (CFs present a much lower cross section compared to the device area), they need to be collected by the CFs and sent to the external circuit. Photogenerated carriers at the Si substrate can easily be driven by the built-in electric field toward the electrodes through the CF. Instead, only carriers photogenerated at NCs close to the CFs will be able to be extracted and thus contribute to photocurrent, since the NC MLs do not present a percolated network at the employed Si excess.<sup>35,36</sup> Due to the fact that the size of the exciton in Si is around 5–10 nm, the presence of a unique CF would result in a poor carrier extraction from Si NCs. Thus, and given that evidence through direct observation is still lacking in the research area, it is plausible to believe that a dense network of CFs should be created across the whole ML stack, giving rise to an effective medium that is electrically connected in the vertical direction.

The hereby presented results have shown that the ZnO/Si NC MLs/*p*-Si structure not only exhibits RS properties, but also that its resistance states can be unequivocally distinguished at 0 V by its exposure to low-power light. Here, the role of Si NC MLs is important, since (i) the presence of  $\text{SiO}_2$  ensures a bottleneck for photocarrier extraction under the HRS (and it therefore limits, or even prevents, photocurrent signal) and (ii) tuning the NC size might help selecting the light wavelength to which the LRS resistance state could be read. Overall, we have demonstrated a RS device structure whose memory state can be read under ambient light using zero electrical power, which paves the way to a future integration of Si NC-based RS devices into photonic integrated circuits.

This work was financially supported by the German Research Foundation (Nos. ZA191/27-3 and ZA191/33-1) and the Spanish Ministry of Economy, Industry and Competitiveness (No. TEC2016-76849-C2-1-R). J.L.-V. and J.L.F., respectively, acknowledge financial support from a “Juan de la Cierva”

postdoctoral fellowship (No. IJCI-2017-33451) from the Spanish Ministry of Economy, Industry and Competitiveness, and the subprogram “Ayudas para la Formación de Profesorado Universitario” (No. FPU16/06257) from the Spanish Ministry of Education, Culture and Sports.

#### DATA AVAILABILITY

The data that support the findings of this study are available from the corresponding author upon reasonable request.

#### REFERENCES

- 1 D. R. Lamb and P. C. Rundle, *J. Appl. Phys.* **18**, 29 (1967).
- 2 I. Valov, *ChemElectroChem* **1**, 26 (2014).
- 3 I. Valov, R. Waser, J. R. Jameson, and M. N. Kozicki, *Nanotechnology* **22**, 289502 (2011).
- 4 R. Waser, R. Dittmann, G. Staikov, and K. Szot, *Adv. Mater.* **21**, 2632 (2009).
- 5 A. Mehonic, T. Gerard, and A. J. Kenyon, *Appl. Phys. Lett.* **111**, 233502 (2017).
- 6 O. Blázquez, J. L. Frieiro, J. López-Vidrier, C. Guillaume, X. Portier, C. Labbé, S. Hernández, and B. Garrido, *Appl. Phys. Lett.* **115**, 261104 (2019).
- 7 W. Lin, K. Zhu, Y. Su, H. Shi, Y. Meng, and H. Zhao, *Appl. Phys. Lett.* **112**, 133504 (2018).
- 8 J. L. Frieiro, J. López-Vidrier, O. Blázquez, D. Yazicioğlu, S. Gutsch, J. Valenta, S. Hernández, M. Zacharias, and B. Garrido, *J. Appl. Phys.* **126**, 144501 (2019).
- 9 C. Hoessbacher, Y. Fedoryshyn, A. Emboras, A. Melikyan, M. Kohl, D. Hillerkuss, C. Hafner, and J. Leuthold, *Optica* **1**, 198 (2014).
- 10 A. Mehonic, M. S. Munde, W. H. Ng, M. Buckwell, L. Montesi, M. Bosman, A. L. Shluger, and A. J. Kenyon, *Microelectron. Eng.* **178**, 98 (2017).
- 11 M. S. Munde, A. Mehonic, W. H. Ng, M. Buckwell, L. Montesi, M. Bosman, A. L. Shluger, and A. J. Kenyon, *Sci. Rep.* **7**, 9274 (2017).
- 12 S. Sonde, B. Chakrabarti, Y. Liu, K. Sankumar, J. Lin, L. Stan, R. Divan, L. E. Ocola, D. Rosenmann, P. Choudhury, K. Ni, S. K. R. S. Sankaranarayanan, S. Dattad, and S. Guha, *Nanoscale* **10**, 9441 (2018).
- 13 P. Iacona, G. Franzò, and C. Spinella, *J. Appl. Phys.* **87**, 1295 (2000).
- 14 P. Iacona, G. Franzò, V. Vinciguerra, A. Irrera, and F. Priolo, *Opt. Mater.* **17**, 51 (2001).
- 15 K. E. González-Flores, B. Palacios-Márquez, J. Álvarez-Quintana, S. A. Pérez-García, L. Licea-Jiménez, P. Horley, and A. Morales-Sánchez, *Nanotechnology* **29**, 395203 (2018).
- 16 K. E. González-Flores, P. Horley, S. A. Cabañas-Tay, S. A. Pérez-García, L. Licea-Jiménez, L. Palacios-Huerta, M. Aveces-Mijares, M. Moreno-Moreno, and A. Morales-Sánchez, *Superlattices Microstruct.* **137**, 106347 (2020).
- 17 M. Zacharias, J. Heitmann, R. Scholz, U. Kahler, M. Schmidt, and J. Bläsing, *Appl. Phys. Lett.* **80**, 661 (2002).
- 18 J. López-Vidrier, S. Hernández, D. Hiller, S. Gutsch, L. López-Conesa, S. Estradé, F. Peiró, M. Zacharias, and B. Garrido, *J. Appl. Phys.* **116**, 133505 (2014).
- 19 J. López-Vidrier, S. Gutsch, O. Blázquez, J. Valenta, D. Hiller, J. Laube, J. Blanco-Portals, L. López-Conesa, S. Estradé, F. Peiró, B. Garrido, S. Hernández, and M. Zacharias, *Adv. Electron. Mater.* **4**, 1700666 (2018).
- 20 J. Laube, D. Nübling, H. Beh, S. Gutsch, D. Hiller, and M. Zacharias, *Thin Solid Films* **603**, 377 (2016).
- 21 H. Beh, D. Hiller, J. Laube, S. Gutsch, and M. Zacharias, *J. Vac. Sci. Technol., A* **35**, 01B127 (2017).
- 22 A. M. Hartel, D. Hiller, S. Gutsch, P. Löper, S. Estradé, F. Peiró, B. Garrido, and M. Zacharias, *Thin Solid Films* **520**, 121 (2011).
- 23 S. Gutsch, J. Laube, A. M. Hartel, D. Hiller, N. Zakharov, P. Werner, and M. Zacharias, *J. Appl. Phys.* **113**, 133703 (2013).
- 24 J. López-Vidrier, Y. Berencén, S. Hernández, O. Blázquez, S. Gutsch, J. Laube, D. Hiller, P. Löper, M. Schnabel, S. Janz, M. Zacharias, and B. Garrido, *J. Appl. Phys.* **114**, 163701 (2013).
- 25 J. López-Vidrier, S. Gutsch, O. Blázquez, D. Hiller, J. Laube, R. Kaur, S. Hernández, B. Garrido, and M. Zacharias, *Appl. Phys. Lett.* **110**, 203104 (2017).
- 26 A. Mehonic, S. Cuffé, M. Wojdak, S. Hudziak, O. Jambois, C. Labbé, B. Garrido, R. Rizk, and A. J. Kenyon, *J. Appl. Phys.* **111**, 074507 (2012).
- 27 J. Yao, L. Zhong, D. Natelson, and J. M. Tour, *Sci. Rep.* **2**, 242 (2012).
- 28 A. Zimina, S. Eisebitt, W. Eberhardt, J. Heitmann, and M. Zacharias, *Appl. Phys. Lett.* **88**, 163103 (2006).
- 29 O. Blázquez, J. L. Frieiro, J. López-Vidrier, C. Guillaume, X. Portier, C. Labbé, P. Sanchis, S. Hernández, and B. Garrido, *Appl. Phys. Lett.* **113**, 183502 (2018).
- 30 M. Lanza, H.-S. P. Wong, E. Pop, D. Ielmini, D. Strukov, B. C. Regan, L. Larcher, M. A. Villena, J. J. Yang, L. Goux *et al.*, *Adv. Electron. Mater.* **5**, 1800143 (2019).
- 31 S. Mirabella, R. Agosta, G. Franzò, I. Crupi, M. Miritello, R. Lo Savio, M. A. Di Stefano, S. Di Marco, F. Simone, and A. Terrasi, *J. Appl. Phys.* **106**, 103505 (2009).
- 32 J. Robertson and R. Gillen, *Microelectron. Eng.* **109**, 208 (2013).
- 33 G. Ledoux, O. Guillois, D. Porterrat, C. Reynaud, F. Huisken, B. Kohn, and V. Paillard, *Phys. Rev. B* **62**, 15942 (2000).
- 34 D. Kovalev, H. Heckler, D. Poisski, J. Diener, and F. Koch, *Opt. Mater.* **17**, 35 (2001).
- 35 S. Gutsch, D. Hiller, J. Laube, M. Zacharias, and C. Kübel, *Beilstein J. Nanotechnol.* **6**, 964 (2015).
- 36 J. Laube, S. Gutsch, D. Wang, C. Kübel, M. Zacharias, and D. Hiller, *Appl. Phys. Lett.* **108**, 043106 (2016).

## 6.4. Photovoltaic improvement with electroforming

The photovoltaic properties of the tandem Si NCs-Si devices studied in the two previous sections have been demonstrated to be maintained even after resistive switching cycling takes place. The possibility of reading the device resistance state through light absorption was thus explored, but the key remained in analyzing the effect of RS on the overall photovoltaic performance of the devices.

Indeed, it was already demonstrated in the previous section that a controlled RS process showed different efficiencies of carrier extraction depending on the state, with LRS being the most efficient. In this state, the CFs are completely formed between the electrodes, aiding in the conduction of photogenerated carriers through the SiO<sub>2</sub> barriers. However, one parameter remained to be modified to study its effect: the CC. This value blocks the overshooting in current produced during the set and electroforming processes, thus avoiding a permanent damage to the devices in the form of too strong CFs. An irreversible LRS would then appear, with such an amount of O ions lost that recuperating them in the reset re-oxidation process is not able to break the connection between electrodes.

A first experiment aimed at proving the overall better performance of the LRS was carried out by setting different devices to each state and comparing their  $I(V)$  curves in darkness and under white light illumination (in this case, a class-B solar simulator, with a power density of 1 kW m<sup>-2</sup>). When compared to dark conditions, an overall increase in conductivity is observed for pristine and HRS states under illumination, associated to a photoconduction effect; instead, this effect is minimal in LRS. More interesting is the analysis of quasi-static near-zero  $I(V)$  curves under illumination, where a photovoltaic effect is observed for the three states. Values for short-circuit current ( $I_{sc}$ ) and open-circuit voltage ( $V_{oc}$ ) for each state are displayed in Table 6.I, where it can be observed that the former increases with lower resistance state while the latter exhibits no significant variation. The fact that CFs are formed through RS creates low resistance sites that can aid in the extraction of photogenerated carriers by reducing their diffusion length (instead of having to reach the electrodes, reaching the closest CF is sufficient).

**Table 6.I.** Short-circuit current ( $I_{sc}$ ) and open-circuit voltages ( $V_{oc}$ ) corresponding to the pristine, HRS and LRS states of the analyzed ZnO/Si NCs-SiO<sub>2</sub>/Si<sub>3</sub>N<sub>4</sub>/Si devices.

Resistance state	Pristine	HRS	LRS
$I_{sc}$ (pA)	10	60	$4 \times 10^4$
$V_{oc}$ (mV)	160	500	280

Once established the better performance of devices when in LRS, especially in terms of enhanced  $I_{sc}$ , the role of the CC for the generation of CFs becomes crucial. Different devices were submitted to electroforming processes in the dark with CC ranging from 1  $\mu$ A to 1 mA, followed by an under-illumination near-zero  $I(V)$  measurement. Figure 6.3 presents the  $I_{sc}$  and  $V_{oc}$  extracted from these measurements. Overall, the conductivity of the devices increases with CC, in agreement with the formation of a stronger network of CFs. Moreover, the values of short-circuit current density ( $J_{sc}$ ),  $V_{oc}$  and the maximum efficiency for each CC can be extracted from the measurements. Following the observations that showed that higher conductive states increase their  $I_{sc}$ , the  $J_{sc}$  also increases with CC, from  $10^{-5}$  to  $1 \text{ A m}^{-2}$ . In addition,  $V_{oc}$  remains almost constant and within the values previously observed  $\sim 300 \text{ mV}$ . Last, the efficiency of the devices also increases with CC, from  $\sim 10^{-6} \%$  to  $10^{-2} \%$ .

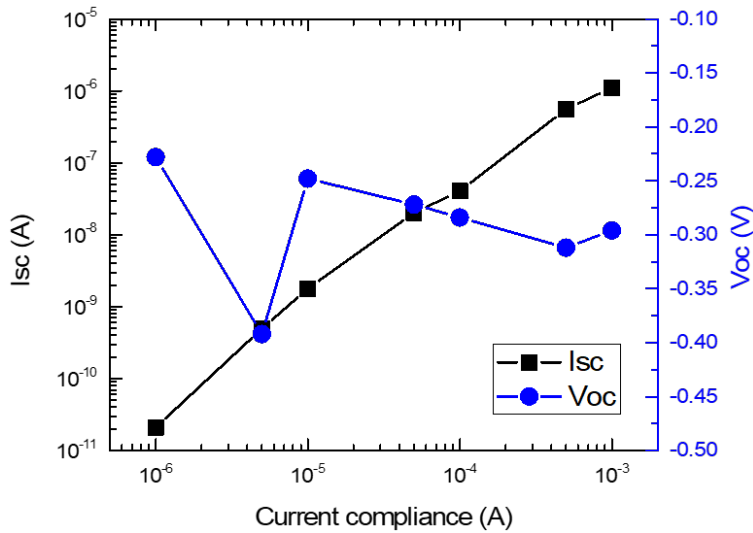


**Figure 6.3.** Short-circuit currents ( $I_{sc}$ ) and open-circuit voltages ( $V_{oc}$ ) for RS Si NCs containing devices after electroforming processes with different CC.

#### 6.4. Photovoltaic improvement with electroforming

These results can be explained in terms of the VCM mechanism. First, the increase of  $J_{SC}$  can be easily related to the presence of more and larger CFs as CC increases, which helps reducing the carrier diffusion length. Just an increase in size of the CFs would not be able to increase the  $J_{SC}$  by many orders of magnitude, as it has been observed, due to the nano-dimensions they have. Moreover, neither the photogeneration nor the number of minority carriers available in the structure is affected by the presence of CFs, and thus the  $V_{OC}$  is maintained fairly constant. Last, the overall increase in efficiency observed is also comparable to that of a pristine device and one at HRS, the former having conversion efficiencies around  $10^{-7}$  % and the latter around  $10^{-6}$  %.

In addition, the effect of the different CC values employed on the optical properties of the devices has also been studied, by measuring the EQE at different wavelengths and comparing it to a reference ZnO/Si sample. The EQE spectra also allow calculating the expected  $J_{SC}$  of the devices, which resulted in the same orders of magnitude and tendency as the ones obtained experimentally, thus corroborating the consistency of the performed measurements. The same features observed in the previous work were maintained for this study, even when applying the largest CC. Indeed, since a larger number of CFs does not break the quantum confinement of all Si NCs in the sample, these are still responsible for part of the absorption of the device.

Overall, this work demonstrates that resistive switching increases the efficiency of tandem Si NCs/Si solar cells, but it might as well be applicable to other solar cell materials that show resistive switching.

The results hereby described were presented, together with the previous work, in the 38th European Photovoltaic Solar Energy Conference and Exhibition (see previous section). In addition, a journal article was published in *Solar Energy Materials and Solar Cells* **230**, 111252 (2021).



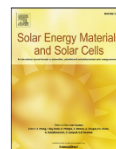
**Paper IX: Electroforming of Si NCs/p-Si photovoltaic devices: Enhancement of the conversion efficiency through resistive switching (DOI: [10.1016/j.solmat.2021.111252](https://doi.org/10.1016/j.solmat.2021.111252))**





Contents lists available at ScienceDirect

## Solar Energy Materials and Solar Cells

journal homepage: [www.elsevier.com/locate/solmat](http://www.elsevier.com/locate/solmat)

# Electroforming of Si NCs/p-Si photovoltaic devices: Enhancement of the conversion efficiency through resistive switching

J.L. Frieiro<sup>a,b</sup>, J. López-Vidrier<sup>b,c</sup>, O. Blázquez<sup>d</sup>, J. Ibáñez<sup>e</sup>, D. Yazıcıoğlu<sup>f</sup>, S. Gutsch<sup>f</sup>,  
M. Zacharias<sup>f</sup>, B. Garrido<sup>a,b</sup>, S. Hernández<sup>a,b,\*</sup>

<sup>a</sup> MIND, Department of Electronics and Biomedical Engineering, Universitat de Barcelona, Martí i Franquès 1, E-08028, Barcelona, Spain

<sup>b</sup> Institute of Nanoscience and Nanotechnology (IN<sup>2</sup>UB), Universitat de Barcelona, Av. Joan XXIII S/N, E-08028, Barcelona, Spain

<sup>c</sup> GECFET, Department of Applied Physics, Universitat de Barcelona, Martí i Franquès 1, E-08028, Barcelona, Spain

<sup>d</sup> Catalonia Institute for Energy Research (IREC), Jardins de les Dones de Negre 1, 2 pl., E-08930, Sant Adrià del Besòs, Barcelona, Spain

<sup>e</sup> Geosciences Barcelona (GEO3BCN), CSIC, Lluís Solé i Sabarís s/n, 08028, Barcelona, Spain

<sup>f</sup> Laboratory of Nanotechnology, Department of Microsystems Engineering (IMTEK), Albert-Ludwigs-Universität Freiburg, Georges-Köhler-Allee 103, D-79110, Freiburg, Germany

## ARTICLE INFO

## Keywords:

Silicon nanocrystal multilayers

Resistive switching

Photovoltaic effect

Solar cells

## ABSTRACT

In this work, the relation between the photovoltaic and resistive switching (RS) properties of metal-oxide-semiconductor devices containing Si nanocrystal (Si NC) superlattices is investigated. A first approximation concludes that the low resistance state achieved by the RS process allows for enhanced photogenerated carrier extraction when compared to the high resistance state and pristine devices. By using different current compliance values during the electroforming process, the low resistance state is further modified, improving its conductivity and the collection probability of photogenerated carriers. Conversion efficiency is enhanced by at least one and up to five orders of magnitude by applying different electroforming processes. In addition to promoting the RS properties in these devices, spectral response measurements demonstrate that Si NCs are partially responsible for the optical absorption, and that their contribution is maintained after electroforming. We thus conclude that the proposed methodology can improve the conversion efficiency of this and other multijunction solar cells or structures that also exhibit RS properties. Through RS, a dense network of conductive filaments is promoted in the insulating region, which reduces the travel distance of photocarriers for their collection.

## 1. Introduction

Silicon nanocrystals (Si NCs) have attracted much attention during the last two decades thanks to their higher radiative-transition rate with respect to bulk Si. Moreover, the electronic quantum confinement within the NCs can be engineered by controlling their size, and thus their band gap energy [1,2]. One of the approaches to achieve control on the NC size is depositing alternated nanometric stoichiometric and non-stoichiometric silicon dioxide multilayers (MLs) and applying afterwards a temperature treatment [3], exhibiting outstanding structural and optical properties. These properties have been exploited in the particular field of photovoltaics, where the combination of higher bandgap Si NCs and bulk Si in a tandem solar cell structure was addressed, aiming at overcoming the Shockley-Queisser limit for single bandgap materials [4,5]. In this frame, several attempts have been

carried out, but with little success owing to the inefficient extraction of carriers generated after photon absorption [6,7]. This low performance is due to the insulating nature of the SiO<sub>2</sub> matrix, which, despite conferring Si NCs an excellent potential barrier that favours quantum confinement, it also makes it difficult for the current to flow through the layers, consequently limiting the electrical conductivity of the system.

To solve the drawback of poor charge extraction, several approaches exist in the literature that address the problem in different ways. On one hand, doping the Si NCs and/or the insulating layers has been a commonly employed strategy in the literature for improving their electrical properties [8,9], by effectively achieving an intrinsic electric field through the Si NCs/SiO<sub>2</sub> MLs, but at the expense of usually employing processes including toxic reactants and inducing some disorder in both the SiO<sub>2</sub> matrix and the Si NCs, which deteriorates the overall optical properties of the system. On the other hand, it is also

\* Corresponding author. MIND, Department of Electronics and Biomedical Engineering, Universitat de Barcelona, Martí i Franquès 1, E-08028, Barcelona, Spain.  
E-mail address: [shernandez@ub.edu](mailto:shernandez@ub.edu) (S. Hernández).

<https://doi.org/10.1016/j.solmat.2021.111252>

Received 22 March 2021; Accepted 18 June 2021

Available online 1 July 2021

0927-0248/© 2021 Elsevier B.V. All rights reserved.

possible to directly influence the operation of the MLs-containing devices without affecting their fabrication. In this case, and associated with the limited electrical conductivity of SiO<sub>2</sub> and other dielectric layers, it has been recently observed that atomic rearrangement can be induced by applying a strong enough external electric field [10–13]. In SiO<sub>x</sub> layers, this electric field can promote a large diffusion of O<sup>2-</sup> ions that, in turn, contributes to the formation of nanometre-sized conductive filaments (CFs), or conductive paths, that may even lead to the electrical connection of both electrodes [14,15]. As a result, there is a sudden, but controlled, by means of a current compliance (CC), change in the electrical resistivity that can be tuned under certain bias conditions. Being this rearrangement process reversible, the creation or destruction of those conductive paths modifies the device conductivity, giving rise to either high or low resistance states (HRS and LRS, respectively). This effect can occur many times and is known in the literature as resistive switching (RS). This novel phenomenon allows dielectric materials to act, when embedded in the proper device structure, as resistive random-access memories (RRAMs), by employing the intrinsic material properties to mimic the digital behaviour used in memory storage.

The operation of RS devices is not trivial, and it requires an adequate combination of applied voltage and injected current at different steps of the cycle. In the most common structure for this kind of devices, a metal-insulator-metal (MIM) capacitor, the initial dielectric nature of the oxide active material sandwiched between the two metallic electrodes makes it necessary to perform an electroforming process in order to promote the first CF generation. Simultaneously to the creation of conductive paths, a network of oxygen vacancies is also created, which plays a major role in successive cycles of partial oxidation and reduction of the aforementioned paths. Actually, this network of oxygen vacancies remains within the dielectric layer throughout device operation after electroforming, making it more conductive than in the pristine state but with little or no influence on the macroscopic optical properties due to their small size relative to the device [16]. A schematic representation of such described RS process and the different resistance states is detailed in Fig. 1 for a MIM design, using a metal oxide as insulator layer.

Apart from the purely electric properties exhibited by RS devices, light interaction with these structures has been demonstrated to strongly influence on both the writing and the reading of their resistance states. On one hand, RS devices using different semiconductor or dielectric materials (like ZnO or SiO<sub>x</sub>) have undergone controlled illumination

with the aim of lowering the required voltage for the electroforming process [17,18]. On the other hand, in a previous work employing analogous Si NCs/SiO<sub>2</sub> MLs on a Si substrate, some of the authors observed the possibility to electrically read the resistance state of the devices at  $V_{\text{read}} = 0$  V, thanks to the photocarriers generated in the substrate and the connections established between the top electrode and the bottom *p*-type silicon substrate [13]. The combination of the excellent optical properties and their improved electrical conductivity in the LRS after the electroforming in Si NCs can be exploited for photovoltaic (PV) applications, overcoming in this way the high energy barriers that SiO<sub>2</sub> pose to carrier extraction [19].

In this work we study the light interaction with Si NCs/SiO<sub>2</sub> MLs deposited on a Si substrate after the electroforming process for different CC values ranging from 1  $\mu$ A to 1 mA. When illuminated with white light at 1000 W m<sup>-2</sup>, a photocurrent enhancement of more than 5 orders of magnitude with respect to the pristine state has been observed for CC higher than 100  $\mu$ A. This study demonstrates the possibility of using the RS phenomenon for solving the limited conductivity presented by the top dielectric-embedded Si NCs layers in tandem solar cells.

## 2. Materials and methods

Devices consisting of 5 × Si-rich silicon oxynitride (SRON)/SiO<sub>2</sub> superlattices (SLs) were fabricated by plasma-enhanced chemical-vapour deposition (PECVD) on *p*-type (100)-Si substrates ([B] ~ 10<sup>16</sup> cm<sup>-3</sup>, resistivity ~1–20  $\Omega$  cm), at a substrate temperature of 375 °C. The thickness of the stoichiometric barrier layer was held constant at 1 nm, found to be optimum for efficient charge transport [20,21], whereas the thickness of the Si-rich sublayers, with a controlled stoichiometry of SiO<sub>0.93</sub>N<sub>0.23</sub> (corresponding to a Si excess of 17 at.%), was nominally fixed at 3.5 nm. Prior to the first SRON sublayer, a 2-nm-thin Si<sub>3</sub>N<sub>4</sub> sublayer was grown on the substrate, with the aim of enhancing electron injection to the MLs in inversion conditions due to the fixed positive charges it contains, consequence of its defective nature [22,23]. A 10-nm capping SiO<sub>2</sub> layer was deposited on top of the structure, thus preventing the samples from further oxidation and keeping the SL structure during the post-deposition annealing process. The SLs were annealed at 1150 °C for 1 h in a high-purity N<sub>2</sub> atmosphere in order to induce the precipitation and crystallization of the Si excess in the form of Si NCs. The existing dangling bonds were afterwards H<sub>2</sub> passivated. The resulting average NC diameter was found to be  $d_{\text{NC}} = 2.9$  nm, as determined by Raman spectroscopy following the same methodology described in Refs. [21,24,25]. After all those processes, the SiO<sub>2</sub> capping layer of 10 nm was removed by wet chemical etching. The final device structure was achieved with a photolithography-patterned 200-nm-thick layer of ZnO deposited by atomic layer deposition on top of the SLs, as transparent conductive oxide (TCO), followed by full-area Al metallization on the bottom of the *p*-type Si substrate, resulting in a final device area of ~7.9 × 10<sup>-3</sup> cm<sup>2</sup> (see scheme in the inset of Fig. 2). The overall structure resembles a tandem photovoltaic device, acting the Si substrate as the bottom junction and the Si NCs MLs as the top multijunction, whereas the whole heterojunction ZnO/Si NC/*p*-Si provide a band offset of about 2 V [22]. Further details on the material and device fabrication processes can be found elsewhere [20, 21, 26].

Current-voltage  $I(V)$  characteristics were performed in dark and under illumination by using an Agilent B1500A semiconductor device analyser. The bottom contact (Al) was grounded, whereas voltage was applied on the top contact (ZnO) that was swept from -7 V to 7 V and/or -1 V–1 V, with slow enough voltage steps to ensure quasi-static conditions (measurements were performed at voltage ramps of 100 mV s<sup>-1</sup> or 8 mV s<sup>-1</sup>, respectively). For measurements under illumination, the devices were illuminated with either a white light source (quartz-halogen lamp) or by using a combination of quartz-halogen and Xe lamps coupled to a monochromator with a 2-nm spectral resolution, which allows for monochromatic excitation. The power density of the white

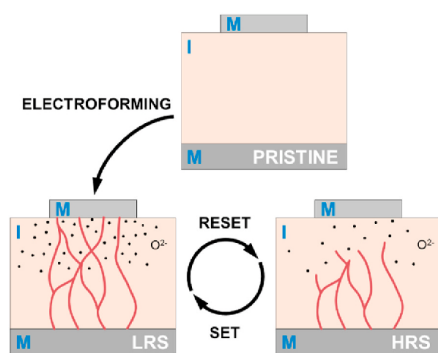


**Fig. 1.** Schematic representation of the complete RS process in a MIM device, with a metal oxide as insulator layer. The insulator is originally in the pristine state. Via an external electric field, the electroforming process is promoted, a network of oxygen ions is liberated from the insulator and CFs are generated, thus achieving the LRS. Under a different electric field polarity, the CFs can be oxidized in the reset process, physically disconnecting the electrodes and reaching the HRS. Similar to electroforming, the set process reconnects the CFs to restore a LRS.

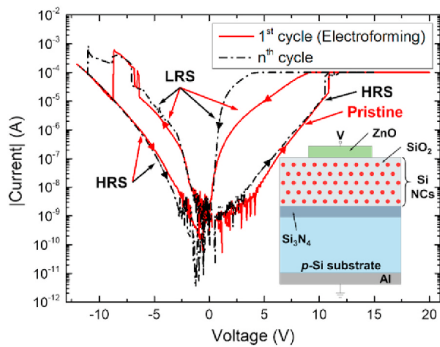


**Fig. 2.** Current-voltage  $I(V)$  cycling applied to ZnO/Si NCS/p-Si devices resulting in RS. The first cycle displays the electroforming and first reset of the device with a solid red line. A representative ( $n^{\text{th}}$ ) cycle with set and reset processes is depicted with a dashed-dotted black line. Both cycles employ 100  $\mu\text{A}$  as current compliance for the electroforming and set processes. Inset includes a schematic sketch of the device. (For interpretation of the references to colour in this figure legend, the reader is referred to the Web version of this article.)

illumination is around  $1 \text{ kW m}^{-2}$ , simulating the optical power of the Sun (solar simulator class B), whereas the power density of monochromatic excitation in the 400–1100 nm spectral range lies in the order of  $\sim 0.4\text{--}1.2 \text{ mW m}^{-2}$ . Electrical current measurements under monochromatic excitation allowed determining the spectral response (SR) of the SL structures. The SR was obtained by measuring the variation, at 0 V, of the current generated under illumination and the residual current existing in dark conditions, and normalized by the incident optical power (i.e., the incident photon flux). The external quantum efficiency (EQE) has been evaluated from the measured SR. Reflectance measurements at normal incidence were carried out with the same monochromator-coupled quartz-halogen and Xe lamps using an integrating sphere.

**3. Results and discussion**

In order to obtain the current-voltage  $I(V)$  characteristics of the three different resistance states (pristine, LRS and HRS) in dark, the ZnO/Si NCS/p-Si devices underwent consecutive  $I(V)$  sweeps. Two complete RS cycles are displayed in Fig. 2. Initially, the voltage was increased up to

20 V, using a CC of 100  $\mu\text{A}$ , to induce the electroforming process (solid red curve in Fig. 2). It is evident from the curves that there is a sudden increase in the current at a voltage around 11 V, reaching this CC value. Reducing the voltage down to zero, the change in the  $I(V)$  characteristic is clear, as the devices exhibit a much lower resistivity: the device is currently in the LRS. Further reducing the voltage down to  $-12 \text{ V}$ , the current starts increasing (in absolute value) until there is another sudden current decrease at  $-9 \text{ V}$ , indicating an increase in its resistivity: the device lies now in the HRS. Please note that our  $I(V)$  curves evidence that the HRS is slightly more conductive than the pristine state, due to the partial formation of the CFs, as it has been reported elsewhere in the literature [27]. After this first voltage sequence, the device underwent subsequent RS cycles alternating from LRS to HRS (a representative one being displayed as the black curve in Fig. 2), as shown in previous works using similar devices [10].

Using these three different states of the ZnO/Si NCS- $\text{SiO}_2$ /p-Si devices (pristine, HRS and LRS), we analysed their  $I(V)$  characteristics under illumination, comparing them to the ones obtained in dark. In Fig. 3, we present the experimental results obtained for each state in dark and under white light illumination ( $1 \text{ kW m}^{-2}$ ). There is a clear current increase at all voltages in pristine and in HRS under illumination (more than one order of magnitude for  $V > 2 \text{ V}$ ) as a consequence of the photocarriers generated within the whole device structure, thus increasing its conductivity. The situation in the LRS is, however, slightly different since only a rather marginal current increase (a factor 2 at high V) can be observed. As a summary, Table 1 compares the associated resistance values for a commonly employed read voltage of  $V_{\text{read}} = 0.1 \text{ V}$ , calculated from the data in Fig. 3. As it can be observed, the resistance decreases from pristine to HRS and again in LRS, both in dark and under white light illumination.

Apart from the already mentioned increase in the conductivity for all states, all the curves present a sizeable current and voltage either at  $V = 0 \text{ V}$  or  $I = 0 \text{ A}$ , respectively (see insets in Fig. 3), revealing weak but non-negligible short-circuit current ( $I_{\text{SC}}$ ) and open-circuit voltage ( $V_{\text{OC}}$ ) in each state. This is due to the fact that the device structure in the pristine state resembles a  $p\text{-}i\text{-}n$  heterojunction, such as the ones devoted to PV applications [28], which allows extracting some of the photogenerated carriers before their recombination. The inset for each RS state in Fig. 3

**Table 1**

Associated resistance values for the different states and measurements performed in Fig. 3, at a read voltage of  $V_{\text{read}} = 0.1 \text{ V}$ .

	$R_{\text{PRISTINE}}$ (M $\Omega$ )	$R_{\text{HRS}}$ (M $\Omega$ )	$R_{\text{LRS}}$ (M $\Omega$ )
<b>In dark</b>	$1.3 \times 10^6$	$2.3 \times 10^3$	$4.6 \times 10^3$
<b>Under illumination</b>	$1.3 \times 10^5$	$1.0 \times 10^3$	$3.3 \times 10^3$

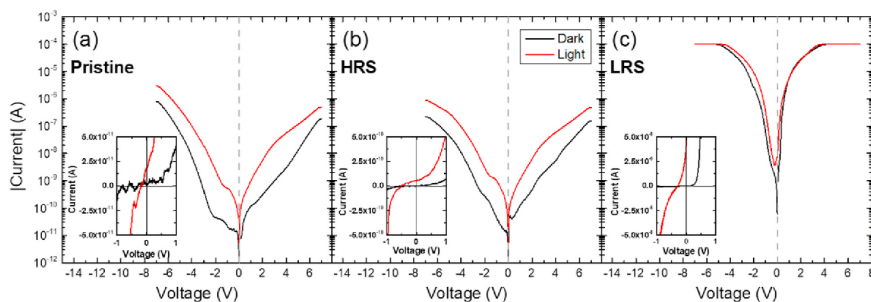


**Fig. 3.** Current-voltage  $I(V)$  measurements of the devices under study at the three different RS states: (a) pristine, (b) HRS and (c) LRS, using 100  $\mu\text{A}$  as CC. Black lines correspond to measurements in dark and red lines to measurements under white light illumination. Insets for each state present a zoom-in of the region close to 0 V, allowing the observation of the generated photocurrent. (For interpretation of the references to colour in this figure legend, the reader is referred to the Web version of this article.)

displays a zoom-in to the measured voltage range close to 0 V, in linear scale. To obtain reliable results in this range and to avoid either charge trapping or other transient effects (especially for the pristine and HRS states), these measurements were performed under quasi-static conditions, by reducing the voltage ramp down to  $8 \text{ mV s}^{-1}$ . Indeed, the device in its pristine state already presents a weak short circuit current of about  $I_{SC} \sim 10 \text{ pA}$  (weak, but well above the resolution limit of our experimental set-up, around  $0.1 \text{ pA}$ ) and an open circuit voltage around  $V_{OC} \sim 160 \text{ mV}$ . In the case of the HRS, there are slightly higher values, obtaining  $I_{SC} \sim 60 \text{ pA}$  and  $V_{OC} \sim 500 \text{ mV}$ , which could be related to the increase in its conductivity with respect to the pristine state that facilitates the extraction of the photogenerated carriers. The most impressive results, however, are observed in LRS, where  $I_{SC} \sim 40 \text{ nA}$ , three orders of magnitude higher than in HRS. In addition, we also observed a  $V_{OC} \sim 280 \text{ mV}$ , lower than the one observed in the HRS but much higher than the one in the pristine state.

The observed change in the electrical behaviour, both in dark and under illumination, can be explained by the RS mechanism. With the application of an external electric field, oxygen migration is promoted from the dielectric layer towards the positively-biased electrode, generating a network of oxygen vacancies and conductive filaments of nanometre-sized dimensions that end up connecting top and bottom electrodes [14]. Thus, the presence of higher conductivity sites distributed throughout the dielectric (i.e., the CFs) increases the diffusion length of the photogenerated electron-hole pairs, thus reducing their recombination. This, in turn, facilitates their extraction, which results in the overall improvement of their PV response in terms of  $I_{SC}$  and, to a lesser extent, of  $V_{OC}$ . Actually, the density of these CFs distributed along the dielectric layer (i.e., Si NCs/SiO<sub>2</sub>) strongly depends on the first electroforming process: an increase in the CC would induce higher oxygen migration, generating a denser network of CFs, that results in an enhanced PV response (although reducing its RS performance).

To analyse the effect of current compliance on the CF formation and their influence on the PV response, an additional study was performed with a set of different devices initially in the pristine state and submitted to an electroforming process, each of them with a different CC value. After the first CF generation, a  $I(V)$  measurement from  $-1 \text{ V}$  to  $1 \text{ V}$  and under illumination was performed. Fig. 4 displays a zoom-in of the  $-0.5 \text{ V}$ – $0.5 \text{ V}$  region of the  $I(V)$  curves obtained in devices in the LRS where different electrical stress were applied. The  $I(V)$  curves show a clear conductivity increase as the limit in the CC during the electroforming process increases, evidencing different LRS. Moreover, all the curves

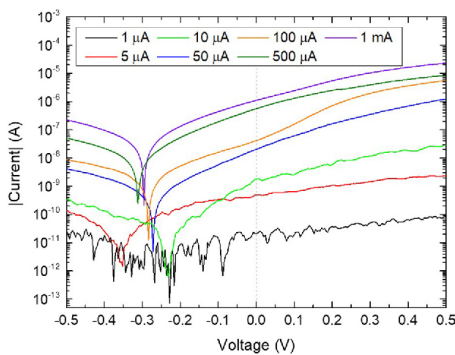


Fig. 4. Zoom-in of the quasi-static current-voltage  $I(V)$  measurements under white light illumination of the devices under study in LRS after an electroforming process with different CC. The representation of the absolute value in logarithmic scale allows visualizing the  $I_{SC}$  as the current at 0 V (dashed line) and the  $V_{OC}$  as the voltage at a peak towards low currents (equivalent to the change of sign in linear scale).

exhibit the same trend observed in Fig. 3c under illumination: there are non-negligible values of  $I_{SC}$  and  $V_{OC}$ . In Fig. 5a and b we have plotted the short-circuit current density ( $J_{SC}$ , which is the short-circuit current normalized by the electrode area), and the  $V_{OC}$  for each CC value:  $J_{SC}$  shows a clear increasing trend, whereas  $V_{OC}$  exhibits a mostly constant tendency although with a higher dispersion than the  $J_{SC}$ . From these measurements, it can also be extracted the point of maximum output power density ( $P_{out,m}$ ) after the electroforming process, given by

$$P_{out,m} = J_m \cdot V_m \tag{1}$$

where  $J_m$  and  $V_m$  correspond to the current density and voltage at the maximum power point, respectively. The values of  $J_m$  and  $V_m$  have been obtained by numerically evaluating the maximum power extracted. From equation (1), the power efficiency ( $\eta$ ) of the devices can be calculated as the ratio between the maximum electrical output power density and the light input power density ( $P_{in}$ ):

$$\eta = \frac{P_{out,m}}{P_{in}} = \frac{J_m \cdot V_m}{P_{in}} \tag{2}$$

In the case of our experimental setup, the light source has an optical power density of  $P_{in} = 1 \text{ kW/m}^2$ . Following equation (2), Fig. 5c displays the efficiency corresponding to the devices under test after the aforementioned electroforming processes: the efficiency increases from  $\sim 10^{-6} \%$  to  $10^{-2} \%$ , when the CC is modified from  $1 \mu\text{A}$  to  $1 \text{ mA}$ , in good agreement with the observed trend in  $J_{SC}$  and  $V_{OC}$ .

The results here presented can relate the trends exhibited by  $J_{SC}$ ,  $V_{OC}$  and the conversion efficiency  $\eta$  to the structural modification taking place in the material. On one hand, for a given incident photon flux,  $J_{SC}$  depends on parameters related to geometry (area of the CFs and their number) and photon-to-electron conversion (photon absorption, charge generation and extraction, diffusion length). Of all these parameters, the carrier diffusion length, and therefore the probability of carriers being

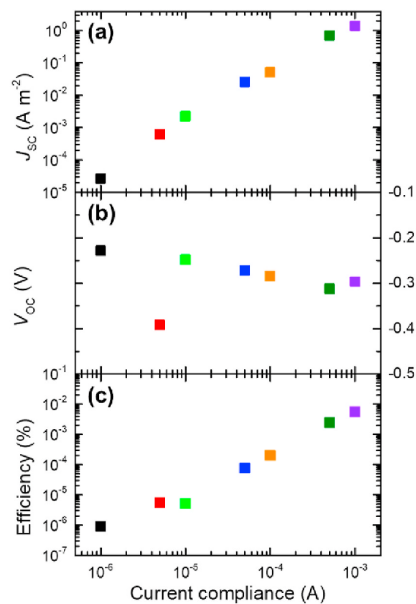


Fig. 5. (a) Short-circuit current density, (b) open-circuit voltage and (c) power efficiency in the LRS as a function of the current compliance applied during the electroforming process to a set of initially pristine devices.



collected by the electrodes, can be largely influenced by the generation of a higher number of CFs, whereas the modification of the rest of the parameters has minor (or negligible) contribution, due to the small CF-to-device volume ratio [16]. Indeed, according to the RS filament model, either the size of the filaments or their number increases as CC increases. In this frame, our increasing  $J_{SC}$  trend in Fig. 5a can be explained with an increase in the number of filaments—or a combination with an increase of their size—that increases the diffusion length of the insulating layer. In order to be extracted before recombination, photogenerated carriers no longer need to travel the whole thickness of the insulating Si NC/SiO<sub>2</sub> but rather the distance to the closest CF. In contrast, just an increase in the CF size without considering an increase in the number of filaments would not be sufficient to collect so effectively the photogenerated carriers.

On the other hand, Fig. 5b shows not so significant an evolution of  $V_{OC}$  with the CC as found for  $J_{SC}$ . Indeed, the  $V_{OC}$  represents the point where photocarrier generation and recombination are in equilibrium, and it is largely influenced by the reverse saturation current density,  $J_0$ , that is, the minority carriers circulating under dark conditions in reverse. Under illumination conditions, the photogenerated carriers recombine with these minority carriers. Since neither the photo-generation nor  $J_0$  are expected to be affected by the presence of CFs, the observed small variation of the  $V_{OC}$  with a high data dispersion can be mainly attributed to device-to-device variability.

From the results displayed in Fig. 5c, measured in the LRS, it is clear that the PV properties of the Si NCs/SiO<sub>2</sub> MLs are strongly dependent on the extent of the applied electroforming process. In particular, a higher CC increases the extraction efficiency of generated photocarriers by giving rise to a denser network of conductive filaments, through which photocarriers are extracted before their recombination. Focusing on the numerical results, it is found that increasing the current compliance by three orders of magnitude (from 1  $\mu$ A to 1 mA) results in a conversion efficiency increase of almost four orders of magnitude (from  $\eta \sim 10^{-6}$  % to  $\eta \sim 10^{-2}$  %). With respect to the pristine state, where extremely low conversion efficiencies of  $\eta \sim 10^{-7}$  % are obtained (not shown here), electroforming using the highest CC results in a LRS state with an efficiency gain of almost five orders of magnitude. When reversing towards the HRS, devices exhibit efficiencies of  $\sim 10^{-6}$  %, again demonstrating that the conductivity level of the pristine state is never reached back, owing to the partial re-oxidation of the CFs.

So far, the PV data proved that the structural modification of the dielectric layer (Si NCs/SiO<sub>2</sub> MLs) induced by controlled electroforming improves charge extraction of the devices under study. Nevertheless, this structural rearrangement can also induce alterations in the optical properties of the devices, especially in terms of optical transmission and absorption, which might be of great interest for solar cell applications. In order to analyse the effect of the RS phenomenon on the optical properties, the EQE of the devices has been determined in the LRS after employing different CC values, from spectral response [SR( $\lambda$ )] measurements (current extracted per incident optical power, in A W<sup>-1</sup>). The SR of the devices has been measured in the range of 300–1100 nm and at 0 V, which allows calculating the EQE of the devices by applying the following relation:

$$EQE(\lambda) = SR(\lambda) \frac{hc}{q\lambda} \quad (3)$$

where  $h$  is the Planck's constant,  $c$  is the speed of light in vacuum,  $q$  is the elementary charge and  $\lambda$  is the wavelength of the incoming photons. The EQE spectra of the devices submitted to electroforming processes at different CC are displayed in Fig. 6. It is evident that there is an increase of the EQE at all wavelengths as the CC increases, indicating a clear improvement of photocarrier extraction ratio at increasing CC. The results hereby reported again demonstrate that the lower the current limitation (i.e., the higher the CC), the more efficient the carrier extraction and thus quantum efficiency.

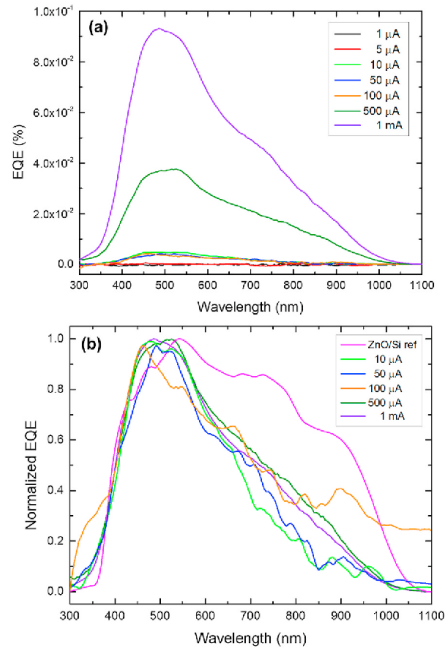


Fig. 6. (a) External quantum efficiency spectra in the LRS for each employed current compliance. (b) Normalized EQE for the higher CC and comparison with a ZnO/Si reference device.

From these spectra, the short-circuit current density ( $J_{SC}$ ) of the devices can be evaluated by considering the solar spectral irradiance  $F(\lambda)$  and the experimentally determined reflectance of the devices  $R(\lambda)$  and integrating in the range from 300 nm to 1100 nm (limiting the integration range to the near UV, where there is little spectral irradiance, and below bulk-Si band-gap energy, where there is no absorption) [29].

$$J_{SC} = J_L|_{V=0} = \frac{q}{h \cdot c} \cdot \int_{300}^{1100} F(\lambda) \cdot [1 - R(\lambda)] \cdot EQE(\lambda) |_{V=0} \cdot \lambda \cdot d\lambda \quad (4)$$

For the calculation of  $J_{SC}$  with Eq. (4), the  $F(\lambda)$  employed corresponded to the AM1.5G standard. When comparing directly measured and calculated from EQE spectra, all values lie within the same order of magnitude and the overall increasing tendency previously observed is maintained. This fact well corroborates that the measurements performed via electrical (current-voltage curves) and electro-optical (spectral response analysis) methods are consistent with each other.

Carefully examining the spectra in Fig. 6a, three distinct regions are observed, where the overall intensity is modified in a different way with the CC: (i) lower compliances below 10  $\mu$ A, which result in almost no modification of the device EQE (as previously stated in Ref. [10], in some cases these limitations result in unstable LRS); (ii) up to 100  $\mu$ A, where there is an increase in efficiency but differences between different CC values are not significant; and (iii) at large compliances, where increase of efficiency becomes evident (although at this point the resistance state is not reversible, i.e., the device is set to a permanent LRS). Indeed, from this last region it becomes evident that the EQE line-shape is barely modified irrespective of the employed current limitation level.

Comparing the line-shapes of the spectra represented in Fig. 6b for different CC, the small differences observable can be identified with

device-to-device variability. The spectral line-shape of these devices compared with a reference Si sample has been previously analysed by some of the authors (the reader is kindly redirected to Ref. [13]). It was concluded in that work that whilst the Si substrate is responsible for most of the absorption, Si NCs also contribute, as deduced from a strong signal at short wavelengths and a blueshift at longer wavelengths, both occurrences being compatible with quantum confinement (and thus the presence of nanostructured Si) within the sample. These features are maintained in the present analysis, as it can be observed by comparison in Fig. 6b with a normalized EQE of the reference device, indicating that even with large CC, CF generation does not induce a lateral percolation of the Si NC networks [30,31], and therefore confinement of the Si NCs is still maintained. It is therefore possible to conclude that, under the current limitations employed in this study, the induced rearrangement of randomly-distributed oxygen vacancies through the dielectric layer results in an increase of the overall electrical conductivity and thus carrier extraction, while barely affecting the optical absorption of the presented devices.

Some authors have previously reported the effect of ferroelectric resistive switching in the photovoltaic properties of ferroelectric materials, where the change in resistance modifies their conduction and the interface with the electrodes [32–35]. These works are mainly focused on the possibility of optically reading the device state, without exploring the possible advantages of RS in tandem PV systems. The presented methodology, namely the utilization of controlled RS on PV absorber materials to improve CF generation, is validated by our results and has shown an improvement in solar cell efficiency. This can be extended to other high-bandgap absorbing materials which simultaneously exhibit RS phenomenon, to further enhance their extraction efficiency.

#### 4. Conclusions

In this work, the RS methodology has been employed in combination with electro-optical measurements in ZnO/(SiNCs/SiO<sub>2</sub> MLs)/p-Si photovoltaic devices. A great enhancement of the PV conversion efficiency of such devices has been achieved after electroforming, inducing controlled nanoscale modifications within the dielectric layer in the form of oxygen vacancies rearrangement and the consequent formation of CFs. In particular, compared to the pristine and HRS states, when the devices lay in the LRS they allow a more efficient photogenerated-carriers extraction under either high-power white-light (class B solar simulator) or low-power monochromatic-light illumination. In addition, the use of higher CC values to limit the LRS is translated into enhanced carrier extraction by increasing the density of the CF network, thus attaining a higher collection probability. Finally, the spectral analysis of photon-to-electron conversion in LRS and its comparison with a reference Si device has identified the non-negligible absorption of Si NCs within the system, which is maintained at larger current compliances indicating a small scale of structural modifications that do not completely eliminate the quantum confinement properties associated to Si nanostructures. Overall, the presented RS procedure applied to multijunction photovoltaic devices greatly improves their carrier extraction efficiency while maintaining the optical properties, resulting in an enhancement in their PV performance.

#### Declaration of competing interest

The authors declare that they have no known competing financial interests or personal relationships that could have appeared to influence the work reported in this paper.

#### Acknowledgements

This work was financially supported by the Spanish Ministry of Economy, Industry and Competitiveness (TEC2016-76849-C2-1-R) and the German Research Foundation (ZA191/27-3 and ZA191/33-1). J.L.F.

acknowledges financial support from the subprogram “Ayudas para la Formación de Profesorado Universitario” (FPUI16/06257) from the Spanish Ministry of Education, Culture and Sports.

#### References

- [1] F. Iacona, G. Franzò, C. Spinella, Correlation between luminescence and structural properties of Si nanocrystals, *J. Appl. Phys.* 87 (2000) 1295–1303, <https://doi.org/10.1063/1.372013>.
- [2] T. van Buuren, L.N. Dinh, L.L. Chase, W.J. Siekhaus, L.J. Terminello, Changes in the electronic properties of Si nanocrystals as a function of particle size, *Phys. Rev. Lett.* 80 (1998) 3803–3806, <https://doi.org/10.1103/PhysRevLett.80.3803>.
- [3] M. Zacharias, J. Heitmann, R. Scholz, U. Kahler, M. Schmidt, J. Bläsing, Size-controlled highly luminescent silicon nanocrystals: a SiO/SiO<sub>2</sub> superlattice approach, *Appl. Phys. Lett.* 80 (2002) 661–663, <https://doi.org/10.1063/1.1433906>.
- [4] P. Würfel, *Physics of Solar Cells*, Wiley, 2005, <https://doi.org/10.1002/9783527618545>.
- [5] M.A. Green, Third generation photovoltaics: solar cells for 2020 and beyond, *Phys. E Low-Dimensional Syst. Nanostruct.* 14 (2002) 65–70, [https://doi.org/10.1016/S1386-9477\(02\)00361-2](https://doi.org/10.1016/S1386-9477(02)00361-2).
- [6] I. Perez-Wurfl, L. Ma, D. Lin, X. Hao, M.A. Green, G. Conibeer, Silicon nanocrystals in an oxide matrix for thin film solar cells with 492mV open circuit voltage, *Sol. Energy Mater. Sol. Cells* 100 (2012) 65–68, <https://doi.org/10.1016/j.solmat.2011.02.029>.
- [7] L. Wu, T. Zhang, Z. Lin, X. Jia, B. Puthen-Veetil, T. Chien-Jen Yang, H. Xia, G. Conibeer, I. Perez-Wurfl, Silicon nanocrystal photovoltaic device fabricated via photolithography and its current-voltage temperature dependence, *Sol. Energy Mater. Sol. Cells* 128 (2014) 435–440, <https://doi.org/10.1016/j.solmat.2014.06.007>.
- [8] D. Hiller, J. López-Vidrier, S. Gutsch, M. Zacharias, K. Nomoto, D. König, Defect-induced luminescence quenching vs. Charge carrier generation of phosphorus incorporated in silicon nanocrystals as function of size, *Sci. Rep.* 7 (2017) 863, <https://doi.org/10.1038/s41598-017-01001-1>.
- [9] D. Hiller, J. López-Vidrier, S. Gutsch, M. Zacharias, M. Wahl, W. Bock, A. Brodyanski, M. Kopnarski, K. Nomoto, J. Valenta, D. König, Boron-incorporating silicon nanocrystals embedded in SiO<sub>2</sub>: absence of free carriers vs. B-induced defects, *Sci. Rep.* 7 (2017) 8337, <https://doi.org/10.1038/s41598-017-08814-0>.
- [10] J.L. Frieiro, J. López-Vidrier, O. Blázquez, D. Yazicioglu, S. Gutsch, J. Valenta, S. Hernández, M. Zacharias, B. Garrido, Silicon nanocrystals-based electrochromic resistive switching device, *J. Appl. Phys.* 126 (2019) 144501, <https://doi.org/10.1063/1.5119299>.
- [11] K.E. González-Hores, B. Palacios-Márquez, J. Álvarez-Quintana, S. A. Pérez-García, L. Licea-Jiménez, P. Hodley, A. Moral-es-Sánchez, Resistive switching control for conductive Si-nanocrystals embedded in Si/SiO<sub>2</sub> multilayers, *Nanotechnology* 29 (2018) 395203, <https://doi.org/10.1088/1361-6528/aad24d>.
- [12] K.E. González-Hores, P. Hodley, S.A. Cabañas-Tay, S.A. Pérez-García, L. Licea-Jiménez, L. Palacios-Huerta, M. Aceves-Mijangas, M. Moreno-Moreno, A. Moral-es-Sánchez, Analysis of the conduction mechanisms responsible for multilevel bipolar resistive switching of SiO<sub>2</sub>/Si multilayer structures, *Superlattice. Microsc.* 137 (2020), <https://doi.org/10.1016/j.spmi.2019.106347>.
- [13] J. López-Vidrier, J.L. Frieiro, O. Blázquez, D. Yazicioglu, S. Gutsch, K.E. González-Hores, M. Zacharias, S. Hernández, B. Garrido, Photoelectrical reading in ZnO/Si NCs/p-Si resistive switching devices, *Appl. Phys. Lett.* 116 (2020) 193503, <https://doi.org/10.1063/5.0005069>.
- [14] A. Mehonik, S. Cneff, M. Wojdak, S. Hudziak, O. Jambois, C. Labbé, B. Garrido, R. Rizk, A.J. Kenyon, Resistive switching in silicon suboxide films, *J. Appl. Phys.* 111 (2012), 074507, <https://doi.org/10.1063/1.3701581>.
- [15] A. Mehonik, M.S. Munde, W.H. Ng, M. Buckley, L. Montesi, M. Bosman, A. L. Shluger, A.J. Kenyon, Intrinsic resistance switching in amorphous silicon oxide for high performance SiO<sub>x</sub> ReRAM devices, *Microelectron. Eng.* 178 (2017) 98–103, <https://doi.org/10.1016/j.mee.2017.04.033>.
- [16] O. Blázquez, J.L. Frieiro, J. López-Vidrier, C. Guillaume, X. Portier, C. Labbé, P. Sanchis, S. Hernández, B. Garrido, Resistive switching and charge transport mechanisms in ITO/ZnO/p-Si devices, *Appl. Phys. Lett.* 113 (2018) 183502, <https://doi.org/10.1063/1.5046911>.
- [17] O. Blázquez, J.L. Frieiro, J. López-Vidrier, C. Guillaume, X. Portier, C. Labbé, S. Hernández, B. Garrido, Light-activated electroforming in ITO/ZnO/p-Si resistive switching devices, *Appl. Phys. Lett.* 115 (2019), <https://doi.org/10.1063/1.5125844>.
- [18] A. Mehonik, T. Gerard, A.J. Kenyon, Light-activated resistance switching in SiO<sub>x</sub> RRAM devices, *Appl. Phys. Lett.* 111 (2017) 1200, <https://doi.org/10.1063/1.5009069>.
- [19] G. Conibeer, M. Green, R. Corkish, Y. Cho, E.-C. Cho, C.-W. Jiang, T. Fangsunannarak, E. Pink, Y. Huang, T. Puzzer, T. Trupke, B. Richards, A. Shalav, K. Lin, Silicon nanostructures for third generation photovoltaic solar cells, *Thin Solid Films* 511–512 (2006) 654–662, <https://doi.org/10.1016/j.tsf.2005.12.119>.
- [20] S. Gutsch, J. Laube, A.M. Hartel, D. Hiller, N. Zakharov, P. Werner, M. Zacharias, Charge transport in Si nanocrystal/SiO<sub>2</sub> superlattices, *J. Appl. Phys.* 113 (2013) 133703, <https://doi.org/10.1063/1.4798395>.
- [21] J. López-Vidrier, Y. Bereneñu, S. Hernández, B. Mundet, S. Gutsch, J. Laube, D. Hiller, P. Löper, M. Schnabel, S. Janz, M. Zacharias, B. Garrido, Structural parameters effect on the electrical and electroluminescence properties of silicon

- nanocrystals/SiO<sub>2</sub> superlattices, *Nanotechnology* 26 (2015) 185704, <https://doi.org/10.1088/0957-4484/26/18/185704>.
- [22] J. López-Vidrier, S. Gutsch, O. Blázquez, J. Valenta, D. Hiller, J. Laube, J. Blanco-Portals, L. López-Conesa, S. Estradé, F. Peiró, B. Garrido, S. Hernández, M. Zacharias, Effect of Si3H4-mediated inversion layer on the electroluminescence properties of silicon nanocrystal superlattices, *Adv. Electron. Mater.* 4 (2018) 1700666, <https://doi.org/10.1002/adem.201700666>.
- [23] Y. Berencén, J.M. Ramírez, O. Jambois, C. Domínguez, J.A. Rodríguez, B. Garrido, Correlation between charge transport and electroluminescence properties of Si-rich oxide/nitride/oxide-based light emitting capacitors, *J. Appl. Phys.* 112 (2012), 033114, <https://doi.org/10.1063/1.4742054>.
- [24] J. López-Vidrier, S. Hernández, D. Hiller, S. Gutsch, L. López-Conesa, S. Estradé, F. Peiró, M. Zacharias, B. Garrido, Annealing temperature and barrier thickness effect on the structural and optical properties of silicon nanocrystals/SiO<sub>2</sub> superlattices, *J. Appl. Phys.* 116 (2014) 133505, <https://doi.org/10.1063/1.4896878>.
- [25] S. Hernández, J. López-Vidrier, L. López-Conesa, D. Hiller, S. Gutsch, J. Ibáñez, S. Estradé, F. Peiró, M. Zacharias, B. Garrido, Determining the crystalline degree of silicon nanodusters/SiO<sub>2</sub> multilayers by Raman scattering, *J. Appl. Phys.* 115 (2014), <https://doi.org/10.1063/1.4878175>.
- [26] A.M. Hartel, D. Hiller, S. Gutsch, P. López, S. Estradé, F. Peiró, B. Garrido, M. Zacharias, Formation of size-controlled silicon nanocrystals in plasma enhanced chemical vapor deposition grown SiO<sub>x</sub>N<sub>y</sub>/SiO<sub>2</sub> superlattices, *Thin Solid Films* 520 (2011) 121–125, <https://doi.org/10.1016/j.tsf.2011.06.084>.
- [27] R. Waser, R. Dittmann, C. Staikov, K. Szot, Redox-based resistive switching memories: nanionic mechanisms, prospects, and challenges, *Adv. Mater.* 21 (2009) 2632–2663, <https://doi.org/10.1002/adma.200900375>.
- [28] J. Valenta, S. Mirabella, *Nanotechnology and Photovoltaic Devices*, Jenny Stanford Publishing, 2015, <https://doi.org/10.1201/b18090>.
- [29] S.M. Sze, K.K. Ng, *Physics of Semiconductor Devices*, John Wiley & Sons, Inc., Hoboken, NJ, USA, 2006, <https://doi.org/10.1002/0470068329>.
- [30] S. Gutsch, D. Hiller, J. Laube, M. Zacharias, C. Kübel, Observing the morphology of single-layered embedded silicon nanocrystals by using temperature-stable TEM membranes, *Beilstein J. Nanotechnol.* 6 (2015) 964–970, <https://doi.org/10.3762/bjnano.6.99>.
- [31] J. Laube, S. Gutsch, D. Wang, C. Kübel, M. Zacharias, D. Hiller, Two-dimensional percolation threshold in confined Si nanoparticle networks, *Appl. Phys. Lett.* 108 (2016), 043106, <https://doi.org/10.1063/1.4940971>.
- [32] L. Zhang, J. Chen, J. Cao, D. He, X. Xing, Large resistive switching and switchable photovoltaic response in ferroelectric doped BiFeO<sub>3</sub>-based thin films by chemical solution deposition, *J. Mater. Chem. C* 3 (2015) 4706–4712, <https://doi.org/10.1039/c5tc00814j>.
- [33] H. Fan, C. Chen, Z. Fan, L. Zhang, Z. Tan, P. Li, Z. Huang, J. Yao, G. Tian, Q. Luo, Z. Li, X. Song, D. Chen, M. Zeng, J. Gao, X. Lu, Y. Zhao, X. Gao, J.M. Liu, Resistive switching and photovoltaic effects in ferroelectric BaTiO<sub>3</sub>-based capacitors with Ti and Pt top electrodes, *Appl. Phys. Lett.* 111 (2017) 252901, <https://doi.org/10.1063/1.4999982>.
- [34] B. Xu, G. Wang, Y. Zhou, Q. Li, Q. Xu, Improving the photovoltaic effect by resistive switching, *Appl. Phys. Lett.* 113 (2018) 133901, <https://doi.org/10.1063/1.5039590>.
- [35] L. Huang, M. Wei, C. Gui, L. Jia, Ferroelectric photovoltaic effect and resistive switching behavior modulated by ferroelectric/electrode interface coupling, *J. Mater. Sci. Mater. Electron.* 31 (2020) 20667–20687, <https://doi.org/10.1007/s10854-020-04600-3>.

## References

- [1] A. Mehonic, S. Cueff, M. Wojdak, S. Hudziak, O. Jambois, C. Labbé, B. Garrido, R. Rizk, A. J. Kenyon, *Journal of Applied Physics* **111**, 074507, 2012.
- [2] M. Zacharias, J. Heitmann, R. Scholz, U. Kahler, M. Schmidt, J. Bläsing, *Applied Physics Letters* **80**, 661, 2002.
- [3] M. Zacharias, P. Streitenberger, *Physical Review B* **62**, 8391, 2000.
- [4] J. López-Vidrier, S. Gutsch, O. Blázquez, J. Valenta, D. Hiller, J. Laube, J. Blanco-Portals, L. López-Conesa, S. Estradé, F. Peiró, B. Garrido, S. Hernández, M. Zacharias, *Advanced Electronic Materials* **4**, 1700666, 2018.
- [5] J. López-Vidrier, S. Hernández, D. Hiller, S. Gutsch, L. López-Conesa, S. Estradé, F. Peiró, M. Zacharias, B. Garrido, *Journal of Applied Physics* **116**, 133505, 2014.
- [6] M. Perego, M. Fanciulli, C. Bonafos, N. Cherkashin, *Materials Science and Engineering: C* **26**, 835, 2006.
- [7] M. D. McCluskey, S. J. Jokela, *Journal of Applied Physics* **106**, 071101, 2009.
- [8] A. A. Zakhidov, B. Jung, J. D. Slinker, H. D. Abruña, G. G. Malliaras, *Organic Electronics* **11**, 150, 2010.
- [9] C. He, J. Li, X. Wu, P. Chen, J. Zhao, K. Yin, M. Cheng, W. Yang, G. Xie, D. Wang, D. Liu, R. Yang, D. Shi, Z. Li, L. Sun, G. Zhang, *Advanced Materials* **25**, 5593, 2013.
- [10] A. Emboras, I. Goykhman, B. Desiatov, N. Mazurski, L. Stern, J. Shappir, U. Levy, *Nano Letters* **13**, 6151, 2013.
- [11] J. López-Vidrier, P. Löper, M. Schnabel, S. Hernández, M. Canino, C. Summonte, S. Janz, B. Garrido, *Solar Energy Materials and Solar Cells* **144**, 551, 2016.



# Summary and Conclusions

---

In this Doctoral Thesis, a new concept of *optical memristors* has been explored and realized. These devices take the resistive switching properties to new applications in Optoelectronics, as controllable light emitters and absorbers. To reach the combination of both properties, different device structures and materials have been analyzed, starting from a different property to afterwards attempt the addition of the other. Fabrication of complete devices required of a series of techniques, including RF magnetron sputtering, EBE, PECVD and ALD.

The process of characterization of these devices has been focused on their electrical behavior. The device structures hereby employed had already been demonstrated in the past and in some cases even optimized, which reduced the necessity for morphological or compositional analysis –though these were also corroborated when considered important. To this end, the main tests employed have been PL, electrical  $I(V)$  measurements, pulsed voltages and constant current or voltage, modelling of charge transport mechanisms, integrated and spectrally resolved EL and photovoltaic characterization [ $I(V)$  curves under light and in dark].

In brief, devices can be separated into three approaches, mainly dependent on the initial property studied, to which the second is then attempted to be incorporated. A list of findings and a short conclusion is given for each.

## 7.1. Rare earth-doped electroluminescence

The possibility of EL and RS properties being combined was first realized in these devices containing optically active and emitting RE ions.

- ZnO is doped with terbium and europium ions, and a thorough study of the post-annealing treatment reports 700 °C to be the best temperature for them to be optically active in the matrix.

## Summary and Conclusions

- RGB light emitting devices are fabricated for ZnO doped structures, achieving red (Eu/Tb) and green (Tb), but unfortunately not blue (Ce); as well as a device combining all emissions.
- Green emission following the electronic transitions of Tb<sup>3+</sup> ions embedded in an Al/Tb/Al/SiO<sub>2</sub> structure was achieved in previously optimized multilayered devices.
- A reduction of the overall emission intensity is observed with the number of measurements, and it is correlated with oxygen movement and CFs being created.
- Red emission in the form of PL is also possible when doping the same structure with Eu<sup>3+</sup>, also following their expected electronic transitions.
- RS is observed in both Tb-doped and undoped devices, with a slight increase in the ratio between resistances and the endurance when the RE is present.

Overall, these studies demonstrate that with proper fabrication methods and device structures, light can be extracted from devices optically transparent to visible light. In addition, the first indications of combined EL and RS are observed, though a low endurance restricts further studies.

## 7.2. Resistive switching of ZnO

The second approach focused on achieving reliable RS devices with an active material that could be suitable for doping with optically active rare earth ions. Given that the latter had already been proved and the former was extensively reported in the literature, ZnO was a perfect candidate.

- Reliable RS of ZnO-based devices was demonstrated in devices lasting thousands of both  $I(V)$  and pulsed voltage cycles.
- Doping with Tb was attempted, and similarly to the case of doped Al/SiO<sub>2</sub> multilayers, an increase of resistance ratio and endurance is obtained.
- Though EL is obtained for one of the states, its origin is in the defects of ZnO rather than the intended Tb. CFs in LRS avoid the excitation of Tb ions and in HRS not enough energy is available for excitation.
- Last, for non-doped ZnO devices, the first combination of RS and light absorption is observed, allowing for a modified electroforming process when devices are illuminated. This points towards the

importance of current in the RS process, normally attributed to voltage.

All these studies conclude that while ZnO shows itself as a promising material for the intended application, the device structure and conditions of operation still require more research for improvement.

### 7.3. Resistive switching of Si NCs in SiO<sub>2</sub>

Finally, a new search of possible materials for combined RS and light interaction resulted in the testing of SiO<sub>2</sub> with embedded Si NCs. Though SiO<sub>2</sub> is difficult to break, hypothetically the presence of optically-active Si NCs would create SiO<sub>x</sub> regions where the breakdown could be initiated.

- The active matrix was deposited via PECVD following the multilayer approach and a high temperature annealing process. Nevertheless, the same process is demonstrated to create the expected network of NCs when depositing the required layers with EBE.
- These multilayers, when enclosed in a proper device structure (up to sixteen combinations of layers were tested, four were successful), present RS properties.
- Emission from Si NCs and the top ZnO electrode is possible when in different resistance states and avoiding the overwriting, thus yielding a controlled optical readout.
- The tandem solar cell structure of these devices also allows for their state readout through light absorption and carrier extraction at 0 V, increased at LRS.
- Further exploring the effect of RS in the photovoltaic effect, it is shown that the presence of stronger CFs allows for improved carrier extraction.

As a result of these works, the main objective of this Doctoral Thesis is achieved, i.e. the fabrication and characterization of *optical memristors*. The selected materials and device structure facilitate the occurrence of RS in an otherwise stable material such as SiO<sub>2</sub>. In addition, its optical transparency is maintained intact due to the nanosized dimensions of the created CFs, allowing for embedded Si NCs to remain optically active, able to emit and absorb light.

## 7.4. Future prospects

The results presented over this Doctoral Thesis correspond to some of the first evidences of light interaction with resistive switching devices reported in the literature. While interesting, these devices are far from their implementation into the Optoelectronics field as presented here, mainly due to the high voltages required for the RS process to take place. To solve this issue, the overall dimensions of the devices should be reduced, with special attention to their thickness.

In terms of the most promising devices presented, those based on Si NCs embedded in SiO<sub>2</sub>, their thickness could be reduced by modifying either the number of layers or their individual thickness. The former approach could be detrimental to the expected performance, as a reduction in the number of layers diminishes the amount of SiO<sub>x</sub> sites available for the RS process to start, as well as the number of Si NCs, thus reducing light interaction. Hence, optimization of these devices is hereby proposed to be more promising by reducing the thickness of the individual layers deposited.

In addition other optoelectronic materials could be explored. Hereby are proposed perovskites as a possible material to fabricate *optical memristors*. These semiconductors have gained a larger attention in the recent years for their light emission and absorption properties. There are also reports for some of them being able of RS, which already opens the possibility of their combination into devices. Nevertheless, most of these materials have their stability compromised to the presence of Pb in their structure. In accordance with partial objectives of this Doctoral Thesis, they could become a promising material if Pb were successfully substituted by other elements, as it is already under research by many groups.

# Resumo en Galego

---

Os dispositivos de conmutación de resistencia van ser un tema dun alto interese, especialmente dende o 2008, coma a mellor posibilidade para a próxima xeración de memorias e procesadores. Estes dispositivos presentan un comportamento que lles permite modificar a súa resistencia eléctrica entre dous ou máis estados e retelos sen necesidade dun aporte externo de enerxía. En comparación coas tecnoloxías de memoria Flash ou DRAM que dominan actualmente o mercado, o almacenamento de información pasa de ser en forma de cargas a resistencia.

A posibilidade de ter dous estados de resistencia (alta resistencia interpretada coma 0 e baixa resistencia coma 1) xa define unha memoria dixital, ca vantaxe de ter alta velocidade de conmutación, menores dimensións para cada dispositivo individual e menor consumo de enerxía, cando se comparan cas memorias Flash actuais. Estes beneficios sinalan ós dispositivos de conmutación de resistencia coma os substitutos das memorias Flash e a súa futura incorporación a memorias RAM.

Dende a súa primeira realización física, moitos foron os avances logrados en termos de materiais utilizados, estrutura dos dispositivos, modelos e integración e escalado en redes e chips. Ademais, as propiedades de estes dispositivos obren as portas a outras aplicacións máis alá de memorias puras e a arquitectura von Neumann convencional. Estas inclúen *computación en memoria*, así coma *computación inspirada no cerebro* e *neuromórfica*, onde a capacidade análoga (máis de dous estados) dos dispositivos de conmutación de resistencia están máis recentemente gañando atención.

No contexto da investigación en conmutación de resistencia, esta Tese Doutoral propoñe un área adicional que se pode beneficiar no futuro da inclusión destes dispositivos: a Optoelectrónica. A combinación de dispositivos electrónicos e fotónicos ten coma obxectivo aproveitar os beneficios de ambos campos e suplir as súas desvantaxes. Dispositivos capaces de emitir, detectar, transmitir e controlar sinais de luz xa son incluídos en telecomunicacións, sensores e biosensores.

O principal obxectivo desta Tese Doutoral é polo tanto o desenvolvemento dun novo concepto de dispositivos que chamamos

*memristores ópticos*. Cando esta investigación comezou, só uns poucos traballos sobre o tema estaban dispoñibles, sendo por tanto o enfoque presentado de gran novidade. En esencia, dous tipos de dispositivos van ser explorados e fabricados: memristores con emisión e absorción de luz. Sen embargo, ambos tiveron un requisito particular: foron necesarios materiais transparentes para que a luz fose transmitida non só a través dos eléctrodos senón tamén das capas activas dos dispositivos.

A primeira aproximación a memristores emisores de luz presentada explora as posibilidades de dispositivos emisores baseados en ións de terras raras. Estes elementos son comunmente utilizados na fabricación de capas de fósforos que son excitadas por un dispositivo emisor azul. Cando se utilizan de maneira apropiada coma dopantes en matrices de materiais óxidos, estes elementos están ópticamente activos e pódense excitar electricamente. Seguindo isto, estúdiouse a emisión de dispositivos con estrutura de Al/Tb/Al/SiO<sub>2</sub>. Unha redución da eficiencia de emisión é identificada con propiedades de conmutación de resistencia, malia que só uns poucos ciclos son posibles.

Unha segunda aproximación comeza con un óxido condutor transparente (TCO) que xa demostra propiedades de conmutación de resistencia na literatura: ZnO. Este material presenta vantaxes con respecto ó TCO máis utilizado, ITO, en forma dun material non tóxico e abundante. A maiores, pódese dopar con ións de terras raras ópticamente activos. Do mesmo xeito que sucedeu no procedemento anterior, a conmutación de resistencia é posible, pero o engadido dos ións de terras raras reduce moito a súa resistencia.

Finalmente, unha estratexia diferente permite conseguir os resultados obxectivo. Óxido de silicio é empregado coma un material con propiedades de conmutación de resistencia xa reportadas, onde nanocristais de silicio (Si NCs) son incrustados coma centros luminescentes. A súa combinación resulta ser óptima para a aplicación obxectivo, lográndose dispositivos duradeiros con emisións ben diferenciadas dependentes do estado de resistencia e que evita a súa reescritura ó ler.

Asemade, o rango de propiedades ópticas que teñen dispoñibles estes dispositivos ca presenza dos Si NCs esténdese á absorción de luz. Estes, poden ser lidos de maneira óptica aproveitando o efecto fotovoltaico da súa estrutura de célula solar tándem, distinguindo alta e baixa extracción de portadores dependendo do seu estado de resistencia.

Por último, explórase o efecto da conmutación de resistencia e a presenza de filamentos condutores nestas células solares, lográndose un alto incremento da eficiencia cando se comparan a dispositivos prístinos.



# Scientific and Academic Contributions

---

## 9.1. List of publications

- G. Vescio, J. L. Frieiro, A. F. Gualdrón-Reyes, S. Hernández, I. Mora-Seró, B. Garrido, A. Cirera; High Quality Inkjet Printed-Emissive Nanocrystalline Perovskite CsPbBr<sub>3</sub> Layers for Color Conversion Layer and LEDs Applications; *Advanced Materials Technologies* (published online, January 27<sup>th</sup>), 2022.
- K. E. González-Flores, J. L. Frieiro, P. Horley, S. A. Pérez-García, L. Palacios-Huerta, M. Moreno, J. López-Vidrier, S. Hernández, B. Garrido, A. Morales-Sánchez; Ultraviolet, visible and near infrared photoresponse of SiO<sub>2</sub>/Si/SiO<sub>2</sub> multilayer system into a MOS capacitor; *Materials Science in Semiconductor Processing* **134**, 106009, 2021.
- **(Paper IX)** J. L. Frieiro, J. López-Vidrier, O. Blázquez, J. Ibáñez, D. Yazıcioğlu, S. Gutsch, M. Zacharias, B. Garrido, S. Hernández; Electroforming of Si NCs/p-Si photovoltaic devices: Enhancement of the conversion efficiency through resistive switching; *Solar Energy Materials and Solar Cells* **230**, 111252, 2021.
- **(Paper I)** C. Guillaume, J. L. Frieiro, O. Blázquez, C. Labbé, J. López-Vidrier, B. Garrido, S. Hernández, B. Liu, L. Khomenkova, C. Frilay, F. Lemarié, C. Leroux, D. Pelloquin, X. Portier; Influence of post annealing treatments on the luminescence of rare earth ions in ZnO: Tb, Eu/Si heterojunction; *Applied Surface Science* **556**, 149754, 2021.
- M. López, J. L. Frieiro, M. Nuez-Martínez, M. Pedemonte, F. Palacio, F. Teixidor; Nanostructure ITO and Get More of It. Better Performance at Lower Cost; *Nanomaterials* **10**, 1974, 2020.
- **(Paper II)** J. L. Frieiro, C. Guillaume, J. López-Vidrier, O. Blázquez, S. González-Torres, C. Labbé, S. Hernández, X. Portier, B. Garrido; Toward RGB LEDs based on rare earth-doped ZnO; *Nanotechnology* **31**, 465207, 2020.

- **(Paper VIII)** J. López-Vidrier, J. L. Frieiro, O. Blázquez, D. Yazıcıoğlu, S. Gutsch, K. E. González-Flores, M. Zacharias, S. Hernández, B. Garrido; Photoelectrical reading in ZnO/Si NCs/p-Si resistive switching devices; *Applied Physics Letters* **116**, 193503, 2020.
- **(Paper V)** O. Blázquez, J. L. Frieiro, J. López-Vidrier, C. Guillaume, X. Portier, C. Labbé, S. Hernández, B. Garrido; Light-activated electroforming in ITO/ZnO/p-Si resistive switching devices; *Applied Physics Letters* **115**, 261104, 2019.
- **(Paper VII)** J. L. Frieiro, J. López-Vidrier, O. Blázquez, D. Yazıcıoğlu, S. Gutsch, J. Valenta, S. Hernández, M. Zacharias, B. Garrido; Silicon nanocrystals-based electroluminescent resistive switching device; *Journal of Applied Physics* **126**, 144501, 2019.
- **(Paper VI)** O. Blázquez, L. López-Conesa, J. López-Vidrier, J. L. Frieiro, S. Estradé, F. Peiró, J. Ibáñez, S. Hernández, B. Garrido; Size-Controlled Si Nanocrystals Fabricated by Electron Beam Evaporation; *Physica Status Solidi A* **216**, 1800619, 2019.
- **(Paper IV)** O. Blázquez, J. L. Frieiro, J. López-Vidrier, C. Guillaume, X. Portier, C. Labbé, P. Sanchis, S. Hernández, B. Garrido; Resistive switching and charge transport mechanisms in ITO/ZnO/p-Si devices; *Applied Physics Letters* **113**, 183502, 2018.
- **(Paper III)** J. L. Frieiro, O. Blázquez, J. López-Vidrier, L. López-Conesa, S. Estradé, F. Peiró, J. Ibáñez, S. Hernández, B. Garrido; Green Electroluminescence of Al/Tb/Al/SiO<sub>2</sub> Devices Fabricated by Electron Beam Evaporation; *Physica Status Solidi A* **215**, 1700451, 2017.

## 9.2. Paper contribution statement

The present Doctoral Thesis is presented by compendium of Journal articles, comprised of a total of nine published articles presented throughout *Chapter 7. Electroluminescence of Rare Earth containing devices*, *Chapter 8. Resistive switching of ZnO* and *Chapter 9. Combined properties in Si NC-containing devices*. The work presented in all of them is original, though there are not introduced in chronological order but rather according to their topic.

From the list of articles marked in the previous section, it should be noted that at least articles II, III, VII, VIII and IX form a selection that respect the regulation established by the University of Barcelona for presentation of Doctoral Thesis by compendium of articles. Papers II, VIII and IX are in the first quartile, while III and VII are in the second, being first author in four of them and second in the other. In addition, only paper VIII corresponds to a letter. The rest of the documents are included for completeness and their scientific relevance, to be evaluated by the Committee. Table 9.I summarizes the contributions of the author to each paper.

**Table 9.I.** Statement of contributions to the papers presented in this Doctoral Thesis.

	I	II	III	IV	V	VI	VII	VIII	IX
Design of experiments									
Measurement									
Data analysis									
Writing									
Discussion									
First author									

### 9.3. Participation in conferences

- G. Vescio, J. L. Frieiro, M. Oszejca, N. Lüchinger, S. González-Torres, A. Fernández-Guerra, J. López-Vidrier, B. Wilk S, S. Öz, Hernández, A. Cirera, B. Garrido; Inkjet-printed Ag<sub>2</sub>BiI<sub>5</sub> and Ag<sub>3</sub>BiI<sub>6</sub> for eco-friendly flexible solar cells; Poster, *EMRS Spring Meeting*, Virtual Meeting, 2021.
- S. González-Torres, A. Fernández-Guerra, A. F. Gualdrón-Reyes, I. Mora-Seró, M. Oszejca, N. Lüchinger, M. Rossier, A. Hauser, F. Linardi, J. L. Frieiro, G. Vescio, A. Cirera, S. Hernández, B. Garrido; Inkjet-printed metal halide perovskite devices; Poster, *EMRS Spring Meeting*, Virtual Meeting, 2021.
- S. González-Torres, A. Fernández-Guerra, J. L. Frieiro, G. Vescio, M. Oszejca, N. Lüchinger, M. Rossier, A. Hauser, F. Linardi, S. Hernández,

## Scientific and Academic Contributions

B. Garrido, A. Cirera; Optimization and performance of all inkjet-printed metal oxide heterojunctions for optoelectronic applications; Poster, *EMRS Spring Meeting*, Virtual Meeting, 2021.

- J. López-Vidrier, J. L. Frieiro, S. González-Torres, J. Bertomeu, S. Hernández, B. Garrido; Photovoltaic response dependence on the resistive switching state of silicon nanocrystal multilayers; Poster, 38th European Photovoltaic Solar Energy Conference and Exhibition, Lisbon (Portugal), 2021.
- J. L. Frieiro, J. López-Vidrier, S. González-Torres, O. Blázquez, K. E. González-Flores, D. Yazıcıoğlu, S. Gutsch, M. Zacharias, S. Hernández, B. Garrido; Silicon nanocrystal multilayers as active material for electro-optical resistive switching devices; Oral presentation, *EMRS Spring Meeting*, Strasbourg (France), 2020.
- J. L. Frieiro, C. Guillaume, J. López-Vidrier, O. Blázquez, C. Labbé, C. Frilay, F. Lemarié, X. Portier, S. Hernández, B. Garrido; Electroluminescent rare earth-doped ZnO for white LEDs; Oral presentation, *EMRS Spring Meeting*, Strasbourg (France), 2020.
- J. Parra, I. Olivares, A. Brimont, J. L. Frieiro, O. Blázquez, S. Hernández, B. Garrido, P. Sanchis; Non-volatile and ultra-compact photonic memory, Poster, *European Conference on Integrated Optics*, Ghent (Belgium), 2019.
- C. Guillaume, J. L. Frieiro, O. Blázquez, C. Labbé, B. Garrido, S. Hernández, C. Frilay, F. Lemarié, X. Portier; Ce, Tb and Eu doped ZnO annealed films for LEDs application; Poster, *EMRS Fall Meeting*, Warsaw (Poland), 2019.
- O. Blázquez, J. L. Frieiro, J. López-Vidrier, C. Guillaume, X. Portier, C. Labbé, P. Sanchís, S. Hernández, B. Garrido; Influence of light on the resistive switching states of ITO/ZnO/p-Si devices; Oral presentation, *EMRS Fall Meeting*, Warsaw (Poland), 2019.
- J. L. Frieiro, J. López-Vidrier, O. Blázquez, D. Yazıcıoğlu, S. Gutsch, J. Valenta, M. Zacharias, S. Hernández, B. Garrido; Silicon nanocrystals-based devices for electroluminescence and resistive switching applications; Oral presentation, *EMRS Fall Meeting*, Warsaw (Poland), 2019. **Graduate Student Award of Symposium A.**

- O. Blázquez, J. L. Frieiro, F. Bonet-Isidro, S. González-Torres, J. López-Vidrier, C. Guillaume, X. Portier, C. Labbé, P. Sanchís, S. Hernández, B. Garrido; Light effect on the resistive switching properties of ZnO-based devices; Poster, *Annual Meeting of the Institute of Nanoscience and Nanotechnology of the UB*, Barcelona (Spain), 2019.
- J. L. Frieiro, J. López-Vidrier, O. Blázquez, D. Yazıcıoğlu, S. Gutsch, J. Valenta, M. Zacharias, S. Hernández, B. Garrido; Resistive switching readout through silicon nanocrystals electroluminescence; Poster, *Annual Meeting of the Institute of Nanoscience and Nanotechnology of the UB*, Barcelona (Spain), 2019.
- F. Bonet-Isidro, J. L. Frieiro, O. Blázquez, J. López-Vidrier, S. González-Torres, C. Guillaume, C.; X. Portier, C. Labbé, P. Sanchís, S. Hernández, B. Garrido; ITO/ZnO/p-Si resistive switching devices property improvement via Tb-doping; Poster, *Annual Meeting of the Institute of Nanoscience and Nanotechnology of the UB*, Barcelona (Spain), 2019.
- J. L. Frieiro, J. López-Vidrier, O. Blázquez, D. Yazıcıoğlu, S. Gutsch, J. Valenta, S. Hernández, M. Zacharias, B. Garrido; Electroluminescence-readable memristor based on silicon nanocrystals; Oral presentation, *EMRS Spring Meeting*, Nice (France), 2019.
- F. Bonet-Isidro, J. L. Frieiro, O. Blázquez, J. López-Vidrier, S. González-Torres, C. Guillaume, C.; X. Portier, C. Labbé, P. Sanchís, S. Hernández, B. Garrido; Effect of Tb-doping on ITO/ZnO/p-Si resistive switching devices; Poster, *EMRS Spring Meeting*, Nice (France), 2019.
- O. Blázquez, J. L. Frieiro, F. Bonet-Isidro, S. González-Torres, J. López-Vidrier, C. Guillaume, X. Portier, C. Labbé, P. Sanchís, S. Hernández, B. Garrido; Light effect on the resistive switching properties of ITO/ZnO/p-Si devices; Poster, *EMRS Spring Meeting*, Nice (France), 2019.
- J. López-Vidrier, S. Gutsch, O. Blázquez, J. L. Frieiro, D. Hiller, S. Hernández, B. Garrido, M. Zacharias; Effect of ZnO electrode on the electroluminescence emission of Si NC/SiO<sub>2</sub> multilayers; Oral presentation, *EMRS Spring Meeting*, Strasbourg (France), 2018.
- O. Blázquez, J. L. Frieiro, J. López-Vidrier, L. López, C. Guillaume, S. Estradé, X. Portier, S. Hernández, F. Peiró, C. Labbé, B. Garrido;

Resistive switching and charge transport mechanisms from ITO/ZnO/p-Si devices; Oral presentation, *EMRS Spring Meeting*, Strasbourg (France), 2018.

- O. Blázquez, J. López-Vidrier, J. L. Frieiro, L. López-Conesa, S. Estradé, F. Peiró, J. Ibáñez, S. Hernández, B. Garrido; Size-controlled Si nanocrystals deposited by electron beam evaporation; Poster, *EMRS Spring Meeting*, Strasbourg (France), 2018.
- J. L. Frieiro, O. Blázquez, J. López-Vidrier, S. Hernández, B. Garrido; The effect of Tb nano-barriers on the SiAlO resistive switching properties; Poster, *EMRS Spring Meeting*, Strasbourg (France), 2018.
- O. Blázquez, J. López-Vidrier, J. L. Frieiro, L. López-Conesa, S. Estradé, F. Peiró, J. Ibáñez, S. Hernández, B. Garrido; Size-controlled Si nanocrystals deposited by electron beam evaporation; *Annual Meeting of the Institute of Nanoscience and Nanotechnology of the UB*, Barcelona (Spain), 2018.
- J. Parra, I. Olivares, J. L. Frieiro, O. Blázquez, S. Hernández, B. Garrido, P. Sanchis; Transparent conducting oxides for optoelectronics and biosensing applications; Invited presentation, *International Conference on Transparent Optical Networks (ICTON)*, Bucharest (Romania), 2018.
- B. Garrido, O. Blázquez, J. López-Vidrier, A. Huguet, R. Pruna, M. López, J. L. Frieiro, S. Hernández; Materials and devices for integrated optoelectronics, biosensing and human centric lighting; Oral presentation, *2nd Workshop on Photonic Integrated Circuits for Telecom & Bio / Life Sciences*; Castelldefels (Spain), 2017.

#### 9.4. Participation in scientific projects

- **Title:** Optoelectrónica impresa basada en óxidos metálicos y perovskitas (PRITES)  
**Principal investigator:** Prof. Blas Garrido Fernández, Prof. Albert Cirera Hernández  
**Funding:** Spanish Ministry of Science, Innovation and Universities  
**Reference:** PID2019-105658RB-I00  
**Amount:** 193 600.00 €  
**Duration:** 01/06/2020 – 31/05/2023

- **Title:** DDrop-on demand flexible Optoelectronics & Photovoltaics by means of Lead-Free halide perovskites (DROP-IT)  
**Principal investigator:** Prof. Blas Garrido Fernández  
**Funding:** European Union  
**Reference:** H2020-EU.1.2.1.862656  
**Amount:** 571 455.00 €  
**Duration:** 01/11/2019 – 30/04/2023
  
- **Title:** Desarrollo de óxidos de metales de transición con tecnología de silicio para conmutadores electrónicos (memristores) y células solares (METALONIC)  
**Principal investigator:** Prof. Blas Garrido Fernández, Dr. Sergi Hernández Márquez  
**Funding:** Spanish Ministry of Economy and Competitiveness  
**Reference:** TEC2016-76849-C2-1-R  
**Amount:** 139 755.00 €  
**Duration:** 30/12/2016 – 29/12/2019

## 9.5. Teaching

- 2020 – 2021 (H.Gr@d: 54.0, H.PDA: 146.68)
  - 360572 Informàtica, TG1035 *Física*, Pràctiques d'ordinadors.  
(H.Gr@d: 52.0, H.PDA: 138.68)
  - 571424 Nanoenergia, M0802 *Nanociència i Nanotecnologia*, Pràctiques de laboratori.  
(H.Gr@d: 2.0, H.PDA: 8.0)
  
- 2019 – 2020 (H.Gr@d: 58.0, H.PDA: 157.35)
  - 360572 Informàtica, TG1035 *Física*, Pràctiques d'ordinadors.  
(H.Gr@d: 52.0, H.PDA: 138.68)
  - 571419 Ciència i Anàlisi de Superfícies, M0802 *Nanociència i Nanotecnologia*, Pràctiques de laboratori.  
(H.Gr@d: 4.0, H.PDA: 10.67)
  - 571424 Nanoenergia, M0802 *Nanociència i Nanotecnologia*, Teoricopràctica.  
(H.Gr@d: 2.0, H.PDA: 8.0)
  
- 2018 – 2019 (H.Gr@d: 58.0, H.PDA: 162.68)
  - 360572 Informàtica, TG1035 *Física*, Pràctiques d'ordinadors.

## Scientific and Academic Contributions

(H.Gr@d: 52.0, H.PDA: 138.68)

- 571419 Ciència i Anàlisi de Superfícies, M0802 *Nanociència i Nanotecnologia*, Pràctiques de laboratori.  
(H.Gr@d: 4.0, H.PDA: 16.0)
- 571424 Nanoenergia, M0802 *Nanociència i Nanotecnologia*, Teoricopràctica.  
(H.Gr@d: 2.0, H.PDA: 8.0)

### 9.6. Supervision of students

- Cerda, G., “Characterization of the ZnO based Memristor”, Master Thesis. *Master in Nanoscience and Nanotechnology* (University of Barcelona), Barcelona (Spain), 2018.
- Mo’awia Khalil, M. E., “Electro-optical properties of ZnO-based resistive switching devices”, Master Thesis. *Master in Nanoscience and Nanotechnology* (University of Barcelona), Barcelona (Spain), 2018.
- Fernández-Guerra, A., “Resistive switching properties of metal oxides for neuromorphic applications”, Bachelor Thesis. *Bachelor’s Degree in physics* (University of Barcelona), Barcelona (Spain), 2019.